In-source high-resolution spectroscopy of holmium radioisotopes

—

On-line tailored perpendicular laser interaction at ISOLDE's Laser Ion Source and Trap LIST

Dissertation
zur Erlangung des akademischen Grades
„Doktor der Naturwissenschaften"
am Fachbereich Physik, Mathematik und Naturwissenschaften
der Johannes Gutenberg-Universität in Mainz

Reinhard Matthias Heinke
geb. in Wiesbaden

Mainz, den 23. Oktober 2019

Datum der mündlichen Promotionsprüfung: 16.10.2019

Abstract

The combination of resonant laser ionization and electromagnetic mass separation has become an extremely powerful and versatile tool for the study of atomic and nuclear physics properties of exotic species over the last decades. It exploits step-wise resonant excitation and subsequent ionization by laser light precisely tuned to unique, fingerprint-like resonances in the electronic shell as a technique, which is both highly efficient and inherently element-selective. It is applied at the majority of large scale radioactive ion beam facilities world-wide, directly coupled to the production of radioactive species which are presented to laser ionization in a hot atomic vapor cavity. This ion source type is an excellent environment for direct laser spectroscopic investigations on the atomic structure. Fundamental ground state properties of the nucleus can be derived from minute effects arising from interactions with the electronic shell. Most commonly, such hyperfine structure investigations are prevented by the limited spectral resolution due to Doppler broadening in the hot atomic vapor.

This thesis comprises the development, characterization and first-time application of a laser ion source specialized for high resolution laser spectroscopy. It is based on the Perpendicularly Illuminated Laser Ion Source and Trap (PI-LIST), which was recently developed in the LARISSA group, and uses a perpendicular geometry between incident laser light and the atomic beam effusing from a hot cavity to overcome Doppler limitations. As this previous setup relies on lateral laser in-coupling through windows at the source vacuum vessel, the upgrade presented here is tailored for installation at radioactive ion beam facilities such as CERN-ISOLDE, where access to the highly radioactive front end area is impossible.

With this novel tool, high resolution hyperfine structure studies on long-lived, radioactive holmium isotopes were performed at the RISIKO mass separator at Mainz University. The extremely dense spectra arising from the coupling of both high nuclear spin and total angular momenta of the atomic states demanded high spectral resolution far beyond the capabilities of a standard hot cavity laser ion source. With outstanding experimental line widths as low as $100\,\mathrm{MHz}$ FWHM, the first-time extraction of nuclear structure parameters of $^{166\mathrm{m}}$Ho was possible. Its nuclear spin was confirmed as $I = 7$. Additionally, the results on the magnetic dipole moment, the spectroscopic quadrupole moment and the first determination of the change in mean square charge radii towards the neutron-rich side of the holmium isotopic chain resolve inconsistencies in literature data and confirm the pronounced prolate deformation in this mid-shell region of the nuclear chart.

The PI-LIST with internal reflection proved to be completely competitive to the previous mode with external lateral laser incoupling in all operational parameters. On dedicated characterization experiments, ultimate line widths of as low as $60\,\mathrm{MHz}$ were achieved, and an overall efficiency of the setup of up to the 10^{-4} regime was confirmed. The PI-LIST is thus proven to be ready for installation at on-line facilities.

IV

Zusammenfassung

Die Kombination von resonanter Laserionisation mit elektromagnetischer Massensepa-ration hat sich über die letzten Jahrzehnte zu einem leistungsfähigen und vielseitigen Werkzeug zum Studium der Atom- und Kernphysik exotischer Spezies entwickelt. Die Methode nutzt schrittweise, resonante Anregung mit abschließender Ionisation durch präzise abgestimmte Laserstrahlung über die spezifischen optischen Übergänge der Atomhülle und stellt damit eine sowohl hocheffiziente als auch inhärent elementselektive Technik dar. Sie wird weltweit an Isotopenfabriken verschiedener Großforschungseinrich-tungen eingesetzt, wo direkte Kopplung an die Erzeugung radioaktiver Spezies besteht, die als Atomdampf in einer heißen Kavität zur Ionisation zur Verfügung gestellt werden. Diese Geometrie ist gleichermaßen eine exzellente Umgebung für laserspektroskopi-sche Untersuchungen der Atomstruktur. Fundamentale Grundzustandseigenschaften des Kerns können über ihre Wechselwirkung mit der Elektronenhülle abgeleitet wer-den. Gewöhnlich verhindert die durch die Dopplerverbreiterung in der heißen Kavität begrenzte spektrale Auflösung jedoch solche Untersuchungen.

Die vorliegende Arbeit beinhaltet die Entwicklung, vollständige Charakterisierung sowie erstmalige Anwendung einer Laserionenquelle, die auf hochauflösende Laserspek-troskopie spezialisiert ist. Sie basiert auf der ebenfalls in der LARISSA-Arbeitsgruppe entwickelten Perpendicular Illuminated Laser Ion Source and Trap (PI-LIST) und ver-wendet transversal zum aus der heißen Kavität austretenden Atomstrahl eingestrahltes Laserlicht, um die Doppler-Limitierung zu überwinden. Während dieser vormalige Auf-bau auf seitlicher Lasereinkopplung durch Fenster an der Quellenvakuumkammer beruht, ist das hier vorgestellte Upgrade maßgeschneidert für eine Installation an Einrichtungen zur Erzeugung radioaktiver Ionenstrahlen, an denen Zugriff auf den hochradioaktiven Quellenbereich unmöglich ist.

Mit diesem neuen Aufbau wurden hochauflösende Hyperfeinstrukturuntersuchungen an langlebigen radioaktiven Holmiumisotopen am RISIKO-Massenseparator der Univers-tität Mainz durchgeführt. Die extrem dichten Spektren, die in der Kopplung von sowohl hohem Kernspin als auch hohem Gesamtdrehimpuls der zugänglichen atomaren Zustände begründet sind, erfordern spektrale Auflösung weit jenseits der Doppler-verbreiteten Situation in einer Standardionenquelle mit heißer Kavität. Durch herausragende experi-mentelle Linienbreiten bis unterhalb von $100\,\mathrm{MHz}$ gelang die erstmalige Bestimmung von Kernstrukturparametern von ^{166m}Ho. Der Kernspin wurde mit $I = 7$ bestätigt. Weiterhin lösen die Ergebnisse für das magnetische Dipolmoment, das spektroskopische Quadrupolmoment sowie die erstmalige Bestimmung der Änderung des mittleren qua-dratischen Ladungsradius auf der neutronenreichen Seite der Holmium-Isotopenkette Unstimmigkeiten in den verfügbaren Literaturdaten und bestätigen die stark prolate Kerndeformation in diesem Bereich der Nuklidkarte.

Die PI-LIST mit interner Laserreflektion hat sich bezüglich aller operativer Para-meter als vollständig ebenbürtig zu dem vormals verwendeten Modus mit externer seitlicher Lasereinstrahlung gezeigt. In dedizierten Experimenten wurden spektrale

Linienbreiten von bis zu 60 MHz erreicht, und eine Gesamteffizienz des Aufbaus bis in den Bereich von 10^{-4} wurde bestätigt. Damit steht die PI-LIST einer Installation an on-line-Einrichtungen zur Verfügung.

Die Arbeit wird abgerundet durch eine Zusammenstellung verschiedener weiterer Entwicklungen im Bereich der Ionenquellen mit heißer Kavität. Dabei stehen die Optimierung von Effizienz sowie die Ionenstrahlreinheit im Vordergrund.

Contents

List of Figures

List of Tables

Introduction

The world we live in is ultimately governed by mechanisms of interactions in the nanoworld. Starting from the beginning of the universe, the appearance and abundance of matter evolved via nuclear reactions in extreme environments such as the big bang scenario, and the interior of stars or supernovae. Profound knowledge of the forces and interactions inside nuclei is necessary to model these processes and is the basis for understanding of the structure and properties of nuclear matter all across the nuclear chart of stable and radioactive nuclides.

Access to this universe of nuclear structure is found in its interplay with the surrounding electronic shell in an atom, even though this so-called *hyperfine structuring* of the atomic spectra is of minute nature compared to dominating effects in the atomic shell. High precision tools for measurements of the atomic system and structure is thus of utmost importance.

A very specific and powerful tool to "shed light" into this situation was found in the production of well-controlled coherent optical radiation by the invention of the *Laser* [1]. After its first demonstration in the 1960s, it rapidly developed into a most versatile instrument in many fields of applications. Of special relevance here is its ability to exclusively address selected transitions in an atomic shell, promoting an electron into a higher excited state and finally detaching it from the atom to form an ion. Presupposed sufficient photon flux, this step-wise technique is a highly efficient process and exhibits inherent element selectivity due to the unique, fingerprint-like structure of atomic levels and transitions for each element. The produced ions can be manipulated by electric and magnetic fields, e.g. for mass separation if extracted as beam an guided through a dipole magnet. This combination of experimental technique called *resonance ionization mass spectrometry (RIMS)* is the core of the work presented in this thesis.

Provision of the species under investigation is commonly done as atomic vapor from thermal evaporation in hot environments. This concept of the *hot cavity* ion source is in use at world-wide leading facilities for production of *radioactive ion beams (RIBs)*. Here, direct coupling to the production process of these species by induced nuclear reactions is employed, e.g. via bombardment of a solid target with high energy projectiles, in the so called *ISOL (isotope separation on-line) method*. The technique was pioneered at the Leningrad Nuclear Physics Institute (LNPI, now PNPI) in 1988 [2], and today *resonance ionization laser ion source (RILIS)* setups are principal ion sources at ISOLDE (CERN, Switzerland), ISAC (TRIUMF, Canada) or IGISOL (JYFL, Finland) [3] (the latter employing a thin target in a buffer gas stopping cell instead of a thick target and hot cavity) to deliver high intensity beams to a variety of connected experimental setups covering a wide range of physics fields. Further applications are found in ultra-trace

analysis [4–6], in preparation of ultra-pure samples for different research projects [7–9], or in clean extraction of medically relevant isotopes from irradiated targets [10, 11].

As the produced ion rate is determined by the cross section of the resonant laser-atom interaction, tunable lasers can also directly be used for investigations on atomic structure inside the hot cavity, in the so called *in-source spectroscopy* method. Spectral position and line shape of driven transitions can be investigated as function of laser frequency. A classical field of application is the analysis of Rydberg state convergence to extract the ionization potential. As a fundamental physico-chemical property, its knowledge for every element in the periodic table is of major importance [12–14]. More recently, the method has also been used to investigate highly dense spectra in atoms with a high number of valence electrons, exhibiting indications of intrinsic quantum chaos, and providing elaborate experimental data for providing comparison to theoretic statistical descriptions [15, 16].

While the hot cavity provides an excellent environment for efficient ionization and thus the ability to work on minute sample amounts or with lowest production rates of radioisotopes in the ISOL method, the spectral resolution is ultimately limited by the Doppler broadening of resonances in the atomic vapor. Figure 1.1 gives an overview of this boundary for a range of realistic experimental parameters. While in some exceptional cases, especially for heavy ions, extraction of relevant quantities is still feasible, commonly the typical total range of a hyperfine structure patterns just coincides with the given line widths, and thus prevents resolution or unambiguous assignment of individual resonances. This task requires additional measures to overcome the Doppler limitations.
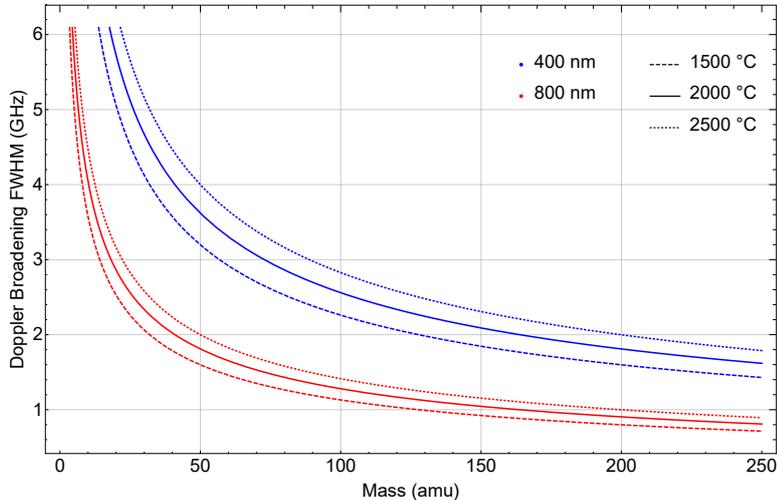
Figure 1.1: Doppler broadening of spectral linewidths in the optical regime for typical hot cavity vapor temperatures.

The challenge has been tackled by various dedicated setups of specific laser spectroscopy techniques. Resolution in the regime of 10 to 100 MHz is e.g. achieved in Doppler-compressed fast ion beams by both fluorescence and resonance ionization detection methods in the CRIS and COLLAPS beam lines at ISOLDE [17], or inside a supersonic gas-jet emerging from a buffer gas stopping cell [18].

Up to today impressive coverage of the nuclear chart by laser spectroscopic investigations on nuclear structure has been achieved. It is nicely depicted in fig. 1.2, compiled

by the group of W. Nörtershäuser of TU Darmstadt and made publicly available online[1]. It follows an initial compilation of E. Otten [19] and incorporates the previous overview in a review by P. Campbell, I. Moore and M. Pearson [3]. The LARISSA group with its decade-long expertise in laser technique and spectroscopic applications contributed to a variety of these results being obtained within various collaborations within the highly linked and very active research community.

Figure 1.2: The chart of nuclides in respect to nuclear structure investigations by optical laser spectroscopy. Stable isotopes are shown in black, red squares indicate published result. "Magical" proton and neutron numbers are marked. The graphic was compiled and made publicly available online by the group of W. Nörtershäuser at TU Darmstadt.

The scope of this thesis was to develop, characterize and employ a new, on-line applicable operation mode of the ISOLDE *Laser Ion Source and Trap (LIST)* for high resolution studies. It was utilized for first-time hyperfine structure spectroscopy on radioactive holmium isotopes at the RISIKO off-line mass separator at Mainz University. This new mode features a perpendicular interaction geometry of the atomic beam effusing from a standard hot cavity with incident laser light in a clean and cold environment. This approach strongly reduces the effective Doppler broadening by interaction with the very narrow distribution of velocity classes in respect to the transversal laser propagation direction. The method itself has been applied in smaller spectrometers already e.g. in trace analysis of ^{90}Sr [20], ^{41}Ca [21] and uranium [22, 23] or for high resolution hyperfine structure spectroscopy in the 100 MHz regime, e.g. on technetium [24] or copper [25].

Initially a high resolution off-line operation mode was incorporated in the LIST by adding lateral laser access through windows at the ion source vacuum vessel [26]. Yet, this design is not applicable for implementation at on-line radioactive ion beam facilities with extremely restricted access to the highly radioactive target and ion source area. A

---

solution was presented by guiding the laser beam along the mass separator ion beam axis with a very small lateral offset angle, and reflecting it into the transversal direction with robust metal mirrors directly inside the LIST corpus. The thesis excessively investigates the technical aspects, operational parameters and limitations of this new setup from a technical point of view, always in respect to possible application at on-line facilities. The scope to produce *isomer*-pure ion beams, which can not be achieved in the mass separator, by selective addressing of specific hyperfine resonances is examined.

The high resolution investigations on radioactive holmium isotopes with the developed design imply the first-time laser spectroscopic hyperfine structure investigations on the extremely complex spectrum of ^{166m}Ho, arising from the coupling of a high nuclear spin with also high total angular momenta of both involved atomic states. The extraction of nuclear parameters was rendered possible and lead to resolving a puzzling situation in the case of the spectroscopic quadrupole moment Q_s of ^{166m}Ho. Here, results from Marshal et al. [27] yielded a negative value of Q_s, denoting an oblate shape of the nucleus, whereas systematics in this mid-shell region of the nuclear chart strongly suggest considerable prolate deformation - a fact that was already stated skeptical by the authors themselves. Additionally, new results were obtained on the nuclear dipole moment as well as on the first determination of the change in mean square charge radii towards the neutron-rich side of the holmium isotopic chain, together with a clear confirmation of the nuclear spin of ^{166m}Ho.

The results of the holmium experiment are also of great interest for the ECHo project, where the LARISSA group is also involved. Goal is the determination of the electron neutrino mass from the decay spectrum following the electron capture of ^{163}Ho, which is implanted into gold absorbers acting as calorimeters. From precise parametrization of this spectrum in combination with sufficient counting statistics from a years long process, the electron neutrino mass can ultimately be deduced with sub-eV accuracy. The task of the LARISSA group is the laser mass spectrometric purification of the chemically pre-cleaned holmium samples with simultaneous implantation into the calorimeters using the RISIKO mass separator [28]. Besides the requirement of highest possible efficiency in this process, the purity of the final product in order to prevent any disturbance in the electron capture energy spectra is of utmost importance. Naturally, the long-lived ^{166m}Ho, which can not be separated by chemical means, might act as a major interference. Investigations on the hyperfine structure therefore also serves to reveal opportunities for additional purification by exploring differences in the isotope-unique excitation patterns.

The thesis is round up by a compilation of different further developments in the hot cavity ion source sector. Special focus is put on the ion bunch time structure imprinted by the pulsed laser system, and exploiting it for maximum ion beam purity without sacrificing efficiency of the ionization and transport process. The characteristics of atom beam effusion from a hot cavity source are investigated and put into context to previous results. Implications for LIST-type ion sources with spatial separation of hot atomization and clean laser interaction region in the emerging atomic beam cone are derived. A fast beam gating technique to completely overcome cross mass contamination stemming from species ionized in the extraction field is presented. Systematic ion trajectory simulations on a laser ion source type producing sharp, time-focused ion bunches are presented and recent technical, prototype-like developments for manipulation of the ion source voltage gradient, implied by its heating current, are shown.

The work presented in this thesis is also partly described in the publications [24, 29–32], all with prominent contributions by the author.

Theoretical Background

2.1 Atomic Level Structure

Knowledge on atomic energy levels and their interaction with nuclear structure and electromagnetic radiation is the basis for the experimental techniques and evaluation methods in the present work to extract information on fundamental physics. These sections give a brief summary of the underlying theory and provide the notation and mathematical background.

Comprehensive and profound descriptions can be found in various textbooks as [33–36] or, with direct scope to the work in the community, in reviews as [3].

2.1.1 Atomic Energy Levels

The correct and complete description of electron orbits around a positively charged nucleus is not possible within the framework of purely classical physics. Instead, the postulation of quantized discrete eigenstates is needed, each characterized by a unique set of quantum numbers. For a fundamental outline, hydrogen (or hydrogen-like atoms with only one valence electron orbiting a positively charged remaining atom core) serves as the most simple atomic system. Its quantum-physical Hamiltonian H can be expressed as

$$H = \frac{-\hbar^2}{2m_n}\Delta_n + \frac{-\hbar^2}{2m_e}\Delta_e - \frac{e^2}{4\pi\epsilon_0 r} \tag{2.1}$$

with Δ_n and Δ_e being the Laplace operators acting on the coordinates of the nulceus with mass m_n and the electron with mass m_e, respectively. The last term is the Coulomb potential of the core with its energy simply depending on the radial distance r between core center and valence electron. Via the Schrödinger equation

$$H|\Psi(\boldsymbol{r},t)\rangle = i\hbar\frac{\partial}{\partial t}|\Psi(\boldsymbol{r},t)\rangle \tag{2.2}$$

the wave function of the electron $\Psi(\boldsymbol{r},t)$ can be determined. This equation can be further simplified by using only the relative coordinate $\boldsymbol{r}$ in respect to the system's center of mass as well as the reduced mass

$$\mu = \frac{m_e m_n}{M_e + m_n}. \tag{2.3}$$

As the kinetic energy of the center of mass's movement does not contribute to the atom's internal energy and the Coulomb potential is not time-dependent, the Schrödinger

equation can be written in a stationary form as

$$H|\Psi(\boldsymbol{r})\rangle = -\frac{\hbar^2}{2\mu}\Delta|\Psi(\boldsymbol{r})\rangle - \frac{e^2}{4\pi\epsilon_0 r}|\Psi(\boldsymbol{r})\rangle = E|\Psi(\boldsymbol{r})\rangle. \qquad (2.4)$$

By transforming into spherical coordinates, the equation can be solved with the ansatz

$$\Psi(\boldsymbol{r}) = R_{nl}(r) \cdot Y_{nl}(\Theta,\phi) \qquad (2.5)$$

with separated, solely radial or angular dependent functions $R_{nl}(r)$ and $Y_{lm}(\Theta\Phi)$, respectively, which are consistently characterized by the quantum numbers

n = 1, 2, 3, ...   principal quantum number
l = 0, 1, 2, ... , $n-1$ angular momentum quantum number, and
m = $-l, -l+1, ... , l-1, l$ magnetic quantum number.

m thereby serves as a quantization of l along the z-axis. The energy eigenvalues E_n of the solutions, i.e. the energies of the corresponding atomic states are only dependent on the principal quantum number n and a priori degenerated in respect to l and m

$$E_n = -\frac{\mu e^4}{8\epsilon_0^2\pi^2\hbar^2} \cdot \frac{1}{n^2} = -R_y\frac{\mu}{m_e} \cdot \frac{1}{n^2} \overset{\mu\approx m_e}{\approx} -R_y \cdot \frac{1}{n^2} \qquad (2.6)$$

with the Rydberg constant $R_y \approx 13.6\,\text{eV}$. For $n \to \infty$, the value of E_∞ at the same time represents the convergence value of excited atomic states in hydrogen and thereby defines the energy required to separate an electron from the nucleus, also denoted as its (first) ionization potential (IP).

In addition to the described quantum numbers, the electron itself also exhibits an intrinsic angular momentum-like property denoted as its spin

$$\mathbf{s} = \frac{\sqrt{3}}{2}\hbar \cdot \mathbf{e}_s \qquad (2.7)$$

with an additional quantum number $m_s = \pm\frac{1}{2}$ for its projection along the z-axis. Altogether, the degeneracy of an atomic level with an energy E_n is then given by

$$\sum_{l=0}^{n-1} 2(2l+1) = 2n^2. \qquad (2.8)$$

External influences or additional interactions within the atomic system itself can remove this degeneracy and introduce splittings and shifts of individual levels, as described in the following sections.

2.1.2 Level Shifts and Splittings

Fine Structure

Effects which cause shifts of atomic energy levels from the treatment in the section before, can be derived using the Dirac equation; they are referred to as fine structure. In the optical range, they appear on a scale of 10^{-3} to 10^{-5} relatively to the transition's absolute frequency. Namely, these effects are

- The correction accounting for **relativistic kinetic energy**, which causes a specific shift to all levels

- **Non-localization effects of the electron's interaction with the electric field of the nucleus** (Darwin term), which only affect s-electrons

- The **spin-orbit coupling** as interaction of the electron's spin with the magnetic field generated by its own angular momentum.

As the latter is especially important for the interaction principles of photons with atomic systems and the notations used to describe individual levels, it will be described in more detail.

The spin with its angular momentum-like nature causes a magnetic moment of the electron as

$$\boldsymbol{\mu_s} = -g_s \frac{e}{2m_e} \boldsymbol{s} = -g_s \frac{\mu_B}{\hbar} \boldsymbol{s} \tag{2.9}$$

with the Bohr magneton μ_B and the Landé-g-factor of the electron g_s (note that $g_s \approx 2$ depicts the special character of the spin of not being a "classical" angular momentum). This magnetic moment interacts with the magnetic field $\boldsymbol{B_e}$ caused by the angular momentum $\boldsymbol{l}$ of the electron itself. As $\boldsymbol{B_e} \propto \boldsymbol{l}$, the shift in energy can be calculated as

$$\Delta E_{SO} = -\langle \boldsymbol{\mu_s} \cdot \boldsymbol{B_e} \rangle = a \langle \boldsymbol{l} \cdot \boldsymbol{s} \rangle = a \frac{\hbar^2}{2} [j(j+1) - l(l+1) - s(s+1)] \tag{2.10}$$

with the new *total angular momentum quantum number* $j = l + s$. The strength of this coupling compared to different mechanisms is relevant for the definition of a total angular momentum quantum number J for an atomic multi-electron system, as will be described in section 2.1.3.

Lamb Shift

The Lamb shift as an additional energy shift of atomic levels not covered by the fine structure is assigned to *quantum electrodynamics* (QED). It is caused by interaction of the electron with virtual particles from vacuum quantum fluctuations which cause a correction to the effective potential energy experienced by the electron. The Lamb shift removes the degeneracy of atomic levels according to the specific total angular momentum quantum number j, leading to a l-dependent splitting.

Hyperfine Structure

The *hyperfine structure* reflects interactions of the electrons in the atomic shell with magnetic and electric moments of the nucleus. As can already be estimated from the size of the nucleus, being 4 to 5 orders of magnitude smaller than the atom, these effects are significantly more diminutive with shifts and splittings about a factor of 1000 lower than those described above. Thus, the hyperfine structure delivers a powerful instrument for "atomic science" of investigating the electronic shell to study the "nuclear science" of the inner structure of the atom's nucleus. The following paragraph covers the two dominant coupling mechanisms, which are relevant for the presented work.

Equivalent to the electron spin described above, also the nucleons exhibit a spin $\boldsymbol{s_i}$ with half-integer quantum number 1/2 and possible projections $\pm 1/2$. Also similar to the electronic shell structure, nucleons occupy discrete energetic levels with corresponding angular momenta $\boldsymbol{l_i}$. Their sum is denoted as the total nuclear spin $\boldsymbol{I} = \sum_{i=1}^{A}(\boldsymbol{s_i} + \boldsymbol{l_i})$, with quantum number I. For nuclei with even numbers of both protons and neutrons a pairwise anti-parallel orientation of the angular momenta is energetically favored and

thus $\boldsymbol{I} = 0$ in the ground state. For different configurations with a non-zero nuclear spin a magnetic moment

$$\boldsymbol{\mu_I} = g_I \frac{\mu_N}{\hbar} \boldsymbol{I} \tag{2.11}$$

with the nuclear magneton $\mu_N = \frac{e}{2m_p}$ and the Landé-g-factor g_I is induced. It couples to the magnetic field $\boldsymbol{B_J} = -B_J(\boldsymbol{r} = 0)\hat{\boldsymbol{e}}_J = -B_J\hat{\boldsymbol{e}}_J$ introduced by the electron's total angular momentum $\boldsymbol{J}$ at the position of the nucleus, resulting in an energy shift of

$$\Delta_{\mathrm{HFS},\mu} = -\boldsymbol{\mu_I} \cdot \boldsymbol{B_J} = -\mu_I B_J \cos(\angle(\boldsymbol{I},\boldsymbol{J})) = \mu_I B_J \frac{\boldsymbol{I} \cdot \boldsymbol{J}}{|I|\,|J|}. \tag{2.12}$$

By introduction of a new total angular momentum $\boldsymbol{F} = \boldsymbol{I} + \boldsymbol{J}$ with quantum numbers $|I - J| \leq F \leq I + J$, it can be rewritten as

$$\Delta_{\mathrm{HFS},\mu} = \frac{A}{2} \cdot [F(F+1) - I(I+1) - J(J+1)] = \frac{A}{2} \cdot C, \tag{2.13}$$

involving the *Casimir factor* $C = F(F+1) - I(I+1) - J(J+1)$. Here, the hyperfine coupling constant

$$A = \frac{\mu_I B_J}{IJ} \tag{2.14}$$

is a characteristic of an atomic level and contains spectroscopically accessible information about the nucleus in the form of its magnetic moment μ_I.

An additional contribution to the hyperfine structure is due to the interaction of the electronic shell with a possible distortion of the charge distribution in the nucleus. This effect can be present in all nuclei with nuclear spin $I > 1/2$. The correspondent energy shift is given by

$$\Delta E_{\mathrm{HFS},Q} = \frac{B}{4} \cdot \frac{\frac{3}{2}(C+1) - 2I(I+1)J(J+1)}{I(2I-1)J(2J-1)}, \tag{2.15}$$

also involving the Casimir factor C and the coupling constant

$$B = eQ_s \left\langle \frac{\partial^2 V_e}{\partial z^2} \right\rangle_{\boldsymbol{r}=0} \tag{2.16}$$

which links B to the *nuclear spectroscopic electric quadrupole moment* Q_s via the averaged second derivation of the potential caused by the electronic shell at the site of the nucleus in z direction. The nucleus exhibits a prolate or oblate shape for $Q_s > 0$ or $Q_s < 0$, respectively. This property again can be related to an *intrinsic quadrupole moment* Q_0 and its manifestation along the nuclear spin axis. For strong coupling, i.e. a significantly deformed nucleus (and $I > 1/2$) [37], the relation is given as

$$Q_0 = \frac{(I+1)(2I+3)}{I(2I-1)} Q_s. \tag{2.17}$$

Thus altogether, the shifts introduced by the nuclear structure on the electronic shell as investigated in this work, are calculated by

$$\Delta_{\mathrm{HFS}} = \Delta_{\mathrm{HFS},\mu} + \Delta_{\mathrm{HFS},Q} = \frac{A}{2} \cdot C + \frac{B}{4} \cdot \frac{\frac{3}{2}(C+1) - 2I(I+1)J(J+1)}{I(2I-1)J(2J-1)} \tag{2.18}$$

To extract the nuclear parameters of interest, i.e. I, μ_I and Q_s from the laser spectroscopic measurements, explicit quantum mechanical calculations on B_J and $\left\langle \frac{\partial^2 V_e}{\partial z^2} \right\rangle$ are required. Although this has been shown to be possible even for high-Z nuclei [38], more easily the proportionality to an isotope with properties known directly from nuclear spectroscopy can be applied, if A and B values are measured for at least one common atomic state on both isotopes:

$$\frac{\mu_I}{\mu_{I,\text{ref}}} = \frac{A\,I}{A_{\text{ref}}\,I_{\text{ref}}} \tag{2.19}$$

and

$$\frac{Q_s}{Q_{s,\text{ref}}} = \frac{B}{B_{\text{ref}}} \tag{2.20}$$

Hyperfine Anomalies

The relation of the A parameter to the respective nuclear magnetic moment μ_I as given in eq. 2.19 is only exact for an infinitely small nucleus. Especially for heavier nuclei, two additional effects play a role. The Breit-Rosenthal effect [39], which is due to the finite extent of the nuclear charge distribution, and the Bohr-Weisskopf effect [40], arising from the distribution of the nucleus' magnetism. While direct observation of these effects e.g. via high-resolution radio-frequency resonance spectroscopy is feasible, a recent compilation [41] shows their influence to be most commonly below $1\,\%$ and therefore most often within experimental uncertainties, which is also the case for the work presented here.

Isotope Shift

Different isotopes of an element differ by their number of neutrons. While the overall charge stays the same, both the mass and the distribution of the charge in the finite size nucleus change. A correspondent shift in the transition frequency ν between two atomic energy levels for two isotopes with mass numbers A, A' can be written as a sum of two distinct effects as

$$\delta\nu_{\text{IS}}^{A,A'} = \nu^A - \nu^{A'} = \delta\nu_{\text{MS}}^{A,A'} + \delta\nu_{\text{FS}}^{A,A'}. \tag{2.21}$$

Here, the *mass shift* $\delta\nu_{\text{MS}}^{A,A'}$ is due to the alteration of mass and the corresponding change of angular momentum in the system. Taking into account different reduced mass values $\mu_A = \frac{m_e \cdot m_A}{m_e - m_A}$, it can be further split up into

$$\delta\nu_{\text{MS}}^{A,A'} = (K_{\text{NMS}} + K_{\text{SMS}}) \frac{m_A - m_{A'}}{m_A \cdot m_{A'}}, \tag{2.22}$$

i.e. the normal and specific mass shift, represented by K_{NMS} and K_{SMS}, respectively. The normal mass shift accounts for the change only considering the single-electron contribution of the valence electron and is analytically accessible as $K_{\text{NMS}} = m_e \nu^A$. Contrarily, the specific mass shift includes electron-electron interactions and related correlations in their movement, and therefore relies on the solution of a many-body-problem. It is only ab-initio calculable for simple systems and in other cases is extracted from semi-empiric approaches or must be determined experimentally. As it can clearly be seen from eq. 2.22, the significance of the mass shift is rapidly decreasing for heavier atoms, as relative changes become smaller.

The *field shift* $\delta\nu_{\text{FS}}^{A,A'}$ results from the change in the charge distribution between different isotopes. As certain electrons, namely s-electrons and relativistic $p_{1/2}$-electrons, have a non-zero probability of their wave function inside the finite size nucleus, this effect also introduces shifts in the energy levels. In a simple approach assuming a spherically symmetric charge distribution, it can be described to be proportional to the shift of the first order quadratic expansion of the mean square charge radius of the nucleus $\delta\langle r^2\rangle_{A,A'}$ according to

$$\delta\nu_{\text{MS}}^{A,A'} = F_{\text{FS}}\,\delta\langle r^2\rangle_{A,A'} \tag{2.23}$$

with the field effect constant F_{FS}. It can be taken from reference measurements on $\delta\langle r^2\rangle_{A,A'}$, e.g. by electron scattering experiments. Alternatively, semi-empirical estimates and ab-initio calculations are used [42]. The model-independence of the laser spectroscopic approach separates it from the majority of different measures of the nuclear charge distribution [3].

In total, the isotope shift results in

$$\delta\nu_{\text{IS}}^{A,A'} = \nu^A - \nu^{A'} = (K_{\text{NMS}} + K_{\text{SMS}})\,\frac{m_A - m_{A'}}{m_A \cdot m_{A'}} + F_{\text{FS}}\,\delta\langle r^2\rangle_{A,A'} \tag{2.24}$$

with the transition-characteristic constants K_{NMS}, K_{SMS} and F_{FS}.

A consistency check of the obtained values can be conducted by comparison of isotope shifts measured in two different atomic transitions in a method called *King plot* [43]. By multiplying eq. 2.24 with the modification factor $\mu_{A,A'} = \frac{m_A m_{A'}}{m_A - m_{A'}}$, the respective modified isotope shifts for transitions i and j yield a linear relation as

$$\mu_{A,A'}\delta\nu_{A,A'}^i = \frac{F^i}{F^j}\cdot\delta\nu_{A,A'}^j + \left(K^i - \frac{F^i}{F^j}K^j\right) \tag{2.25}$$

2.1.3   Atomic Multi-Electron Configurations

For the simple one-electron system as the hydrogen atom discussed in section 2.1.1, assignment of characteristic quantum numbers n, l, m_l and m_s to a specific level is trivial. As this work covers investigations on much more complex systems, this section aims to give an overview on atomic states involving several electrons: Resulting quantum numbers, coupling mechanisms and notations are explained.

LS Coupling

If the interaction between individual electrons dominates over individual coupling of single electron's spin and angular momentum, the respective moments couple to a total angular momentum and spin

$$\boldsymbol{L} = \sum_i \boldsymbol{l}_i \qquad\qquad \boldsymbol{S} = \sum_i \boldsymbol{s}_i \tag{2.26}$$

and consequently to the level's total angular momentum

$$\boldsymbol{J} = \boldsymbol{L} + \boldsymbol{S} \tag{2.27}$$

with respective quantum numbers $|L - S| \leq J \leq |L + S|$. This is the dominant coupling mechanism for light atoms with $Z \leq 30$. The resulting atomic state is described via the *term symbol*

$$^{2S+1}L_J^{(o)}, \tag{2.28}$$

where an o indicates odd parity of the wave function, while with no superscript the parity is even. For historical reasons $L = 0, 1, 2, 3, ...$ is not given as number but as letter $S, P, D, F, ...$ (derived from characteristics of correspondent spectroscopic lines: $s$harp, $p$rincipal, $d$iffuse; then in ongoing alphabetical order with J being omitted). The term $2S + 1$ denotes the *spin multiplicity*, derived from the number of possible fine structure states of J for given L and S, which are also commonly located nearer to each other than states with different L or S.

jj Coupling

If the coupling of the individual electron's angular momentum and spin dominates, individual momenta

$$\boldsymbol{j_i} = \boldsymbol{l_i} + \boldsymbol{s_i} \tag{2.29}$$

arise and then couple to the overall angular momentum

$$\boldsymbol{J} = \sum_i \boldsymbol{j_i} = \sum_i (\boldsymbol{l_i} + \boldsymbol{s_i}). \tag{2.30}$$

A total angular momentum $\boldsymbol{L}$ and a total spin $\boldsymbol{S}$ are no well defined quantities in this case. This mechanism predominantly occurs for heavy atoms with $Z > 60$, and for higher excited atomic states. As the typical multiplet clustering structure of levels as in LS coupling is not present, more complex spectra are expected. Along the Periodic Table a steady and smooth transition from pure LS to pure jj coupling is found and in general an intermediate coupling scheme with properties of LS coupling at low excitation energies developing into jj coupling for higher energies is present.

$\text{J}_\textbf{1}\text{K}$ Coupling

For atoms with more than one open, i.e. not fully occupied atomic shell, usually a sub-group of electrons couples to a total angular momentum $\boldsymbol{J_1}$. An additional electron with angular momentum $\boldsymbol{l}$, or a second group of electrons with resulting $\boldsymbol{L_2}$, then couples to this $\boldsymbol{J_1}$, resulting in

$$\boldsymbol{K} = \boldsymbol{J_1} + \boldsymbol{L_2} \tag{2.31}$$

with quantum numbers $|J_1 - L_2| \leq K \leq |J_1 + L_2|$. The total angular momentum of the atomic level is then given by the coupling of K to the spin S_2 of the second group as

$$\boldsymbol{J} = \boldsymbol{K} + \boldsymbol{S_2} \tag{2.32}$$

with according quantum numbers $|K - S_2| \leq J \leq |K + S_2|$. The whole electronic configuration, with sub-configurations $n_i l_i^{N_i}$, is given as

$$n_1 l_1^{N_1} \,(\text{Term symbol 1}) \, n_2 l_2^{N_2} \,(\text{Term symbol 2}) \, {}^{2S_2+1} [K]_J^{(o)} \tag{2.33}$$

Anyhow, as stated above, for most atoms a combination of all the aforementioned mechanisms occurs. Correspondingly, in these cases specific atomic levels appear only as mixture of different well assigned electronic configurations. A general identification and assignment is complex if not impossible at all.

2.1.4 Electronic Transitions

The detection of the properties of distinct atomic levels, especially regarding their intrinsic nuclear information via the hyperfine structure, is done by spectroscopic investigation of resonance *transitions* between different levels with energies E' and E. An atom can change its state by emitting or absorbing a photon γ with correspondent energy

$$E_\gamma = \Delta E = E' - E = h\nu = h\frac{c}{\lambda} = hck, \tag{2.34}$$

where h is the Planck constant and ν, λ and k the photon's correspondent frequency, wavelength and wavenumber[1].

The strength and therefore intensity of such a transition can be described by the Einstein A coefficient A_{21}, which gives the probability of absorption of a photon with appropriate energy. It is linked to the expectation value of the transition dipole moment $M_{21} = \langle \boldsymbol{p}_{21} \rangle$ according to "Fermi's golden rule" as

$$A_{21} = \frac{16\pi^3 e^2 \nu_{21}}{3\epsilon_0 c^3 h} |M_{21}|^2 = \frac{16\pi^3 e^2 \nu_{21}}{3\epsilon_0 c^3 h} \left| \int \psi_2^* \boldsymbol{r} \psi_1 \, \mathrm{d}\tau \right|^2. \tag{2.35}$$

Via the dipole moment's properties also selection rules for transitions can be defined (Tab. 2.1). Historically, these dipole transitions are called "allowed", whereas higher order multipole transitions are called "forbidden". Although their transition strength is highly suppressed in comparison, they can still occur nevertheless or be induced by powerful laser radiation.

Table 2.1: Selection rules for "allowed" optical electric dipole transitions. Besides the generally valid rules, for distinct coupling mechanisms additional constraints apply.

Rigorous rules
$\Delta J = 0, \pm 1$ ($J = 0 \leftrightarrow J = 0$ forbidden)
$\Delta M = 0, \pm 1$
For LS coupling
Transition of one electron: $\Delta L = \pm 1$
If $\Delta S = 0$, then $\Delta L = 0, \pm 1$ ($L = 0 \leftrightarrow L = 0$ forbidden)
For intermediate coupling
If $\Delta S = \pm 1$, then $\Delta L = 0, \pm 1, \pm 2$

Additionally, state changes induced by the absorption of a photon are always associated with a change in the wave function's parity.

Hyperfine Transitions

Transitions between different hyperfine structure components are of special relevance to this work. Additionally to the rules described in the section above, the constraint

$$\Delta F = 0, \pm 1 \tag{2.36}$$

for the total angular quantum number as introduced in section 2.1.2 applies. Without external disturbances, the relative intensities $S_{F,F'}$ of the individual hyperfine structure

---

[1]In this work, as it is common in optical spectroscopy, frequencies are often denoted as wavenumber, even though the symbol ν is used.

transitions as fraction of the unperturbed overall fine structure state intensity $S_{J,J'}$ can be calculated via

$$S_{F,F'} = (2F+1)(2F'+1) \left\{ \begin{array}{ccc} F & F' & 1 \\ J' & J & I \end{array} \right\}^2 S_{J,J'}, \tag{2.37}$$

where $\{...\}$ is the Wigner 6-j symbol. While in general these intensities aid in the assignment of individual components and are especially valuable for the determination of an unknown nuclear spin, various effects from the experimental spectroscopic method can alter corresponding measured count rates.

2.1.5 Ionization Processes

This section gives an overview over the atom ionization mechanisms which play a role in the presented work and are characteristic to the exploited techniques. Whereas the highly element selective resonant laser ionization, which also offers insight into nuclear structure via the atomic state's hyperfine structure, is the key technique of this work, effects from the occurring competing mechanisms of surface and electron impact ionization have to be considered and suppressed.

Surface Ionization

An atom can lose an electron at contact with a sufficiently hot surface and thus be ionized. The effect is dependent on the ionization potential E_{IP} of the species and the work function of the surface material Φ. In thermal equilibrium, the relative fraction of the ionic flux n_i to the atomic flux n_0 can be described by the Saha-Langmuir equation

$$\frac{n_i}{n_0} = \frac{g_i}{g_0} \exp\left(\frac{\Phi - E_{\text{IP}}}{k_B T} \right) \tag{2.38}$$

with g_i and g_0 as the statistical weights of the ionic and atomic ground states, k_B the Boltzmann constant and T the absolute temperature. The full derivation is found in [44] and based on the works of Saha [45] and Langmuir [46], while a scope towards application in ion sources is given e.g. in [47].

On the one hand, this relation promotes low temperatures in order to keep atoms in a neutral state for efficient laser ionization. On the other hand, reasonably high temperatures are required in order to ensure full vaporization and molecule dissociation of a sample, and keep wall sticking times low for extraction of short-lived radioactive species. Therefore, in general high-melting-point metals as tantalum, tungsten or rhenium with work functions Φ between 4 and 4.5 eV are used as construction material. Low work function materials would be favorable to minimize the disturbing process of surface ionization, but these compound materials are fragile and not sufficiently robust against mechanical stress and other effects induced by higher temperatures and in addition show rather rapid degradation effects over time [48].

A "radical" approach therefore is the complete spatial separation of the hot and "dirty" atomization/vaporization environment from awell localized cold and "clean" interaction volume for the desired ionization mechanism as it is realized in the LIST [49].

Electron Impact Ionization

Detachment of an electron from the atomic shell can also be induced by bombardment with projectiles, e.g. electrons with sufficient kinetic energy above the atom's ionization

potential. This process is exploited for instance in the Electron Beam Ion Source (EBIS) where it is used to produce even highly charged ions [50].

The current density J of electrons from a hot surface is given by the Richardson equation

$$J = AT^2 e^{-\frac{\Phi}{k_B T}} \tag{2.39}$$

with the Richardson constant $A = 1.201\,73 \cdot 10^6 \, \frac{\text{A K}^2}{\text{m}^2}$ and the other parameters as in eq. 2.38. Thus, increasing material temperature promotes a huge increase in electron density in its direct vicinity. Although thermally emitted electrons in a hot cavity environment exhibit a low average energy $E = k_B T$ in the range of only some tenth of an eV, the high energy tail of the Maxwell-Boltzmann-distribution can still contribute to ionization. Even more crucial is the possibility of electrons being released from hot surfaces in great amounts and afterwards being accelerated by electric potentials in or near the source. While in FEBIAD (Forced Electron Beam Induced Arc Discharge) type ion sources this is used to form a reasonably dense plasma [51], in concepts involving electric guiding fields and corresponding electrodes, this process has to be taken into account as source for interfering non-element-selective ionization.

Resonant Laser Ionization

By exploiting the discrete energy levels of the electronic shell as described in section 2.1.4, an atom can be excited consecutively by photons of properly adjusted energy. Finally, the electron can be detached, producing an ion and a free electron. As the level structure is unique to every chemical element, lasers with well tuned wavelengths and suitable spectral width can therefore act as powerful tools for inducing an inherently element-selective ionization process. This mechanism is a key of the presented work and will therefore be discussed in detail, following the description in [4]. An extensive, dedicated elaboration of the technique including theoretical background and references to experimental works is given in textbooks as e.g. [52].

A schematic overview of involved processes is given in fig. 2.1. A crucial parameter is the efficiency of the process, ensuring high ionization rates at reasonable technical expense. A characterization can be given by discussion of individual cross sections of the involved mechanisms. For resonant transitions, the absorption cross section for photons in the visible regime is in the order of $\sigma = \lambda^2/2\pi \approx 10^{-10}\,\text{cm}^2$ for atoms at rest. With the excitation probability $dW(t) = \sigma J(t)dt$ a photon flux of $J(t) \approx 10^{18}$ photons/(cm^2 s) is required for saturation of a transition in the 10 ns lifetime regime, corresponding to a power density of $\approx 0.5\,\text{W/cm}^2$ in continuous laser operation for blue photons ($h\nu = 3\,\text{eV}$). In real applications, due to different velocity classes in hot atom vapors, an effective cross section can be a factor of 100 smaller. Anyhow, with this already considered, pulsed laser systems with appropriate beam focusing can still easily provide these photon fluxes. For example, a 10 kHz pulsed system with a temporal pulse width of 50 ns, focused into an area of 3 mm diameter as used in this work would require an average power of only some mW to provide the flux during its pulses. This also gives the scope for the different final laser ionization techniques: Non-resonant excitation of an electron into the continuum with very low cross sections in the $10^{-17}\,\text{cm}^2$ range accordingly requires very high pulse power. Favorable are therefore transitions into auto-ionizing states resulting from the simultaneous excitations of two or more electrons into a state with total energy above the ionization potential, and subsequent (fast) decay of this state into an ion and a free electron. The occurrence of these states is explicitly pronounced for elements with rich atomic spectra originating from several excitable electrons, e.g. in the lanthanides, in actinides or in many transition metals [22,

53]. Here, saturation can be achieved in the power regime of some few W. Alternatively, the excitation of high-lying Rydberg states and successive ionization by influences from black body radiation, from far infrared photons, from collisions or from electric fields is possible with comparable efficiency.
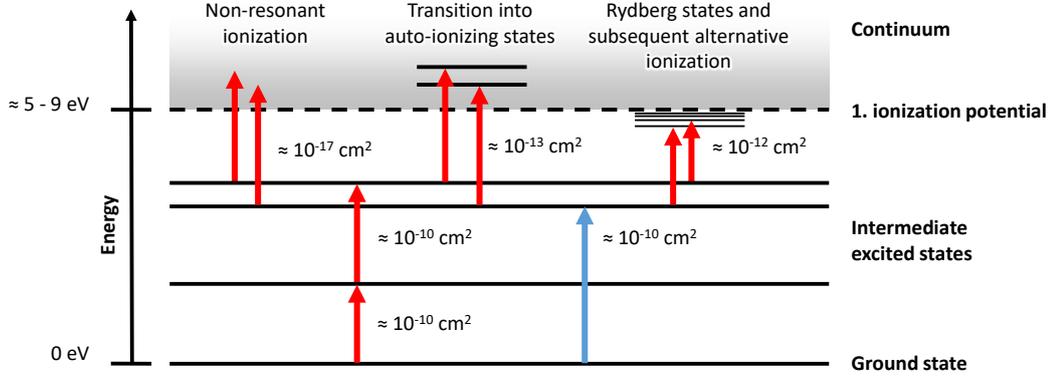
Figure 2.1: Schematic overview of the mechanisms involved in laser resonance ionization. The electronic shell is excited consecutively by laser radiation precisely tuned to the atomic transitions. The final step for ionization can be achieved by different processes as described in the text. Cross sections of the involved transitions are indicated as rough orders of magnitude. Graph adapted from [4].

2.1.6 Transition Line Shapes and Broadening Effects

As the ability to precisely determine the energetic position of resonances and unambiguously distinguish also closely adjacent peaks, an understanding of the involved effects of broadening and shape distortion is essential. While some mechanisms are inherent to the method of measuring, others can be overcome by exploitation of tailored techniques. The effects presented here as an overview in general are well-understood and extensively treated in various textbooks as e.g. [33, 34]. The term *linewidth* of a resonance will be used throughout this work in the meaning of *full width at half maximum* (FWHM) of the correspondent peak structure.

Natural Linewidth

An atomic state with a finite lifetime τ has an intrinsic energy uncertainty, resulting in a *Lorentzian profile* of a connected resonance line as

$$I(\nu) = I_0 \frac{\gamma^2}{(\nu - \nu_0)^2 + \gamma^2} \tag{2.40}$$

around the center frequency ν_0 with a FWHM linewidth of $\Delta\nu_{\mathrm{nat}} = 2\gamma$. I_0 denotes the intensity at resonance. The broadening is directly linked to the state's life time via

$$\Delta\nu_{\mathrm{nat}} = \frac{1}{2\pi\tau}. \tag{2.41}$$

The resulting width of the transition profile between two states with respective τ_1 and τ_2 is given by the sum of their respective widths

$$\Delta\nu_{\mathrm{nat,res}} = \frac{1}{2\pi}\left(\frac{1}{\tau_1} + \frac{1}{\tau_2}\right) = \Delta\nu_{\mathrm{nat,1}} + \Delta\nu_{\mathrm{nat,2}}. \tag{2.42}$$

Typical optical transitions for efficient laser excitation exploit states with lifetimes in the 10 ns regime, yielding linewidths of tens of MHz.

Doppler Broadening

Atoms not at rest experience a *Doppler shift* of the incident laser radiation. In their reference frame, the frequency is shifted to

$$\nu' = \nu \left(1 + \frac{v}{c} \right) \tag{2.43}$$

with initial frequency ν and the speed of light c.

In the presented work, the atoms are exposed to the laser radiation as a gaseous sample at a distinct temperature. Their velocity distribution is thus described via the *Maxwell-Boltzmann equation* with evenly spread directions. The broadening of the absorption profile from different velocity classes which are in resonance with the incident radiation at different Doppler shifts results in a *Gaussian profile*

$$I(\nu) = I_0 \exp \left[- \left(\frac{\nu - \nu_0}{\nu_0 v_w / c} \right)^2 \right] \tag{2.44}$$

with the ensembles most probable speed $v_w = \sqrt{2k_B T/m}$, center frequency ν_0 and maximum intensity I_0. The correspondent FWHM linewidth $\Delta\nu_{\text{Doppler}}$ is given as

$$\Delta\nu_{\text{Doppler}} = \nu_0 \sqrt{\frac{8k_B T \ln(2)}{mc^2}}. \tag{2.45}$$

It is not to be confused with the Gaussian profile's σ width related by $\Delta\nu_{\text{Doppler}} = 2\sqrt{2\ln(2)}\sigma$. Naturally, the width increases with rising temperature and for lighter atoms. Figure 2.2 depicts the relation for typical experimental settings. In fact, the Doppler broadening is the ultimate limiting effect on the resolution of spectroscopic investigations in hot cavity environments, restraining it to the GHz regime, which is already orders of magnitude higher than natural linedwidths. On the other hand, if the resolution or precise location of individual components of the optical resonance is not needed but maximum efficiency in ionization is desired, the spectral bandwidth of the laser system should match or even slightly surpass this value in order to address all velocity classes of atoms.
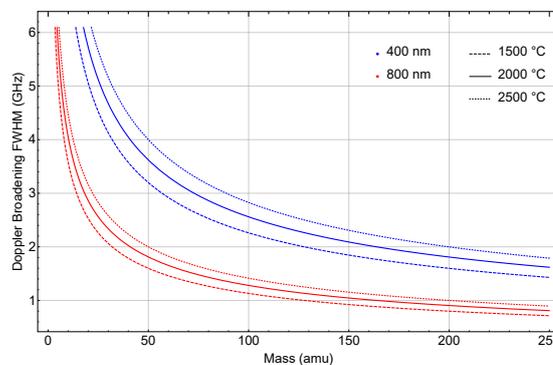
Figure 2.2: Doppler broadening of spectral linewidths in the optical regime for typical source vapor temperatures.

Power Broadening

Laser radiation of high intensity can lead to an additional broadening of the optical resonance studied. A simplified approach on the mechanism can be given by considering a two-level system with lower state $|1\rangle$ and upper state $|2\rangle$ and its correspondent Lorentzian natural line profile with center frequency ν_0 and linewidth $\Delta\nu_{\mathrm{nat}} = 2\gamma$. By introducing the *saturation parameter*

$$S_0 = p_{12}/\bar{R} \tag{2.46}$$

as the ratio of the pump rate p_{12} from state $|1\rangle$ to $|2\rangle$ to the mean relaxation rate $\bar{R}$, it can be calculated that the frequency-dependent absorption coefficient increases to

$$\alpha(\nu) = \alpha_0(\nu_0)\frac{\gamma^2}{(\nu - \nu_0)^2 + (1 + S_0)\gamma^2} \tag{2.47}$$

in respect to the unperturbed absorption coefficient α_0 at resonance ν_0. This is again a Lorentzian profile with enlarged width

$$\Delta\nu_{\mathrm{sat}} = 2\gamma\sqrt{1 + S_0}. \tag{2.48}$$

Descriptively spoken, the broadening arises from the fact that, in the center of the resonance the transition into the excited upper state saturates more easily, i.e. at lower laser power, than on its wings, leading to a vertical "compression" of the whole peak shape. Note that in a two-level-system saturation corresponds to equal population of both, lower and upper states.

In terms of accessible observables, the saturation parameter can be expressed as a relative laser intensity

$$S_0 = \frac{I_{\mathrm{Laser}}}{I_{\mathrm{sat}}} \tag{2.49}$$

in respect to the saturation intensity I_{sat}. Therefore, the resulting linewidth depends on overall laser power and focusing of the laser in the interaction region. The effect can be monitored by probing the resulting ion production rate r (using e.g. additional lasers for the subsequent ionization step) in respect to the incident laser power as

$$r(I) = r_{\max}\frac{I/I_{\mathrm{sat}}}{1 + I/I_{\mathrm{sat}}} + \alpha_{\mathrm{lin}} + r_0. \tag{2.50}$$

At an intensity equal to I_{sat}, half of the asymptotically achievable maximum ionization rate is reached. The additional terms include a potential contribution which is developing linearly with laser power caused by non-resonant ionization, if the photon energy is sufficiently high. r_0 accounts for constant background or signal due to non-laser related mechanisms.

From these considerations it is already evident that the relative strength of a transition (see sec. 2.1.4) may not directly be translated into a corresponding ionization rate but primarily and non-linearly depends on the incident laser power. For maximum efficiency in ionization, a working regime far above the saturation threshold is favorable to not be sensitive to prevent influences from laser power changes, while for spectroscopic investigations broadening may have to be reduced at the cost of overall signal rate.

Although the above mentioned mechanisms are most often sufficient to describe the occurring effects in hot cavity environments and are also well reproduced in quasi-two-level schemes using continuous-wave lasers [54], at high resolution applications with

pulsed laser systems additional effects have to be considered. Here, especially the time of probing the population in the upper state plays an important role. In fact, specifically the population at the outer wings of the resonance curve exhibits a very transient character and is only pronounced during the time of presence of the laser light [55]. Delaying the subsequent laser step to a time when the excitation pulse is already over, can completely suppress the effect [56] of power broadening. A precise description using rate equation calculations and experimental data obtained from pulsed collinear laser spectroscopy is given in [55].

Also two additional broadening effects can be counteracted this way. On the one hand, the presence of an additional depopulation channel of a state (as subsequent excitation or ionization) effectively reduces its lifetime and therefore increases its width as described at the beginning of this section 2.1.6. On the other hand, a potential influence on asymmetry in the line shape and width induced by the AC Stark effect in a strong laser field [57] can also be avoided by delaying the subsequent step behind the laser for the transition under investigation.

The applicability of the technique of delayed, temporally non-overlapping laser pulses depends on the lifetime of the involved states. In fact, almost the same efficiency as in synchronous irradiation can be preserved, if the lifetime of the excited state is sufficiently long and exceeds the laser pulse duration and thus no significant decay losses occur. Additionally, high resolution spectroscopy benefits from the choice of these weaker transitions, as they are intrinsically more narrow.

Convoluted peak shapes - the Voigt profile

As pointed out so far, the actual spectroscopic line shape of an atomic resonance transition is subject to different fundamental aspects and experimental influences exhibiting both Lorentzian and Gaussian character. On top, the bandwidth and (usually Gaussian) spectral profile of the exciting laser is to be taken into account. Therefore a mathematical description of recorded resonances is done using a convolution of a Lorentzian and a Gaussian function with respective widthes γ and σ, the *Voigt function*

$$V(\nu; \sigma, \gamma) = (G * L)(\nu) = \int G(\nu') L(\nu - \nu') \mathrm{d}\nu'. \tag{2.51}$$

As there is no analytical solution to this integral, a numerical approximation is usually chosen. An efficient computational implementation with high accuracy is found in using the Faddeeva function

$$w(z) = e^{-z^2} \mathrm{erc}(-iz) = e^{-z^2} \left(1 + \frac{2i}{\sqrt{\pi}} \int_0^z e^{t^2} \mathrm{d}t \right) \tag{2.52}$$

in the alternative representation of the Voigt function as

$$V(\nu; \sigma, \gamma) = \frac{\Re[w(z)]}{\sqrt{2\pi}\sigma} \qquad \text{with} \qquad z = \frac{\nu + i\gamma}{\sqrt{2}\sigma}, \tag{2.53}$$

with $\Re[...]$ denoting the real number part of the function.

A fast computing algorithm based on Fourier expansion to calculate values on this function [58, 59] was implemented for the fitting procedures in this work. As correspondingly also no analytical way of extracting the resulting FWHM $\Delta\nu_\mathrm{V}$ from the Voigt function is at hand, also here a numerical approximation is used [60]. The value is calculated from the fit parameters of Lorentzian and Gaussian FWHM $\Delta\nu_\mathrm{L} = 2\gamma$ and

$\Delta\nu_{\mathrm{G}} = 2\sqrt{2\ln(2)}\sigma$ as

$$\Delta\nu_{\mathrm{V}} = 0.5346\Delta\nu_{\mathrm{L}} + \sqrt{0.2166\Delta\nu_{\mathrm{L}}^2 + \Delta\nu_{\mathrm{G}}^2}. \qquad (2.54)$$

This calculation exhibits an accuracy of $0.02\,\%$ [60], which is considerably smaller than all the inaccuracies arising from the experimental data.

2.2 Tunable Laser Sources

For the presented investigations, several titanium:sapphire lasers with different properties, which were tailored for specific applications have been used. These systems are standard tools in the repertoire of the LARISSA working group and have been developed there as well as in a number of international collaborations over about two decades. This section summarizes basic principles, technical implementations and characteristics. More detailed descriptions are given in different theses dedicated on laser development [22, 26, 61, 62] and standard textbooks [34].

2.2.1 Principles of Lasing

The principle of the production of laser radiation relies on the mechanism of stimulated emission in a medium, meaning the induced creation of photons in a radiative transition between two energy levels caused by the presence of at least one initial photon with appropriate characteristics. Based on a necessarily required predominant population of the upper state. called population inversion, which prevents dominance of induced absorption, this mechanism can produce high intensity, monochromatic and coherent radiation by progressive self-amplification.

Population inversion, with more than half of the population within an energetically higher excited state, can not be met in a simple two-level scheme, where the competition of stimulated emission and absorption limits value to $\leq 50\,\%$. Therefore, a suitable medium must feature a specific arrangement of states and interconnecting transitions. The least complex set is a scheme consisting of three levels, where excitation first takes place from the initial state $|1\rangle$ into a high lying state $|2\rangle$, followed by fast decay (which is crucial to enable additional pumping into this state) into the upper state $|3\rangle$ of the lasing transition, which deescites into the initial state again. For a three-level scheme, an efficient pump process from state $|1\rangle$ to $|2\rangle$ is required to widely "empty" state $|1\rangle$ and ensure population inversion between $|3\rangle$ and $|1\rangle$. It can be implemented in several ways, e.g., an optical excitation itself or through electric discharges or currents.

For a four-level laser scheme, an additional level as lower one for the laser transition is introduced, as depicted in fig. 2.3a. With a fast decay from this state into the initial state of the pumping transition. Population inversion of the two levels of the laser transition is easily ensured. In all cases, a resonator configuration with optical mirrors placed around the lasing medium strongly enhances the achieved amplification through the feedback of the emitted photons.

2.2.2 The Titanium:Sapphire Laser Medium

The previously mentioned mechanisms naturally only work on the emission wavelength of the given lasing transition. For the work presented here and the requirements of facilities which have to be able to switch between different laser schemes for several elements and especially to perform scans over a broad wavelength range, lasers with

tunable output frequencies are needed. Therefore, an active laser medium with the ability to emit radiation covering a certain continuous spectrum is used. In titanium-doped sapphire crystals ("Ti:sapphire", $Ti^{3+}:Al_2O_3$) this is achieved by the coupling of the Ti^{3+} ground state to the field and vibrational modes of the sapphire lattice. This coupling introduces a splitting into two continuous vibrational energy bands, as shown in fig. 2.3b. Those two bands can be exploited to host a four-level scheme with rapid vibrational (non-radiative) decay within the bands and a longer-lived lasing transition in between them. The width of the lower band causes the resulting broad emission range spanning from 650 to 1100 nm, with its peak around 800 nm. The pumping transition absorbs in the range of 370 - 670 nm and can be efficiently driven by commercially available frequency-doubled Nd:YAG (532 nm) or Nd:YLF (527 nm) solid state lasers. The Ti:sapphire laser was introduced in the 1980's by Moulton [63] and has become a widely used source for tunable laser light in the visible wavelength regime.

(a) Four-level laser scheme   (b) Ti:sapphire laser medium
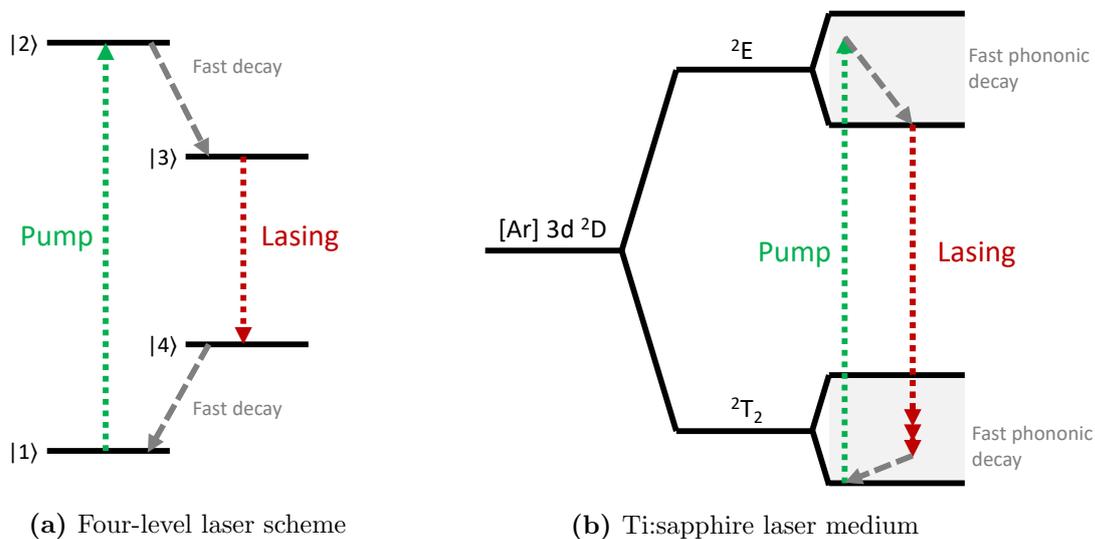
Figure 2.3: Level schemes for a classical 4-level laser and the Ti:sapphire laser medium. See text for detailed description.

In order to select a distinct wavelength from the emission spectrum (with a certain spectral bandwidth), usually one or a combination of frequency selective elements is inserted into the laser resonator. This allows only amplification of a certain frequency, while introducing loss sources for the remaining range, such as

- absorption or transmission out of the resonator, e.g. by the coating of the mirrors

- rotation of polarization (e.g. with birefringent materials) and subsequent reflection on Brewster-cut surfaces and

- polarization-dependent amplification inside the active medium.

The technical implementations for the setup used are described in section 3.2.

2.3 Frequency Conversion

The available wavelength range of the Ti:sapphire laser system can be extended from the fundamental infrared output by means of frequency mixing and higher harmonic generation in phase-matched non-linear crystals. The lasers used for this work are

operated in pulsed mode, featuring high pulse energies and peak powers, which is crucial for this process. A complete description of the involved mechanisms can be found in various textbooks [34, 64]. The process is based on non-linear response of a medium's polarization to an incident oscillating electromagnetic field $E(t,z)$ and corresponding emission of an respectively altered frequency.

The polarization density of a medium $P(t,z)$ can be described by a Taylor series in respect to different orders of the incident electric field

$$P(t,z) = \epsilon_0 \left(\chi^{(1)} E(t,z) + \chi^{(2)} E^2(t,z) + ... \right) \tag{2.55}$$

with $\chi^{(n)}$ as susceptibility of order n. If two plane electromagnetic waves as from an incident laser light beam are present in this medium, their field superimposes to

$$E(t,z) = E_1 \cos(\omega_1 t + z) + E_2 \cos(\omega_2 t + z). \tag{2.56}$$

From eq. 2.55 it is evident, that for non-linear media (meaning $\chi^{(2)}$ being considerably different from 0) the quadratic term of the trigonometrical function (note $\cos^2(x) = \frac{1}{2}(1 + \cos(2x))$) gives rise to oscillations on the sum and difference frequencies $\omega_\pm = \omega_1 \pm \omega_2$, and the respective higher harmonics $2\omega_1$ and $2\omega_2$. For the case of only one incident wave, as realized in the experiment by focusing a single laser beam into the medium, this simplifies to predominant generation of the doubled frequency. Moreover, the intensity of these first higher harmonic scales with the square of the original intensity, $I(2\omega) \propto I^2(\omega)$, requiring highest possible field strength. Therefore, a pulsed laser system with high peak power is favored.

The utilization of these effects to form a light beam of the created frequency additionally demands the oscillating dipoles of the medium to have the right *phase relation*, which is achieved by phase matching of the resultant frequency's wave vector with the sum of the incident one's as

$$\boldsymbol{k_3} = \boldsymbol{k_1} \pm \boldsymbol{k_2}. \tag{2.57}$$

For regular materials, this condition can not be fulfilled due to chromatic dispersion. This problem can be overcome by using birefringent non-linear crystals with their refractive index being dependent on propagation direction and polarization of the incident light. Most commonly, phase matching can be achieved by two methods: In *non-critical phase matching*, tuning of the refractive index is done via control of the temperature. In *critical phase matching*, angular orientation of the crystal is utilized to adjust the extraordinary refractive index.

In the presented work, higher harmonic generation is used to generate frequency-doubled light in the blue color regime. Commonly used techniques in the setup as well as at other facilities, where the Mainz laser system is in use, also comprise frequency quadrupling by subsequently applying the technique again on an already frequency-doubled laser beam. Additionally, third harmonic generation is realized by re-using the fundamental, infrared part of the laser radiation which has not been transformed in a doubling unit and merging it again with the frequency-doubled output. A more sophisticated approach is mixing the outputs of several different lasers. This enables more easy wide-range scanning and can extend the laser wavelength range beyond the boundaries of fundamental, doubled, tripled and quadrupled range of the Ti:sapphire laser. Experimental applicability of difference frequency generation (DFG) in the orange regime has been demonstrated with the Mainz laser system [65]. Figure 2.4 gives an overview of the accessible wavelengths with the Mainz University Ti:sapphire laser systems and the routinely used higher harmonics, indicating maximum achievable

output powers. Conversion efficiency in the simple single pass setups reaches up to 30 % for second harmonic generation (SHG) and about 7 % for both, third (THG) and fourth harmonic generation (FHG). These values can be increased by applying the technique inside a resonance enhancement cavity at the cost of increased experimental complexity, which is commonly not realized due to the achievable powers being sufficient for saturation in standard ion production and spectroscopic applications.
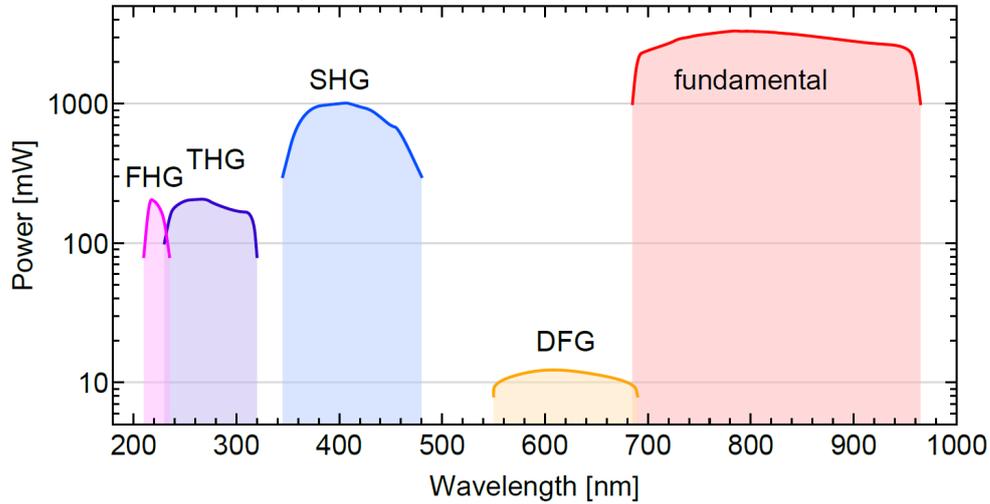
Figure 2.4: Accessible wavelength regimes of the Ti:sapphire, expanded by frequency conversion with maximum achievable power output. See text for details. Graph adopted from [66]

3

Chapter

Experimental Setup

The technical developments and all measurements presented in this work were performed using the method of resonance ionization mass spectrometry. The aim of this chapter is to explain this method, and give an overview of the experimental setup at Mainz University, where it is implemented. Special focus is put on the different types of laser ion sources and their evolution over the years. The highly selective LIST will be presented, as well as its recently developed upgrade for high resolution spectroscopy in a setup of crossed laser and atom beam geometry to drastically reduce Doppler broadening. This PI-LIST is the starting point and serves as benchmark for the work presented in this thesis.

3.1   Resonance Ionization Mass Spectrometry

All activities presented here rely on the concept of the combination of the highly element-selective laser ionization with subsequent mass separation. The produced ions, which are transmitted through a spectrometer on one distinct mass value directly depict the position or pattern of an optical transition for one specific isotope of this element with high accuracy and detection efficiency. The concept is visualized in fig. 3.1.
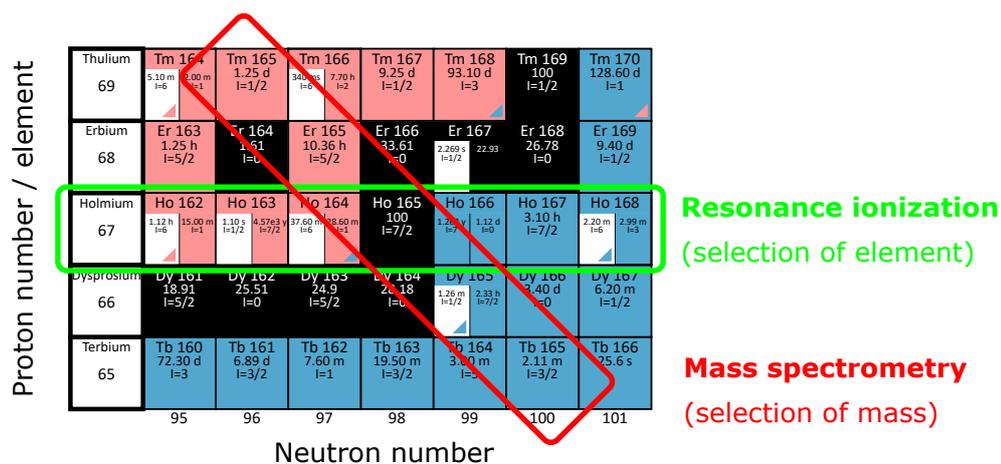
Figure 3.1: Schematic visualization of the concept of resonance ionization mass spectrometry on a section of the nuclear chart. Laser light tuned to step-wise excitation and ionization of one specific element ensures exclusive and efficient ion formation of this species. Subsequent mass separation enables selection of one isotope of choice for either highly pure ion beam production or spectroscopic investigations.

23

This method is implemented both in laboratories working on pre-treated samples or at large scale research facilities where experiments are directly coupled to the production of radioisotopes in the so-called ISOL method (Isotope Separation On-Line). In that way, even shortest-lived species far-off stabilities at the edges of the nuclear chart can be studied. RIMS is perfectly suited to this application due to its inherent selectivity and thus corresponding suppression of contaminants and its high efficiency. Consequently, ion beam production based on resonant laser ionization is today one of the principal techniques at the world-wide leading ISOL facilities as ISOLDE (CERN, Switzerland), ISAC (TRIUMF, Canada) and IGISOL (JYFL, Finland) [3]. First utilization of this technique was pioneered at the Leningrad Nuclear Physics Institute (LNPI, now PNPI) in 1988 [2]. The achievable high ionization efficiency of up to above $50\,\%$ [66, 67] also give rise to off-line applications in ultra-trace analysis [4–6], for preparation of ultra-pure samples for different research projects [7–9] or for medical applications [10, 11].

While some on-line facilities exploit thermalization and transport of the generated species in a laminar gas flow towards the laser interaction volume, the scope of this work will be on hot cavity based laser ion sources. Here, generated radionuclides diffuse as cluster, molecules or atoms into a tubular oven cavity which can be heated to above $2000\,°C$. The high temperature causes dissociation and atomization of possible chemical compounds, vaporization and ensures low sticking times on the cavity walls. In common cavity geometries of few mm diameter and a length of some cm, the mean residence time of an atom with medium atomic mass can be estimated to be about $100\,\mu s$ [68]. The use of a pulsed laser system with a repetition rate of $10\,kHz$ therefore provides both the necessary high peak photon flux (see also section 2.1.5) and guarantees that the atoms experience at least one pulse before exiting the oven.

Besides the implementation of highest possible efficiency in ionization and inherent suppression of contaminations present in the source, laser ion sources themselves already offer a dedicated experimental environment for investigations on atomic structure. Individual optical resonances can be precisely located and characterized even on lowest atom numbers [14]. A classical field of application is then the identification of Rydberg states and the analysis of their convergence to extract the ionization potential, a fundamental physico-chemical property [12, 13].

Insight into the structure of the nucleus can be achieved by evaluation of the hyperfine structure of atomic levels (section 2.1.2). In most cases, these investigation are beyond the scope of the in-source laser spectroscopy approach: The Doppler broadening in the hot atom vapor ultimately limits the spectral resolution far beyond the typical scales, which are orders of magnitudes smaller than in atomic structure cases. Thus, dedicated techniques have to be applied. Resolution in the tens of MHz regime is e.g. achieved in Doppler-compressed fast ion beams by both fluorescence and resonance ionization detection methods [17], or inside a supersonic gas-jet emerging from a buffer gas thermalization cell [18]. This work will explore possibilities of implementing a greatly Doppler-reduced measurement technique to a hot cavity laser ion source.

On the laser system side, the securing of operation stability is crucial. Namely, four fundamental parameters have to be optimized and permanently monitored and stabilized:

- **I**ntensity of the laser radiation, i.e. average output power,

- **S**pectral adjustment of the lasers, i.e. wavelength tuning onto the atomic resonances,

- **S**patial positioning of the laser beams, i.e. overlap and focusing of all individual beams into the ion source volume and

- **T**emporal control, i.e. synchronization of individual laser pulses.

They will be referred to as **ISST** parameters. As uncontrolled variations can cause losses in efficiency as well as artificial features in recorded spectra, both long-term and short term stability have to be guaranteed. Besides, automation is desired for potential stand-alone applications and relief of operators ("turn-key laser system").

3.2 LARISSA Laser Systems

This section will give an overview of the laser systems as used in the LARISSA laboratory in Mainz for the presented experiments concerning both, highly efficient ionization processes in a hot cavity ion source as well as dedicated high resolution narrow bandwidth applications. All systems are pulsed high-power titanium:sapphire solid state lasers with broad tuning range in the near-infrared spectrum (see also section 2.2.2), as developed in the group and refined, adapted and optimized over various generations and in international collaborations. As of today, the Mainz-based design is used almost exclusively in most of the world-wide leading on-line facilities with laser ion sources.

3.2.1 Standard Titanium:Sapphire Laser

The most often utilized laser type is the standard model developed in [69], which e.g. also is part of the laser ion source setup at ISOLDE [70] and is being described in its latest development stage in [26] (including the working principles of the frequency selective elements, which also can be found in various textbooks as e.g. [34]). The design is depicted in fig. 3.2. It is based on a standing wave resonator in Z-geometry, with the Ti:sapphire crystal mounted in a central water-cooled copper housing. Pumping is done by an external, commercial frequency-doubled Nd:YAG laser ($\lambda = 532\,\mathrm{nm}$) at a repetition rate of $10\,\mathrm{kHz}$ and with average power of 10 - 20 W with a spatially multi-mode profile in p-polarization. The resonator geometry consists of two curved mirrors for focusing the resonator mode into the crystal, which are transparent for the incident pump light. It is closed by a high reflective mirror on one end, and a slightly wedged output coupler with 80 % reflectivity in the fundamental Ti:sapphire emission spectrum at the other. Wavelength selection and tuning possibility from this band is realized by several frequency selective elements within the resonator. At first, the coating of the inserted mirrors gives a broad pre-election. While a so-called "broad-band" mirror set enables tuning over the majority of the gain curve, more specialized sets favor reflection on the high- and low frequency part, and prevent competing pulse build-up near the gain maximum. Thus, including correspondent combinations of these sets, overall an output range from 690 to 960 nm is accessible. Further mode selection is realized by the combination of a 3-plate Lyot-filter and a Fabry-Pérot etalon (realized as a plane-parallel substrate with double-sided coating) in the resonator. The Lyot filter's free spectral range (FSR) of 100 THz allows for one roughly 100 GHz wide amplification window in the range given by the mirror set. The standard etalon (0.3 mm thick glass substrate with a 40 % reflectivity coating) exhibits an FSR of 330 GHz, thus enabling only one transmission peak inside the Lyot filter's window, with a resulting spectral width of 3 to 5 GHz. This final laser output implies a few of the about 30-50 allowed longitudinal cavity modes (with a Fourier-limited bandwidth corresponding to the 50 ns pulse duration) which appear on a pulse-per-pulse base with a Gaussian-like probability distribution around the central wavelength. For a set of consecutive pulses this mechanism effectively forms an also Gaussian-like spectral output profile.
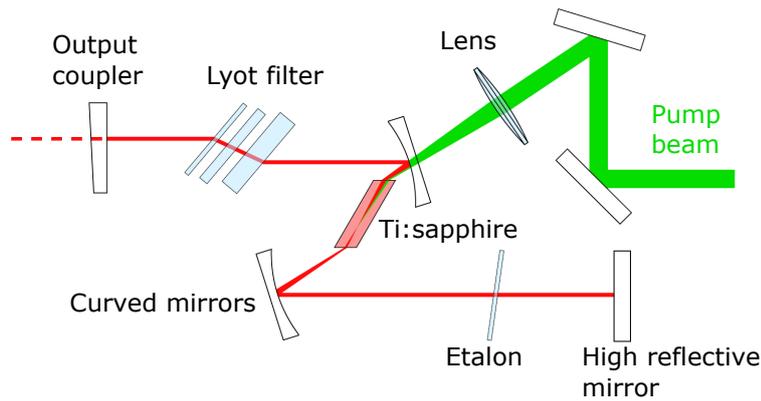
Figure 3.2: Schematic layout of the standard Ti:sapphire laser Z-cavity system. Frequency selection is achieved by combination of specific mirror sets, a Lyot filter and a Fabry-Pérot etalon. See text for details. Graphic adapted from [26].

With the operation parameters described above, average output powers in the range of 2 - 5 W can be achieved. The remaining spectral width nicely matches the typical Doppler broadening ot the atom ensemble within a hot cavity ion source, providing coverage of all velocity classes. Correspondingly, saturation of the atomic transitions of all atoms within all velocity classes present in the interaction volume can be reached in most cases, rendering the standard Ti:sapphire laser the "work horse" for efficient ion production. Automation regarding the control and preservation of the lasers' ISST parameters (see section 3.1) can be implemented in rather convenient ways [71, 72]: Regulation of the frequency is done by a feedback control of the etalon in respect to the readout of a wavelength meter. In an environment of constant temperature, and absence of dust, the output power of the solid state lasers should expectedly remain constant by itself. Nevertheless, stabilization can be implemented by a combination of a tunable $\lambda/2$-plate for rotation of the outgoing (p-polarized) beam and a subsequent element with polarization-dependent transmission. Temporal pulse synchronization is most easily done by providing respective trigger signals for individual q-switched pump lasers, while optimum focusing and spatial overlap in the ion source volume can be ensured with commercially available systems based on position-sensitive detectors installed at a proper reference spot and a full motorization of the laser beam transport components.

3.2.2   Injection-Locked Ring-Titanium:Sapphire laser

For high resolution spectroscopy with pulsed lasers with envisaged line widths of some MHz, the standard Ti:sapphire laser is not applicable. In fact, operation on a single longitudinal mode of the resonator and is requires with a bandwidth only constrained by the Fourier-limit of the pulse duration. In a standing wave geometry like the Z shape, this is not possible due to the effect of *spacial hole burning*. In particular with the active medium located in the center of the resonator, the nodes of a longitudinal mode of order n just spatially coincide with the anti-nodes of a standing wave with order $n \pm 1$ (which both naturally have nodes on the resonator end mirrors). Therefore, population inversion will not be depleted entirely by the desired mode n, but a least one neighboring mode will also be amplified. An arrangement to overcome this problem is a ring-type resonator with a propagating wave instead of a standing wave, which can achieve uniform and complete depletion. The system used for this work is realized in a so-called bow-tie geometry as shown in fig. 3.3.
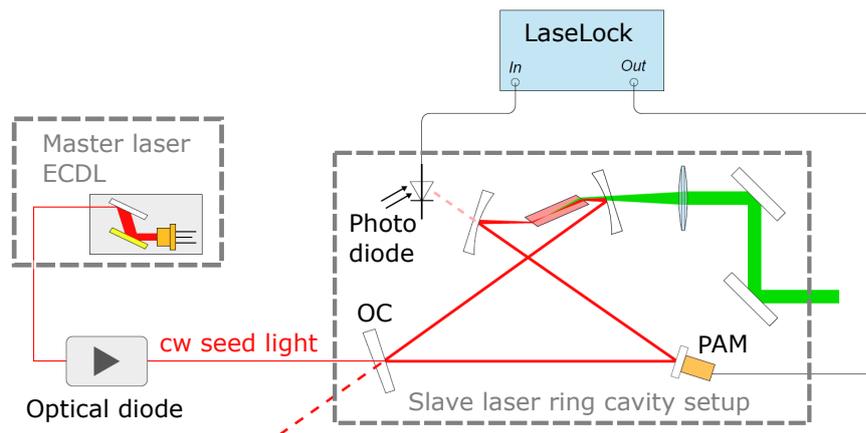
Figure 3.3: Schematic layout of the ring-Ti:sapphire laser in combination with an injection-seeding home-built ECDL master laser for narrow bandwidth applications. A commercial system stabilizes the ring cavity via a piezo-actuated mirror (PAM) on resonance. The pulsed high power radiation taken from the output coupler (OC) is used at the experiment. See text for details. Graphic adapted from [26].

In principle, this setup is able to provide narrow bandwidth output of only one longitudinal mode. A prerequisite is the stabilization of the cavity length to resonance at the desired wavelength, i.e. to an integer multiple of $\lambda/2$. Due to pressure and temperature fluctuations or acoustic noise, this stabilization has to be applied steadily and in a feedback-controlled way, both preventing fast jitter on a short term basis as well as slow drifts on long term. As the operation of a pulsed system only provides feedback during the actual lasing phase, operation as a standalone-system is hard to achieve (but has nevertheless been proven to work in a prototype way, as discussed in [66]).

To overcome this problem, the system is used in a slave configuration with seeding photons from an independent laser, operating in *continuous wave (cw)* mode. This has two advantages:

- On the one hand, the permanent presence of photons of the desired wavelength enables the stabilization of the cavity length on resonance, which is done in between the pulses of the pump laser.

- On the other hand, these photons also act as *seed* for the stimulated emission on their wavelength. In this way, complete depletion of population inversion going along with maximum amplification and pulse build-up on this frequency is forced. This fact even makes any further frequency-selective elements in the resonator usually obsolete.

The technical implementation is shown in fig. 3.3 as well. A detailed description of the setup and its development stages can be found in [22, 61, 62]; specifically and most up-to-date in [73]. The master laser to provide radiation on the desired wavelength is an *external cavity diode laser (ECDL)* with a home-built system for frequency stabilization. Apart of active temperature control via Peltier elements, this system includes a commercial TEM iScan[1] laser stabilization unit providing fast regulation via both the operational current of the laser diode as well as the setting of the external grating of the cavity and it operates in. On top of that, an Arduino microprocessor based

---

[1]Technical information at http://www.tem-messtechnik.de/iscan.htm

reference system designed around a commercial stability-certified He-Ne-Laser (SIOS SL 03[2], $\pm 2.5\,$MHz absolute frequency stability on the $632.8\,$nm output) using fringe offset locking in a scanning Fabry-Pérot interferometer (SFPI) [74] ensures absolute frequency definition. The overall accuracy of this setup results in a remaining locking jitter of typically $3\,$MHz.

The ECDL light is then coupled into the ring laser cavity. The sensitive system of the ECDL and its stabilization has to be protected from the high power output during the slave laser's pulsed operation. For this purpose, a set of three Faraday rotators are used to act as absolute light-tight optical diodes against any returning radiation or optical feedback. To achieve the desired operation, the seed light and the spatial mode propagating in the resonator have to be matched precisely, as even slight misalignments can still cause competing modes within the Ti:sapphire gain spectrum to rise, interfere or even possibly dominate the seed mode. Active stabilization of the optical path length of the ring cavity is done by a commercial TEM LaseLock[3] system. A home-built $10\,$kHz switchable fast photo diode assembly, which is electronically blanked and protected during pump pulse arrival and Ti:sapphire laser pulse build-up for about $8\,$µs [62] allows for almost permanently monitoring the radiation leaking through one of the curved cavity mirrors to provide an electronic feedback. Based on this, manipulation of the cavity length is done by a voltage controlled piezo actuator moving one of the cavity mirrors. Voltage modulation at a high frequency of about $42\,$MHz and a small amplitude (so-called *dithering*), produces the response signal for cavity optimization. The LaseLock system uses this input to stabilize the cavity in lock-in amplifier mode via a PID regulating process onto maximum output signal, representing the situation that the cavity length is resonant to the input seed light.

For operation of this system, the required pump power is similar to that of the standard Z-cavity laser. Nevertheless, as the presence of seed photons causes a much faster build-up of the laser pulse, temporal synchronization of the injection-locked ring Ti:sapphire laser to a standard laser is not possible if both are pumped by one single pump laser - a dedicated pump laser is required. Additionally, in contrast to the standard laser system, a high pump beam quality (meaning transverse spatial single-mode profile (TEM$_{00}$) and good focusing characteristics ($M^2 \approx 1$)) aid in matching of the ring cavity mode to the seeding beam and prevent pumping of the active medium outside, significantly suppressing competing mode build-up. Regarding output power, the free running ring laser (without seed light) exhibits two output beams according to the two directions of propagation. When the seed light mode is matched well, all output is forced into one direction, resulting in the sum of the power of both previous beams in the output beam (referred to as $100\,\%$ seed efficiency). This overall power again is in the range of 1-3 W. As the bandwidth is in the order of 10-20 MHz [62], the spectral power density is about a factor of 50 higher than the one of the standard laser, resulting in adequately higher efficiency in frequency conversion.

The overall tuning range of this setup is determined by the seed laser, i.e. the diode laser. Typically, the laser diodes installed operate in a regime of some $10\,$nm. The local continuous tuning range when the setup is optimized to one working point spans up to some $10\,$GHz, which is for most cases sufficient to cover a complete hyperfine splitting. Alternatively, a slight variation of the working point can be achieved by minor changes in the operation temperature of the diode.

---

[2]Technical information at https://sios.de/produkte/stabilisierte-he-ne-laser/stabilisierter-he-ne-laser-sl-03/

[3]Technical information at http://www.tem-messtechnik.de/laselock.htm

In this system, a set of several diodes is required to access the whole Ti:sapphire range. Changing the wavelength to another diode might include several hours up to days of work for realignment and optimization of the stabilization system. Thus, a cw Ti:sapphire laser itself would be a natural alternative choice as master laser. Commercial systems like that are in use e.g. at the CRIS collaboration at CERN, while a compact, reliable and cost-efficient system is also being developed in the collaboration right now [75].

3.2.3 Laser Frequency Measurement

Absolute laser frequency measurement and recording is done by two different wavelength meter models. A HighFinesse WS6-600[4] ($200\,MHz$ 1σ-accuracy, but limited to $20\,\%$ of the laser line width) is used for the broad band standard lasers. For the narrow bandwidth laser system, the diode master laser is monitored by a HighFinesse WSU30 (now sold as WS8-30[5], $10\,MHz$ 1σ-accuracy, limited to $20\,\%$ of the laser line width). Bot devices are calibrated to the stabilized He-Ne-laser also used for the SFPI fringe offset locking described in sec. 3.2.2.

3.3 The RISIKO Mass Separator

The presented work has been conducted at the RISIKO mass separator at Mainz University. It comprises an ion source to create charged species of elements or molecules, an electrostatic acceleration stage to form an ion beam of typically $30\,keV$, subsequent mass-to-charge-ratio separation and different ion detection units. Originally, the RISIKO was built for trace analysis applications on radioactive strontium isotopes in environmental samples in the aftermath of the Chernobyl reactor incident [76]. A comprehensive and detailed description of its current status after almost three decades of steady development can be found in [77]. The main scope of this work at hand will be put on the ion source section and especially the LIST ion source, which has been significantly upgraded to provide a tailored environment for high resolution spectroscopy in an way that is also applicable for an installation at on-line facilities. Similarities and differences to the ISOLDE setup will be discussed.

3.3.1 Technical Layout

A schematic overview of the RISIKO mass separator is given in fig. 3.4, in its current status in standard configuration for in-source laser ionization applications. The front end part containing the ion source setup resembles the ISOLDE 2 design, thus making technical developments easily adaptable to on-line applications in a natural way. This part is kept at typically $30\,kV$ electrical potential, whereas the rest of the apparatus is on laboratory ground potential and accessible at all times. The ions are accelerated in a two-stage extractor system. A subsequent einzel lens, horizontal and vertical deflectors as well as a quadrupole triplet enable beam shaping and position correction to ensure optimum acceptance by a double-focusing 60° sector field magnet on its design path and provide a horizontal focus at the position of a vertical slit separating beams of different mass-to-charge ratios. The desired species can than be analyzed downstream

---

[4]Technical documentation at https://www.highfinesse.com/en/wavelengthmeter/wavelengthmeter-further-information/technical-information-wavelengthmeter-ws6-600-series.pdf

[5]Technical documentation at https://www.highfinesse.com/en/wavelengthmeter/wavelengthmeter-further-information/technical-information-wavelengthmeter-ws8-30-series.pdf

by different detectors, as e.g. a Faraday cup for ion currents above $\approx 100\,\text{fA}$ or by single particle counting with time resolution in a secondary electron multiplier. A more detailed description of these essential parts is given in the following subsections. Typical working parameters are vacuum conditions in the $10^{-7}\,\text{mbar}$ range, maintained by a system of turbomolecular and rotary vane pumps arranged in four independently accessible sections (source, magnet, separating slits, detection). The mass separator exhibits an isotopic sensitivity of $S \approx 10^{-4}$ and a mass resolution of $R = \frac{M}{\Delta M} \approx 1000$. It has been proven that overall experimental efficiencies including sample atomization, laser ionization, ion beam transport and ion detection can surpass $50\,\%$ [26, 67]. Transmission and detection efficiency close to $100\,\%$ can be assumed, while the ionization in the cavity is seen as the bottleneck of this process.
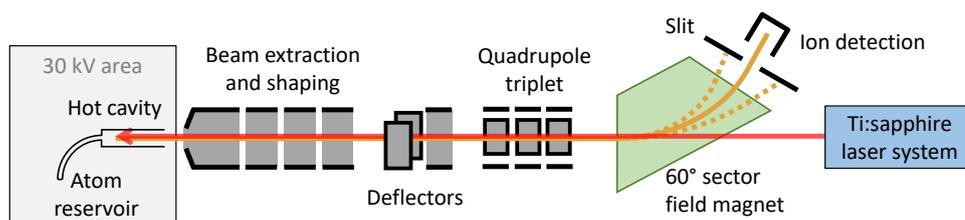
Figure 3.4: Schematic overview of the RISIKO mass separator in standard configuration with its essential components. A thin capillary sample reservoir is independently heated to provide atomic vapor which diffuses into the hot cavity, where ionization by the incident laser light takes place. The ions are extracted by a $30\,\text{kV}$ acceleration potential, shaped to a beam and guided through the separation magnet. In its focal plane, a vertical slit separates beams of different mass-to-charge ratios. The transmitted ion current is monitored subsequently by different types of detectors. A second focusing and deflection system downstream the separation slit is omitted in this sketch for the sake of simplicity.

Ion Source

The standard ion source in operation at the RISIKO facility as well as constituting principal source used today at ISOLDE and many other (radioactive) ion beam facilities worldwide is the Resonance Ionization Laser Ion Source (RILIS) [3, 78]. An overview of the geometry used at Mainz is depicted in fig. 3.5. It evolved from conventional surface ionization source designs, where ionization is achieved by transfer of an electron from a free atom to a hot surface (see sec. 2.1.5). Construction comprises rather simple arrangements of hollow cylindrical cavities with attached capillaries and electrodes. For application as a laser ion source, primary purpose is to provide a well-enclosed, defined environment where the species of choice are provided in a mono-atomic and vaporized state for unperturbed interaction with the incident laser radiation. Heating is realized by resistive power dissipation of a longitudinally applied electrical current of up to some $100\,\text{A}$, which also imposes a voltage gradient oriented in a way to guide ions towards the exit orifice to enter the mass separator. For all components, high melting point materials as molybdenum, tantalum, tungsten or rhenium are used to easily reach temperatures of $2000\,°\text{C}$ and above while maintaining mechanical stability and robustness during operation. For more specialized cases, different materials with specific properties regarding adsorption behavior (e.g. quartz, for suppression of alkali elements [79]), low work function (e.g. LaB_6, for surface ionization reduction or negative ion production [80, 81]) or electrical resistance (glassy or highly ordered carbon as high-temperature, high-resistance material [82]) may be used. They may induce drawbacks

as, e.g. more difficult machining, critical fragility, lowered thermal resistance or rapid degradation over time [80]. Therefore, tantalum most often is the material of choice, and all measurements presented in this work were conducted in a cavity of this type.
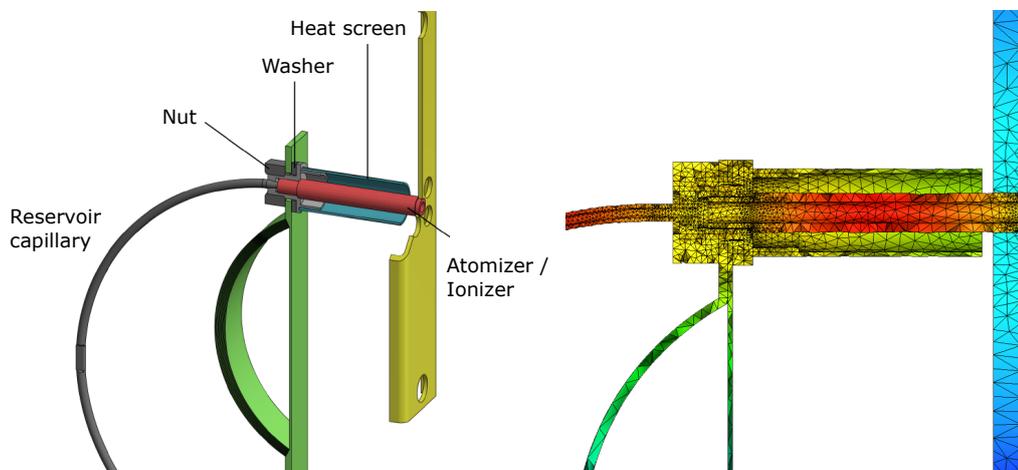
Figure 3.5: Left hand panel (adapted from [26]): CAD cut view of a RILIS setup as installed at the RISIKO mass separator. The ionizer cavity and reservoir capillary can be heated independently. Right hand panel (courtesy of T. Kieck): Simulation of temperature distribution using Autodesk CFD®. A significant gradient is apparent, in the presented case between 2000 °C at the center and 1500 °C at both end parts of the ionizer. Alternatively, a cavity which is completely closed at the hottest part can be used. See text for details.

The RISIKO central ion source is a 35 mm long cavity with an inner diameter of 2.2 mm. The electrical current is fed in through a water-cooled copper rod and a flexible mounting structure consisting of multiple tantalum sheets. This structure additionally holds a cylindrical metallic heat screen around the cavity. The exit part of the atomizer is fixed in a solid tantalum panel with gaps designed to minimize heat flow away from the cavity. This panel again is fixed on the similarly water-cooled front end chassis. In the course of linked thermo-electrical simulations and experimental validation, the design was optimized to avoid cold spots in the setup (while still maintaining similarity to the ISOLDE design), especially at the interconnection section [83, 84]. Heat radiation was identified as major reason and counteracted by reduced surface areas and choices of low emissivity materials (molybdenum instead of graphite). Nevertheless, the setup still exhibits a colder part at the back end as well as at the interconnector (see fig. 3.5) which may cause long release times and efficiency losses. One way to run the source was therefore chosen to produce cavities which are completely closed in the center at their hottest part at about 20 mm distance from the exit orifice and place the sample directly inside.

The regular way of operation is to supply the atoms of choice via a sample reservoir, which is located in a thin tantalum capillary of 1.1 mm inner diameter attached directly to the ionizer back (resembling the ISOLDE "mass markers"). This reservoir is heated independently and controls the provision of sample atoms into the ionizer.

The atom samples in Mainz are usually provided as solutions, e.g. as a calibrated standard bought from a specialized supplier company or resulting from chemical in-house pre-treatment. After diluting this solution to the desired concentration, an amount of some µL is pipetted onto a metallic carrier foil (most commonly with a melting point higher than that of the sample and with specific chemical properties to prevent the formation of oxides, such as zirconium or hafnium). After evaporation of the solvent

and crystallization of the remnants, the foil is folded to fully enclose the sample and inserted into either the reservoir or the hot cavity itself.

Ion Beam Extraction, Shaping and Separation

The whole ion source unit and front end chassis sits on high voltage platform, which is set to a potential of 30 kV for operation. The ion beam is attracted by an extraction electrode shaped in Pierce geometry [85] to counteract space charge effects. While at ISOLDE this extraction electrode is biased directly to ground potential but variable in distance (with a safety minimum margin of 1 mm/kV), at RISIKO an earlier two stage extraction system avoiding moving parts is used. The electrode is fixed at a distance of 40 mm to the source exit and can be set to any potential (typically 20 kV), while the full acceleration energy is finally reached after a drift distance of 400 mm at the passage into the first segment of an einzel lens. This combination of two focusing elements acts as a telescope and allows for adjustment of the beam's size and divergence at the entrance of the magnet, which affects mass resolution. Adjustments for the resulting focus to be properly placed at the separating slit's position is assisted by subsequent vertical and horizontal deflectors that are used to correct slight transversal beam offsets, caused e.g. by thermal distortions of source components. In normal operation, only some 10 V are required, primarily affecting the vertical direction. An additional quadrupole triplet has been installed most recently and enables adjustments to beam astigmatisms, which is especially important for a controlled spot size and shape at the detection region, where ion implantations with microfocus are carried out for another project of the group [86]. The two latter components also exhibit a possibility to implement an ion beam gating technique, by which the beam can be deflected by fast (sub-µs) high voltage switching of one element for a given time, e.g. a fraction of the pulse laser duty cycle. This will be discussed in detail in section A.3. Mass separation is realized by the 60° sector field magnet with a maximum magnetic field of 0.6 T. The selected mass passes a vertical slit of adjustable width, which is set as well chosen compromise between mass resolution and transmission. At this position, an insertable Faraday cup is installed. Further downstream, another system of focusing optics and deflectors is installed to control positioning on either the implantation Faraday cup, or the single ion detector for the measurements presented here.

Ion Detection and Data Acquisition

For the measurements conducted in the course of this work, two different detector types have been used for determination of the ion current. A home-built Faraday cup is used for monitoring of currents above about 100 fA (corresponding to roughly 500.000 singly charged particles per second) at a location directly behind the separating slits. The current impinging on its end plate is measured and by a Keithley 617 electrometer. A negatively biased ring electrode suppresses potentially emitted electrons to ensure correct acquisition of the incident beam current. Below the ion detection limit mentioned above, a signal is hidden within electrical noise. Similarly, time structure investigations in the domain of the 10 kHz repetition rate of the laser system can not be achieved because of the intrinsic integration time of the device. This limitation is overcome by using an additional detector specialized for single ion counting. A secondary electron multiplier amplifies each incident particle along an array of biased dynodes to generate an electron avalanche, which can be detected as a some 10 mV high signal spike of a few ns. A subsequent discriminator/amplifier system translates these pulses into TTL-conform

signals which are monitored either by counter electronics or via a multi-channel analyzer card (FAST ComTec) with a time resolution of 100 ns.

Data acquisition, visualization, first-level processing and storage are implemented in home-built programs of the system design software National Instruments LabView (version 2014) on a control PC. Also almost all experimental parameters can be controlled and monitored this way and a variety of automated scanning routines is available for systematic investigations or optimization. Still, the system is in a steady development stage reacting on the highly flexible and altering demands on the machine for different projects and trying to provide easy access and adjustment to individual requests and specific requirements.

3.4 The Laser Ion Source and Trap LIST

While the "standard" RILIS ion source is presented in section 3.3.1, this chapter will introduce a specifically upgraded ion source concept for highest element selectivity and optimum suppression of non-laser related ion beam contamination. The Laser Ion Source and Trap LIST relies on spatial separation of the hot atomization cavity environment and a clean laser-atom interaction volume. Thus, isobaric contaminations, which can not be separated in the magnet, arising from un-selective surface ionization can be suppressed, even if usually present in overwhelming fractions. Aim is production of intrinsically mono-isotopic ion beams, with the figures of merit being the *LIST suppression factor (LSF)* of the contamination compared to standard RILIS operation, and the *LIST loss factor (LLF)* quantifying the unavoidable efficiency or intensity decrease.

While the LIST in standard operation mode with collinear laser beam guidance equivalent to the RILIS has been successfully implemented at ISOLDE already some years ago [87, 88], a recently developed technique of lateral irradiation of the atoms which effuse from the hot cavity inside the quadrupole structure will be presented. This Perpendicularly Illuminated LIST (PI-LIST) is the starting point for the work presented in this thesis.

3.4.1 Initial Concept and History

The concept of separating the hot atomization cavity with its intrinsic property of surface ionization of contaminations from the specific "cold and clean" laser ionization volume was first proposed in [49], and a setup was constructed and characterized in the course of [89]. A schematic overview is given in fig. 3.6. Both electrons and positively charged ions (mostly surface ionized contaminants) are suppressed directly downstream of the hot cavity atomizer by two repelling electrodes with negative and positive voltages. Inside a radio-frequency quadrupole (RFQ) structure which provides radial confinement, the neutral atoms which effuse out of the cavity as somewhat collimated beam are resonantly ionized by the element-selective multi-step laser process. A buffer gas filling would provide cooling of these atoms while they are guided through the system by a corresponding DC potential superimposed on the segmented RFQ rods. Near the exit, the ions could be trapped and accumulated in a potential minimum. By fast switching of the last RFQ elements, a temporally well defined bunch of ions with a low transverse emittance due to the cooling can be ejected into the subsequent beam line and mass separation system.
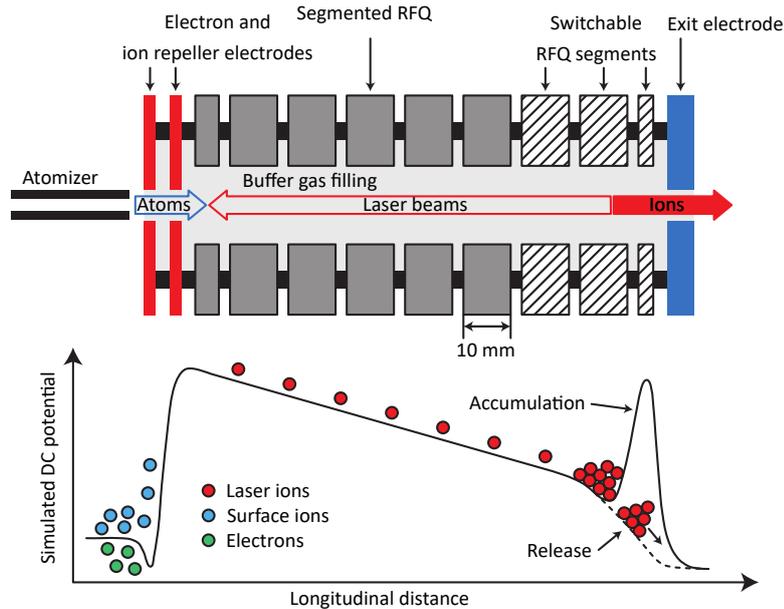
Figure 3.6: Schematic overview of the original setup of the Laser Ion Source and Trap LIST.
Both ions and electrons from a hot atomizer are hindered from entering a radio-frequency
quadrupole (RFQ) section filled with buffer gas. Ions created by laser radiation inside there
are accumulated by a longitudinal guiding field imposed by segmentally controllable DC
voltages on the rods. Finally, by switching the potential on the last segments and exit
electrode, a contamination-free bunch of ions can be delivered to the beam line system. The
bottom panel shows the respective longitudinal electric potential on the central axis, and the
effect on the charged species. Figure adapted from [89].

3.4.2   The LIST at ISOLDE

For the implementation and specific demands at ISOLDE, the concept was adapted and
had to undergo drastic simplifications. Operation with buffer gas was dropped due to
incompatibility of the front end vacuum pump structure, as a large amount of potentially
radioactively activated gas can neither be stored nor recycled. Segmentation of the rods
and introduction of an internal longitudinal field has been skipped for infrastructure
reasons, as the number of voltage feedthroughs made available at the ISOLDE front end
was very limited. The RFQ is operated in an AC-only mode without superimposed DC
potentials. Also the second repelling electrode was omitted initially. In the course of the
work presented in [90], a corresponding downgraded prototype was built and proved to
provide the desired characteristics in selectivity enhancement and efficiency. Essentially,
the LIST lost its application as an actual "trap", but the acronym was kept. A complete
integration of the LIST at ISOLDE and first ever on-line experiments utilizing its
properties were done during the theses of D. Fink [91] and S. Richter [77], with extensive
descriptions of operation characteristics presented in [87, 92]. Additionally, a detailed
technical construction manual was compiled, which is accessible upon request to the
LARISSA working group or the ISOLDE target and ion source development (TISD)
team. The results for hyperfine structure of neutron-rich polonium isotopes, which were
previously inaccessible due to an overwhelming fraction of isobaric, surface ionized
francium isotopes in the beam are given in [88]. This "standard" version of the LIST
was the starting point for upgrades featuring lateral laser access for significant reduction
of experimental Doppler broadening effects and will be briefly characterized here.

A CAD view of the whole source setup at the ISOLDE front end, including the radioactive isotope production target, is given in fig. 3.8. The LIST structure itself is introduced as an addendum to a standard RILIS cavity (as described in sec. 3.3.1). At a distance of 2.5 mm downstream its exit (being considered a safety margin to not provoke electrical contact by thermal expansion, material build up or condensation), a 90 mm long radio frequency quadrupole structure (RFQ) is placed, following a 1 mm thick ring-shaped electrode with a central orifice of 11 mm diameter. All parts are fabricated either from stainless steel for the electrical conducting parts, or the high-temperature resistant boron nitride for insulators.

An integral part of the LIST ion source unit is also the required supply for the RF voltage with sufficient amplitude. Especially under on-line conditions, where the power supplies are separated from the highly radioactive front end area by a distance of about 20 m, transport of an AC potential of ≈ 1 MHz and high amplitudes through a long cable with unavoidable parasitic electrical capacities is difficult, leads to significant losses and distortions of the waveform. Ideally, two anti-symmetric sinusoidal signals of equal amplitude have to be supplied to opposite pairs of rods. The implemented solution is a resonance circuit directly attached to the target front end unit called *transducer box*, which acts as a transformer for voltage enlargement and provides symmetrication. As it can not be constructed from standard electronic parts which would quickly degrade or be destroyed by the high radiation dose, it is made of air coils and all-metal rotary variable capacitors. A photo of the setup, together with a schematic circuit diagram is given in fig. 3.7 and described in [77] in more detail. The circuit is fed by one phase of the chosen frequency from a home-built pre-amplifier over a 20 m long coaxial cable and tuned to resonance before connection to the front end. Via two individually tunable coupled LC circuits, two anti-symmetric signals of up to 1000 V peak-to-peak amplitude can be delivered to the respective quadrupole rods. While in off-line operation these outputs can be monitored e.g. on an oscilloscope, this option is not existing for installation at the on-line separators. Also no final precision tuning can be done anymore, which would include manual manipulation of the capacitors. Thus, in the current setup, one has to rely on stability after the last optimization.

For operation of the LIST, its repeller electrode allows for two different modes: A negative bias effectuates extraction of ions created in the source, which are subsequently transversally confined and drift through the LIST towards the final high voltage extraction into the ion beam line. This so-called *ion guide (IG) mode* resembles standard, efficient RILIS operation with the LIST just being a "passive" element. Contrarily, the *LIST mode* operation comprises positive voltage on this repeller electrode, which inhibits all positively charged species (more specifically, the surface-ionized contaminants) from entering the RFQ and allows only passage of neutral atoms in. Laser resonance ionization then takes place in this clean environment, resulting in sole ion production of the element of interest. Again, these particles are guided towards beam line extraction and subsequent mass separation by their initial velocity and the very weak acceleration field leakage into the RFQ structure. While no buffer gas cooling or ion trapping is foreseen in this simple design anymore, the main purpose of the quadrupole structure and terminal exit electrode is shielding of the extraction field in the range of kV/mm, which would otherwise cause creation of ions on different, lower starting potentials, resulting in different trajectories in the separating magnet. A closer look on this effect and its general implications for laser ion sources is given in section A.1.

A natural way of characterizing the LIST's performance is the comparison between IG and LIST mode, and for operation with and without resonant laser ionization. This is commonly done by a complete scan of the repeller voltage, as shown in fig. 3.9. At

(a) Photograph of the LIST target/ion source unit with attached transducer box.

(b) Schematic circuit diagram of the RF supply for the LIST RFQ.
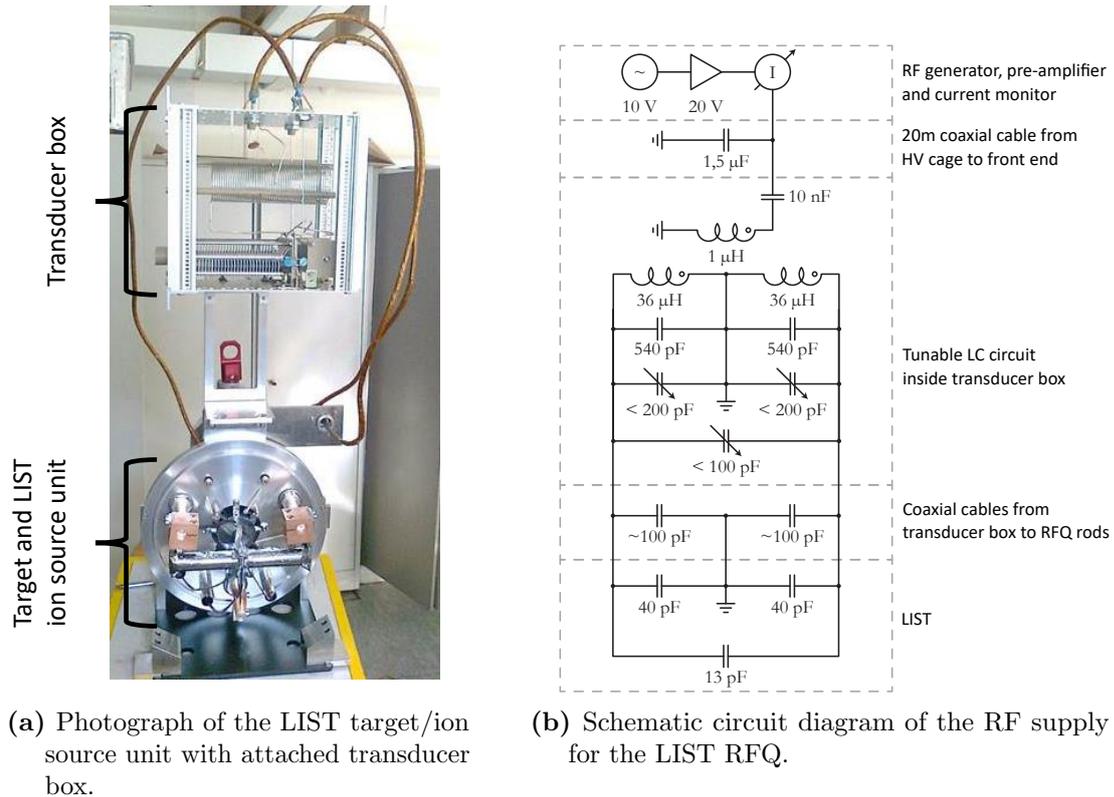
Figure 3.7: Overview of the LIST transducer box for transformation and symmetrication of the RF voltages for the RFQ as implemented for the harsh radiation environment at the ISOLDE on-line front ends. Figures adapted from [77].

negative voltages, the ion signal is higher and resonantly tuned lasers enhance the production rate further. A working point of maximum ion current output can be found by careful adjustment of the repeller potential. If, alternatively, the repeller is positively biased, all ions created in the source (laser ionized species as well as those created by non-selective surface ionization) are extracted. Also in this regime, a specific working point with maximum laser ion current can be found. Between these two settings, the LIST loss factor (LLF) gives the loss in intensity, while the LIST suppression factor denotes the relative reduction of non-laser related ionized species when the lasers are turned off. The ratio of these two figures gives the enhancement in ion beam purity compared to conventional RILIS operation, referred to as *LIST quality factor (LFQ)*. A prerequisite for this description is the assumption that the efficiency in ion guide mode is indeed the same as the one of the conventional RILIS source. Overall efficiency measurements by integrating the ion current during evaporation of a calibrated sample in the source, which were conducted on stable magnesium [88] and ytterbium isotopes confirm this [77] for a wide range of operation conditions. Anyhow it must be noted, that for a high ion load in the hot cavity a considerably higher negative potential has to be applied to the repeller electrode to still efficiently extract all ions, and that transmission limitations through the RFQ structure in IG mode, which are attributed to space charge effects, occur as well. Both situations decrease the efficiency of IG operation compared to RILIS, but do not significantly affect the LIST mode. This might leas to a certain underestimation of the LIST loss factor, which then no longer gives the proper decline in efficiency compared to operation without LIST.
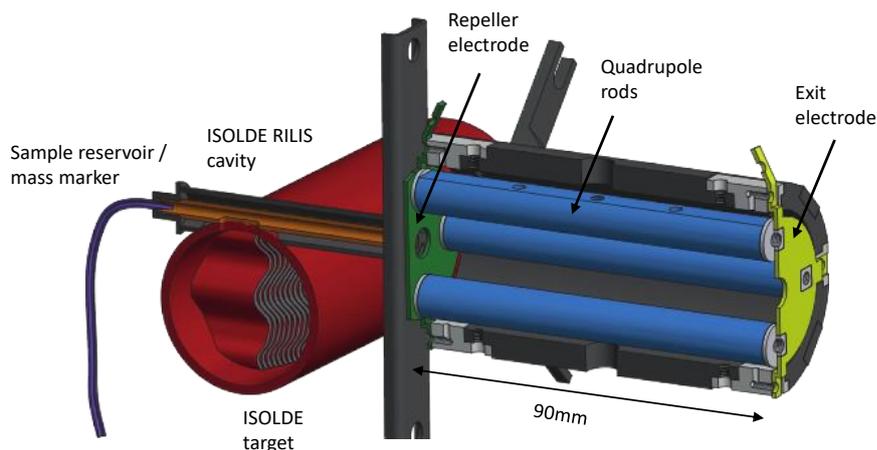
Figure 3.8: CAD view of the LIST as implemented at ISOLDE in 2012, as an addendum to a standard RILIS and connected to the target for radioactive isotope production. The LIST structure is mounted directly downstream the hot cavity exit with a margin of 2.5 mm. Positively charged species are either blocked from our guided into the radio frequency quadrupole (RFQ) structure by an electrostatic electrode, depending on the operation mode. In LIST mode, ions are solely created by resonant laser radiation inside the RFQ, transversally confined and drift towards extraction into the beam line system. Figure adapted from [77].

A surprising result from the first on-line applications was the observation of a strong isotope-dependence of the suppression factor within the chain of a single element, with values of LLF = 70 for ^{212}Fr and > 700 for ^{220}Fr [87]. This effect could be assigned to effusion of strongly dominating volatile radioactive material at mass 212 (^{212}Fr) from the hot cavity into the RFQ and subsequent condensation on cold surfaces such as the quadrupole rods. After possible re-evaporation, the non-laser related process of electron impact ionization caused these species to contribute to the outgoing beam as contamination. This assumption was strongly supported by observation of the extremely short-lived isotopes ^{216}At (300 µs) and ^{217}Rn (540 µs) isotopes, for which the half-lives are not compatible with extraction from the target but which have to be produced in the LIST structure itself as decay products. To overcome these limitations, reduction of the potential surface areas for condensation was proposed, e.g. by thinner quadrupole rods and a mesh as exit electrode. An alternative approach is inhibiting the passage of electrons emitted from the hot ion source cavity into the LIST structure by a negative electric potential, similar to the one for positive ions and applied on a second repeller electrode.

If the above described effects are not present, typical suppression factors measured for the ISOLDE LIST source are in the 10^3 regime, while loss factors are between 20 and 50. The highest suppression factor observed so far was reached for ^{26}Na with $> 10^5$. Even more advantageous loss factors down to 4 measured on ^{208}Po can be attributed to the misleading effects of high ion load in the cavity and RFQ transmission limitations described above, which lead to an underrepresentation of the ion current in IG mode.

For a complete compilation of hot cavity type ion sources involving electrostatic surface ion suppression and subsequent laser ionization, also the Ion Guide Laser Ion Source (IG-LIS) at TRIUMF-ISAC in Vancouver, Canada has to be mentioned. A CAD view of this type is given in fig. 3.10. It comprises a much more compact design of only 35 mm length and a field-free diameter of 10 mm between the RFQ rods. The setup also features a water-cooled copper heat screen between hot cavity and repeller, and the
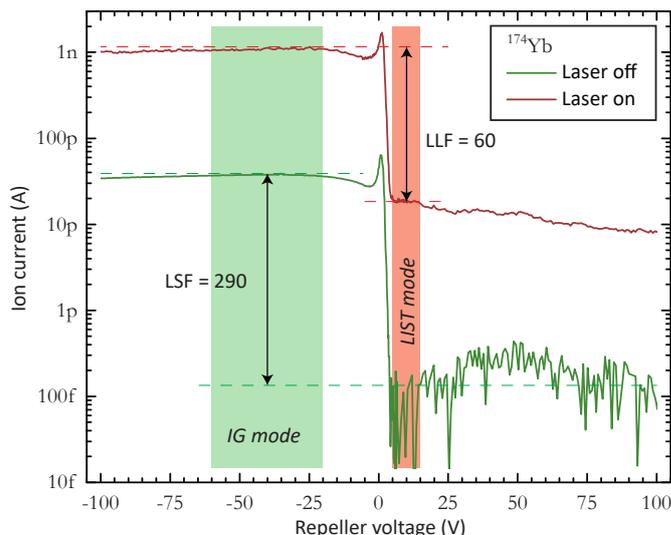
Figure 3.9: Exemplary repeller scan with the standard LIST as implemented at ISOLDE, measured on the isotope ^{174}Yb. Negative voltages resemble "standard" RILIS operation (IG mode), while positive voltages block all ions created in the hot cavity and only allow laser-ionized species from inside the RFQ structure in the beam (LIST mode). The *LIST loss factor (LLF)* describes the intensity loss between both situations, while the *LIST suppression factor (LSF)* gives the reduction of charged species from inside the hot cavity when the lasers are switched off. Figure adapted from [77].

possibility to vary the electric potential of the target/ion source unit in respect to the front end ground potential. With this source, suppression factors of up to 10^7 and yield loss factors (meaning comparisons to previous runs with standard TRILIS sources) of only around 10 are reported [93].

3.4.3   The Perpendicularly Illuminated PI-LIST

A complete novel field of application for the LIST ion source is the implementation of lateral laser access to the RFQ structure, which was introduced in the work of T. Kron [66] and is technically documented in [29]. This makes it possible to perform high resolution spectroscopy in a setup, where Doppler broadening is drastically reduced. The general concept implies to avoid laser interaction with the entire velocity distribution of the atomic vapor inside the hot cavity but addressing a strongly reduced set of velocity classes only. A number of experimental approaches are available for this task:

- In the approach of collinear laser spectroscopy, the ensemble with initial thermal velocity distribution from the ion source is accelerated as an ion beam to some 10 keV of beam energy, resulting in compression of the Doppler broadening. This technique is applied either followed by fluorescence detection as in the COLLAPS experiment [17], or subsequent ionization and charged particle detection as done at the CRIS setup [94].

- At gas cell-based facilities, where atoms are thermalized and transported by a flow of high purity noble gas into the mass separator system, the formation of a sharply directed and intrinsically low temperature supersonic jet out of the cell can be achieved by using an appropriately shaped nozzle and matching of the in-cell and jet ambient pressures. In this case, a laser can be applied perpendicular to the jet and benefit from the low spread of velocities in this lateral direction [18, 95, 96].
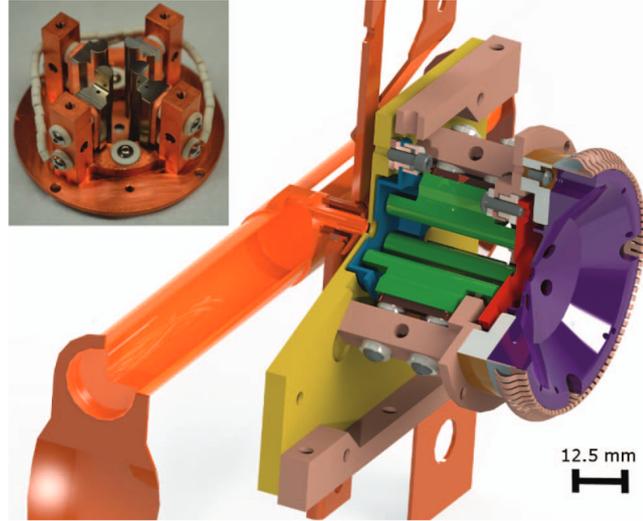
Figure 3.10: CAD view and photograph inset of the LIST-type Ion Guide Laser Ion Source (IG-LIS) as implemented at ISAC/TRIUMF. The setup is compact and features a water-cooled copper heat screen and the ability to electrically bias the target/hot cavity unit. Figure taken from [93].

The PI-LIST pursues a rather similar, yet more simple approach as the latter and exploits the directed movement of the effusing atomic beam from the hot cavity. This technique has already been applied at other hot cavity systems, e.g. in smaller mass spectrometers for highly sensitive isotope separation in trace analysis of ^{90}Sr [20], ^{41}Ca [21] and of uranium [22, 23], or high resolution hyperfine structure spectroscopy in the 200 MHz regime, e.g. on technetium [24] or copper [25]. Incorporation into the LIST structure with lateral laser access allows the adaption to the RISIKO facility, representing a high-transmission mass separator in use for studying e.g. limited sample sizes (e.g. for fulfilling legal restrictions in handling of radioisotopes), and paves the way for adaption to on-line separators such as ISOLDE. A schematic sketch of the setup is given in fig. 3.11.

A standard hot cavity does not offer specific means of atom beam shaping, as e.g. available at gas jet systems. Atoms thermally effuse from the oven's orifice in a cone-like profile instead of a sharply directed beam. The situation is depicted in fig. 3.11. Values for its total opening angle β in respect to the central axis have been given as $\beta \approx \pm 20°$ (with 15 % of all atoms being in a central, more directed cone of $\pm 4°$) in the original LIST proposal publication [49]. Later, $\pm 13°$ were measured using uranium [23]. Most recent experiments conducted in the scope of this thesis support the higher values and are discussed in section A.1.

A simple theoretical estimate on resulting lateral Doppler broadening is based upon scaling its width $\Delta\nu \propto \sqrt{T}$ (eq. 2.45) to the resulting lateral velocity distribution, characterized by its mean value $\bar{v}$ from the Maxwell-Boltzmann equation. As also $\bar{v} \propto \sqrt{T}$, a value of $\Delta\nu_{\text{perp}} \approx 700$ MHz can be estimated from a total line width of 2 GHz (see sec. 2.1.6) using the triangular relation $v_{\text{perp}} = \sin(\beta) \cdot v_{\text{therm}}$. To reduce this value down to the 100 MHz range would imply to address an opening angle of only $\beta \approx \pm 3°$. This can be technically realized e.g. by adding slit diaphragms in the atomic beam path to only let its central component pass. Alternatively it is achieved if the laser for ionization is introduced longitudinally as a well collimated, narrow beam on the atomic beam axis. Albeit the perpendicular laser radiation still potentially excites atoms within the entire transversal Doppler profile, only those atoms which are at the same time
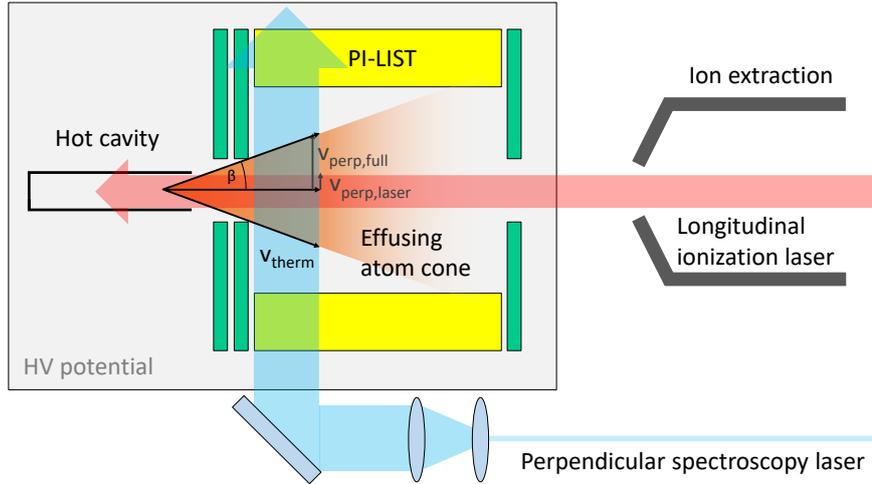
Figure 3.11: Sketch of the PI-LIST operation principle for Doppler-reduced spectroscopy. While in collinear laser interaction the whole velocity *distribution* v_{therm} is probed, the number of perpendicular velocity classes $v_{perp,full}$ which are resonant to a laser guided in laterally is significantly smaller. Additionally, only the excited atoms which are located in the volume of the still collinear ionization lasers are converted to ions, thus narrowing down the selection even further ($v_{perp,laser}$).

situated within the interaction volume with the longitudinal ionization laser beam are finally converted to ions and detected. Therefore, only atoms in the intersection region of all lasers actually contribute to the recorded resonances. On the other hand, this implies that the method exhibits an intrinsic efficiency loss by atoms effusing out of this region - while the initial cone-like effusion process naturally provides the highest atom density directly behind the hot cavity exit orifice.

The technical adaption of the PI-LIST at RISIKO includes two major adaptions of the general LIST structure. For lateral access into the case, 7.5 mm high and 36 mm long openings were machined into the outer housing. In addition, the whole unit including the hot cavity was shifted away from the front end flange by about 45 mm to simplify access. These alterations do not effect the internal potential distribution, as the extraction field is still completely shielded by the remaining housing structure. The opening's dimensions are chosen to fully access the free space between the quadrupole rods by laser light and to address the highest atom density right behind the repelling electrode. Two 30 mm diameter windows have been installed at dedicated lateral ports at the vacuum vessel, the far side one for being used for alignment and monitoring of the outgoing beam. A CAD view and photographs of the setup are given in fig. 3.12.

An additional adaption comprises the installation of the second, electron repelling electrode. It was machined as a copy of the one applied for surface ion suppression and placed at a distance of 1 mm in front of it, while maintaining the margin to the hot cavity exit. Its application was already foreseen and implemented in the LIST's very early development stages (sec. 3.4.1), but omitted for the ISOLDE version (sec. 3.4.2). The necessity nevertheless became evident again at experiments on minute amounts of technetium isotopes $^{97-99}$Tc. A detailed description is found in the B.Sc. thesis of M. Trümper [97] and will be briefly summarized here. A correspondent graph depicting the second repeller's influence is given in fig. 3.13 as comparison between both configurations.

The depicted contamination arising in "standard", single-repeller LIST mode has already been seen at on-line experiments with the standard LIST, as described in section 3.4.2. The use of a graphite atomizer in the technetium experiment (providing
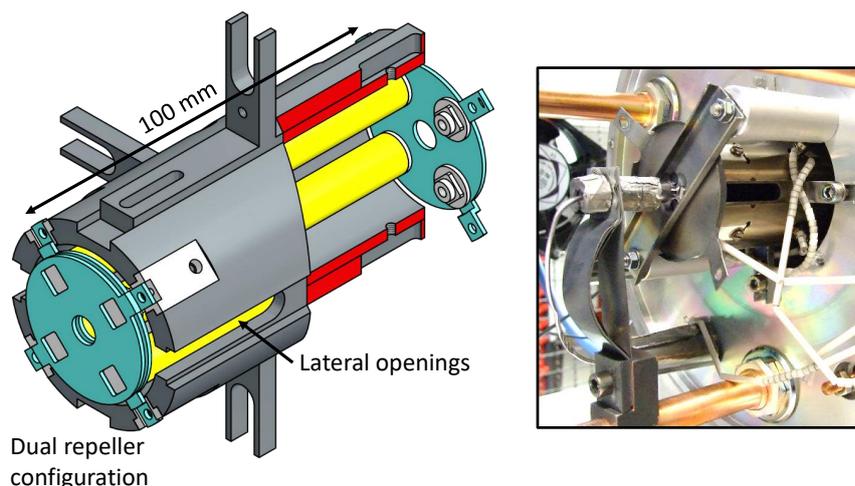
Figure 3.12: CAD view (adapted from [29, 97]) and photograph of the PI-LIST as installed at RISIKO. Lateral openings of 7.5 mm height and 36 mm length allow for perpendicular laser irradiation right at the beginning of the quadrupole structure. The whole unit, including the hot cavity, was offset away from the front end flange accordingly to shine in lasers through dedicatedly installed lateral windows in the front end vacuum housing.
Additionally, a second repelling electrode was installed to enable both electron and ion suppression.
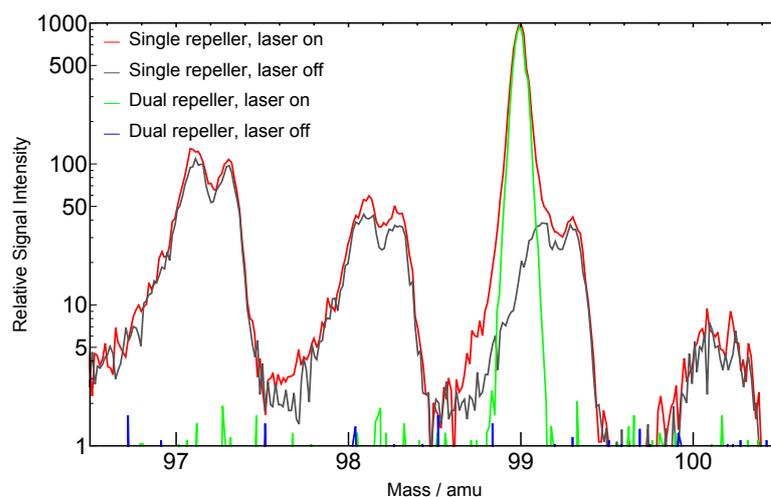
Figure 3.13: Mass spectra in the technetium region with a sample of ^{99}Tc. Non-laser related contamination signal is apparent for the standard LIST configuration with a single, positively biased repeller. The implementation of a second repeller on negative potential, inhibiting also electrons from entering, completely suppresses this effect. The data was recorded on different occasions and does not reflect actual signal ratios. Figure taken from [29].

a variety of carbon complex molecules which are ionized in the LIST and show up as background peaks on every mass in fig. 3.13) intensified this problem. By comparing the experimentally derived voltage combinations applied to both repellers to regain complete suppression of this contamination to elctrostatic simulation using SIMION [98], indeed the passage of electrons from the hot cavity into the LIST structure could be confirmed as reason for the background.

In the same investigations, significant influence of the RF voltage amplitude on the production of the contaminant ions was observed, with higher amplitude producing higher

currents. Corresponding simulations showed that almost immediately after entering the structure, the very light electrons are attracted to the positive quadrupole rods within less than half a period of the MHz radio frequency. On this path, they gain sufficient energy to efficiently ionize any atoms present in the way. The double peak background structure in fig. 3.13 without the negative repeller can therefore be attributed to two distinct ionization positions of high electron density and slightly different electric starting potential (resulting in transmission on different apparent masses through the magnet): On the central axis right after entering the structure, and in the direct vicinity of the rods.

Spectral Resolution

Finally, the applicability of the PI-LIST for high resolution spectroscopy directly at a hot cavity ion source was successfully demonstrated in hyperfine structure investigations on technetium. Figure 3.14 shows a scan of the structure observed in the transition from the ground state $4d^5\,5s^2\,{}^6S_{5/2}$ to the excited state $4d^5\,5s\,5p\,{}^6P^o_{7/2}$ at $23\,265.32\,\text{cm}^{-1}$ [99] for ^{97}Tc. While the detailed analysis and the extraction of hyperfine parameters and nuclear structure information is described in [66] and subject to a forthcoming publication, the spectroscopic characteristics in terms of spectral resolution will be briefly discussed here, as a benchmark for the developments carried out in this thesis.
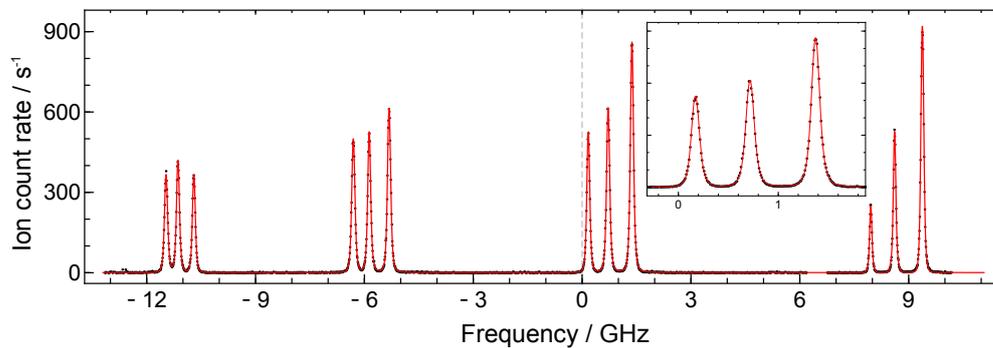
Figure 3.14: Hyperfine structure spectrum of the transition from the ground state $4d^5\,5s^2\,{}^6S_{5/2}$ to the excited state $4d^5\,5s\,5p\,{}^6P^o_{7/2}$ at $23\,265.32\,\text{cm}^{-1}$ for ^{97}Tc with detailed view of the third triplet as inset. The fit of a Voigt profile to the data exhibits an overall FWHM of slightly below $100\,\text{MHz}$. Figure taken from [29].

The experiment was conducted with the injection-locked ring laser system described in section 3.2.2, operating with a spectral bandwidth of $35\,\text{MHz}$ in the frequency doubled regime. Evaluation of altogether three ground-state transitions on each of the three isotopes $^{97-99}$Tc yield typical experimental line width (Voigt FWHM) down to slightly below $100\,\text{MHz}$. For these scans, the techniques described in section 2.1.6 were exploited, implying attenuation of the scanning laser power to below $1\,\text{mW}$ and temporal delay of the subsequent ionization steps by $40\,\text{ns}$, just after decrease of the spectroscopy laser pulse. Additionally, the second and third step lasers were shaped and focused to $1\,\text{mm}$ spot size, thus selecting a small axial volume for ionization inside the LIST and efficiently discriminating contributions from atoms with lateral velocity. Nevertheless, the overall experimental line width still showed a dependence on the oven temperature.

Efficiency Considerations

A common way of determining the efficiency of hot cavity type ion sources is full, exhaustive evaporation of a calibrated sample placed either in the source or a connected reservoir, and comparison with the integrated ion current over the whole process. This has been done for the standard LIST in collinear mode on ytterbium and magnesium [77, 92]. The experiments yielded values of 10 % and 2.5 %, respectively, in the ion guide mode resembling standard RILIS operation. These values reflect the previously recorded values from a "normal" RILIS source quite well. The correspondent efficiencies for LIST mode are 0.2 % and 0.08 %, which is in good agreement to the reported LIST loss factors LLF in the range of 20 to 50. Based on these considerations, the efficiency may also be inferred from data on ion signal ratios between different operation modes, as no additional absolute efficiency measurements were conducted for the new perpendicular irradiation mode.

An additional loss should be due to the geometric difference between collinear laser irradiation, where the whole length of the LIST is illuminated, and the technical constraint of only being able to illuminate about 30 mm through the lateral openings in PI-LIST mode. With the most probable speed of the atoms in a Maxwell-Boltzmann distribution $\hat{v} = \sqrt{2k_B T/m}$, which is in the range of some cm per laser repetition interval of 100 µs, on average these atoms should experience only one laser pulse while being inside the LIST. Thus, a *PI-LIST loss factor PLLF* of 3 is expected. However, because of the cone-like effusion from the hot cavity, the situation is more complex. A large fraction of the atoms escapes laterally, leading to a reciprocally quadratic decrease in atom density on the central axis. A significant remaining amount is only found roughly within the first 20 mm behind the repeller, which was already investigated in [77], and is strongly supported by [66] and the work presented in section A.1. These atoms are the main fraction of extracted ions in both PI-LIST and standard LIST mode, diminishing the advantage of the more elongated illumination volume in standard LIST-mode. In fact, experimental PLLF values varied between a factor of 2 - 3 up to only 20 % decline when changing from longitudinal to perpendicular mode.

The PLLF values mentioned above were realized with a standard laser in perpendicular mode and a sufficient spectral bandwidth to address the majority of the transition's hyperfine splitting. For sole geometric investigations this gives a meaningful result of potentially equal to only slightly reduced ionization efficiency compared to standard LIST mode. However, in the foreseen application of high resolution spectroscopy, a narrow-bandwidth laser system and techniques to reduce the experimental line width are applied. The ion signal is then strongly dependent on the strength of the individual hyperfine components and the compromise between narrow line width and "sacrificed" count rate when decreasing laser power or using pulse-delay methods. For the technetium experiments, a line width of 100 MHz FWHM was accompanied by a signal loss factor of 100 compared to collinear broad band operation, while only 10-fold decrease in count rate was achieved when accepting lower resolution with line widths of 400 MHz.

To conclude, the expected efficiency loss for high resolution laser spectroscopy in PI-LIST mode compared to a standard RILIS (without LIST) can be inferred to be in the order of 10^4. If a realistic total ionization efficiency value of e.g. 10 % is assumed for RILIS, the correspondent ionization rate would than be 10^{-5}, thus producing 1 ion per 100.000 atoms. This efficiency was sufficient for successful application of the technique on minute size samples of only 10^{11} atoms of ^{227}Ac to study five different atomic transitions over the course of some days [29].

4

An On-Line Applicable Adaption of the PI-LIST

One scope of this thesis was the development to technically adapt the operation mode of perpendicular illumination inside the LIST to the demands of an on-line facility, and to prove its applicability by evaluation of high resolution spectra from spectroscopy on radioactive elements.

This chapter will describe the specific demands and the correspondent technical adaptions which were implemented, and how they behave in typical operation environments. Parts of the presented work were subject also of the diploma thesis of C. Weichhold [100].

4.1 Technical Realization

In terms of day-to-day operation, one of the biggest differences between an off-line separator like RISIKO in Mainz and on-line facilities is the access to the front end part, especially the target/ion source unit. During operation with bombardment by the primary beam to produce radioisotopes, access is completely impossible, and also in between or after irradiation the highly activated material causes extremely hostile conditions. An ion source thus has to be designed for stable and reliable operation over its whole life time of days to weeks, and can not be easily diagnosed or repaired in case of malfunction. As already described in section 3.8 for the case of the electronic parts in the RF amplification circuit, general robustness is highly crucial and utilized materials have to be radiation proof.

The concept of lateral laser access to this area can thus not easily be overtaken from the PI-LIST setup in Mainz: Laser beam transport into the front end zone would require an aperture in its shielding, which is at least hardly justifiable. An even more thorough problem in terms of operation are the necessary windows in the front end vacuum vessel and associated optical elements for beam reflection. Neither glass, fused silica or quartz components nor any optical coatings do exhibit an appropriate high level irradiation hardness and are bound to immediately lose their reflecting or transmitting properties. With these constraints and the premise of introducing as little complexity as possible, a different approach of laser transport and perpendicular reflection was developed: The spectroscopy laser will also be guided through the separator's beam line itself, entering through the same entrance window in the magnet as the other lasers in standard configuration. This beam then travels with a very slight angle to the central axis, resulting in arrival at a point inside the LIST with lateral offset to the hot cavity

exit. At this point, reflecting surfaces of polished metal are installed inside the LIST corpus, which provide perpendicular reflection just behind the repeller electrode. The laser beam is then retro-reflected by a similar system of two mirrors on the opposite side to provide an extended spatial coverage of the laser intersection volume on the LIST's central axis. A CAD view of the adapted unit is shown in fig. 4.1. The position below the third mirror in passage order of the laser can be used to install an additional plane reflector for beam retro-reflection in order to increase the effective laser power in the interaction region, but was not installed in the experiments. The corresponding screw thread channel was instead used for optical control of the initial laser beam path setup of the unit.
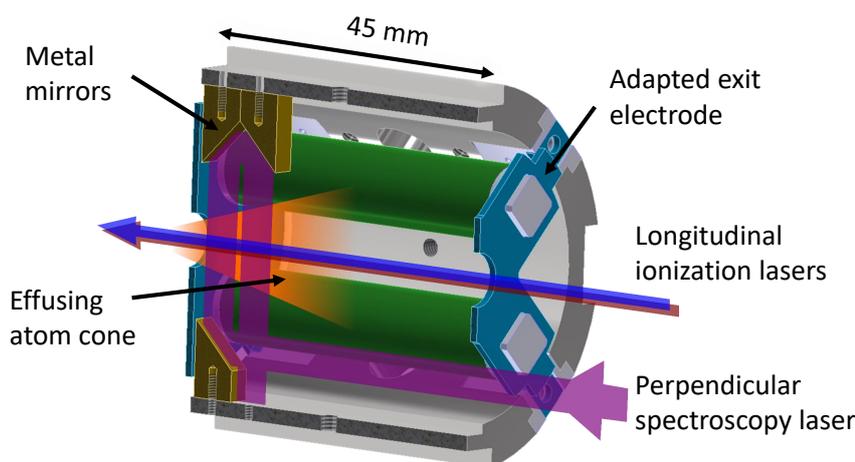
Figure 4.1: CAD view of the PI-LIST with internal reflection. As lateral laser access by windows is impossible at on-line facilities, the spectroscopy beam is guided through the beam line itself and reflected by robust metal mirrors within the LIST corpus.

Some additional changes have been conducted in comparison with the PI-LIST presented in section 3.4.1. The exit electrode was adapted to have lateral cutouts for passage of the beam. The overall unit was shortened to 45 mm for better handling, as anyhow the overwhelming fraction of ionization in any operation mode only happens within the first 2 cm behind the repeller electrode.

The dimensions of the whole setup cause a quasi-parallel entrance of the spectroscopy laser in respect to the collinear ones: While typically the distance between the magnet entrance window, where the last manipulation to the lasers by mirror adjustments can be done, and the ion source is in the order of some m, the lateral off-set of the metal mirrors is only 1.5 cm. The resulting angle e.g. for the RISIKO separator with a distance of 3 m is correspondingly 5 mrad or less than 0.3°, which naturally decreases further if a mirror more distant to the source is utilized to adjust the offset. The distance e.g. at ISOLDE is in the order of 20 m. Thus, the metal mirrors are machined with a 45° angle for simple perpendicular reflection.

However, this "quasi off-axis" guidance of the laser requires free line of sight from the entrance window to the reflection point. Fortunately, almost all of the ion optical components installed have a larger diameter to permit for a large parallel ion beam before entrance into the magnet, which causes a better mass resolution. The only component blocking the line is the extraction electrode, which in both RISIKO and ISOLDE designs exhibits a single central orifice of 6 mm diameter. For implementation of the unit in Mainz, the electrode has been adapted to additionally comprise four

cylindrical lateral orifices of 9 mm diameter with an offset from the beam center of 12 mm, arranged in a symmetric fourfold pattern. A cut view of the design and a photograph of the adapted electrode tip is shown in figure 4.2 for the installation at RISIKO with fixed distance of 40 mm between LIST exit and electrode. As these additional orifices present a major change to the extraction system, possible distortions to the acceleration field and subsequent influences on ion beam emittance are investigated in detail in section 4.1.2. At RISIKO this electrode was in use for more than a year after the presented measurements, also in the standard RILIS configuration without a LIST unit. No negative impact on transmission efficiency, beam characteristics or mass separation behavior was apparent.
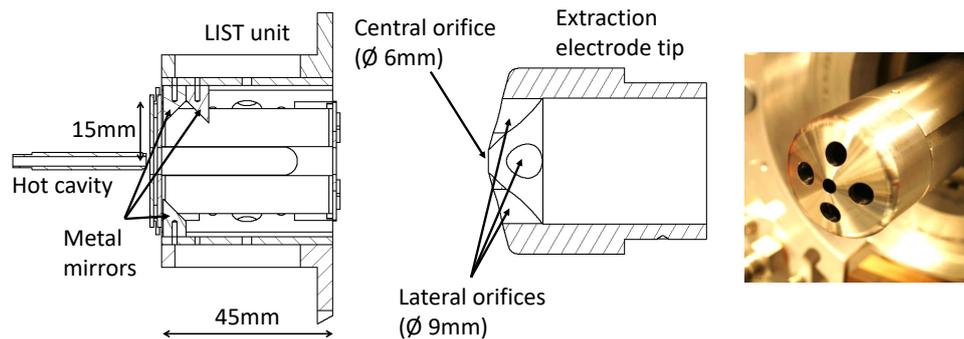
Figure 4.2: Technical cut view of the setup with internal reflection PI-LIST and adapted extraction electrode as installed at RISIKO. Four lateral orifices were added in a symmetrical pattern.

4.1.1 Performance of the Metallic Mirrors

The core pieces of the new design are the reflecting metal surface units. As all other ion source, LIST and extraction system parts, they were built at the mechanical workshop of the Institute of Physics at Mainz University. As they had to be robust against ambient temperatures of some 100 °C and direct light from the up to 2000 °C hot cavity, and for reasonable machinability regarding their base size of only 6 mm x 6 mm, stainless steel was chosen as material. The treatment before installation included mechanical polishing by the workshop. Additionally, specific coatings in a home-built apparatus for pulsed laser deposition could be applied. A broad overview of this technique, which is only exploited as a tool in this work, can be found in [101]. The device used is described in [102] and [28].

Reflectivity

Un-coated metallic surfaces were used initially. The reflectivity was measured in a test setup with the available laser beams in the course of [100] and yielded a reflectivity of 60 to 65 % for both fundamental (798 nm) and the frequency-doubled (406 nm) Ti:sapphire laser output. With laser powers available in the Watt regime and typical saturation values of some mW (e.g. 1 mW for the investigated ground state transition in holmium [86] or in the high resolution work on technetium [26]), these values are sufficient for spectroscopic applications, as operation below saturation is favored for narrow line width. Nevertheless, the retro-reflecting path involves two more mirror interactions, therefore significantly profits from higher reflectivity, which directly contributes to better overall spatial covering of the atomic beam. Therefore, pulsed laser deposition of

aluminum, gold and silver onto the polished surfaces was tested[1]. Aluminum exhibits a good spectral coverage of the complete range accessible with the Ti:sapphire system including higher harmonics generation and would thus be a natural choice. Nevertheless, the parts deposited with aluminum showed a gradual decrease in reflectivity compared to the uncoated ones. This might be due to either very inhomogeneous coverage of the material during the coating process. Furthermore, the layer showed a white coloring after only one day, which implies fast oxidation and therefore impracticality. Also, the robustness against high temperatures would have to be evaluated, as aluminum has a quite low melting point of 660 °C.

Coatings with gold exhibited reflectivity values of 80 % in the IR range, 40 % for blue light and showed to be robust against environmental influences. Finally, as optimum a silver coating with 80 to 85 % measured reflectivity for both wavelength regimes was chosen. A photograph of a selection of mirrors is given in fig. 4.3.
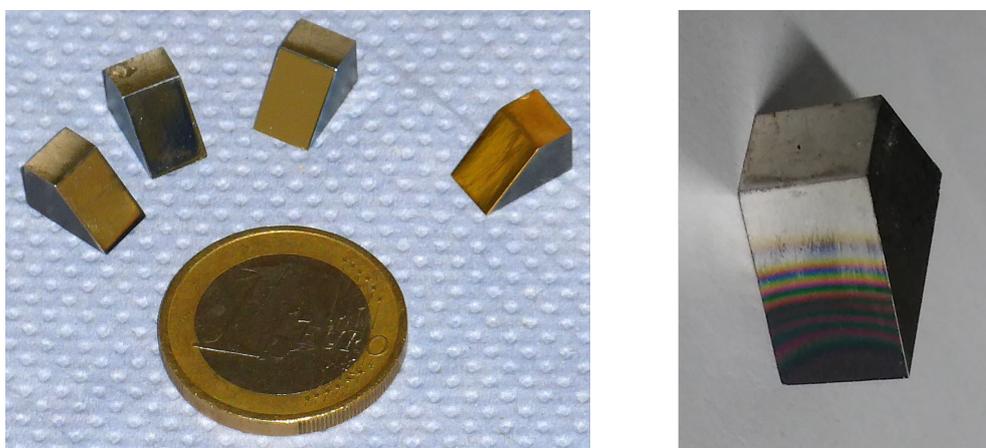
Figure 4.3: Photograph of the metallic mirrors installed in the internal reflection PI-LIST. The left-hand picture (taken from [100]) shows three silver-coated units (left) and a gold-coated one, made from a 6 mm x 6 mm stainless steel block. The picture on the right hand side depicts the mirror farthest away from the LIST entrance after three weeks of operation, with clearly visible surface degradation due to direct heat radiation and material deposition from the hot cavity.

Besides initial performance, the long-time stability under realistic operation conditions is crucial. For this course, the mirrors were de-installed after some duration of operation and inspected. The units without coating used for the first run of three weeks showed a slight decrease of reflectivity, from previously 60 to 65 % down to 50 to 60 % for the two mirrors next to the repeller electrode, which is not critical. In contrast, an important difference was seen for the mirror further away, which provides the final reflection and experiences direct line of sight to the atomizer with its surface. A circle-sector-shaped coloring was seen on the lower part, stemming from heat radiation and effusing material from the hot cavity. A photo is shown on the right-hand part of fig. 4.3. In fact, the remaining clean part directly corresponds to the part being shielded by the repeller electrode, corresponding to directed evaporation from the cavity at least within a cone of $\beta = 25°$ lateral angle. In the affected area, the reflectivity decreased to below 20 %. This process is hard to avoid without major changes to the repeller design. Anyhow, the laser beam in this part of the LIST contributes significantly less to the overall ionization rate compared to the one nearer to the cavity exit, due to the reduced atom density

---

[1]The choice was derived from standard coatings of commercial optics, e.g. at https://www.layertec.de/de/capabilities/coatings/metallic

at this place and to power decrease by the two additional reflections. Therefore, this aspect was not addressed further.

For the silver coated units, after six weeks of operation in a second run period, the reflectivity decreased from the 80 to 85 % mentioned above to values between 75 and 85 % for the shielded mirrors. As a positive result from the experience gained throughout this work, this treatment thus is highly recommended for standard implementation.

Laser Beam Quality

Besides the reflection characteristics in terms of power, the quality of the laser beam after passing the mirror units is crucial. Especially any effects that cause a deviation from a directed, quasi-parallel beam to a scattered or dispersed, multi-directional radiation light would directly cause a significant loss in achievable resolution, and would on top imply asymmetric line shape effects: Laser beam fractions exhibiting a non-perfect transversal direction induce Doppler shifts in respect to the propagating atom beam. The concept fundamentally relies on solely perpendicular irradiation. To investigate this properties, the mirrors were placed into a laser beam, and the resulting cross section profile was measured with a beam profiling camera (CinCam CMOS 1202) for several distances after reflection. One typical result in comparison to the incident laser beam is shown in fig. 4.4.
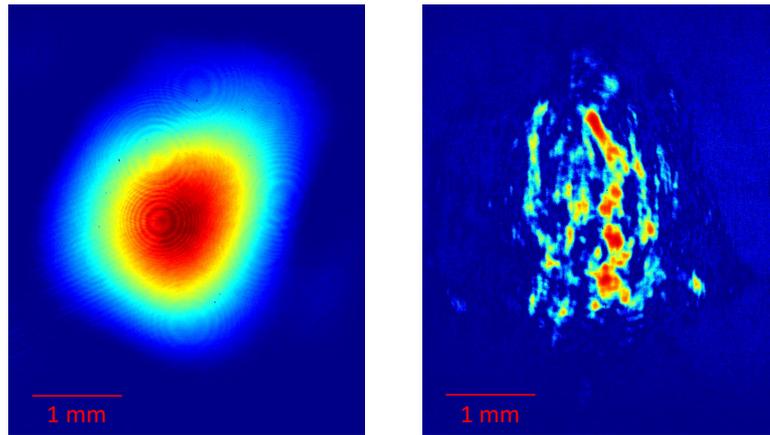
Figure 4.4: CMOS camera picture of typical laser beam cross section profiles directly before and 15 cm behind reflection by a metallic mirror as installed inside the LIST. While the incident beam can be well described with a 2D Gaussian profile, its shape clearly gets distorted into distinct speckles. Nevertheless, it preserves a directed and quasi-parallel beam profile and does not show significant scattering or dispersion. Pictures taken from [100].

The right-hand side picture shows the profile 15 cm after the mirror, thus vastly exceeding the maximum traveling distance of reflection via all mirrors inside the LIST, which is roughly 5 cm. A distortion of the beam, which can previously well be described by a two-dimensional Gaussian intensity distribution, is clearly evident, yielding multiple spots instead of a smooth profile. Nevertheless, even after this distance, there is no significant change in overall beam diameter, which suggests a quasi-parallel propagation. No beam widening, additional halo or other scattering or dispersion effects are observed.

4.1.2 Adaption of the Extraction Electrode

The adaption of the extraction electrode with off-center orifices to provide direct line of sight on a laterally offset path through the ion optics array is a serious change in a

well-known and routinely operated system. Ion source development so far was oriented to be compatible with the electrode as an integral part of the machine. Especially at the ISOLDE separators, an easy routine exchange of the electrode is not foreseen. It naturally is exposed to a lot of contamination of both ionic and neutral radioactive species emerging from the target/ion source unit and can thus not be handled without extreme radiation safety precautions. Therefore the effects of adaptions in several geometries have to be investigated very carefully, especially regarding their influence on the extracted ion beam.

For these investigations, an electrostatic model of the ISOLDE extraction geometry was implemented in the finite element simulation software SIMION (version 8.1) [98]. The model is slightly different to the one installed at RISIKO (which is depicted in fig. 4.2). Most prominently, a smaller inner diameter of only 26 mm forces the additional holes to be closer to the center. The tested geometries exhibit, besides the standard central hole of 6 mm diameter, side bores of 6 mm diameter (which corresponds to the doubled dimension of the atomizer and is matched to the mirror size) and a lateral distance of their centers to the central axis of 10 mm, thus only leaving 4 mm of solid material in between. Three different geometries were simulated in comparison with the standard configuration:

a) A single hole on one side, representing the least-invasive change.

b) Four holes arranged in a symmetrical pattern, similar to the part machined and installed at RISIKO.

c) An almost ring-like configuration with eight holes, to apply possible distortions in the most uniform way.

Correspondent graphical representations are given in fig. 4.5.
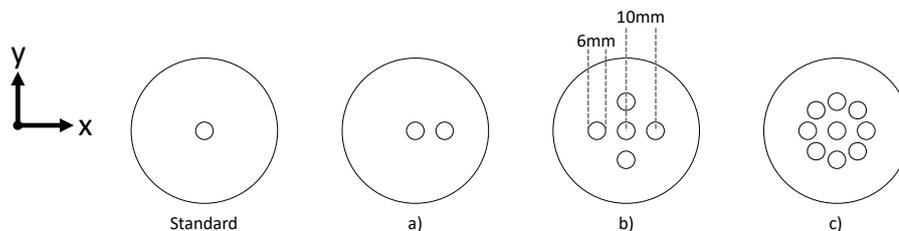
Figure 4.5: Front view of the simulated extraction electrode geometries, including dimensioning and coordinate system. Labeling according to text. An exemplary 3D view for geometry b) is given in fig. 4.6.

For all models, the ion source was represented by a standard tubular cavity of 3 mm diameter and a length of 34 mm, and a distance of 40 mm to the extraction electrode's entrance. Only the first 34 mm of this electrode were included in the model, and terminated with a "virtual" plane at the back, so that simulated particles would hit here and their properties could be recorded by the software. A similar representation was used for simulations of the LIST ion source in [77]. The whole model is surrounded by a housing, and a continuous gradient of electrical potential could be applied to the cavity by means of implementing it as a serious of single electrode rings with in- or decreasing potential. The grid size of the simulation was set to 0.1 mm in every canonical direction. The model is exemplarily visualized for the case of four side holes (configuration b) in figure 4.6.
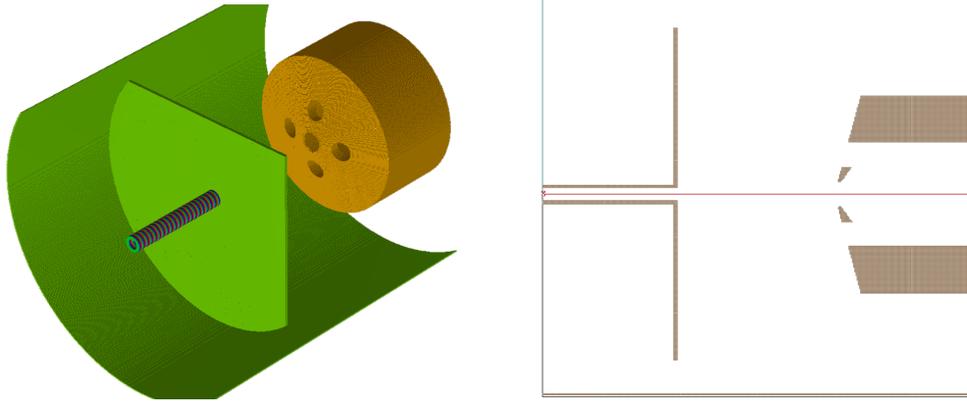
Figure 4.6: Overview of the simulation model as implemented in SIMION 8.1, at the example of the four side hole geometry. A 34 mm long cavity (with the ability to apply a longitudinal potential gradient) is placed 40 mm apart from the tip of the extraction electrode. Another 34 mm inside, the path is terminated by a solid "virtual" plate (on the same potential as the extractor), where simulated ions splat and their properties are recorded.

A total number of 17.000 ions were simulated in each run, initiated with a uniform spatial distribution inside the cavity and a three-dimensional Maxwell-Boltzmann velocity profile corresponding to a temperature of 2300 K. The particle mass was set to 150 u. For realistic starting conditions, a potential drop of 2 V was applied longitudinally over the cavity to guide the ions towards the extraction (as it is given by the ohmic voltage because of the resistive cavity heating in the real source). Radial confinement inside the oven, which usually is given by a plasma potential resulting from thermal electron emission from the cavity walls, was approximated by a linear potential increase in radial direction ($V \propto r$) of 2.2 V (as given as a typical value for the "trough depth" in [47]). This implementation is rather coarse, as in reality the repulsive force should be much more pronounced in the direct vicinity of the cavity walls. A corresponding adaption was omitted, as near the cavity walls artificial disturbing effects due to the finite grid size of 0.1 mm are present, rendering the wall as no smooth curvature but with sharp edges. Including the radial confinement effect in some way nevertheless allows a better treatment of particles with significant radial initial velocity components, which would otherwise be more likely to hit the cavity walls and not be treated by the simulation anymore. An accelerating potential of 30 kV was chosen for all ion trajectory simulations. This is on the lower side of typical values at ISOLDE in the range of 20 to 60 kV, and should allow for a better visibility of changes in the lateral motion characteristics of the ions.

Figures for evaluation are extracted from the ion's characteristics after they passed the acceleration stage, entered the extraction electrode and were terminated at the "virtual plane". The x- and y-coordinates were used to extract both, a potential change in the mean beam position ($\langle x \rangle$ and $\langle y \rangle$) as well as the distribution characterized by the standard deviation (σ_x and σ_y) to see possible deviations in beam shape. The same was done for the lateral velocity components v_x and v_y. Additionally, as a figure of merit most commonly referred to in terms of ion beam quality, the transversal root mean square (RMS) emittance ϵ_{RMS} was calculated. It describes the phase space volume in the x,x'-plane, with x being spatial positions and x' correspondent momenta (in this case to be determined as the angle in beam direction v_x/v_z in mrad). For a finite

number of particles as in the simulation, the RMS emittance can then be calculated as

$$\epsilon_{\mathrm{RMS}} = \sqrt{\langle x^2 \rangle \langle x'^2 \rangle - \langle xx' \rangle^2}. \tag{4.1}$$

The corresponding coordinates always have to be given not absolute but relative to their mean values $\langle x \rangle$, $\langle x' \rangle$ and $\langle xx' \rangle$, respectively, and can be easily extracted from the recorded data fo the x- and y-directions. Exemplary density histogram plots with a bin size of $0.05\,\mathrm{mm}$ and $0.5\,\mathrm{mrad}$ are shown in figure 4.7.

Standard configuration   One single side bore
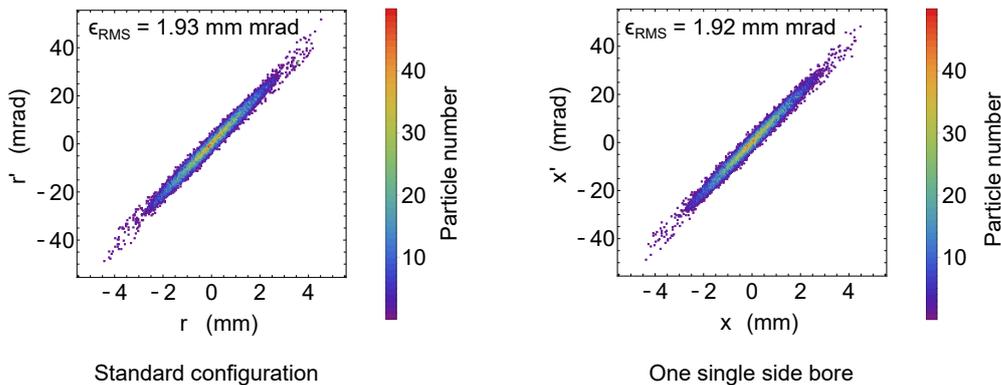
Figure 4.7: Exemplary density histogram plots for the emittance derived from simulations for the standard extractor geometry, and with one additional side bore. As well as in the absolute number for ϵ_{RMS}, no significant difference is visible in the plot shape.

A summary of all results for the investigated geometries is compiled in table 4.1. For completeness, results are always given for x- and y-direction also in the fully symmetric cases, to illustrate the random deviations caused by the Monte-Carlo-type particle initiation.

Table 4.1: Beam characteristics compilation, evaluated from simulations for the different geometries of off-center holes as described in the text. Besides a visible overall beam deflection in the case of one single side hole (mean velocity $\langle v_x \rangle$), no significant differences occurred.

	Standard	Single bore	Four bores	Eight bores
$\epsilon_{\mathrm{RMS},x}$ (mm mrad)	1.92	1.92	1.95	1.92
$\epsilon_{\mathrm{RMS},y}$ (mm mrad)	1.93	1.90	1.91	1.92
$\langle x \rangle$ (mm)	0.0013	-0.0361	0.0025	0.0111
$\langle y \rangle$ (mm)	0.0141	0.0021	-0.0028	0.0122
σ_x (mm)	1.15	1.16	1.17	1.15
σ_y (mm)	1.16	1.16	1.15	1.16
$\langle v_x \rangle$ (mm/µs)	0.0049	-0.1668	0.0069	0.0225
$\langle v_y \rangle$ (mm/µs)	0.027	0.0020	-0.0047	-0.0283
σ_{v_x} (mm/µs)	2.38	2.37	2.41	2.38
σ_{v_y} (mm/µs)	2.38	2.40	2.37	2.39

The results suggest no significant change in the investigated beam parameters compared to the standard configuration for any of the models. The standard deviations of the distributions and most importantly also the RMS emittances are essentially the same. The most prominent difference for the case of one single additional hole is a slightly pronounced mean lateral velocity of the resulting ion beam in the contrary transversal direction. This can easily be understood in the assumption of ideal potential superposition, as in positive x-direction the attractive potential of the missing part of

the electrode has to be subtracted. Anyhow, as said before, the beam quality parameters are not affected and the beam deflection angle can easily be corrected by deflector plates downstream in the beam line.

It is clear that these simulations can only provide a simplified approach to the geometry characteristics. At least, they serve as a qualitative comparison between the different models, and towards the standard configurations. From this point of view, no fundamental problems could be identified. Also, the determined absolute ϵ_{RMS}-values are in the range of values between 1 and 2 mm mrad, which were measured at RISIKO before with the same acceleration potential of 30 kV [103], supporting the adequacy of the model. Before a definitive decision can be taken, actual measurements of the beam parameters and especially the RMS emittance as fundamental beam parameter, determining e.g. focusability, should be conducted. A potentially applicable, compact device for this task, based on the pepperpot method, is described just recently in [104].

Additional concerns are related to possible electric flash arcs, which would be favored on the introduced sharp edges of the side holes for highest extraction voltages. Although this could not be tested at RISIKO due to its maximum operational voltage of 30 kV, some existing ion source constructions exhibit sharp or pointed parts in this environment. For example, the LIST outer casing or the screws used to fix the exit electrode to the insulators, are also protruding towards the extraction electrode, but have so far never caused problems. Similarly, possible material build-up from strongly outgassing units is not expected to disturb more than in the standard configuration.

A technique to entirely rule out the slight changes in the extraction field introduced by the side holes would be complete coverage with a coarse metal mesh or grid. In that case, the influence on laser beam shape and quality would have to be investigated. Another alternative is a routine exchange of the extraction electrode every time a PI-LIST source is required. Indeed, the holding system at ISOLDE only uses a plugging mechanism for the electrode's tip. Although it's inadequate to have this work done by a human worker in the highly contaminated area, a dedicated target unit with an internal, remotely or automatically controlled setup for exchanging this tip could be constructed.

Finally, it has to be stated again, that at RISIKO the extraction electrode with four side holes (yet with a higher distance to the central axis, 12 mm instead of 6 mm, but with a larger diameter of 9 mm, see section 4.1) was in use for more than a year after the experiments with the internal reflection PI-LIST were finished, also in the configuration with a standard RILIS source. At no point, a negative influence regarding ion beam quality (in terms of focusability or mass resolution) or transmission was evident. In contrast, exceptionally high overall values on ionization efficiencies were measured in this period on several lanthanide elements. These results a subject to a publication in progress.

Technical Characteristics and Limitations of the PI-LIST

5.1 Spectral Resolution

The applicability of the PI-LIST in its standard configuration or with internal mirrors for hyperfine structure spectroscopy is profoundly demonstrated in chapter 6 on nuclear structure investigations of radioactive holmium isotopes. To appraise its limits for different applications especially regarding even higher spectral resolution, systematic explorations on Doppler broadening (eq. 2.45, see also fig. 2.2) are required. To benchmark the system towards achievable minimum line width, three parameters are essential:

- Low absolute transition frequency,

- low ensemble temperature,

- high particle mass,

with the first being most important, as the line width scales linearly instead of via a square root function.

5.1.1 PI-LIST with Internal Mirrors: Rubidium

As an exemplary element to determine a resolution benchmark, rubidium was chosen for several reasons. On the one hand, it fulfills the requirement of exhibiting a transition from the ground state in the fundamental Ti:sapphire laser range as the lowest accessible frequency available in the laboratory. Its low melting point of $39\,°C$ [105] and a vapor pressure of $\approx 1\,$mbar at room temperature [106], significantly exceeding those of the most other common chemical elements [107]. Thus, it allows supply of large amounts of atoms in the gas phase at moderate temperatures. Its atomic weight of 85 and $87\,$u is roughly half that of holmium, but lies in a region with elements of general high interest for laser spectroscopy, such as tin with a doubly magic isotope at $100\,$u. On the other hand, rubidium and especially the chosen $5s\,^2S_{1/2} \to 5p\,^2P^o_{3/2}$ ground state transition in ^{87}Rb with a nuclear spin of $I = 3/2$ [108] is also a spectroscopically extremely well characterized case (e.g. serving as absolute frequency reference for wavelength meters in commercial saturated absorption spectroscopy cells) and thus provides highly precise hyperfine parameters for systematic cross checks in the data evaluation.

For the experiment, the setup as described in sec. 4.1 was installed with gold covered metal surfaces for rectangular laser deflection. In this experiment, the injection-locked

ring cavity was not seeded by a home-built ECDL cw laser as described in sec. 3.2, but by a commercial Toptica DL Pro cw laser for the 780 nm regime[1]. A standard tantalum oven tube was used in connection with a reservoir capillary. Rubidium was provided by evaporating 12 µL of 1000 µg/mL Rb_2CO_3 in 5 % HNO_3 solution[2] on zirconium foil, which was afterwards folded and placed in the capillary, corresponding to a sample size of $\approx 10^{17}$ atoms of natural rubidium (72.2 % ^{85}Rb, 28.8 % ^{87}Rb).

The full laser ionization scheme as used for the measurements is shown in fig. 5.1. The narrow bandwidth laser was scanned across the $5s\,^2S_{1/2} \rightarrow 5p\,^2P^o_{3/2}$ transition from the ground state to resolve individual hyperfine structure components. A second, broadband laser with an output power of 1.9 W was employed to further resonantly excite from all upper hyperfine states into the $5d\,^2D_{1/2}$ state. Finally, excitation into the continuum above the ionization potential is achieved non-resonantly via this same lasers, as the photon energy is sufficient to surpass the ionization potential in a third step. On top, an additional laser with an arbitrary wavelength of $12\,213\,\mathrm{cm}^{-1}$ and an output power of 2 W was introduced, not driving any resonant transition but also contributing to the non-resonant ionization step. The left hand panel of fig. 5.1 shows a full range scan across the whole structure which can be used to extract the respective hyperfine A and B parameters of the levels.
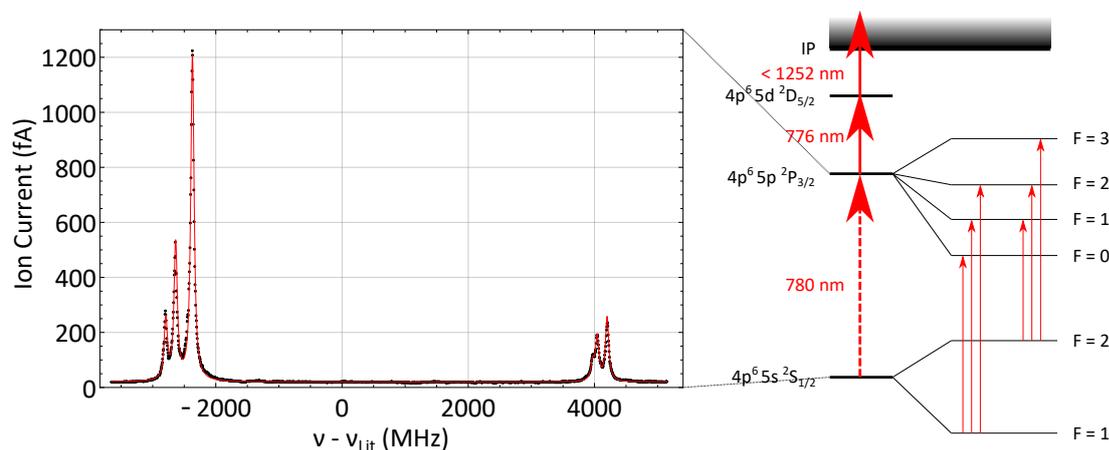
Figure 5.1: Overview of the laser resonance ionization scheme used for ^{87}Rb. The perpendicular, narrow bandwidth laser was scanned across the $5s\,^2S_{1/2} \rightarrow 5p\,^2P_{3/2}$ transition from the ground state (indicated with a dashed arrow) to resolve individual hyperfine structure transitions, as shown on the left hand panel. A second, broadband laser was employed to further resonantly excite from all upper hyperfine states into the $5d\,^2D_{5/2}$ state, and subsequent ionization was ensured by non-resonant laser excitation into the continuum above the ionization potential.

To explore the limit of highest possible resolution, the laser and ion source parameters were optimized carefully. The cavity was heated by a current of only 50 A (14 W power delivery of the supply), which was already sufficient to release enough atoms for the measurements. A temperature information in this regime is difficult, as pyrometrical measurements are not possible without glow emission of visible light. Anyhow, the absence of this light puts an upper limit of roughly 500 °C (meaning 820 MHz Doppler FWHM from eq. 2.45), most likely being significantly below this value. While this is

---

[1]Technical information available at https://www.toptica.com/products/tunable-diode-lasers/ecdl-dfb-lasers/dl-pro/

[2]Alfa Aesar 88091 Rubidium, AAS standard solution, Specpure®

clearly far away from standard operation parameters e.g. at on-line facilities, it is helpful to explore the absolute limits.

On laser side, the method of delaying the subsequent steps to a time regime when the spectroscopy pulse has already ended (see sec. 2.1.6) was applied with a delay of 50 ns in respect to maximum signal. Additionally, the spectroscopy laser power was reduced to an extreme low value of only 8.5 µW before the separator incoupling window. The resulting scan of the low-energy triplet, starting from the F = 2 hyperfine level of the ground state is shown in fig. 5.2.
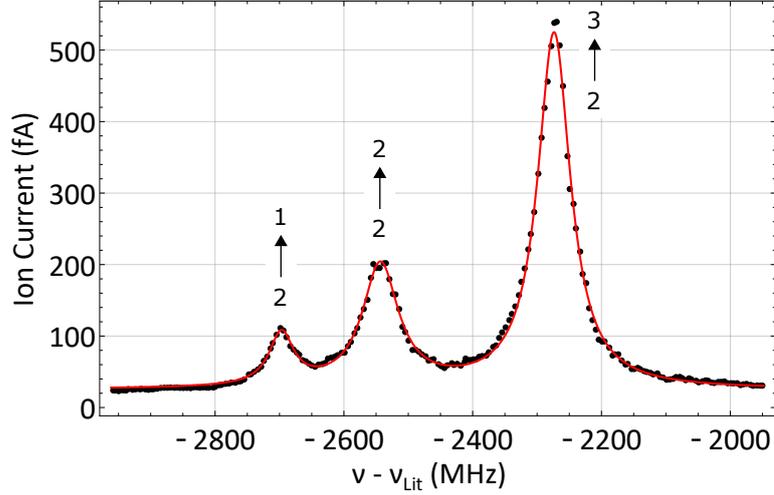
Figure 5.2: Detail scan of the low-energy triplet of the $^2S_{1/2} \rightarrow \, ^2P_{3/2}$ transition in ^{87}Rb. Respective ground and upper state F values are indicated. The peak shapes feature an average FWHM of 62(9) MHz and are completely Lorentzian-dominated, implying no significant influence of remaining Doppler broadening.

A fit of three individual Voigt profiles to the data yields purely Lorentzian peak shapes with an FWHM of 46(3) MHz, 68(2) MHz and 61(1) MHz respectively, or a weighted average FWHM of 62(9) MHz with the error described by the standard deviation as a measure of scattering. The absence of a Gaussian fraction in the Voigt fit proves complete suppression of Doppler broadening related line width effects. However, the lifetime of the $^2P_{3/2}$ state of 26.20(9) ns [109] corresponds to a natural line width of 6 MHz, thus there are still different effects stemming from the setup. Besides the spectral bandwidth of the laser of 20(5) MHz, the only remaining source is power broadening. Nevertheless, a line width of 60 MHz already strongly approaches the domain of collinear in-beam spectroscopy as e.g. performed in the dedicated beam lines of CRIS and COLLAPS at ISOLDE.

Besides the pure evaluation of single resonance widths, the whole spectrum can be used to cross check the reliability of the experimental setup in respect to replicability of well-known literature values of the hyperfine structure in rubidium. This was done on the dataset depicted in fig. 5.1. The comparison to literature data is given in tab. 5.1.

The uncertainties are those calculated by the fitting routine, which is for the A parameters combined with the relative fraction of the chosen 5 MHz bin width in respect to the ≈ 7.5 GHz whole spectrum width. The extracted hyperfine structure values perfectly correspond to the precise literate data. As such, the system consisting of experimental setup and measurement devices provides a consistent result also along a scan range of several GHz. Nevertheless, the deviation in the absolute frequency position of the transition's center is quite striking. The shift towards the literature value,

Table 5.1: Hyperfine structure parameters of ^{87}Rb derived in this work in comparison to literature data. Subscript 0 refers to the $^2S_{1/2}$ ground state, 1 to the $^2P_{3/2}$ state. ν_c is the absolute transition center frequency. See text for details.

Parameter	This work	Literature
A_0 (MHz)	3418(2)	3417.341 305 452 45(45) [110]
A_1 (MHz)	84.6(2)	84.7185(20) [111]
B_1 (MHz)	12.4(8)	12.4965(37) [111]
ν_c (cm^1)	12 816.5463(4)	12 816.549 389 93(21) [111]

$\delta\nu = \nu_{c,\text{meas}} - \nu_{c,\text{Lit}}$, is calculated as 92(11) MHz, with the specified 1-σ uncertainty of the WSU 30 wavelength meter and the calibration He-Ne laser already included. A possible explanation for this is a slight predominance in direction of the atoms away from the spectroscopy laser, resulting in a correspondent Doppler shift towards higher photon energies. In fact, slight misalignment or thermal drifts of material in the PI-LIST setup can not completely be avoided. The measured shift can be translated with the Doppler shift formula for non-relativistic velocities to a velocity v via

$$\delta\nu = \frac{v}{c_0}\nu_0 \qquad (5.1)$$

with the speed of light c_0. It yields a value of approximately 70(8) $\frac{\text{m}}{\text{s}}$ or 0.070(8) $\frac{\text{mm}}{\text{µs}}$. This is completely reasonable when compared to the considerably higher mean velocity of the Boltzmann distribution for e.g. 300 °C, being 0.37 $\frac{\text{mm}}{\text{µs}}$. Yet, it corresponds to an angle tilting of already approximately 13° in respect to perfect perpendicular orientation, which would be surprisingly high. This might also hint towards additional effects, e.g. a systematic shift for the calibration source for the wavelength meter. Anyhow, this effect has an offset-only character and only plays a role for the relative measurements performed in hyperfine structure spectroscopy (depending on frequency differences between single resonances) if the setup is changed in between measurements. The test case rubidium therefore confirms the applicability of the PI-LIST with internal reflection.

In the course of this experiment also a different method for high resolution spectroscopy in hot cavity ion sources was tested in the very same setup. The so-called 2-photon spectroscopy uses counter-propagating laser beams in the atom vapor provided by a retro-reflecting surface inside the source and eliminates the first order Doppler broadening completely. These investigations lie outside the scope of this work, but are presented recently in [32] in respect to their applicability at on-line facilities.

5.1.2   PI-LIST in Standard Configuration: Uranium

As stated at the beginning of this chapter, the limits in resolution of the PI-LIST method can be explored by further reducing the initial Doppler broadening in the atom vapor to start with. Besides using low photon energy provided by the fundamental output of the Ti:sapphire lasers instead of higher harmonics, this was achieved in the case of rubidium by low source temperature at a medium atomic mass. An experiment conducted on actinium with the PI-LIST in standard configuration, using perpendicular laser spectroscopy through a lateral window in the ion source vacuum vessel, provided an opportunity to perform a complementary systematic test on ^{238}U, which was used for machine setup. In this case, the mass is significantly higher, but more routine-like source operation temperatures in the order of 2000 K are used. Thus, a picture at rather realistic conditions can be taken, while the high mass and an accessible second step

transition in the fundamental Ti:sapphire range still provide the prerequisites for another benchmark.

^{238}U was introduced into the system as approximately 10^{15} atoms of natural uranium in solution, dried on zirconium foil and placed in the reservoir capillary. The applied resonance ionization scheme is depicted in the right-hand side of fig. 5.3. The first and second step was composed from information in [8, 112], while the final ionization step was found by performing a quick manual scan searching for auto-ionizing states, which are commonly numerous in the actinide region. As an advantage of ^{238}U for investigating peak shapes, its nucleus with both even proton and neutron number exhibits a nuclear spin of $I = 0$ and consequently no hyperfine structure splitting but only one single resonance.
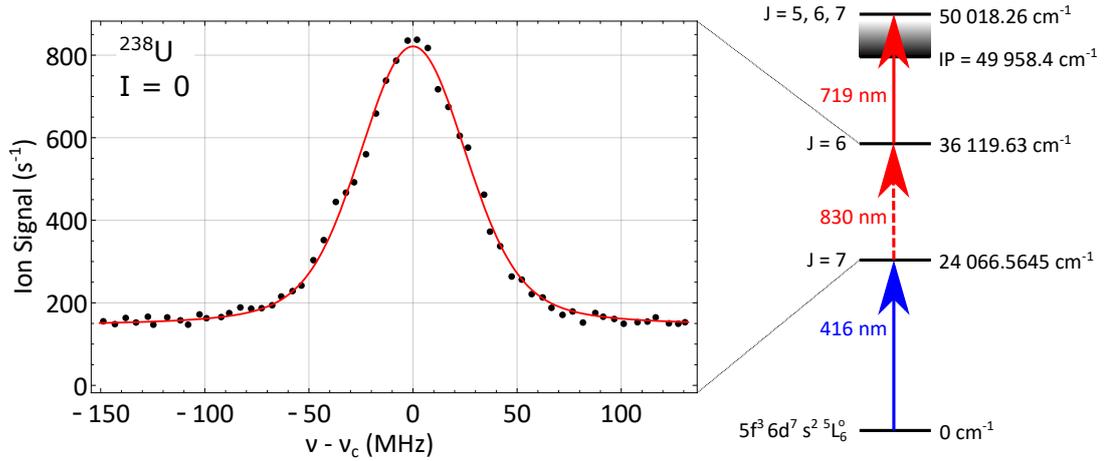
Figure 5.3: Overview of the laser resonance ionization scheme used for ^{238}U in the PI-LIST in standard configuration. The perpendicular, narrow bandwidth laser was scanned across the second step transition, indicated by the dashed arrow. The remaining steps were provided by broadband lasers in standard collinear geometry. Information on the first and second step was taken from [8, 112], while the third step was found by a quick manual search for auto-ionizing states. The scan of the second step transition on the left-hand side features an FWHM of 60(3) MHz with a dominating Gaussian contribution of 47(2) MHz.

The perpendicularly introduced spectroscopy laser was set up to scan the second step transition, as it lies in the red wavelength regime. The first (output power 200 mW) and last step (3.1 W) were provided by standard broad band lasers. In contrary to the other scans presented in this work using the LIST, it was not possible to provide optimum background suppression, as the frequency-doubled laser driving the first step already caused ion signal. The laser, although not capable of causing direct excitation above the ionization potential by a single additional photon, near-resonantly populates a high-lying state slightly below the IP and then ionizes. While the LIST is able to suppress interfering ions from inside the hot cavity, it can not inhibit background signal arising inside the quadrupole structure itself.

Also in this experiment, the individual laser pulses were delayed by 50 ns against each other, relative to the respective maximum ionization rate. For the scan depicted in fig. 5.3, the laser power was reduced to 100 mW at its output. This value is only hardly comparable to the other power values given for spectroscopy steps in this work, as it afterwards uses a beam path originally set up for a laser beam in the blue regime and therefore decreases significantly until arriving at the source. Additional reduction of the power did not cause any further decline in line width. The ion source was run at a

heating current of 260 A and a dissipated power of 475 W, measured by voltage probe wires directly attached to front and rear part of the oven. A temperature of roughly 2000 K can be estimated.

A Voigt profile fit to the data features an overall FWHM of 60(3) MHz. The individual fractions are a Lorentzian FWHM of 22(3) MHz and a Gaussian of 47(2) MHz. Thus, the Doppler broadening is not completely suppressed, in contrast to the experiment on rubidium. Equation 2.45 yields a total Gaussian FWHM of 750 MHz for the complete atomic ensemble. The difference can be explained by the different modes of operation. In the uranium case, the PI-LIST with external in-coupling of the perpendicular laser allows a much wider coverage of the LIST volume (instead of just the laser diameter wide spot of interaction in the mode with internal reflection) and thus also for more overlap between all lasers. This consequently also covers more volume lateral to the central axis, where atoms with considerable transversal velocity can be found (see also fig. 3.11). Additionally it should be mentioned, that from the rather small scanning range around the peak and especially due to the fluctuating background signal the assignment of the Lorentzian part featuring wide tailings might be underestimated by the fitting routine.

In conclusion, also the experiment on uranium as a heavy-ion-at-typical-temperature case provides an excellent benchmark of 60(3) MHz overall FWHM line width, nicely suited to high resolution spectroscopy.

For all investigations presented in this section, overall efficiency of the setup was not in focus. It is clear that increase in resolution comes with a decline in addressed atoms and therefore reduced efficiency and ion signal rate. For actual experiments, a compromise between envisaged linewidth and required efficiency is always demanded.

5.2   Ion Beam Quality

In order to get a full understanding of the PI-LIST with internal reflection in respect to its use as an ion source in combination with the separator system, the characteristics of the resulting bunched ion beam were investigated and compared to measurements on different laser ion sources. Two properties are of fundamental interest: On the one hand, the temporal structure of the ion bunch in respect to time-resolved data acquisition systems and additional purification techniques such as the ion beam gating described in sec. A.3. On the other hand, the behavior in the mass separation system, bound to the beam's properties in emittance and especially energy spread.

5.2.1   Ion Bunch Time Structure

The time structure of ion bunches created from laser ion sources (RILIS and LIST type) has been investigated thoroughly in the past. This section focuses on a comparison of these known structures to the ones induced by the PI-LIST both with external laser in-coupling and internal reflection and discusses its implications.

Different representative time structures for the individual modes of operation of the LIST are depicted in fig. 5.4, in both linear and logarithmic scale. The measurements were taken within the holmium campaign on the stable ^{165}Ho isotope in the course of [100]. Broad band lasers were used for all excitation steps, the first step being introduced laterally. The data for the comparison of standard collinear LIST mode and external in-coupling of the perpendicular laser in PI-LIST mode was taken on the same occasion and thus reflects the actual signal ratio between these modes for this setup. The structure for the internal reflection was taken later and is arbitrarily scaled. The

LIST repeller electrodes were set to $-20\,\mathrm{V}$ and $20\,\mathrm{V}$, respectively, and the lasers were spatially adjusted for maximum ion current.
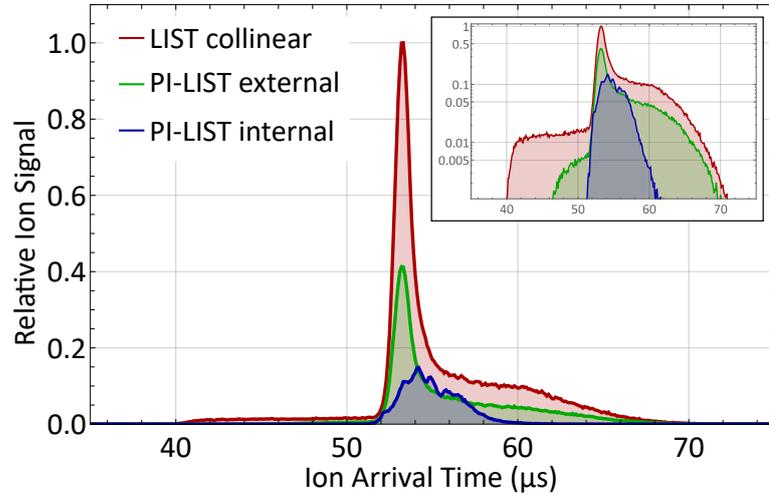
Figure 5.4: Ion bunch time structure for different operation modes of the LIST and PI-LIST, in linear and logarithmic scale. LIST and PI-LIST external reflect actual signal ratios for that setup, while the data for the internal reflection has been taken on a different occasion and is arbitrarily scaled. The structure clearly shows the different ionization volumes. See text for details.

Considering the well-understood time structure of the standard LIST, essentially three domains can be identified, which are also described in various previous works for the LIST [77, 91, 92] and TRIUMF's IG-LIS [93]:

1. A sharp peak, were most of the ions are concentrated. They are created in the region directly behind the repeller electrodes and "pushed out" by their positive potential.

2. A smooth tailing towards longer arrival time. These are ions created in the middle of the quadrupole unit with only minimum axial electric guiding field, essentially drifting out by their initial thermal velocity.

3. Early arriving ions, which are produced in the direct vicinity of the exit electrode and immediately accelerated there. A sharp cut-off, sometimes focused as small pre-peak, is caused by the spatially rapidly changing starting potential causing transmission of ions created even further downstream to be transmitted on lower nominal masses through the separator magnet.

A dedicated elaboration on linking spatial creation region to temporal arrival at the detector is discussed under a different scope in sec. A.1.2 and gives an additional confirmation of this description.

The time structures of the different operation modes of the PI-LIST consistently fit into this picture. The mode with external illumination through a lateral window along the first 30 mm of the central axis shows both features of the sharp main peak and the longer tailing. At the same time, the earliest arriving ions have vanished, no laser ionization occurs in the end part. For internal reflection, the whole structure is consequentially even more compact. Its maximum is located on slightly later arrival, and the peak and shoulder structure is much less pronounced but smeared out. There are

no ions arriving earlier than the ones from directly behind the repeller. The shape can be easily understood by the geometry. Only a small volume directly behind the repeller is addressed, delimited by the diameter of the transversally reflected laser beam (and its significantly power-reduced retro-reflection some mm downstream by the additional mirrors, see fig. 4.1 and 4.2). The best overall ion signal is achieved, if the laser is not placed on the very edge of the metal reflectors (meaning closest distance to the repeller in highest available atom density) but more to its center, so that less of its overall size is cut off. Thus, compared to standard LIST or PI-LIST operation, atoms in the volume slightly further downstream are favored for ionization, which arrive slightly later due to the less pronounced "push" by the repeller potential. In fact, if the time structure can be monitored during setup of the system, it offers a valuable tool to ensure best possible perpendicular illumination: Early arriving ions then indicate laser irradiation of the LIST back part, caused either by diffusion of laser light from a non-perfect mirror surface, from stray reflections from components in the beam path or even from halo photons still arriving in the collinear path through the extraction electrode's central bore. Spectral resolution in this situation is then subject to a much larger effective Doppler broadening. The spatial position of the laser beam has to be optimized to minimize this effect.

The short duration of the bunch exhibits an additional opportunity for ion beam purification by suppression of non-laser related beam components. A rapidly switched electrostatic deflector, the so-called beam gate, can be run in synchronization with the 10 kHz repetition rate of the laser system. Opening it e.g. for only a period of 5 µs at the time of the bunch's passage and deflecting the beam for the remaining time, allows for an additional suppression of a factor of 20 for ions which are produced in a non-laser pulse related way and which appear as an effectively DC-type beam admixture. Also, this technique can be used to completely remove the possible fraction of early ions created in the LIST's back part described above. An alternative approach to the physical gating is the application of software-based gating in the data acquisition, depending on how harmful deposition of the contaminants in the detection system is.

The small volume of ion creation also intrinsically comprises a very narrow starting potential spread. Consequently, the energy deviation after full acceleration is very narrow as well, implying high beam quality for shaping by ion optical components in the beam line and especially focusing by magnetic mass separators in their property as momentum filter.

5.2.2 Mass Separation Characteristics

An important parameter for an ion beam facility is its resolving power in mass resolution. It is linked to the starting parameter spread of the ions in the source, which will cause them to experience different trajectories through ion optical components. A direct inspection on this aspect can thus be given by examining the peak width and shape in the mass spectrum after transmission through the mass separating magnet for different nominal masses. During the experiment on holmium as described in chapter 6, a set of such mass scans was taken and is depicted in fig. 5.5.

It shows the peak structure for the different LIST operation modes. The scans for standard collinear LIST and PI-LIST with internal reflection have been performed in the same run and with broad band lasers on all steps, so that all holmium isotopes are equally ionized, and the count rate directly reflects the signal ratio for the specific setup. The spectrum for external in-coupling was performed with a narrow-band laser employed on the first step, optimized on ^{165}Ho, to prevent ionization of ^{166m}Ho with its
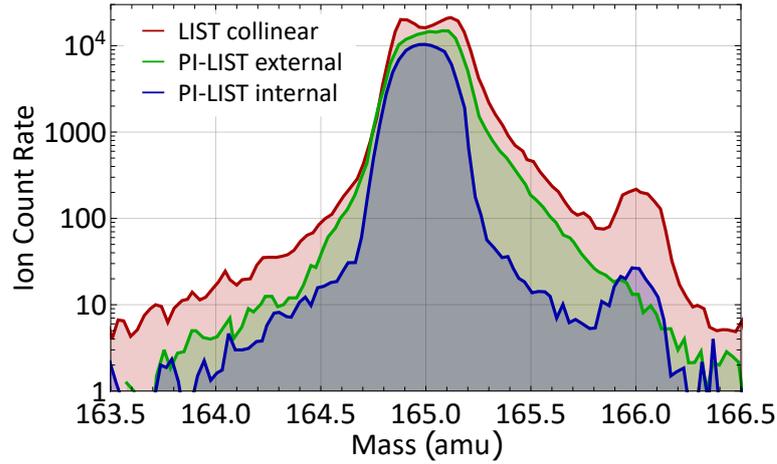
Figure 5.5: Mass peak structure for different LIST modes on laser-ionized holmium. The scans for standard collinear LIST and PI-LIST with internal reflection have been performed on the same occasion and with broad band lasers on all steps, so that also the ^{166m}Ho is apparent. The spectrum for external in-coupling was performed with a narrow-band laser employed on the first step, optimized on ^{165}Ho. A reduction in peak width for the internal reflection mode with its very confined ion origin is clearly evident.

different hyperfine structure. The most prominent feature is the different peak width and shape for the different modes, especially on the higher intensity parts. The standard LIST and "external PI-LIST" modes produce broader peaks, which are significantly more pronounced on the high mass side. A direct approach to describe this effect would be to relate this to higher starting potentials, which would cause ions to be transmitted on higher nominal masses, as they gain higher momentum during acceleration (see also the more detailed elaboration in sec. A.1.3). However, a nominal mass shift of 0.5 u in this regime already corresponds to 90 V change in potential compared to the nominal 30 kV - a value well above all applied voltages in the ion source region. Thus, alternative effects have to be considered. With the limited tools of diagnosis, an explicit assignment is not possible within the scope of this work. Nevertheless, it is obvious, that the operation mode with internal reflection produces a narrower and more symmetric peak shape. Its similarity on the low mass side with the external PI-LIST mode, namely a less pronounced tailing than the standard collinear LIST mode, is explained by the absence of ionization in the extraction field, i.e. on lower starting potentials. On the high mass side, the wider tailing of both LIST and standard PI-LIST is ascribed to less spatial confinement within the repeller electrode potential. This translates into a higher deviation in energy itself, but also transversal angle and radial distance to the central axis at the point of extraction, after traveling through the RFQ structure. Respective changes in transmission trajectories result in a broader peak shape as well.

A common number for mass resolution is a mass peak's half-height width in reciprocal comparison to its absolute mass value, $R = m/\Delta m$. For the recorded spectra, a coarse evaluation is given in tab. 5.2.

Values of $R \approx 400$ have already been reported with a 100 mm long LIST version on ytterbium, also determined on the RISIKO mass separator [77]. During the first application of the PI-LIST in its 90 mm long version on technetium, exceptionally high values even around $R \approx 1200$ could be determined for both modes [97], also with a slightly higher value for the perpendicular illumination. On the one hand, this shows that the value of mass resolution is not directly reproducible, but is strongly dependent on

Table 5.2: Calculated mass resolution for the different LIST modes on ^{165}Ho.

Mode	Δm	R
LIST	0.39	420
PI-LIST external	0.34	490
PI-LIST internal	0.21	790

additional aspects than just the installed ion source, as the setup of the whole separator apparatus. On the other hand, a similarity in standard LIST and external in-coupling mode is affirmed and the assumption of somewhat higher beam quality, given by an improvement in neighboring mass and removal of cross contaminations is attested.

5.3   Efficiency Considerations

No direct measurement on the overall efficiency of the PI-LIST in its internal reflection mode has been done so far, as this value strongly depends on the individual experiment. As already remarked in sec. 3.4.3, this includes the envisaged resolution, as reduction in spectral line width is linked to decrease in overall ionization rates. Additionally, structures with a multitude of transitions inevitably exhibit a lower count rate on the individual resonances in comparison to broad band excitation covering the whole structure. Nevertheless, at least geometrically based considerations can be taken into account, including the effective average time for which atoms are potentially available for laser ionization in every mode. A direct deduction of this can be done by broad band laser excitation in all modes, comparing count rates and scaling known efficiency values accordingly. Such an estimation is given in tab. 5.3, also including the previous results described in sec. 3.4.3.

Table 5.3: Efficiency estimations for different modes of laser ion source operation. Values for (a) are taken from [77] on the case of ytterbium. (b) is based on count rate comparisons in [26, 29, 97] for external and [100] for internal reflection in broad band (BB) mode, and investigations on relative signal heights in sec. 6.2.1 in high resolution spectra. (c) is derived by interpolating the peak current during a hyperfine structure measurement on actinium in narrow band (NB) mode.

Operation mode	Estimated efficiency (%)	Method of determination
Standard RILIS	20	
LIST ion guide mode	10	Direct measurement (a)
LIST suppression mode	0.2	
External PI mode (BB)	0.1	Ion rate comparison (b)
Internal PI mode (BB)	0.1 .. 0.02	
External PI mode(NB)	0.001 .. 0.02	Interpolation from experiment (c)

Starting point are the absolute efficiency measurements conducted on ytterbium in [77]. Values of some 10 % in standard RILIS operation are quite usual and may even be excelled in some cases, e.g. with over 50 % reported in [66] on palladium. The reduced efficiency in LIST mode is also reflected by the LIST loss factor directly deducible from switching between ion guide and suppression mode, which is also reported as 30 - 50, e.g. in [92]. Additional decrease in ionization rate by lateral broad band laser

illumination through the side window (external PI mode) has been examined in [26, 29, 97] and yields additional loss factors of 2 - 3, while in some cases also only a reduction of only around 20 % was seen. From a geometrical point of view, an only minor decrease is understandable, as a range of 30 mm along the central axis can still be covered. Equivalent analyses in [100] using the internal reflection mode with broad band lasers (internal PI mode) yield average loss factors also around 2 - 3, while in section 6.2.1 a conservative factor of 4.5 is derived from ^{165}Ho hyperfine spectra in both PI-LIST operation modes. The total spatial overlap volume of all lasers, where ionization solely can take place, is considerably smaller in the case on internal reflection. It is determined by the diameter of the perpendicular laser, which can not be expanded in the setup. Internal retro-reflection enables a second laser passage with reduced power, yet the maximum covered length is still in the order of only a few mm. The essentially identical loss factors and especially the atom density evolution investigations described in sec. A.1 show that the volume right behind the repeller electrodes is indeed most crucial for efficient ionization, as the emerging atomic beam cone still is confined enough at this place to be covered by all lasers, as further downstream the majority of atoms already laterally effused out of the beam path from the central axis.

It should also be noted that the modes with lateral laser illumination also have a feature positively effecting the efficiency in respect to standard collinear mode. Here, not only species from ionized by different mechanisms in the hot cavity are suppressed, but also those atoms of interest which are already ionized by lasers within. If perpendicular irradiation is applied, this loss channel for atoms from the hot cavity is omitted, and more neutrals can effuse into the LIST structure. This effect is particular pronounced in per se highly efficient ionization schemes, which correspondingly lead to high ion formation already inside the hot cavity.

A more application-oriented number for overall efficiency in (external) PI mode was deducted from an experiment on the actinium isotope ^{225}Ac at the RISIKO mass separator. It was conducted in the course of the nuclear structure evaluation campaign involving also actinium isotopes measured on-line at the LISOL facility in Louvain-la-Neuve as described in [18]. While its nuclear physics relevant scientific results on hyperfine structure will not be covered in the scope of this work, the data was analyzed in terms of temporal evolution of maximum count rate in respect to the overall sample size until complete exhaustion. As such, it gives a realistic picture under actual experimental conditions when the PI-LIST is used for narrow bandwidth applications. The investigated sample contained an activity of 3 kBq, corresponding to $3.7 \cdot 10^9$ atoms of ^{225}Ac (calculated from its 9.9 d half-life [113]), and was provided by the Institute of Nuclear Chemistry at Mainz University. It was manufactures in an analogue way to the other experiments described in this work, delivered as a dried solution on a folded zirconium carrier foil and placed directly inside a centrally closed tantalum oven. The transition under investigation, starting from the $6d7s^2$ ground state with a total angular momentum of $J_0 = 3/2$ to a $J_1 = 5/2$ excited state at $23\,898.86\,\text{cm}^{-1}$, followed by a resonant transition into an auto-ionizing state at $48\,318.15\,\text{cm}^{-1}$. With a nuclear spin of $I = 3/2$, a total of 9 hyperfine resonances occur. The scheme is shown on the right-hand side of fig. 5.6. While the first step was scanned with the frequency-doubled narrow bandwidth seeded laser described in sec. 3.2, the ionization step was provided by a standard broad band laser, also using second harmonic generation of its output. With temporal delay of 50 ns between the two laser pulses in respect to maximum signal rate, an experimental linewidth of roughly 200 MHz was achieved, yielding a typical setting for experiments with the PI-LIST. A total of four longtime scans over the whole structure were performed, with step-wise increase of the atomizer temperature

in between in order to counteract signal decrease by ongoing depletion of the sample. After these scans, the sample was treated as exhausted, as even further heating did not increase the already significantly lowered overall count rate anymore, and no additional data could be taken. The whole process, including initial setup using best temporal overlap of the pulses for maximum signal at the cost of resolution, took slightly more than 2 h. The count rates on the $F_0 = 0$ to $F_1 = 1$ singlet resonance, yielding the highest ion signal of all components, are depicted on the left-hand side in fig. 5.6 in respect to the point in time when they were scanned. Interpolation and integration of the count rate over the whole experiment, i.e. all four scans, was used to extract a crude total number of potentially detectable ions, with the assumption that the laser would remain on this exact resonance throughout the whole time. This is indicated by the shaded area underneath.
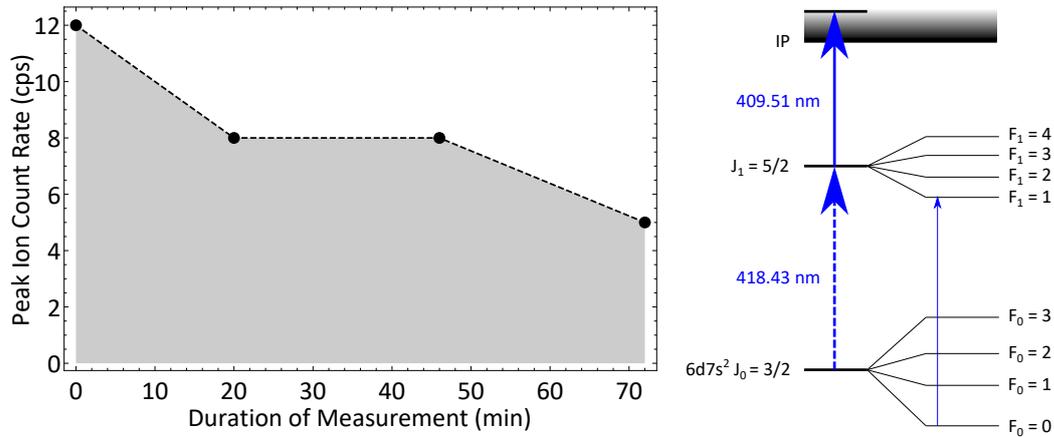
Figure 5.6: Interpolation of the signal rate in PI mode over the course of four longtime scans across the whole hyperfine structure, for assessment of its total efficiency. The count rate on the $F_0 = 0$ to $F_1 = 1$ transition as indicated on the right-hand scheme, yielding the highest ionization rate, was used. Comparison of the integrated amount of 38 520 ions to the sample size of $3.7 \cdot 10^9$ atoms results in an efficiency value of $1.0 \cdot 10^{-5}$.

The integration of the interpolated ion count rate over the whole time yields a value of 38 520 potentially produced ions. In comparison with the sample size of $3.7 \cdot 10^9$ atoms, this results in an efficiency value of $1.0 \cdot 10^{-5}$, i.e. stating that 1 in 100 000 atoms will be ionized under these realistic experimental conditions.

This number again can be compared to the count rate during setup phase of this experiment. With the parameters adjusted to optimum count rate at a still reasonable FWHM line width of $\approx 300\,\text{MHz}$, a tenfold higher signal was achieved on the same resonance. Scaling the count rate accordingly, and taking into account the additional time of 1 h for the setup at the start of the experiment, a total efficiency of $2 \cdot 10^{-4}$ is derived. These two numbers are added to tab. 5.3.

It has to be noted again, that these values can only give a very crude estimation, as individual hyperfine resonances within one transition may exhibit very different count rates. Nevertheless, the results clearly state that off-line high resolution investigations on sample sizes as small as around 10^9 atoms are feasible with the PI-LIST.

High Resolution Spectroscopy of Radioactive Holmium

6.1 Scientific Background

The hyperfine structure of isotopes with both high nuclear spin and total angular moment of accessible atomic states results in exceptionally complex spectra with dozens of individual resonances. A successful measurement ultimately requires spectral resolution which by far exceeds the capabilities of Doppler-broadened laser spectroscopy in a hot atom vapor. A downright showcase-like situation is found in the isotopic chain of the lanthanide element holmium.

A series of 14 isotopes and additionally 5 nuclear isomeric states of neutron-deficient holmium nuclides, spanning the mass numbers 152 to 165, were investigated by Alkhazov et al. in 1989 [114]. They employed high resolution resonance ionization laser spectroscopy perpendicular to an atomic beam at the IRIS mass separator at LNPI, Troitsk. IRIS is coupled to a synchrocyclotron, producing the short-lived isotopes by bombardment of a tantalum target with 1 GeV protons via the ISOL-method. The evolution of the nuclear parameters, i.e. magnetic moments, spectroscopic quadrupole moments and changes in mean square charge radii was extracted and compared to theoretical descriptions. A more and more deformed nucleus is expected if more neutrons are added, moving away from the magic $N = 82$ closed neutron shell at ^{149}Ho.

Yet, no laser spectroscopic experiments on nuclear structure for the neutron-rich side of holmium nuclides above the only stable isotope ^{165}Ho were conducted to further track this evolution. Consequently, there is no information on the hyperfine structure parameters A and B available, even not for the ground state of the neighboring isomer ^{166m}Ho, which is still accessible by off-line experiments due to its long half-life of 1132(4) years [115]. On a more fundamental point of view, even its nuclear spin $I = 7$ is found uncertain and not validated in compendia [116], while other sources state it as certain [117]. The nuclear magnetic dipole moment has been measured by a set of different complementary methods. In contrast, a particularly interesting situation is given in the case of the spectroscopic quadrupole moment. Mashak et al. determined it to be $-3(3)\,eb$ in 1981 [27], but at the same moment stated that this result contradicts the expectation of a prolate shape ($Q_s > 0$) which is expected for nuclei in this mass regime. The experiments discussed here shed light on all these open questions and also expand the knowledge on the evolution of mean square charge radii, where also no investigations have been done so far.

Hyperfine structure ground state parameters for the stable ^{165}Ho were measured with very high precision by the atom beam magnetic resonance technique by Dankwort et al. in 1974 [118]. The availability of this data enables systematic checks on the results presented here, keeping in mind that the PI-LIST ion source, either in standard or in the new internal reflection mode, still is a quite new development.

The application of the PI-LIST for long-lived radioactive holmium isotopes is also linked to the involvement of the LARISSA working group in the ECHo project on determination of the electron neutrino mass [7]. Here, the decay spectrum following the electron capture of ^{163}Ho ($T_{1/2} = 4570(50)$ a [119]) is recorded in cryogenic metallic-magnetic micro-calorimeters via implantation into gold absorbers. From precise parametrization of this spectrum in combination with sufficient, year-long counting statistics, the electron neutrino mass can ultimately be deduced with sub-eV accuracy. The task of the LARISSA group is the laser mass spectrometric purification of the chemically pre-cleaned holmium samples with simultaneous implantation into the calorimeters using the RISIKO mass separator [28]. Besides the requirement of highest possible efficiency in this process, the purity of the final product in order to prevent any disturbance in the energy spectra is of utmost importance. Naturally, the long-lived ^{166m}Ho, which can not be separated by chemical means, is major challenge to face. Investigations on the hyperfine structure therefore also might reveal opportunities for additional purification by exploring differences in the isotope-unique excitation patterns.

The samples of ^{163}Ho and ^{166m}Ho for this work stem from the total stock of the ECHo project, originating from enriched ^{162}Er irradiated at the high flux reactor at ILL, Grenoble. They are provided and prepared for the experiments presented here by the Institute for Nuclear Chemistry of Mainz University. The production and purification process is described in [120].

Laser Ionization Schemes for Holmium

Two transitions from the atomic ground state in different ionization ladders were chosen for extensive studies on the isotopes ^{163}Ho, ^{165}Ho and ^{166m}Ho, the latter one being the first optical spectroscopy on this long-lived isomer (the nuclear ground state ^{166}Ho with a short half-life of 26.794(23) h [121] is not available to these investigations). The respective schemes, both addressed by frequency-doubled titanium:sapphire laser light in the first step and fundamental output in the subsequent ones, are summarized in fig. 6.1 and are elaborately discussed in the next sections. Scheme A exhibits a dedicatedly chosen weak transition with long lifetime to fully exploit the methods developed for highest possible resolution. Scheme B was used in a first phase of highly efficient ionization of holmium for the ECHo project with an overall efficiency of 32(5) %. More recently, the second and third steps were replaced by direct excitation into an auto-ionizing state with a second laser at 418.3 nm, pushing the efficiency up to 69(5) % [67]. The first step was maintained, so that detailed knowledge about its properties regarding the isotopes of interest, especially in respect to specific ways of enhancing selectivity, is of high importance.

All measurements were performed at the RISIKO mass separator, both in the PI-LIST in standard configuration as described in section 3.4.3 as well as in the new configuration with internal reflection as presented in section 4.1. A centrally closed atomizer oven was used (see sec. 3.3.1). The transition from the ground state was scanned with frequency-doubled light from the injection-seeded narrow bandwidth laser driven by an appropriate ECDL cw diode laser (see sec. 3.2.2). The fundamental output
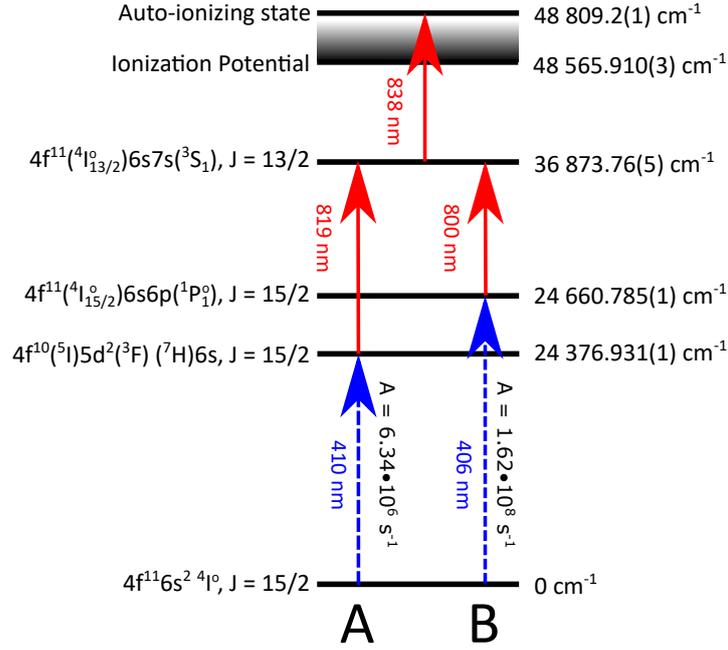
Figure 6.1: Holmium laser resonance ionization schemes, with the respective steps for hyperfine structure investigations marked by dashed lines. Scheme A denotes the dedicatedly chosen weak transition for highest possible spectral resolution, while scheme B is used for highly efficient ionization and implantation in the ECHo project [86]. Level configurations, energies and Einstein coefficients are taken from [86, 99, 122–124] and this work.

of standard Z-cavity lasers (sec. 3.2) was used for broad band excitation in the second step and ionization via an auto-ionizing state.

Common to all spectroscopic cases in the holmium isotopes of interest is the high total angular momentum of the initial and final state of the transition, $J = 15/2$, and the significant nuclear spin of $I = 7/2$ for ^{163}Ho and ^{165}Ho, and $I = 7$ for ^{166m}Ho. These values result in 22 individual hyperfine resonances for the low-spin cases, and an extremely dense spectrum of 43 lines in the ^{166m}Ho case.

6.2 Transition to the $4f^{10}(^5I)5d^2(^3F)(^7H)6s$ State

As described in sec. 2.1.6, an atomic level with sufficient lifetime to temporally decouple the probing laser pulse from the subsequent excitation and ionization steps offers several advantages for the achievable resolution while best possibly maintaining the signal rate. Previous ionization scheme development on holmium with the main scope of highly efficient ionization focused on strong transitions, which are easy to saturate with the available laser powers, but consequently go along with short lifetimes of the involved states. For the high resolution work presented here, a weak transition, characterized by a low Einstein coefficient A_{ki}, and corresponding to a longer lifetime of its upper state, was chosen from literature. The selected $4f^{11}6s^2 \rightarrow 4f^{10}(^5I)5d^2(^3F)(^7H)6s$ transition connects the J = 15/2 atomic ground state to a J = 15/2 level at $24\,376.91\,\text{cm}^{-1}$ with an A coefficient of $6.338 \cdot 10^6\,\text{s}^{-1}$ [123]. This is more than a factor of 25 lower than the ground state transition for the $4f^{11}6s6p$ (J = 15/2) state used at the ECHo project. These two transitions are only 5 nm apart, making it convenient to utilize the same known second excited state and subsequent ionization via an auto-ionizing state. Furthermore, both first step transitions can be investigated within the wavelength range of the same master

laser diode of the injection seeded system and thus without major, time consuming changes to the setup.

Lifetime of the $4f^{10}(^5I)5d^2(^3F)(^7H)6s$ State

In a first step of the experiment, the effective lifetime of the excited $4f^{10}(^5I)5d^2(^3F)(^7H)6s$ state was investigated. By exploiting the structure of short laser pulses for the different excitation steps in the scheme, this can be done in a direct way. After the first pulse transferred population into the state of interest, the (simultaneous) pulses for the two further excitation steps are delayed by a fixed time difference via the electrical trigger signals for the respective pump lasers using a pulse delay generator. A step-wise change of this difference translates the remaining state population at this time directly into the ion signal rate. The resulting data is shown in fig. 6.2.
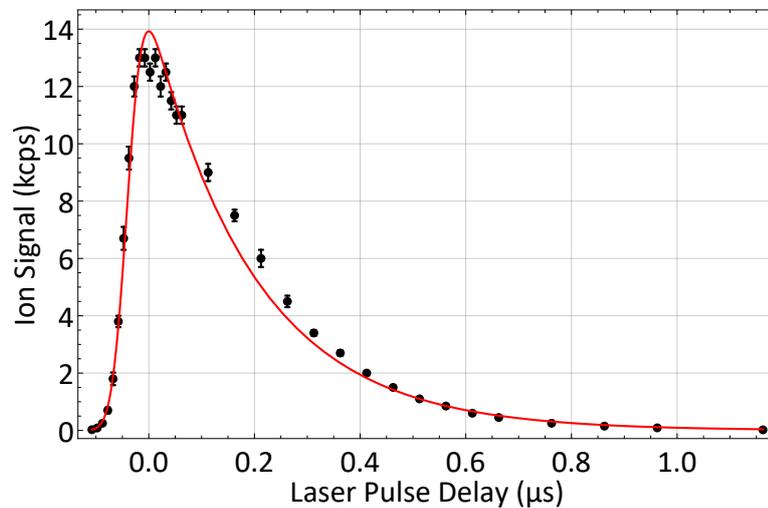
Figure 6.2: Lifetime measurement of the excited $4f^{10}(^5I)5d^2(^3F)(^7H)6s$ state in holmium by delay of the coinciding second and third step laser pulses in respect to the first. The ion signal evolution is fitted by an exponentially modified Gaussian function, taking into account both the Gaussian temporal shape of the laser pulses and the exponential decay of the state's population. A lifetime of $\tau = 197(4)\,\text{ns}$ (respectively $T_{1/2} = 137(3)\,\text{ns}$) is deduced from the fit.

Besides the exponential decay described above, a second phenomenon is present. In the time domain before separation, the signal evolution is governed by the temporal overlap of the Gaussian-like laser pulses, e.g. exhibiting a sharp onset. Thus, as a model for mathematical description, an *exponentially modified Gaussian distribution* for the sum of independent normal and exponential variables was chosen as

$$I(x) = A \cdot \frac{\lambda}{2} \cdot \exp\left(\frac{\lambda}{2} \left(2\mu + \lambda\sigma^2 - 2x \right) \right) \cdot \text{erfc}\left(\frac{\mu + \lambda\sigma^2 - x}{\sqrt{2}\sigma} \right) + I_0, \qquad (6.1)$$

with the exponential relaxation time $\lambda = 1/\tau$, mean value μ, Gaussian standard deviation σ as well as a scaling factor A and a constant offset I_0. erfc(...) is the analytically non-explicit *complementary error function*

$$\text{erfc}(x) = 1 - \text{erf}(x) = \frac{2}{\sqrt{\pi}} \int_x^\infty \exp(-t^2)\mathrm{d}t. \qquad (6.2)$$

The exponentially modified Gaussian distribution is widely used in chromatography, where such peak shapes are common [125].

The fit yields a decay constant of $\tau = 197(4)$ ns, or respectively $T_{1/2} = \ln(2) \cdot \tau = 137(3)$ ns. Additionally, a full-width at half maximum temporal width of $\Delta_{\text{FWHM}} = 2\sqrt{2\ln(2)}\sigma = 54(2)$ ns is extracted for the Gaussian part. This resulting part is the convolution of two single Gaussian profiles, the first step and the simultaneous subsequent steps. Assuming an equal width, the individual $\Delta_{\text{FWHM,single}} = \frac{1}{\sqrt{2}}\Delta_{\text{FWHM}} = 38(2)$ ns can be derived, which is in very good agreement with the commonly given laser pulse specifications of 30 ns - 50 ns [78], supporting the eligibility of the model.

The lifetime τ of the state itself is linked to the Einstein coefficients A of the transitions connecting it to lower states, being the atomic depopulation channels. In the most simple approach, only the strongest transition is used for approximation, resulting in the relation

$$\tau = \frac{1}{A}. \tag{6.3}$$

From the value of $A = 6.338 \cdot 10^6\,\text{s}^{-1}$ listed in [123], a lifetime of $\tau = 158$ ns can be calculated, whereas a direct measurement by laser-induced fluorescence yielded 173 ns [126]. The discrepancy between the values found in literature (and keeping in mind that a direct lifetime measurement should always yield a shorter value than one derived from one single decay channel, as additional losses might be present) shows the more approximate nature of these numbers. However, the state lifetime in the order of 165 ns or 137(3) ns as measured in this work conveniently allows temporal separation of the excitation laser pulse used for spectroscopy and the subsequent ionization with only moderate loss in signal rate. For example, a typically chosen delay of 80 ns in respect to maximum signal, ensuring complete separation of the pulses, results in signal rate decrease of only about 30 %.

For comparison, the $4f^{11}(^4I^o_{15/2})6s6p(^1P^o_1)$ state used in scheme B is stated to have a lifetime of 5.0 ns in [126], while calculation from the Einstein coefficient of the corresponding ground state transition, $A = 1.622 \cdot 10^8\,\text{s}^{-1}$ [99], yields 6 ns. Both are at least a factor of 25 lower and thus well below the pulse width of the individual laser pulses, preventing efficient use for the delay method.

6.2.1 Hyperfine Structure Investigations - ^{165}Ho

The sequence of the presentation of results as given here follows the chronology of the measurements. On the reference isotope ^{165}Ho, details of the experiment are stated and the data analysis method is discussed. Results for the radioactive ^{163}Ho are presented afterwards. ^{166m}Ho as the most advanced case is shown at the end, exhibiting altogether 43 individual hyperfine structure resonances, and additionally an admixture of the neighboring ^{165}Ho isotope which could not completely be suppressed in the mass separator.

Ionization Scheme Investigations

The first experiments were performed on the stable ^{165}Ho isotope. The holmium atoms were taken from AAS standard solution[1] as Ho_2O_3 in 5 % HNO_3 solution, which was initially further diluted as 1:49 in de-ionized water. 2 μL of this solution were then pipetted onto a 4 x 4 mm^2 zirconium foil. The sample was evaporated to dryness, folded to fully enclose the remnants, and placed directly in the centrally closed version of the

---

[1]Alfa Aesar Specpure® Ho 1000 μg/ml, https://www.alfa.com/de/catalog/088070/

atomizer. To prevent the sample itself from direct exposure to laser light, which might cause local heating and uncontrolled evaporation, a second, empty zirconium foil was coarsely folded into a sphere-like shape and placed ahead of the sample.

From dilution and pipetting, a total amount of $1.46 \cdot 10^{14}$ atoms of ^{165}Ho is calculated. This amount was used for systematic tuning of the operation parameter and finally for all scans in both standard PI-LIST and internal reflection mode.

A schematic overview of the hyperfine structure in the transition under investigation is given in fig. 6.3. The angular momenta of the initial and final states of $J = 15/2$ couple to the nuclear spin of $I = 7/2$, resulting in 8 hyperfine levels each, spanning from $F = 4$ to $F = 11$. With the selection rule $\Delta F = $ -1,0,+1 in total 22 individual transitions are present. The resulting pattern is depicted in the upper panel, covering a spectral range of roughly 24 GHz.
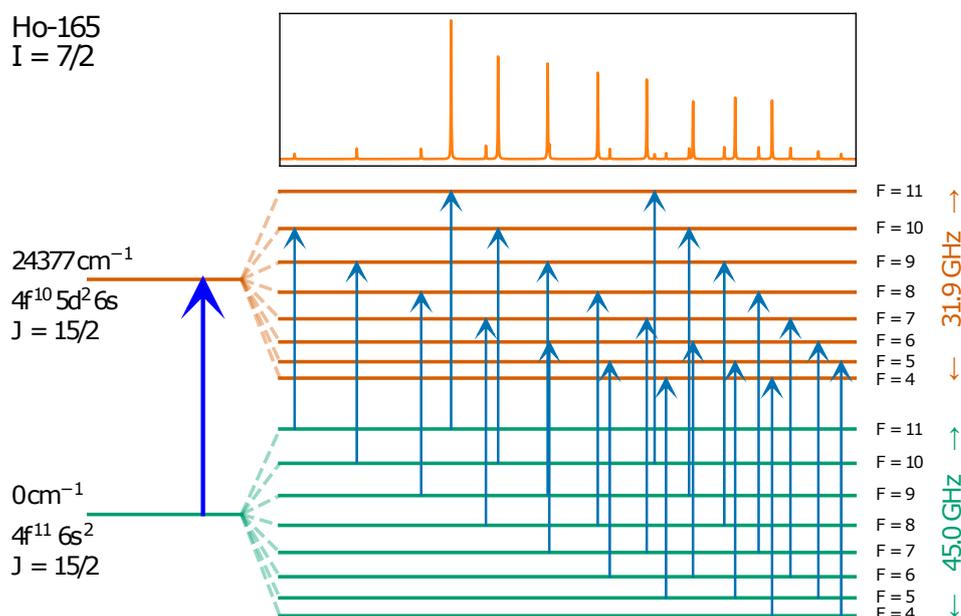
Figure 6.3: Schematic overview of the hyperfine structure pattern in the transition under investigation in laser scheme A. Altogether 22 individual resonances are present.

As shown in fig. 6.3, the total splitting of the upper state extends over a range of already more than 30 GHz. This might cause a problem if the subsequent excitation laser is spectrally too narrow to cover all sub-levels for further excitation and final ionization. The transitions to the outer-most levels would then not be visible in the ion signal. To counter-act this effect, the second step standard Ti:sapphire laser (as described in sec. 3.2) was equipped with a thinner etalon (0.2 mm instead of 0.3 mm) compared to standard operation, resulting in a broader spectral profile. A scan of this laser was then performed with the narrow bandwidth first step laser populating only the lowest ($F = 4$) or highest ($F = 11$) hyperfine level of the first excited state, respectively. The result is shown in fig. 6.4.

Although the optimum adjustment differs significantly, the investigations show that for the intersection point of both curves at $12\,496.7 \, \text{cm}^{-1}$ chosen as working point for this laser, further excitation into the 2nd excited state and subsequent ionization is guaranteed for the whole hyperfine structure. Yet, relative intensities can not be preserved, as e.g. for the outer-most sub-levels already a reduction in signal rate by a factor of 2 compared to maximum is observed.
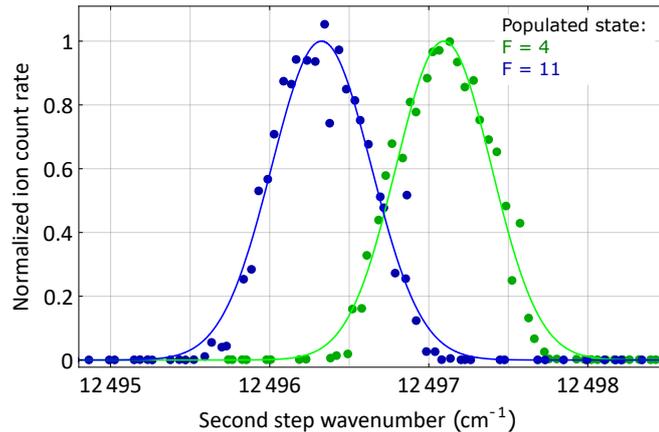
Figure 6.4: Laser wavelength scans of the second step broad band laser, while the first step narrow band laser only populates one of the outer most hyperfine structure levels of the first excited state. The data is scaled to its respective maximum and fitted with a Gaussian profile. By choosing the intersection at $12\,496.7\,\text{cm}^{-1}$ as working point, further excitation into the second excited state and subsequent ionization is ensured.

The same examination was also performed for the third, final laser excitation step into the auto-ionizing state above the ionization potential. The narrow band first step laser was again adjusted to only populate either the $F = 4$ or $F = 11$ sub-level, the second step was tuned to the respective maximum signal rate as derived from fig. 6.5, and a wavelength scan of the third laser was performed. Figure **??** shows the result. In an analogue way to the second step, also here a working point can be defined at $11\,935.1\,\text{cm}^{-1}$ to ensure ionization from all first excited state hyperfine sub-levels and thus ion signal sensitivity to all transitions from the ground state.
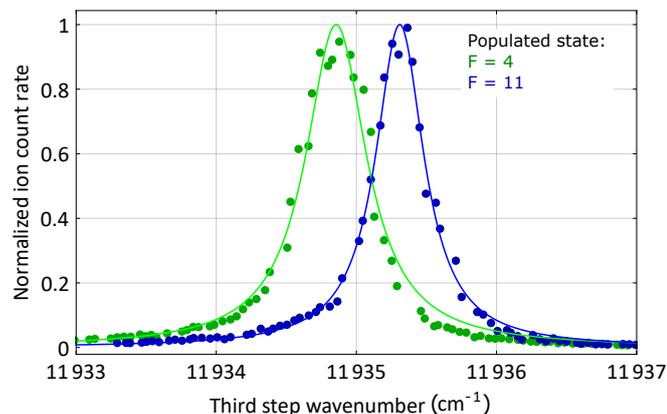
Figure 6.5: Laser wavelength scans of the third step broad band laser. The first step narrow band laser only populates one of the outer most hyperfine structure levels of the first excited state, and the second step laser is tuned to respective maximum signal rate according to fig. 6.4. The data is scaled to its respective maximum and fitted with a Lorentzian profile. Analog to the second step, a working point to guarantee ionization via all channels is found at the intersection at $11\,935.1\,\text{cm}^{-1}$.

After this preparatory work and before the full scans of the whole hyperfine structure, systematic checks on the influence of different parameters regarding spectral resolution and signal rate were performed. For stable ^{165}Ho, the spectral linewidth of the observed experimental resonances was optimized to $100\,\text{MHz}$ in both operation modes of the

PI-LIST, as was the minimum achievable value with the setup. Key parameters are, as stated above, the temporal delay between the spectroscopy pulse and the subsequent ionization laser pulses, and the overall power of the spectroscopy laser. Additionally, the collinear second and third step lasers were guided through an iris aperture right before their entrance into the separator to cut off halo light and to provide an optimum narrow geometric channel in the LIST for best selection of Doppler velocity classes with lowest lateral velocity. The ion optical parameters of the separator were then slightly adapted to provide best signal in both PI-LIST operation modes.

With the settings at hand, one full scan of the hyperfine structure was performed in each operation mode within on the same day. The heating current of the atomizer was kept at the same level of 120 A with a total power delivery of 87 W from the power supply. The oven temperature was not recorded directly at these measurements. A direct, pyrometric investigation of the current dependency of the temperature was made in [84] for a similar ion source at the RISIKO separator, which suggests a temperature of significantly less then 1200 °C, which was the minimum measurable temperature with the pyrometer and recorded for a heating current of 150 A.

For both scans, the laser pulse delay was chosen to 80 ns to ensure complete temporal separation. In internal reflection mode, the power of the spectroscopy laser was 7 mW before the entrance into the separator. In standard PI-mode with incoupling through the lateral window at the ion source vessel, the maximum available laser power of 70 mW measured in front of the cylindrical beam shaping telescope before the window was used, as no further improvement in linewidth was observed by attenuation.

Investigations on Spectral Resolution and Limitations

The two datasets are shown in fig. 6.6. The scanning procedure was done by stepwise alteration of the master laser wavelength in steps of 5 MHz every 4.1 s (in the range between the peaks this was lowered to 1.1 s). The wavelength readout of the WSU wavemeter was recorded every 1 s, together with the accumulated ion count in this time. In off-line analysis, a binning procedure with widths of 10 MHz, 20 MHz and 30 MHz was applied afterwards. Error bars on the single data points are calculated from an assumed Poisson distribution on the individual count number within 1 s serving as weights for the averaging procedure. The whole spectrum is then fitted by a single function via a least square optimization method. The individual peak positions relative to the transition's center are calculated directly from the A and B hyperfine structure parameters of both involved states via eq. 2.18 as described in sec. 2.1.2. For ^{165}Ho these 5 different parameters are over-determined by the 22 resonances and as such sensitive to inconsistencies within the data set. All resonances are fitted as Voigt profiles and share a single parameter for their Gaussian width, as this contribution is caused by remaining Doppler broadening and thus is identical for all resonances. Additionally, each peak has an individually assigned Lorentzian width and an independent amplitude, to account for different remaining fractions of saturation effects caused by power broadening, and the different relative ionization efficiency by the subsequent laser steps as discussed above.

In ^{165}Ho, the high resolution of the spectrum yields completely separated peaks in almost all cases, just $F = 7 \rightarrow F = 6$ overlaps with $F = 9 \rightarrow F = 9$ and $F = 9 \rightarrow F = 10$ is very close to $F = 6 \rightarrow F = 6$. The fitting procedure thus can assign the individual peak widths properly. The results for the average FWHM and its constituents for both operation modes as figure of merit for the spectral resolution is given in tab. 6.1.

As described above, the Gaussian fraction and its error can be taken directly from the fitting results. For the Lorentzian values, a mean value weighted by the inverse quadratic
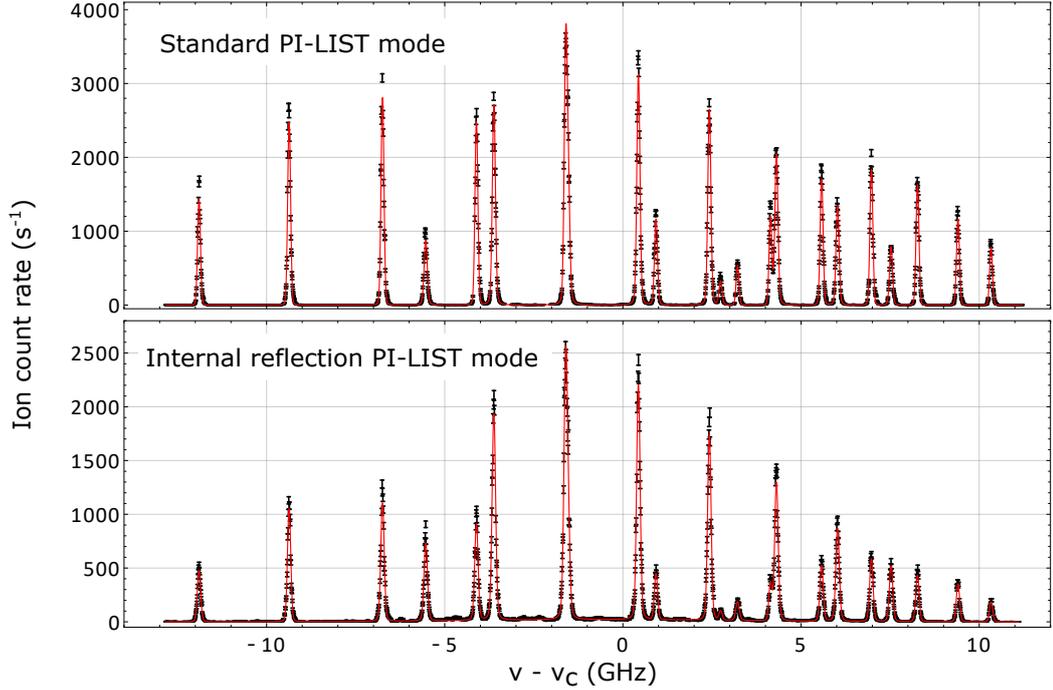
Figure 6.6: Full scans of the 1st step hyperfine structure of ^{165}Ho both in standard PI-LIST mode with lateral laser incoupling through a window in the ion source vacuum vessel, and internal reflection mode via the built-in metal mirrors. Frequency is given in respect to the transition's measured center of $\nu_c = 24\,376.9312(6)\,\mathrm{cm}^{-1}$. The fit using Voigt profiles exhibits an average FWHM of 99 MHz for the first and 114 MHz for the latter case. See text for details.

Table 6.1: Average FWHM widths of the resonances in the ^{165}Ho spectra in fig. 6.6 for both PI LIST operation modes. In both cases the shapes are governed by their Gaussian fraction, implying limitation by the remaining Doppler broadening in the effusing atom cone. See text for details.

		FWHM (MHz)	
	Voigt	Lorentzian	Gaussian
Standard PI mode	99(1)	10(1)	94(1)
Internal reflection mode	114(1)	18(1)	104(1)

of the individual fitting errors was calculated. This method favors well-determined single values with a small error, i.e. peaks which can be treated well by the fitting routine. On overlapping resonances, where an individual assignment of the width is not possible, larger errors are given by the fitting procedure and these less reliable parameters are weighted accordingly less. The overall error on the resulting Lorentzian width is calculated according to this weighted mean procedure, and the final error on the Voigt profile from its constituents as described in eq. 2.54. It is to be noted that the actual values of the individual Lorentzian fraction, even of those which are well separated, exhibit a spread between values of 5 MHz - 20 MHz with an unweighted standard deviation of 6 MHz. This shows the coarse nature of the overall value, and supports the assumption of different contributions of the saturation-dependent Lorentzian part for individual resonances. Besides this power dependency, the Lorentzian part stems from the transition's natural linewidth, which can be derived from its comparatively long lifetime of $\tau = 197(4)\,\mathrm{ns}$ via eq. 2.41 to exhibit an FWHM of $2\gamma_{\mathrm{nat}} = 1.6\,\mathrm{MHz}$. Thus, a significant influence is

also ascribed to the injection-seeded pulsed laser with its fundamental linewidth of 10 to 20 MHz [62], and a factor of $\sqrt{2}$ broadening in the frequency-doubled regime. This minimum linewidth is surprisingly not found in the Lorentzian parts in tab. 6.1, which shows the underestimation of the errors by the fitting routine. It is explained as an artifact of the fitting routine routine in case of very different Lorentzian and Gaussian contributions.

Nevertheless, the relative comparison between Gaussian and Lorentzian fractions clearly shows that the resolution in the spectrum is governed by the Doppler broadening dependent Gaussian part (see sec. 2.1.6). In this geometry the method is therefore limited by the remaining lateral velocity spread in the emerging atomic beam cone, determined by the ionization volume in the intersection of all, lateral and collinear, laser beams.

The slightly broader line shape in the case of internal reflection can be caused by two geometric effects, as also described in sec. 4.1 and visualized in fig. 3.11 and 4.1. On the one hand, the optimum perpendicular laser incoupling can be arranged and controlled more easily in the standard PI-LIST setup. The mirrors outside of the vessel can be optimized in respect to the light exiting from the window on the opposite side. In internal reflection mode, no monitoring of laser beam reflection quality and angle is possible. Both effects lead to potential addressing of more velocity classes and thus a larger Gaussian width. On the other hand, the spatially elongated laser beam of the standard PI-LIST mode also addresses a region further downstream in the LIST structure. The resulting atomic beam cone opening angle accepted for ionization by the collinear lasers is significantly smaller in this place. Overall, this results in a larger fraction of atoms being ionized with lower Doppler broadening compared to the internal reflection mode.

In the spectrum recorded in the internal reflection mode, an additional very weak contribution from an underlying broad structure became apparent in post analysis, which is barely visible in fig. 6.6. This structure can be described by adding a background Gaussian profile with an FWHM of $\Delta_{\mathrm{FWHM}} = 8.5(5)\,\mathrm{GHz}$, and a shift from the center value of the hyperfine structure of $600(200)\,\mathrm{MHz}$ towards lower photon energy. It can be interpreted as a fraction of the incoming light, or halo, of the spectroscopy laser not hitting the internal metal mirrors but still being present on the longitudinal axis. This shift in center frequency corresponds to a relative mean velocity of $250(80)\,\frac{\mathrm{m}}{\mathrm{s}}$ anti-collinear to the laser propagation, corresponding to a temperature of $220(310)\,°\mathrm{C}$ of a respectively effusing atom beam. This value seems significantly lower than the assumed oven temperature itself. Yet, a definite comparison is not possible due to its large error and to only having an upper bound for the oven temperature. In turn, the FWHM of $8.5(5)\,\mathrm{GHz}$ fits fairly well to an assumed envelope for the whole, approximately $16\,\mathrm{GHz}$ broad spectrum. Therefore, the assumption of resonant ionization of the holmium atoms via this transition in a Doppler-broadened way is supported. A consistent explanation, also for the inconclusive temperature assignment, can be given by part of the laser light being reflected or scattered at some other part of the LIST setup than the mirrors, and crossing the emerging atomic beam cone at a certain angle instead of only in anti-collinear propagation.

Anyhow, it is also to be noted that the hyperfine structure parameters extracted from the fit do not show any significant dependence on implementing this structure in the fitting function or not. In further scans on different isotopes, this underlying structure could completely be avoided by more careful and proper shaping and alignment of the spectroscopy laser beam.

Relative Efficiency Allocation

From the spectra recorded in fig. 6.6, the technical characteristic of relative efficiency of the operation modes can be extracted from the two measurements being performed right after one another, at the same oven settings and optimized for best possible spectral linewidth of 100 MHz as experimental goal. The count rate for transitions into sub-states located in the middle of the structure of the upper level was compared. For these sub-states, namely $F = 6$ to 9, possible wavelength fluctuations of the subsequent broad band lasers only play a minor role compared to the outer F levels, where this influence is significant, as shown in figures 6.4 and 6.5. For simplicity, only the transitions with highest count rate, i.e. those starting from ground state sub-levels with identical F value, are considered. The results are compiled in tab. 6.2.

Table 6.2: Compilation of count rates on selected transitions for efficiency estimations between both operation modes. The spectral position of the respective peaks in fig. 6.6 is annotated in the second column. Considering sample exhaustion rate over time on top of the calculated ratios, a conservative value of a signal loss factor of 4.5 is deduced. See text for details.

Transition $F_1 \rightarrow F_2$	Spectral position (MHz)	Standard PI mode Count rate (s^{-1})	Int. reflection mode Count rate (s^{-1})	Ratio
$9 \rightarrow 9$	-1530	3600	2500	1.44
$8 \rightarrow 8$	430	3200	2200	1.45
$7 \rightarrow 7$	2430	2500	1700	1.47
$6 \rightarrow 6$	4310	2000	1200	1.67
Mean value				1.5
Including sample exhaustion (conservative)				**4.5**

On average, a count rate and thus efficiency ratio of a factor of 1.5 is deduced between both operation modes. Yet, it is also to be noted that over the course of several hours of the measurement, an overall decline of the ion signal in the same order, due to exhaustion of the sample, was observed. With the available data, a full consideration of this effect can not be conducted. Reference checks were only performed on the outermost peaks, where, as stated above, the influence of the second and third laser wavelengths plays an important role on the ion signal, so that a reduction may not only be ascribed to a decline of evaporation rate from the source. Obtained values are reduction factors of 3 for the course of the internal reflection scan, and 1.5 for the standard PI mode scan. As the latter scan was performed later, a conservative correction factor of 3 is ascribed on top of the one derived from the count rates, resulting in an expected efficiency difference factor of a maximum of 4.5. Additional dedicated examinations of this efficiency loss factor are presented in section 5.3, where a significantly lower loss rate extending up to unity is derived and backed up by geometrical considerations. In summary, both operation modes thus yield an efficiency in the same order of magnitude.

Data Analysis Method

This section describes the subsequent steps which were undertaken in the data analysis procedure, successively including more effects and error sources. The goal is not only to most precisely extract the final values for the hyperfine parameters for stable ^{165}Ho, but also to give a blue print for the analyses of the other isotopes, especially the previously unknown structure of ^{166m}Ho.

The results extracted from the spectra discussed above were taken from a fit to the recorded data, i.e. the value given by the wavelength meter respective to the count rate while the laser is tuned to this frequency. In a later stage and on different experiments it was discovered that this readout of the wavelength meter might not be reliable in the required accuracy range in the MHz regime. This problem affects the whole community of high resolution laser spectroscopists, and is therefore right now treated for proper correction by a collaboration of several institutions, including the LARISSA group, and the manufacturer. The topic was also discussed on several specific meetings and congresses and is subject to a dedicated publication, which is in the process of submission [127]. In the frame of this thesis, only a brief overview will be given, and respective consequences for data handling are analyzed and discussed.

In the commercial wavelength meters commonly used for high resolution laser spectroscopy, the determination of the wavelength of the incoupled light is done by software evaluation of the fringe pattern in a series of specifically designed interferometer cavities. The accuracy is determined by the finest interferometer with, in the case of the LARISSA group's WSU 30, a free spectral range (FSR) of 2 GHz. While in most cases such a wavelength meter is the only available device for determination of the *absolute* wavenumber, the *relative* shift between two (narrow bandwidth) frequencies can also quite conveniently be recorded by different means. For example, a scanning Fabry-Perot interferometer (SFPI) (as described in sec. 3.2) is used in the LARISSA laboratory to employ fringe offset locking in respect to a commercial, frequency stabilized helium-neon laser by converting the temporal information of the fringes' positions within its scanning ramp into frequency differences via the known free spectral range. This system is used to stabilize and control the diode master laser for the injection-seeded pulsed spectroscopy laser. In the presented holmium experiment this SFPI data was not recorded as the reliability of the wavelength meter was not in question. Later on, in dedicated experiments on various different diode lasers, the discrepancy between the relative SFPI readout and the wavelength meter was investigated in detail. In approximation, the result is a periodic, triangle-like deviation $\Delta(\nu) = \nu_{\text{SFPI}} - \nu_{\text{WSU30}}$ with a constant amplitude and cycle throughout the accessible wavelength range of the Ti:sapphire laser system as

$$\Delta(\nu) = \frac{4\Delta_0}{T}\left((\nu + S) - \frac{T}{2}\left\lfloor\frac{2(\nu + S)}{T} + \frac{1}{2}\right\rfloor\right) \cdot (-1)^{\left\lfloor\frac{2(\nu+S)}{T} + \frac{1}{2}\right\rfloor} \tag{6.4}$$

in respect to the wavelength meter readout ν, with the amplitude Δ_0, period T and phase offset S. $\lfloor...\rfloor$ is the floor operator, i.e. rounding to the nearest lower integer value. Fitting this function to sample data recorded with the WSU 30 yields the parameters $\Delta_0 = 2.6(2)$ MHz and $T = 1.918(18)$ GHz consistently for the tested frequency ranges. The gaps between those ranges are too large to permit investigation on the constancy of the phase offset S. A visualization of the behavior is given in fig. 6.7 on randomly computer generated data. The actual measurements are also subject to the publication in preparation [127] and thus are not shown here.

The evaluated period T is close to the finest interferometer FSR of the wavelength meter. This finding is consistent to the same measurements by different groups on their respective wavelength meter models with different FSRs. Correspondences with the manufacturer indeed confirmed the possible occurrence of such inaccuracy in the automatic software processing on the very edge of the pattern, where the fitting routine is not adequately able to describe the shape. However, the determined peak-to-peak amplitude of $2\Delta_0 = 5.2(3)$ MHz is within the specified accuracy of the device, given as
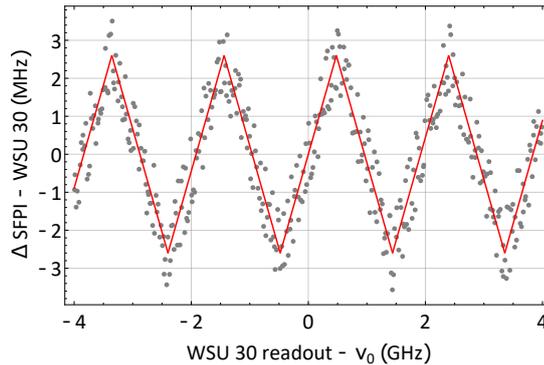
Figure 6.7: Visualization of the periodic, triangle-like deviation of the measured wavelength differences Δ between WSU 30 readout and scanning Fabry-Perot interferometer (SFPI) in respect to the WSU 30 readout around an arbitrarily chosen absolute frequency ν_0. The red line is given by eq. 6.4, the data is randomly computer generated for illustration. Actual data is subject to an upcoming publication [127].

10 MHz for a 1-σ-confidence interval (The number in WSU 30 refers to the 3-σ interval) - it is only a priori unexpected that these deviations already occur in relative measurements across small ranges and not only effect the absolute frequency determination.

Data from the SFPI also can be used as sole source for relative frequency positions and hence the wavelength meter problem can be omitted. An alternative is to precisely measure the shift of the SFPI data towards the wavelength meter separately for the range needed for the spectroscopic measurements. The wavelength meter data can then be corrected and linearized in post-analysis. Unfortunately, the diode laser system used in the holmium experiment was not available later on and these corrections could not be measured and applied. To investigate the influence on the extracted hyperfine structure constants, a statistical approach was chosen instead. Multiple modified data sets were created from the original recorded data. Therefore, the frequency data was converted with eq. 6.4 with the known values for the Δ_0 and T parameters, but with an arbitrarily chosen phase shift S for each new set. A total of 50 of these processed data sets were then fitted again with the hyperfine structure function described at the beginning of this section. As a priori no knowledge exists about the value of S in the examined scan range, all set are weighted equally and the resulting mean value and standard deviation of the parameters extracted from the fit provide a measure of the uncertainty stemming from the non-linearity of the wavelength meter readout.

The different results for the hyperfine structure parameters of the ground state and the upper state, A_0, B_0 and A_1, B_1 as well as the transition's center frequency ν_0 are shown in fig. 6.8 as function of chosen triangle modulation phase shift S. Mean values and standard deviations are indicated. The individual error bars are taken from the respective fit. A slight systematic deviation up to above a factor of 3 above these error bars is evident.

After applying this procedure, a comprehensive value for the parameters and their errors as determined by the least square fit procedure and including the uncertainty in the wavelength meter readout can be given. While the data shown up to here was always treated in bin sizes of 10 MHz, also values of 20 MHz and 30 MHz were used in the evaluation to check for possible systematic effects of the binning procedure. The results are in all cases consistent within the error margins, and weighted mean values with the previously determined standard deviation as error are given in table 6.3.
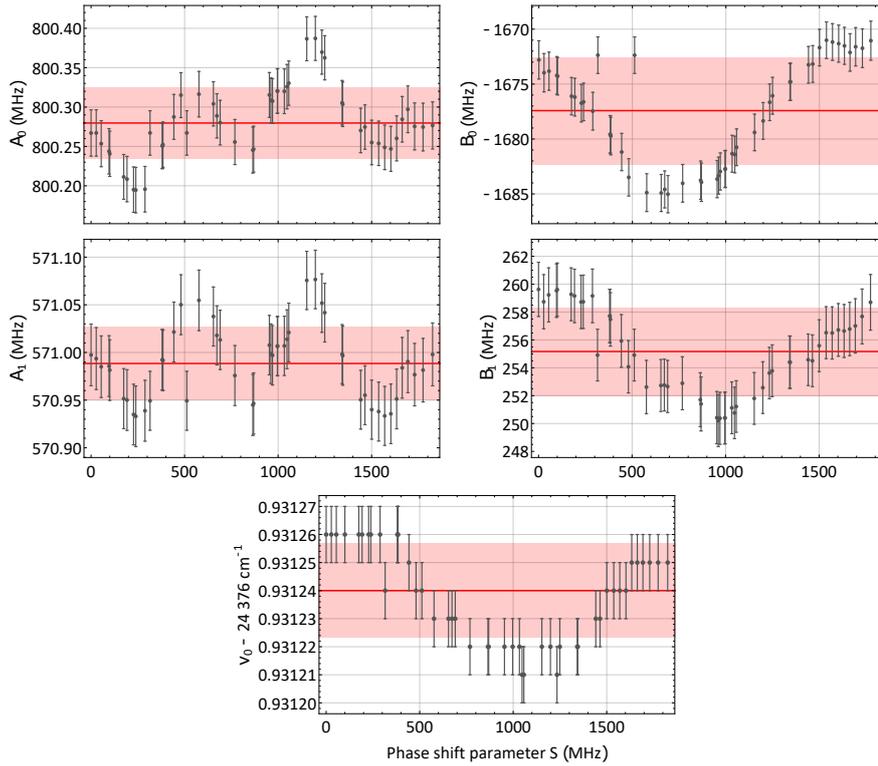
Figure 6.8: Dependence of extracted hyperfine parameters on the phase offset S. Respective mean values and standard deviations are indicated. See text for details.

Table 6.3: Overview of the extracted hyperfine parameters of ^{165}Ho in the first analysis stage, i.e. after treatment of the wavelength meter uncertainty. In respect to the errors derived up this stage, there are significant discrepancies between both modes. The deviation towards the high precision literature data from atomic beam magnetic resonance [118] also points towards additional systematic effects. See text for details.

	Standard PI mode	Int. reflection mode	Literature [118]
ν_0 (cm^{-1})	$24\,376.931\,23(1)$	$24\,376.931\,05(1)$	
A_0 (MHz)	$800.28(5)$	$800.12(5)$	$800.583\,173(36)$
A_1 (MHz)	$570.98(4)$	$570.84(4)$	
B_0 (MHz)	$-1677(5)$	$-1676(7)$	$-1668.078\,70(330)$
B_1 (MHz)	$256(3)$	$264(4)$	

The measurements on ^{165}Ho additionally offer the opportunity to compare these results to extremely precise values obtained by the atomic beam magnetic resonance method [118], exhibiting superior relative uncertainties in the 10^{-8} and 10^{-6} range for the ground state A_0 and B_0 parameter, respectively. Thus, possible additional systematic effects not treated yet can be identified and discussed. Significant deviations in the order of up to five times the error margins are indeed clearly evident for the two operation modes. On top, the even more severe systematic deviations towards the literature data points to additional effects.

A direct explanation is given for the discrepancy in the transition center ν_0: The scans in both operation modes were performed in the same way and after calibration of the wavelength meter to the helium-neon laser described in sec. 3.2.2. Taking into account its certified stability of ± 2.5 MHz and the 1-σ-uncertainty of the WSU 30 wavelength

meter of 10 MHz, already an error on absolute wavelength measurements in the order of $0.0003\,\mathrm{cm}^{-1}$ can be derived. As frequency-doubled light is used, the doubled value must be applied. This leads to good agreement of the two center frequency values.

The underestimation of the hyperfine structure value errors can be retraced if the resulting influence on the whole structure is taken into account. The derived errors of A_0 and A_1 are in the order of a relative uncertainty of 6 to $7 \cdot 10^{-5}$. Scaling these values over the whole hyperfine level structure with an absolute size of 45 GHz in the ground state and 32 GHz in the upper state (see fig. 6.3) result in an absolute shift of the outer levels of only 2 to 3 MHz. The inner levels correspondingly exhibit an even smaller shift, and are also stronger weighted by the fit because of their higher count rate. The given uncertainty in frequency acquisition, on top of the discussed triangle-like modulation with a peak-to-peak amplitude of 5 MHz, is also effected by the frequency jitter of the diode master laser in the order of 3 to 5 MHz. As the transition under investigation uses frequency-doubled light might occur up twice this size. Even though these effects in part are averaged out by the binning procedure, yet at least a complete bin width of 10 MHz must be assumed as realistic total error over the whole resulting resonance structure of roughly 22 GHz (see fig. 6.6). Scaling the resulting relative uncertainty back to the A parameters, and combining it with the previously determined error from the fitting procedure, yields refined error values of 0.4 MHz for the ground state and 0.3 MHz for the upper state. The B parameters already exhibit more conservative errors as they depend less strongly on small deviations in the spectral data.

Final Results

With these considerations a final result can be extracted from the two spectra recorded on ^{165}Ho in both PI-List operation modes. A correspondingly altered compilation is given in tab. 6.4.

Table 6.4: Overview of the final result for hyperfine structure values for ^{165}Ho with errors including all investigated effects. The data is consistent between both operation modes, and supported by the high precision values from [118].

	Standard PI mode	Int. reflection mode	Literature [118]
ν_0 (cm^{-1})	24 376.9312(6)	24 376.9311(6)	
A_0 (MHz)	800.3(4)	800.1(4)	800.583 173(36)
A_1 (MHz)	571.0(3)	570.8(3)	
B_0 (MHz)	−1677(5)	−1676(7)	−1668.078 70(330)
B_1 (MHz)	256(3)	264(4)	

The consistency between both operation modes and towards the high precision literature value of [118] confirm the adequateness of the data handling and error allocation process described above. As such, not only hyperfine parameters could be derived for a previously unknown atomic state, but also a realistic scope for error treatment with the PI-LIST and data acquisition technique was developed. This will be applied in the evaluation on radioactive isotopes presented in the sections below. On top, it can be stated that the first-time implementation of the operation mode with internal reflection works as reliable as the mode with lateral laser-incoupling.

The relative uncertainties in the A values are smaller than 1 % and as such appropriate for the determination of unknown magnetic moments via eq. 2.19, where the precision is usually limited at about 1 % by the hyperfine structure anomaly.

6.2.2   Hyperfine Structure Investigations - ^{163}Ho

The sample of the long-lived, radioactive ^{163}Ho were prepared from the stock of the ECHo project at the Institute of Nuclear Chemistry, also at Mainz University. It was treated in the same way as described above on ^{165}Ho and placed in the centrally closed version of the atomizer, plugged with a second zirconium foil. The information provided by the institute specified the composition as $1.7 \cdot 10^{14}$ atoms of ^{163}Ho (817 Bq) and additionally $3.5 \cdot 10^{15}$ atoms of stable ^{165}Ho.

The hyperfine structure of ^{163}Ho is very similar to that of ^{165}Ho. Both isotopes have a nuclear spin of $I = 7/2$. The ground state hyperfine parameters as measured in [114] are also equal to roughly 1 %. As the ratio between the parameters in the lower and upper state remains constant (except for hyperfine anomalies) as well, also the upper state structure is similar and as such no big deviation from the ^{165}Ho resonance pattern is expected. The transition scheme of fig. 6.3 can thus also be used as coarse overview. The total span of the ground state levels changes to 45.5 GHz, that of the upper state to 32.2 GHz.

The recorded spectra are presented in fig. 6.9 for both PI-LIST operation modes. This time, the data was not taken directly in consecutive scans, but on different days and with slightly different settings. The scans were performed at a line heating current of 120 A (90 W power delivery from the supply) for standard PI-LIST mode, and 131.5 A (110 W) for internal reflection mode. Thus, the first scan is comparable to the ones in ^{165}Ho, the latter one exhibits a slightly higher oven temperature. Compared to [84], the resulting temperature should still be well below 1200 °C at the hottest point.

The delay between the spectroscopy laser pulse and the subsequent ionization pulses was also chosen as 80 ns for full temporal separation. Standard PI-LIST mode was operated as in the ^{165}Ho case on full available power of 70 mW measured before the cylindrical telescope at the in-coupling stage. For the internal reflection mode, the laser was attenuated to 0.2 mW before entering the separator.

Data analysis is performed in the same way as described for ^{165}Ho in the section 6.2.1. The originally recorded data is processed with the triangle-pattern for handling the wavelength meter inaccuracy. The errors on the final parameters are scaled to the overall width of the structure. Final values are given in tab. 6.5 with a comparison to the results obtained in [114]. Also here, the hyperfine parameter data is consistent between both operation modes with overlapping error margins, and improves the uncertainty from the literature values also obtained by resonance ionization laser spectroscopy by almost 2 orders of magnitude.

Table 6.5: Overview of the final results for hyperfine structure values for ^{163}Ho with errors including all investigated effects. The hyperfine parameter data is consistent between both operation modes with overlapping error margins, and improves the uncertainty from the measurements of [114] by almost 2 orders of magnitude.

	Standard PI mode	Int. reflection mode	Literature [114]
ν_0 (cm^{-1})	24 376.9392(6)	24 376.9402(6)	
A_0 (MHz)	809.1(4)	808.3(4)	812(8)
A_1 (MHz)	577.2(3)	576.6(3)	
B_0 (MHz)	−1642(5)	−1637(5)	−1726(320)
B_1 (MHz)	255(3)	261(3)	
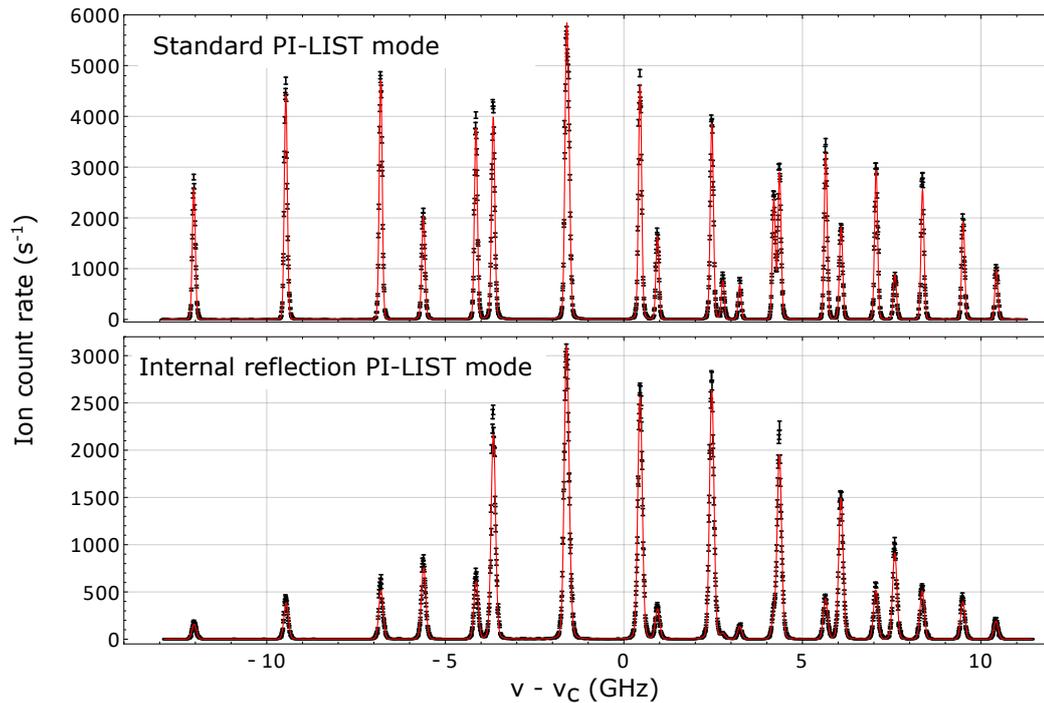
Figure 6.9: Full scans of the 1st step hyperfine structure of ^{163}Ho both in standard PI-LIST and internal reflection mode, relative to the transition's center frequency of $24\,376.9312(6)\,\mathrm{cm}^{-1}$.

A comparison of individual line widths and their composition from Lorentzian and Gaussian fraction was also done for these spectra, analogous to the investigation on ^{165}Ho. The results are compiled in tab. 6.6.

Table 6.6: Average FWHM of the resonances in the ^{163}Ho spectra in fig. 6.9 for both PI LIST operation modes. See text for details.

	FWHM (MHz)		
	Voigt	Lorentzian	Gaussian
Standard PI mode	102(1)	8(1)	97(1)
Internal reflection mode	146(1)	15(1)	138(1)

Here, the result regarding relative contributions within the Voigt profile is essentially the same as already discussed on ^{165}Ho and presented in tab. 6.1. A difference is apparent in the case of internal reflection, where the line width (mostly stemming from the Gaussian fraction) is almost 50 % higher. Besides the already discussed reasons lying in the perpendicular laser beam alignment and atomic beam cone coverage, at this occasion also the slightly higher oven temperature in internal reflection mode leads to a higher Doppler broadening.

6.2.3 Hyperfine Structure Investigations - $^{166\mathrm{m}}$Ho

The most relevant and at the same time most challenging experiment was performed on the long-lived radioactive $^{166\mathrm{m}}$Ho isomer. It is also present in the initial holmium stock of the ECHo project, being the actual reason why an isotopic purification of the sample before implantation into the micro calorimeters is needed in the first place. As such, its availability not only enables the first-time laser spectroscopic experiment on this isotope

and respective extraction of nuclear ground state properties. Profound knowledge of the hyperfine structure pattern can possibly also directly be transferred into potential enhancement in the isotopic purification process.

From an experimental point of view, the major challenge is the highly dense spectrum of the transition. A nuclear spin of $I = 7$ couples with the angular momenta of $J = 15/2$ of the ground and excited states to 15 sub-levels each, spanning from $F = 1/2$ to $F = 29/2$. Besides the outermost levels of the ground state, which exhibit two allowed transitions each, all sub-levels are connected by three respective resonances into the upper state. This altogether gives rise to 43 peaks in the spectrum. An attempt on visualizing this situation is done in fig. 6.10.
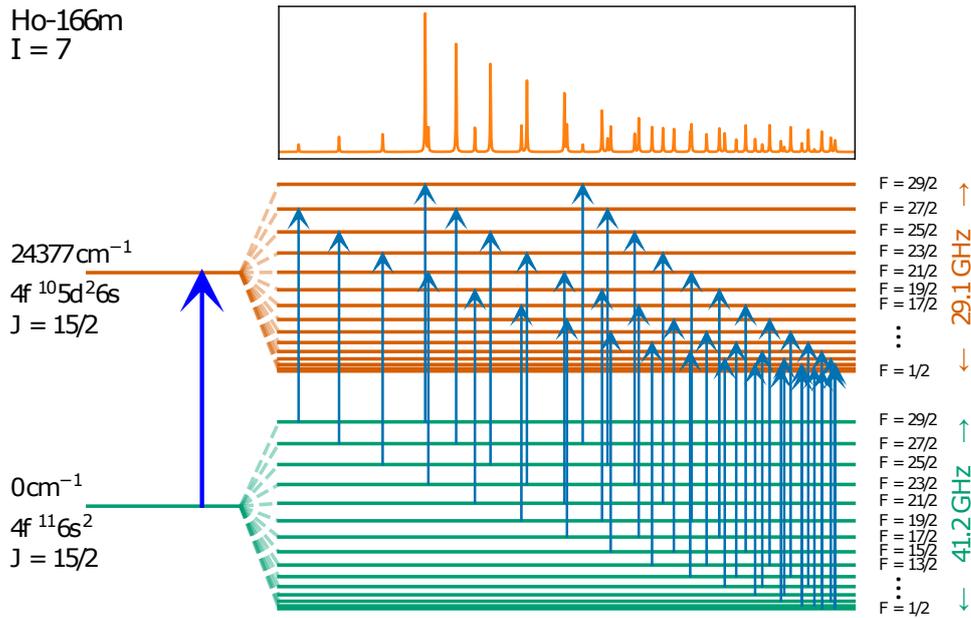
Figure 6.10: Schematic overview of the ^{166m}Ho hyperfine structure pattern in the transition under investigation in laser scheme A. Altogether 43 resonances are present.

The sample provided by the Insitute for Nuclear Chemistry was specified as $1.8 \cdot 10^{13}$ atoms of ^{166m}Ho (329 Bq), and additionally $3.2 \cdot 10^{15}$ atoms of stable ^{165}Ho deposited on a zirconium foil. The sample placed was inserted into the same oven as before, and was again plugged with a second folded zirconium foil to prevent direct laser irradiation of the enclosed sample material.

The operation parameters of the source for these scans were a heating current as low as 85 A (62 W) for standard PI-LIST mode, but 148 A (151 W) in the internal reflection case. The scans were taken on different occasions, every time with a new sample as described above. In between, the separator was in use for different other projects, so that the LIST setup was essentially completely de-installed and re-commissioned several times. Laser pulse delay and lasers powers were kept at the respective values as found on the experiments on holmium before, being 80 ns pulse delay and 70 mW for the external incoupling at the cylindrical telescope, and 0.8 mW in the internal reflection case before entering the separator vessel.

The measurement on ^{166m}Ho was additionally complicated by the presence of a strong surplus of stable ^{165}Ho. As shown in fig. 6.11, which was taken with broad band lasers in all excitation steps and thus ionizing all holmium isotopes in the same way, the high mass tailing of the ^{165}Ho mass peak overlaps with the isotope to be investigated

on nominal mass 166 u, as the mass resolving power of the separator is not sufficient to completely suppress this admixture. A detailed investigation on mass resolving behavior in different operation modes is found in section 5.2.2.
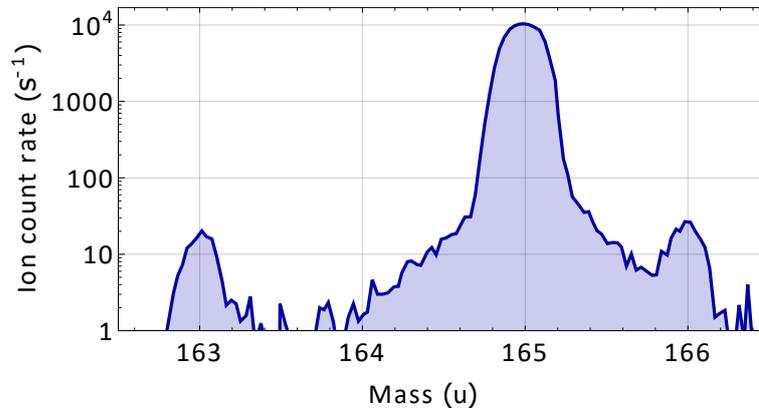
Figure 6.11: Mass scan of the holmium region with broad band lasers in all steps on the ^{166m}Ho sample. The resolution of the mass separator is not sufficient to completely suppress the surplus of ^{165}Ho at nominal mass 166 u.

Consequently, also the hyperfine structure pattern of the transition in ^{165}Ho appears in the recorded spectrum of ^{166m}Ho, adding its 22 resonances. The resulting experimental spectra in both PI-LIST operation modes are shown in fig. 6.12, with the respective fitting functions for both isotopes.

Data handling to implement both functions was done in a stepwise approach. At first, all data points around the known positions of the ^{165}Ho resonances in a range of ± 180 MHz were omitted and solely a function describing the ^{166m}Ho resonances was applied. This method allowed a first approach to the parameters. With these initial values the detailed approach of using the sum of two hyperfine structure functions was implemented. For the ^{165}Ho part, the ground state hyperfine parameter $A_{0,165}$ and $B_{0,165}$ were fixed to the precisely known literature values from [118]. The respective Lorentzian widths of each peak were taken from the fitting results of the sole ^{165}Ho scan presented in sec. 6.2.1 and also kept fixed. Thus, the parameters kept free for the fitting routine in ^{165}Ho were the individual peak amplitudes (initiated with the ones from the sole ^{165}Ho scan), both upper state hyperfine parameters $A_{1,165}$ and $B_{1,165}$ (which serve as consistency check), and a frequency offset towards the transition center frequency of ^{166m}Ho. The Gaussian fraction of the line width was one single parameter shared by all resonances of both isotopes. For the ^{166m}Ho function, all parameters were kept free, initiated with the ones from the treatment with deleted data around the ^{165}Ho resonances as described above. Although the immense number of 118 free parameters might at first glance suggest arbitrariness of the results, one has to remind that the peak positions are still determined by only five parameters (center frequency plus two hyperfine parameters each for lower and upper state) for ^{166m}Ho and three (frequency offset and hyperfine parameters of the upper state) for ^{165}Ho, which are already widely overdetermined by the visibly well-resolved resonances. Thus, possible impracticalities of the fitting routine to assign individual amplitudes and widths for overlapping peaks only have negligible influence on the determination of the nuclear parameters.

A compilation of the results together with the ones from the ^{165}Ho admixtures to check for consistency, is given in tab. 6.7. The same data handling and error allocation procedure as described excessively in sec. 6.2.1 for ^{165}Ho was applied. The error scaling procedure on the A parameters in respect to the 16 GHz wide ^{166m}Ho transition structure
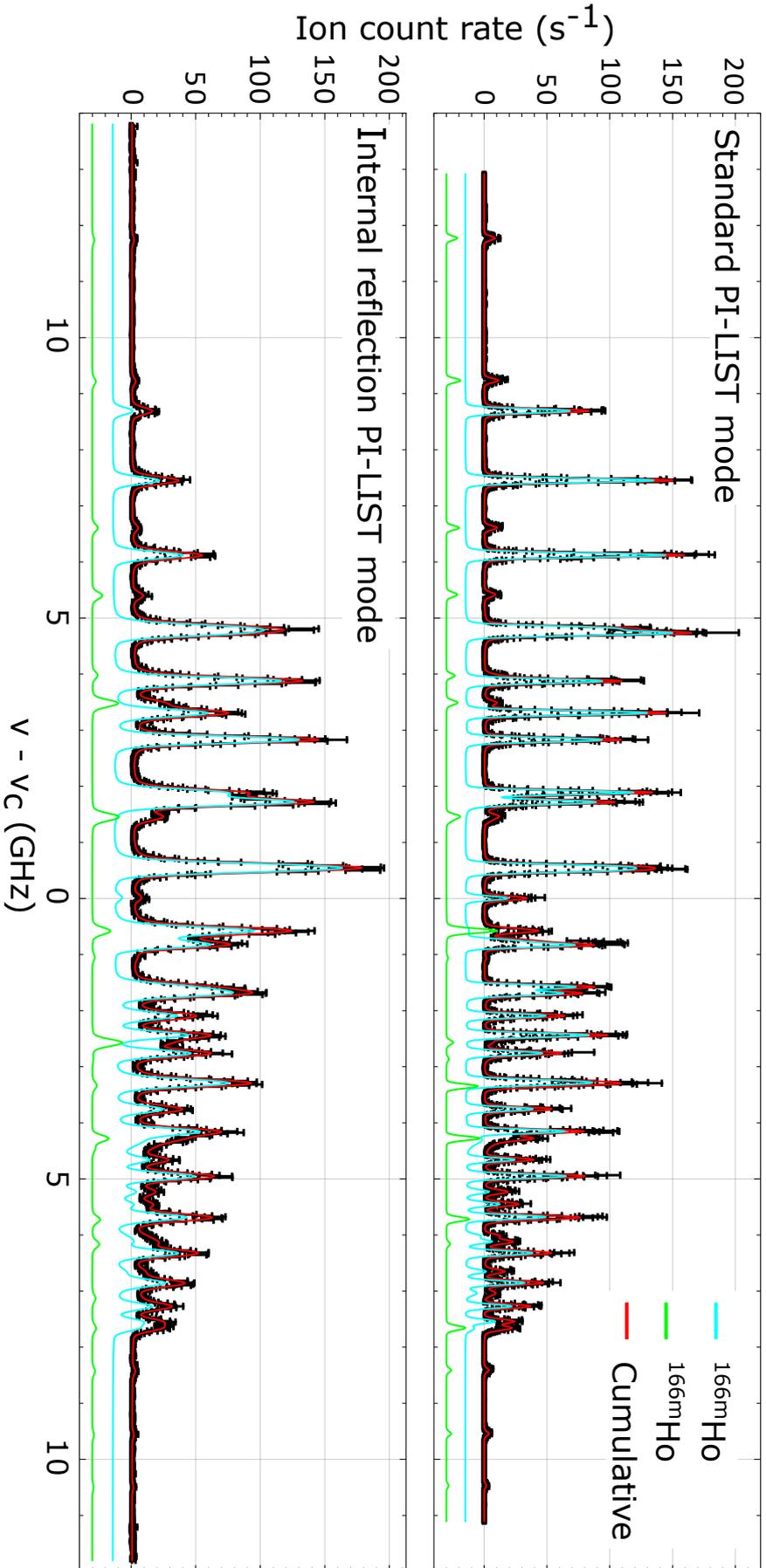
Figure 6.12: Full scans of the first step hyperfine structure of ^{166m}Ho both in standard PI-LIST and internal reflection mode, relative to the transition's center frequency of $24\,376.9281(6)$ cm^{-1}. The spectra are fitted with the sum of a function for the known structure for ^{165}Ho and a function comprising the 43 resonances of ^{166m}Ho. An artificial offset is added to the individual isotope functions for better visibility. For details see text.

produces error values of 0.2 MHz, typical values given by the fitting routine are roughly 0.1 MHz. The final error is combined from these by Gaussian error propagation.

Table 6.7: Overview of the final result for hyperfine structure values for ^{166m}Ho with errors including all investigated effects. The values extracted from the ^{165}Ho (where the ground state parameters were fixed to the literature values from [118] in the fit) admixture are given in comparison to the results from the sole ^{165}Ho. $\Delta\nu_{166m,165} = \nu_{0,165}$ - $\nu_{0,166m}$ is the difference between each isotope's transition center directly taken from the fit. For details see text.

	Standard PI mode	Int. Reflection mode	^{165}Ho fit (tab. 6.4)
ν_0 (cm-1)	24 376.9281(6)	24 376.9274(6)	
A_0 (MHz)	366.1(2)	366.3(2)	
A_1 (MHz)	260.9(2)	261.1(2)	
B_0 (MHz)	−2373(9)	−2398(9)	
B_1 (MHz)	421(9)	390(9)	
$\Delta\nu_{166m,165}$ (MHz)	130(2)	142(3)	
$A_{0,165}$ (MHz)	800.583 (fixed to [118])		800.2(5)
$B_{0,165}$ (MHz)	-1668 (fixed to [118])		−1677(6)
$A_{1,165}$ (MHz)	571.1(3)	571.2(3)	570.9(3)
$B_{1,165}$ (MHz)	239(6)	243(8)	260(4)

The ^{166m}Ho center and A parameter results are consistent between both operation modes. The B parameters already require three error margins to be conform. As no systematic effects have been observed in the other experiments between the two modes, this discrepancy is ascribed to the more dense spectrum with at the same time lower counting statistics. Individual peaks with a high dependency on the B parameters might be mistreated by the fitting routine if they overlap with other resonances. A similar conclusion can be drawn from the comparison between the upper level parameters derived from the ^{165}Ho admixture. The A factor perfectly agrees to the one extracted from the sole ^{165}Ho spectrum, while the B parameter significantly differs. In this case, also an additional systematic effect from the wavelength meter readout inaccuracy has to be taken account. Fixing of the ground state parameters only leaves the upper ones free to react to the triangle modulation and set a certain, non-statistical bias. The influence of setting $B_0 = -1668$ MHz can be retraced to force a higher absolute value in fig.6.8. The error treating procedure thus underestimates the values severely.

The resonance's line widths and their respective constituents have also been investigated for this case. The results are shown in tab. 6.8. As explained in the section on ^{165}Ho, the average value for the Lorentzian part has been computed by weighting the individual peak widths with their errors. Thus, overlapping peaks, where the fitting procedure allocates a big uncertainty, are essentially not contributing and the value is dominantly determined by the isolated resonances with clear profiles.

Table 6.8: Average FWHM widths of the resonances in the ^{166m}Ho spectra in fig. 6.12 for both PI LIST operation modes. See text for details.

	FWHM (MHz)		
	Voigt	Lorentzian	Gaussian
Standard PI mode	95(2)	11(1)	89(1)
Internal reflection mode	157(4)	40(1)	135(2)

The pattern in standard PI-LIST mode exhibits the most narrow line width of all investigated scans. This can be attributed to the exceptionally low oven temperature. In contrast, in internal reflection mode and the highest used heating current for the oven, the overall line width is also the widest of all scans. Interestingly, the procedure also yields an unusually high Lorentzian fraction. As power broadening effects should not play a more important role as in the other isotope cases, a different explanation can be found in the data quality. The recorded scan exhibits the lowest signal-to-noise ratio and a background rate of roughly 1 count per second, in contrast to essentially 0 in the other cases. This is also due to the higher oven temperature, which causes in general more surface ionization of contaminants in the hot cavity. A small fraction of these are not suppressed by the LIST repeller configuration. Additionally, the repeller electrodes themselves can heat up slightly by the increased heat radiation and evaporate minute amounts of contamination themselves. Although this background signal rate is principally covered by a constant offset in the fitting function, the routine tends to allocate longer tailings to the peaks and thus a more Lorentzian-like shape.

6.2.4   The PI-LIST for High Resolution Spectroscopy on Holmium - Conclusion

The experiments and data analyses presented above impressively prove the PI-LIST ion source as a powerful tool to perform hyperfine structure spectroscopy in complex atomic spectra. Holmium with its high nuclear spins and angular momenta of accessible states is an excellent case to underline the necessity of techniques to overcome the Doppler broadening limitations in hot atomic vapors. In combination with the availability of samples in the framework of the ECHo project, it enabled the first ever laser spectroscopic hyperfine structure investigation on ^{166m}Ho.

The adaption of the standard PI-LIST technique into a compact, standalone device featuring the internal perpendicular laser reflection, also proved its applicability. Whereas its limits in resolution and overall efficiency are explored in chapter 5, the holmium experiments verify the principle equivalence of both operation modes. The relative efficiency, depicted in resulting signal rate, was shown to be equal within a maximum factor of 4.5. In direct comparison, optimized on best possible resolution under identical experimental conditions, the internal reflection mode exhibits a slightly broader line shape by less than 20% . With higher oven temperature in the internal mode, this factor could rise to 50% at maximum due to the higher residual Doppler broadening.

With both modes, the hyperfine structure parameters of the ground and excited state could be determined in a straight forward way. Whereas center frequencies and A parameters were measured completely consistent in both modes as well as against literature within the allocated errors, the data analysis routines seem to slightly underestimate the errors on the B parameters in some cases. With the scope to finally extract fundamental nuclear properties from the measured hyperfine structure constants of the states under investigation, a comprehensive data compilation for each isotope is given in tab. 6.9.

The presented numbers are calculated as mean values from both operation modes, weighted by the inverse quadratic error. The final uncertainty is assigned via propagation of the weighted mean error and the minimum individual error. For the ^{165}Ho upper state parameter, also the values derived from the cumulative fit in the ^{166m}Ho case are used. In this case, also the directly extracted isotope shift is shown in comparison to the one calculated from the different transition center frequencies in respect to ^{165}Ho. The ratio of the A values is constant within the error margins, indicating no significant presence

Table 6.9: Compilation of extracted parameters for all investigated holmium isotopes on laser scheme A. These final results are derived as weighted mean values from both PI-LIST operation modes. See text for details.

Isotope	Parameter	This work	Literature
^{163}Ho	ν_0 (cm^{-1})	24376.9397(9)	
	$\Delta\nu_{165}$ (MHz)	-256(33)	
	A_0 (MHz)	808.7(5)	812(8) [114]
	A_1 (MHz)	576.9(4)	
	B_0 (MHz)	-1640(6)	-1726(320) [114]
	B_1 (MHz)	258(4)	
	A_1/A_0	0.7134(8)	
	B_1/B_0	-0.157(2)	
^{165}Ho	ν_0 (cm^{-1})	24376.9312(6)	
	A_0 (MHz)	800.2(5)	800.583173(36) [118]
	A_1 (MHz)	571.0(4)	
	B_0 (MHz)	-1677(6)	-1668.0787(330) [118]
	B_1 (MHz)	255(4)	
	A_1/A_0	0.7136(6)	
	B_1/B_0	-0.152(2)	
^{166m}Ho	ν_0 (cm^{-1})	24376.9278(8)	
	$\Delta\nu_{165}$ (MHz)	102(30)	
	$\Delta\nu_{165,\text{fit}}$ (MHz)	136(9)	
	A_0 (MHz)	366.2(2)	
	A_1 (MHz)	261.0(2)	
	B_0 (MHz)	-2386(11)	
	B_1 (MHz)	406(11)	
	A_1/A_0	0.7127(8)	
	B_1/B_0	-0.170(5)	

of hyperfine anomalies. The ratio of the B factors deviates in the case of ^{166m}Ho, which is ascribed to the discussed underestimated uncertainties and systematic effects implied by the wavelength meter readout correction procedure. If the individual errors of the B parameters are scaled with a factor of 3, agreement of the ratios in their error margins can also be established.

6.2.5 Extraction of Nuclear Parameters

As described in sec. 2.1.2, the hyperfine structure of atomic levels is directly linked to the interaction of the electronic shell with the nucleus. A direct calculation of the nuclear ground state properties, namely the nuclear magnetic dipole moment and the electric quadrupole moment, as well as the change in nuclear size indicated in the isotope shift, requires theoretical input based on various models and powerful calculation algorithms. In contrast, the model-independence of deriving these properties from a known, independently measured reference isotope onto unknown ones can act as a benchmark for these theories. In the case of holmium, where high precision data is available for the stable ^{165}Ho isotope, especially expansion towards ^{166m}Ho is of high

interest, as no hyperfine structure parameters were available for direct comparison up to this experiment.

The most direct determination of a nuclear parameter addresses the nuclear spin of ^{166m}Ho. The value of $I = 7$ is only given in brackets in the most recent compendium by Stone et al. [116], indicating uncertainty in its assignment. This might be traced back to the work of Postma et al. [128] on anisotropies and linear polarization of γ-radiation from ^{166m}Ho oriented in Nd-ethyl-sulphate, where they refrain from a clear assignment. Yet, in the compilation by Baglin [117] the spin is already determined to $I = 7$. This value is confirmed by the investigation presented in this thesis. Fitting routines using any different suggested value between 6 and 9 are not able to reproduce the recorded pattern.

The Nuclear Magnetic Dipole Moment

There are several published values for the nuclear dipole moments of the three holmium isotopes under investigation as compiled in [116]. The most precise is the one given by Dankwort et al. [129] using the direct measurement method of atomic beam magnetic resonance on stable ^{165}Ho with a value of $\mu_I = 4.17(3)$ nuclear moments (n.m.). For the case of ^{166m}Ho, altogether 3 values are listed from different sources. Tab. 6.10 gives a comparison for the data available in literature to the values derived in this work. Here, eq. 2.19 is used with the determined ground state A values from tab. 6.9 and the Dankwort value as reference.

Table 6.10: Overview of derived magnetic dipole moments in comparison to literature data, including a weighted mean value (WMV) of all data available for ^{166m}Ho. For this work, ^{165}Ho was used as reference.
Methods: RIMS = Laser resonance ionization mass spectrometry; ABMR = Atomic beam magnetic resonance measurement; SNO/γ = γ detection in static nuclear orientation.

Isotope	μ_I (n.m.)	Source	Method	Year
^{163}Ho	4.23(4)	[114]	RIMS	1989
	4.21(3)	**This work**		
^{165}Ho	4.17(3)	[129]	ABMR	1974
	3.60(16)	[130]	SNO/γ	1981
	3.65(13)	[27]	SNO/γ	1981
^{166m}Ho	3.60(5)	[131]	SNO/γ	1980
	3.61(4)	WMV		
	3.82(3)	**This work**		

In the case of ^{163}Ho, which was also derived via hyperfine structure laser spectroscopy in [114], the values correspond nicely. For ^{166m}Ho, the result of this work delivers a systematically higher value than the in itself consistent available literature data. Although coincidence with the less precise ones can be almost established taking both error margins into account, this points towards a systematic difference in the evaluation methods.

The values in literature were all obtained by investigations on angular distribution of γ radiation from statically oriented ^{166m}Ho nuclei. Besides the input from the measurement data, this method relies on knowledge of the so-called total magnetic hyperfine field H_e. This quantity is the magnetic field arising from the $4f$ electrons in the lanthanide

electronic shell, averaged over the distribution of nuclear magnetism over the whole nucleus. It can be calculated from experimentally accessible quantities as

$$H_e = \frac{J \cdot A}{7.6228\,g_n} \qquad (6.5)$$

from a state $J_z = J$ with the the total angular momentum J, the hyperfine parameter A and the nuclear g-factor g_n [132]. For determination of the ^{166m}Ho μ_I literature values, $H_e = 717(5)$ T was used. It was derived from a value of $(J \cdot A) = 6497(8)$ MHz for the $J = 8$ ground state of the triply charged ^{165}Ho^{3+} as given in [132], in combination with the calculation of g_n from the μ_I value of ^{165}Ho derived in [129]. As this is the same reference as for the determination in this work, possible systematic deviations only might arise from the value of $(J \cdot A)$. Its relative uncertainty of $\approx 0.1\%$ linearly progresses in the determination of μ_I and is thus not the limiting factor. Yet, a systematic shift in the literature value of $(J \cdot A)$ would apply to all ^{166m}Ho μ_I literature values in the same way, requiring a $\approx 6\%$ deviation to be consistent with the μ_I value derived in this work. Additionally, as already stated in the introduction of [132] and also by the authors of [27], H_e might change across an isotopic chain due to different distribution of the nucleus' magnetism. In the literature evaluations on ^{166m}Ho, a constant H_e was assumed as no additional information was available. Thus, the systematic deviations of all values determined with the method of angular distribution measurements on γ radiation in oriented crystals, might be attributed to this effect.

On the side of the method used in this work, deviations from the linear correlation given in eq. 2.19 can arise from hyperfine anomalies, as described in sec. 2.1.2. As stated there, this effect is most commonly significantly below 1%, and would require to be in the order of 5% to establish consistency to the un-scaled literature results here. Although this can per se not be excluded, the available data shows no evidence. The calculated A_1/A_0 factors on all isotopes are identical within their error margins of around 0.1%, i.e. the investigated states either show no significant anomaly. Nevertheless, a relative error of 1% is additionally allocated to conservatively include this effect.

An error evaluation or definite confirmation based on the excellent agreement to the μ_I value for ^{163}Ho derived in [114] is not applicable, as it utilized the same method of hyperfine structure laser spectroscopy on the nuclear ground state and respective scaling of the μ_I values as this work, implying identical systematic effects.

The Nuclear Electric Quadrupole Moment

A very interesting case is presented in the literature data available for the spectroscopic electric quadrupole moments Q_s. Marshak et al. [27] investigated this property in the same work as on the nuclear magnetic dipole moment, using the angular distribution of γ rays emitted by the Er daughter of ^{166m}Ho, which was embedded in ^{165}Ho single crystals. They determined a value of $Q_s = -3.4(34)$ eb and stated that "although our value for Q has a large uncertainty associated with it, the fact that it favors a negative value is very puzzling!" as well as "[...] from what is known about the systematics of other nuclei in this mass region, we have to view the negative Q value with some skepticism". Indeed, this region is dominated by in many cases highly deformed nuclei exhibiting prolate shapes, i.e. $Q_s > 0$.

A second interesting point is the systematic deviation in results between two different methods of Q_s determination already in the case of stable 165 Ho as listed in the compendium by Stone [116]. Hyperfine structure measurement on mesonic systems produce values which aggregate around roughly 3.5 eb, while complementary investigations using

the atomic beam magnetic resonance (ABMR) technique yield significantly lower values of 2.7 eb.

Table 6.11 lists the available Q_s literature data for the isotopes under investigation. In order to derive results from the determined hyperfine parameters in this work vie eq. 2.20, a reference value has to be selected. The significant deviations between the two principal experimental methods have already been discussed, e.g. in [133], where they are ascribed to strong quadrupole shielding (the so-called Sternheimer effect), probably due to core polarization effects.

Table 6.11: Overview of derived spectroscopic electric quadrupole moments Q_s in comparison with literature data as compiled in [116]. In the case of ^{165}Ho, literature values determined by atomic beam magnetic resonance techniques strongly deviate from those measured in mesonic systems. As discussed in the text, a weighted mean value (WMV) from the mesonic systems data is used as reference for the calculations in this work.
Methods: RIMS = Laser resonance ionization mass spectrometry; Pi-X = Pionic X-ray hyperfine structure (HFS); Ka-X = Kaonic X-ray HFS; Mu-X = Muonic X-ray HFS; ABMR = Atomic beam magnetic resonance; SNO/γ = γ detection in static nuclear orientation.

Isotope	Q_s eb	Source	Method	Year
^{163}Ho	3.6(6)	[114]	RIMS	1989
	3.48(8)	**This work**		
^{165}Ho	3.58(2)	[134]	Pi-X	1983
	2.716(9)	[133]	ABMR	1982
	3.60(2)	[135]	Pi-X	1981
	3.41(8)	[135]	Ka-X	1981
	3.53(8)	[136]	Pi-X	1978
	3.49(3)	[137]	Mu-X	1976
	2.73(6)	[129]	ABMR	1974
	3.56(2)	WMV omitting ABMR data		
^{166m}Ho	-3.4(34)	[27]	SNO/γ	1981
	5.08(13)	**This work**		

A method to resolve this discrepancy and select the most appropriate value is to trace the absolute Q_s values back to the respective intrinsic quadrupole moment Q_0, and compare the results to complementary measurements and theoretical predictions. As described in sec. 2.1.2, Q_0 can directly be calculated by eq. 2.17 from Q_s for the present case of strongly deformed nuclei. Such a study was already performed in [114] in respect to a sharp shape transition in neutron-deficient holmium isotopes between $N = 89$ and 90, or respectively $A = 156$ and 157. Their results, derived from 3.49(3) eb for ^{165}Ho by [137] (from a mesonic system) are shown in fig. 6.13, together with theoretical calculations based on the macroscopic-microscopic approach and from the deformed Hartree-Fock method with SKM' force, directly taken from [114]. It is clearly evident that these results show a strong correspondence to the theoretical descriptions. In contrast, a reference value around $Q_s = 2.7$ eb (as suggested by the ABMR results) would scale down all Q_0 values equally by a factor of about 0.77, significantly and systematically below the theoretic curve. Additionally, a direct experimental value for Q_0 in the case of ^{165}Ho was determined as 7.4(4) eb by the completely complementary method of photodisintegration [138]. Instead of the perfect agreement as shown in

fig. 6.13, e.g. the ABMR Q_s value of 2.73(6) eb as derived in [129] would result in $Q_0 = 5.85(12)$ eb, almost four error margins apart.

Consequently, as both theoretical predictions and a complementary measurement method favor the values derived from mesonic systems, a weighted mean value of these literature values is selected in this work for the final determination of the Q_s values for ^{163}Ho and ^{166m}Ho as listed in tab. 6.11. The corresponding Q_0 values, derived from the same $Q_s = 3.49(3)$ eb reference value as used in [114], are added to fig. 6.13 as $Q_{0,163} = 7.33(17)$ eb and $Q_{0,166m} = 7.46(21)$ eb. They confirm the rather flat and smooth trend at a strongly pronounced prolate deformation level, as described by the theoretical models. The reason for the discrepancy between ABMR and mesonic literature data in the ^{165}Ho case can not be addressed in the scope of this work.
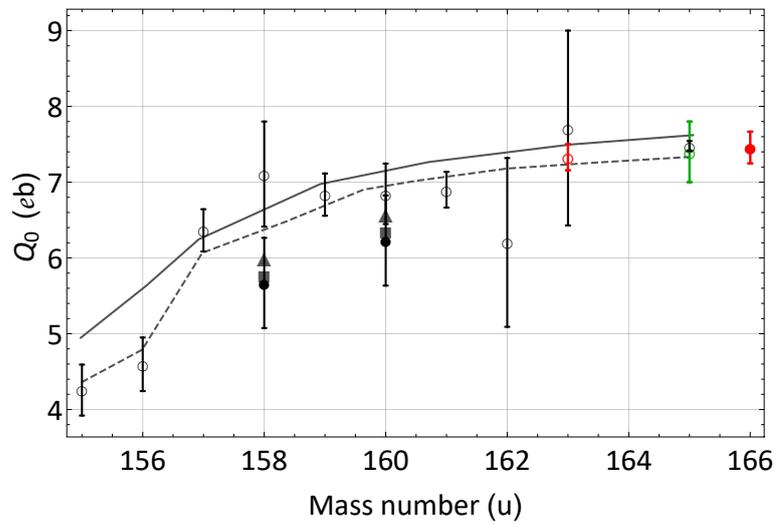
Figure 6.13: Q_0 values in comparison to theoretic models as taken from [114], using the mesonic measurement of $Q_{s,165} = 3.49(3)$ eb [137] as reference. Open circles depict nuclear ground states (gs), filled circles isomeric states (is). The solid line (gs) and triangles (is) show theoretical predictions from the deformed Hartree-Fock method with SkM' force, the dashed line (gs) and crosses (is) for the macroscopic-microscopic approach. The green value indicates a direct Q_0 value measurement by [138]. The red values are derived in this work, using the same $Q_{s,165}$ reference value as [114]. The theoretical descriptions are consistently reproduced and strongly favor the ^{165}Ho Q_s values derived from mesonic experiments against those derived from ABMR, which would appear on 0.77 times lower total values. See text for details.

Calculations of the final Q_s values were done by using both the ratio of the B values of the ground and upper state in each isotope as given in tab. 6.9. To comply with the slight inconsistency in the ratio of these values especially in the ^{166m}Ho case, all individual error values were tripled as described in sec. 6.2.4. The final value is then the weighted mean of from evaluation of both B_0 and B_1 factors. Indeed, regardless of the reference value or the error allocation, no negative value for Q_s of ^{166m}Ho were derived, and the skepticism of Marshak et al. on their result was confirmed. In contrast, the isotope even exhibits the most pronounced prolate shape of the whole known holmium chain. Such an increase in nucleus deformation is expected, as adding more neutrons implies moving further away from the magic neutron number $N = 82$ (^{149}Ho) towards the mid-shell regime.

Isotope Shifts and Changes in Mean Square Charge Radii

A valuable observable of the shape evolution of nuclei along either neutron (isotopes) or proton chains (isotones) to to obtain insight into the underlying nuclear structure is the isotope shift in spectroscopic transitions. A description is given in sec. 2.1.2. Neutron-deficient holmium isotopes down to $A = 152$ were investigated in [114]. Unfortunately, as a different atomic transition was utilized (which lies outside the titanium:sapphire laser spectrum and could therefore not be applied in this work), direct expansion of these results to the first-time measured ^{166m}Ho isotope is not possible. The King plot analysis is not applicable as well, as not enough overlap in measured isotopes is present. Yet, a very crude first glimpse on the change in mean square charge radii $\delta\langle r^2 \rangle$ compared to ^{165}Ho can be derived.

The isotope shift as given in eq. 2.24 essentially consists of two parts: The mass shift and the field shift contribution. While the latter is directly proportional to $\delta\langle r^2 \rangle$, the former again is composed by two constituents. The normal mass shift $\delta\nu_{MS,N}^{A,A'}$ can trivially be calculated as

$$\delta\nu_{MS,N}^{A,A'} = \frac{\nu_0}{1822.9}\frac{A - A'}{A \cdot A'} \tag{6.6}$$

with the transition energy ν_0 and respective mass numbers A and $A' > A$. For the transition under investigation here, $\delta\nu_{MS,N}^{A,165}$ results in $-30\,\text{MHz}$ for the shift towards ^{163}Ho, and $15\,\text{MHz}$ for ^{166m}Ho. No information is available about the specific mass shift $\delta\nu_{MS,S}^{A,A'}$ for this transition. Yet, as stated in [3], it can be seen from the data compiled in [139], that for a closed d-shell as in the case of holmium, the absolute magnitude of the specific mass shift is typically smaller than that of the normal one. For the evaluation presented here, the full magnitude of $\delta\nu_{MS,N}^{A,165}$ has hence been assigned as a conservative uncertainty estimation. Correspondingly, after subtracting $\delta\nu_{MS,N}^{A,165}$ from the respective isotope shifts $\Delta\nu_{165}$, only the linear relation

$$\left(\Delta\nu_{165} - \delta\nu_{MS,N}^{A,165}\right) = F_{\text{FS}}\,\delta\langle r^2 \rangle_{165} \tag{6.7}$$

with the field shift parameter F_{FS} remains.

The results for the isotope shifts $\Delta\nu_{165}$ and the extracted $\delta\langle r^2 \rangle_{165}$ values are shown in tab. 6.12. The $\Delta\nu_{165}$ values are taken from tab. 6.4, while the ^{166m}Ho value is calculated as weighted mean from comparison of the respective transition centers and the direct extraction of the shift from the shared fitting procedure. The ^{163}Ho reference value for $\delta\langle r^2 \rangle_{165} = -0.123(6)\,\text{fs}^2$ is taken from the compendium of [140], where a higher moment correction according to [141] was applied on the value derived in [114].

Table 6.12: Overview on isotope shifts of the investigated transition and extracted approximation of $\delta\langle r^2 \rangle$ for ^{166m}Ho from the reference value of $\delta\langle r^2 \rangle_{163,165}$ given in [140]. See text for details.

Isotope	$\Delta\nu_{165}$ (MHz)	$\delta\langle r^2 \rangle_{165}$ (fm^2)
^{163}Ho	-256(30)	-0.123(6)
^{165}Ho	0	0
^{166m}Ho	133(12)	0.061(16)

The full picture of changes in mean square charge radii, including the value derived in this work for ^{166m}, are compiled in fig. 6.14. For sure this result can only be a first approximation. The relative uncertainty is more than a factor of 3 larger than for the

data from [114], and systematic effects could not be investigated with the scarce data available. On top, it is difficult to compare to the existing data, as it concerns a nuclear isomeric instead of a ground state. As such, derivation of nuclear structure information is not attempted in this work. Nevertheless, it is the first-time measurement on $\delta\langle r^2\rangle$ for ^{166m}Ho and serves as a milestone towards further investigations.
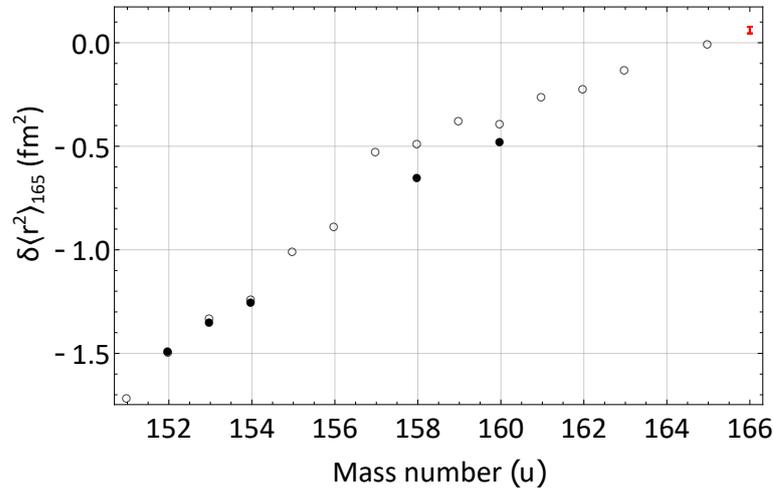
Figure 6.14: Changes in mean square charge radii in respect to ^{165}Ho, as taken from [140] and initially measured by [114]. Open circles indicate nuclear ground states, full circles indicate isomers. Error bars are too small to be visible. The red value shows the ^{166m}Ho isomer value derived in this work.

6.3 Transition to the $4f^{10}(^4I^o_{15/2})6s6p(^1P^o_1)$ State

The transition in the previous section was chosen with the scope of best possible spectral resolution. In particular, its long lifetime and thus possibility of relative laser pulse delay without forfeiting the majority of ion signal rate was utilized. Yet, as already summed up in sec. 6.1, a laser scheme with a different (short-lived) first excited state has been identified to be highly efficient and reliable for laser ionization in the ECHo project. The two schemes are compared in fig. 6.1. In order to check for consistency of the results from section 6.2 and to explore opportunities of additional purification by differences in hyperfine structure patterns for the different isotopes, also the first-step transition of scheme B was investigated with high resolution.

6.3.1 Hyperfine Structure Spectroscopy of ^{165}Ho and ^{166m}Ho

The hyperfine structure patterns of the first step in laser scheme B are depicted in fig. 6.15. Only the two isotopes ^{165}Ho and ^{166m}Ho were investigated and compared. The spectra's complexity is comparable to the situation in scheme A, as the total angular momentum of the respective upper state is the same, $J = 15/2$. As such, also here 22 (^{165}Ho) and 43 (^{166m}Ho) resonances are present. Yet, the overall span of the whole spectrum is smaller.

The scans for the two isotopes are shown in fig. 6.16. ^{165}Ho was measured in the PI-LIST configuration with internal reflection at the beginning of the campaign, with an oven heating current of 137 A (170 W power delivery from the supply). As the lifetime of the state is in the order of the pulse duration of the lasers, only 40 ns of delay between
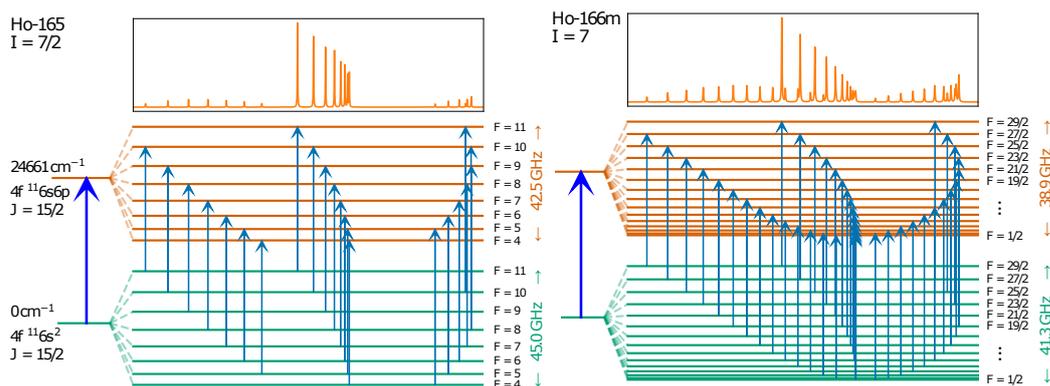
Figure 6.15: Schematic overview of the ^{165}Ho and ^{166m}Ho hyperfine structure pattern in the first step transition of laser scheme B as depicted in fig. 6.1.

the first and subsequent step pulses was chosen to still retain sufficient signal rate. Laser power of only 0.08 mW was used in order to avoid saturation of this strong transition. The resulting overall Voigt profile FHWM in the regime above 200 MHz reflects these compromises compared to scheme A. Nevertheless, the resolution was still sufficient to perform a fitting procedure with unambiguous results.

The case of ^{166m}Ho is more complex. The spectrum was recorded in standard PI-LIST mode with the remaining sample on the last day of the campaign, after quickly switching the ECDL master laser system back from scheme A to scheme B. Unfortunately, this non-optimized setup resulted in a higher jitter of the stabilization. Additionally, the oven temperature also had to be increased more to utilize the exhausting sample. A heating current of 170 A (200 W) was applied. In this case, a longer pulse delay of 70 ns was chosen, and the full available laser power was coupled into the cylindrical telescope before the vacuum vessel. The spectrum shown in the bottom panel of fig. 6.16 exhibits a Gaussian FWHM of more than 300 MHz, and correspondingly, the Lorentzian fraction could not be deduced unambiguously. Obviously also the admixture of ^{165}Ho, which was already described in sec. 6.2.3, plays an even more important part here, as it even exceeds the signal rate on ^{166m}Ho. Under these circumstances, only a small fraction of the whole scanning range can be clearly attributed to ^{166m}Ho.

The fitting procedure was adapted to this situation in order to gain as much as possible information from the ^{166m}Ho fraction. The hyperfine parameters of ^{165}Ho were fixed to the precise literature values in the ground state and those derived from the sole ^{165}Ho investigation, as well as the ratio of the B parameters. The ground state parameters of ^{166m}Ho were also fixed to the results in tab. 6.9. The remaining free parameters were the A_1 factor of the upper state, and the center frequency of the whole structure. An initially also implemented isotope shift fitting parameter could not be determined by the fitting routine.

All parameters extracted from these scans are compiled in tab. 6.13. No wavelength meter readout correction procedures have been applied due to the broader peak structures with inherently less precision. The absolute center frequency of the transition ν_0 is calculated as weighted mean from both scans. For ^{165}Ho, the full set of hyperfine structure parameters could be extracted. The ground state A value shows no, and the B value the already discussed slight deviation from the results derived in tab. 6.9 and towards literature, implying consistence in the experiments and data analyses. The only determinable value from the ^{166m}Ho data also is in perfect agreement with the expectations of constant A_1/A_0 ratio values across an isotopic chain. An isotope shift
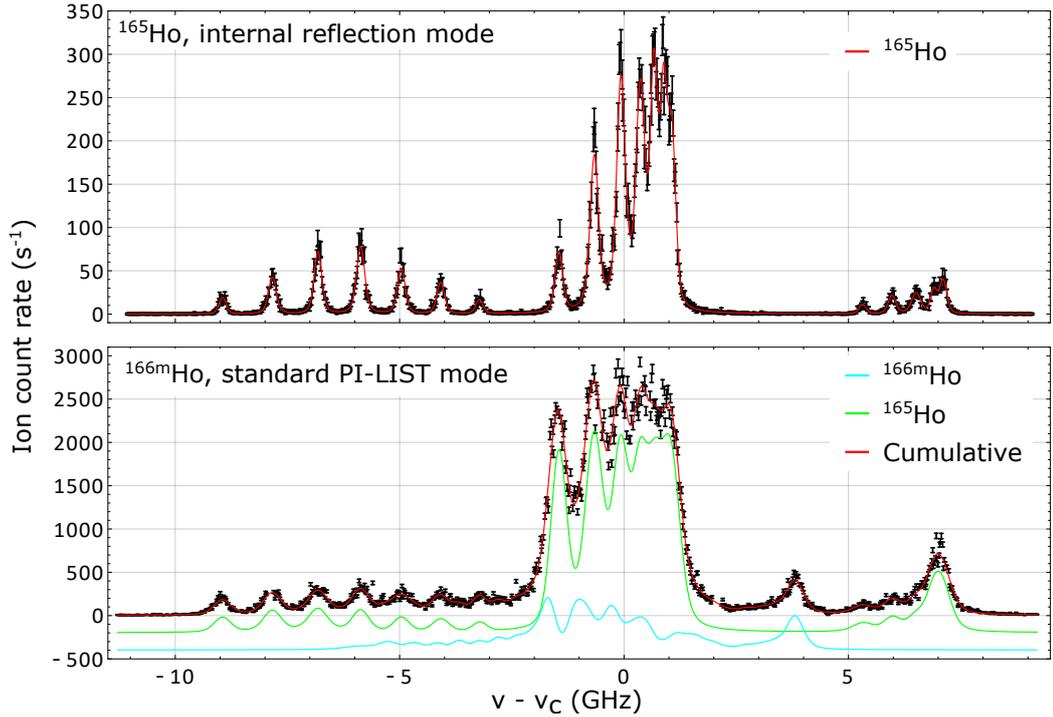
Figure 6.16: Recorded hyperfine structure patterns for ^{165}Ho and ^{166m}Ho in indicated operation mode on the "ECHo-transition" of laser scheme B in respect to the ^{165}Ho center frequency $\nu_0 = 24\,660.7846(8)\,\mathrm{cm}^{-1}$. In the lower panel, the individual fit functions for both isotopes are shown with an artificial offset for better visibility. Although most of the ^{166m}Ho pattern is superimposed by interfering ^{165}Ho admixture, the structure between 2 and 5 GHz is reproduced. See text for details.

could not be extracted, but is therefore expected to not be larger than the one derived for the transition in scheme A.

In fact, with the constant ratios of A and B factors, the full set of parameters for ^{165}Ho already enables a transfer towards the hyperfine structure patterns for different isotopes on this specific transition. Implications on additional purification prospects using the highly efficient standard in-source (instead of high resolution PI-LIST) technique are presented in the next section.

6.3.2 Implications for Purification within the ECHo Project

Valuable information can be drawn from the hyperfine structure investigations regarding the exploitation of differences in the patterns along an isotopic chain in respect to wavelength-dependent selective ionization. The ECHo project depends on as pure as possible ^{163}Ho samples implanted into the micro-calorimeters, as interfering radiation sources would disturb the energetic decay spectrum. In its current state, the combination of chemical purification and electromagnetic separation at the RISIKO separator already reaches a relative ^{166m}Ho fraction of as low as $4(2) \cdot 10^{-9}$ [67], which is very close to the design goal of $1 \cdot 10^{-9}$. While the electromagnetic separation will also profit from improvements at RISIKO e.g. by the beam gating technique against heavy mass cross contamination (sec. A.2.2), also the investigated schemes might contain so far unused opportunities.

For production of the requested number of detectors and utilization of the available stock, efficiency is as important as purity for the ECHo project. Therefore, the standard

Table 6.13: Overview of hyperfine structure parameters derived from the investigations on the "ECHo scheme" B. The ^{165}Ho results provide all information needed for transfer to other isotopes and are consistent with the scarce data extracted from ^{166m}Ho.

Isotope	Parameter	Value
^{165}Ho	ν_0 (cm^{-1})	24660.7846(8)
	A_0 (MHz)	800.4(5)
	A_1 (MHz)	743.4(5)
	B_0 (MHz)	-1656(10)
	B_1 (MHz)	-2518(10)
	A_1/A_0	0.9413(8)
	B_1/B_0	1.52(1)
^{166m}Ho	A_0 (MHz)	366.2 (fixed to result in tab. 6.9)
	B_0 (MHz)	-2386 (fixed to result in tab. 6.9)
	A_1 (MHz)	345(7)
	A_1/A_0	0.942(2)
	B_1/B_0	1.52 (fixed to ^{165}Ho result)

in-source laser ionization technique (see sec. 3.3.1) is usually employed at RISIKO, reaching absolute efficiencies up to 69(6) % [67]. The PI-LIST with its high resolution capability at the cost of reduced efficiency is thus not applicable. However, the hyperfine parameters, which can only be derived in the high resolution mode, can be utilized to simulate individual resonance patterns on different isotopes with adjustable line width. Respective results for the two transitions investigated in this work, with scheme B being the one already used within the high efficiency scheme for ECHo, are shown in fig. 6.17.
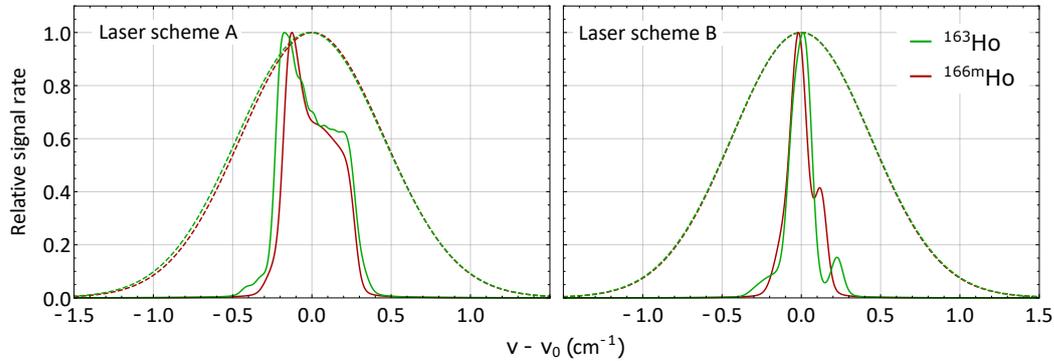
Figure 6.17: Simulated spectra of the two transitions investigated in this work, with adjusted line widths as they would occur in in-source operation. Besides the thermal Doppler broadening calculated from an oven temperature of 1500 °C, the dashed lines use the FWHM of 33(2) GHz as measured in [67], while the solid lines indicate the minimum possible resolution using a 1.4 GHz broad laser profile.

For the simulations, the isotope shift has only be taken into account for scheme A, where it could be measured. It is set to 0 for scheme B, but not expected to introduce a significant change. It is evident that in the "standard" configuration as used in [67], where an FWHM line width of 33(2) GHz has been measured for the first step of scheme B using the full output power of a frequency-doubled standard Z-cavity laser (see sec. 3.2), no additional selectivity enhancement opportunities are present. In contrast, if the laser system is tailored to its minimum achievable linewidth of around 1.4 GHz, slight

deviations in the individual patterns appear. However, there are no obvious points where a really significant improvement would be possible without sacrificing a considerable amount of signal on the required isotope. In both cases, optimizing the laser frequency for maximum signal on ^{163}Ho will additionally always introduce a very slight decline in ^{166m}Ho ionization rate.

It should be noted that, although these considerations do not add direct benefit to the day-to-day work on the ECHo project, the first-time determination of the ground state hyperfine structure parameters of ^{166m}Ho is extremely valuable. The hyperfine structure of other potential excitation steps can be studied in high precision without need for high efficiency on the stable ^{165}Ho isotope and simply be transferred to the radioactive species to forecast their pattern. If information on the isotope shift is also desired, at least one different isotope has to be measured and the coarse linearity to the changes in mean square charge radii as discussed in sec. 6.2.5 can be utilized.

Conclusion and Outlook

The presented work comprises the development, characterization and first-time application of a resonance ionization laser ion source for high resolution spectroscopy experiments, in a geometry tailored for installation at on-line radioactive ion beam facilities such as CERN-ISOLDE. This so called PI-LIST (Perpendicularly Irradiated Laser Ion Source and Trap) in internal reflection mode, featuring laser irradiation perpendicular to the atomic beam effusing from a hot cavity in a cold and clean interaction volume, allows for spectral resolution by far exceeding the Doppler broadening limitations of hot vapor environments.

The novel PI-LIST internal reflection mode was proven as completely competitive to the previous operation mode with lateral laser access through windows in the ion source vacuum vessel. This also only quite recently developed device, which has become a standard tool for hyperfine structure spectroscopy at the Mainz RISIKO facility in the mean time, is as such not applicable at on-line facilities due to impossible access to the highly radioactive front end area. Additional required adaptions to the separator system to imply the upgraded PI-LIST, namely off-center laser guidance through the beam extraction system, have been excessively investigated. Lateral holes in the electrodes did neither show any significant influence on ion beam quality in ion trajectory simulation studies, nor in proceeding standard operation of the RISIKO separator over several months. The home-built robust metal mirrors for the internal reflection were proven to withstand operation in the direct vicinity of the hot cavity over the coarse of weeks.

The method enabled the investigation on extremely dense hyperfine structure spectra of radioactive holmium isotopes. With an experimental linewidth of 100 to 150 MHz, in total 22 individual hyperfine resonances in the case of ^{163}Ho and ^{165}Ho and up to 43 in the case of first-time laser spectroscopic nuclear structure investigations on ^{166m}Ho were well resolved and assigned. This allowed the extraction of new information on fundamental nuclear shape characteristics. The nuclear spin of ^{166m}Ho was confirmed as $I = 7$. A puzzling inconsistency in literature data for the nuclear spectroscopic quadrupole moment Q_s, initially indicating a sudden unexpected change from pronounced prolate to oblate shape, was resolved to not be present. A first value for the change in mean square charge radii towards neutron-rich holmium isotopes was determined. The findings confirm a pronounced deformed shape distortion in this mid-shell region of the nuclear chart.

Additionally, the determined hyperfine parameters deliver valuable information for the ultra pure implantation of ^{163}Ho for the ECHo project on the measurement of the electron neutrino mass. With this new reference at hand, isotope-selective laser

ionization can be optimized, further contributing to highest possible sample purity after chemical treatment and electromagnetic mass separation.

Both operation modes of the PI-LIST have been excessively tested to explore their limitations in spectral resolution and ionization efficiency. Dedicated experiments were conducted on rubidium and uranium, which intrinsically promote narrow resonance linewidth by low evaporation temperature and high mass, respectively, and availability of laser transitions in the fundamental instead of frequency-doubled Ti:sapphire laser regime. Ultimate FWHM linewidths of as low as $60\,\mathrm{MHz}$ were achieved, approaching the regime of specific high-resolution spectroscopy experiments such as CRIS and COLLAPS, which are situated in specific dedicated beam line apparatuses. In terms of absolute ionization efficiency of the setup, values of $1 \cdot 10^{-5}$ up to $2 \cdot 10^{-4}$ were determined from both, relative comparisons in different operation modes as well as interpolation of measured ion rates over a whole experiment up to total exhaustion of the sample. Mapping of complete hyperfine spectra with minute amounts in the order of only 10^9 atoms are feasible.

Installation of the PI-LIST unit with internal laser reflection at ISOLDE is foreseen and will not only enable direct in-source high resolution spectroscopy of short-lived, exotic nuclides throughout the nuclear chart, but also permit *isomer*-pure production of ion beams for various experiments and users through exploitation of hyperfine structure differences accessible by narrow bandwidth laser excitation.

As presented in the appendix to this thesis, dedicated investigations were also performed on the effusion characteristics of atomic beams from hot cavities. This work linked to exploitation for highest possible efficiency by best geometrical laser coverage, but also to rule out cross mass contamination arising in collinear laser operation without shielding of the strong extraction field. Ions created on respective lower starting potential appear on trajectories of lower nominal masses. By compilation of previous results and new findings a full characterization of this effect was established. Most importantly, a counter measure exploiting the time structure of this contamination imprinted by the pulsed laser system via synchronized, fast ion beam gating techniques was demonstrated.

The pulsed, periodic ion creation can also be utilized in specifically constructed laser ion source setups, which intrinsically produce a brief, time-focused laser ion bunch. Geometric constraints for these Time-of-flight laser ion source (ToF-LIS) concepts, comprising high resistance cavity materials for steep potential gradients as well as an adjacent field-free drift volume, were investigated by ion trajectory simulations in the scope of implementation at ISOLDE. A LIST of adapted length was shown to be a very promising candidate. Additionally, a prototype of a fast high current switching unit for reversal of the cavity voltage or pulsed heating to increase the voltage during the time of laser ion creation, is presented.

Appendix

A

Ion Source Development

Besides its applicability in high resolution spectroscopy and its prospects in the production of ultimately isomer-pure ion beams, the PI-LIST also proved to be a valuable tool for detailed investigations of the conditions directly in front of the exit hole of a standard hot cavity ion source. The characteristics of effusing (neutral) atoms, especially their transversal distribution and its development along the central axis is of high interest: On the one hand, LIST-type ion sources (in both collinear and perpendicular laser irradiation modes) can be geometrically optimized to access an optimum fraction of the emitted particles. On the other hand, in standard RILIS operation, laser ionization inside the strong electric acceleration field directly at the cavity's exit produces ions which are transmitted through the separator magnet on trajectories of lower nominal masses, thus appearing as contamination for those ion beams. For the latter, a fast, pulsed ion beam gating technique exploiting the bunched structure imprinted by the 10 kHz repetition rate laser system can be applied to completely overcome this problem.

Direct, laser ionization based screening mechanisms of this area with different techniques are presented in this chapter, and implications for laser ion source designs and operation are derived. The work presented in the corresponding sections continues previous investigations by S. Richter [77], T. Kron [66] and F. Schneider [142], adds additional results and establishes a link to the theory of particle emersion from tubular channels in low pressure regimes. It closely follows and excerptedly reprints the recent publication [30] primarily by this thesis' author, with kind permission from Elsevier. Several figures are reproduced. Yet, additional and supplemental measurements and material are presented here.

A.1 Atom Effusion Characteristics

LIST-type laser ion sources use the effusion of neutral atoms from the hot cavity into an electrostatically separated, clean and cold volume for laser interaction. The efficiency is thus strongly dependent on the characteristics of the effusing atomic ensemble as well directed beam or as diffuse vapor. In fact, extensive information on shape and especially type of lateral distribution can be found in corresponding literature and previous works. In general, a directed beam would be favorable against a rapidly expanding cone, as more atoms can be addressed within a well defined cylindrical laser interaction volume along the central axis. Yet it has been shown, that reducing the distance between the LIST quadrupole unit and the hot cavity from 5 mm to 2.5 mm reduced the loss factor between ion guide (IG) and LIST mode (see sec. 3.4.1) by more than a factor of 2 [92].

This fact implies that the majority of the available atoms are present very near to the atomizer exit. Additionally, widely distributed contaminations from condensation of particles from the cavity were located inside the LIST structure, displaying significant lateral distribution of the effused atom ensemble.

A.1.1   Theoretical Description of Atom Beam Emersion

Model descriptions for molecule emersion from both simple orifices and elongated tubular connections between two reservoir volumes have been developed on the basis of the kinetic gas theory and were experimentally verified as early as during the first half of the last century. Of special interest are the works in the low pressure regime, where mean free path lengths are considerably higher than the geometric dimensions of the ion source. Here, the process is governed by individual trajectory evolution of each particle within the outer boundaries and not by mutual interaction. Typically measured pressures in the target unit vessel are below the 10^{-5} mbar regime, corresponding to free path length in the order of meters. This assumption even holds valid if the the partial pressure inside the source is significantly higher, up to the 10^{-2} mbar regime. Models for

1. emersion from an orifice (essentially a cosine distribution) and

2. emersion through a tubular channel with a length of $l_{cav} = 35$ mm and an inner diameter of $d_{cav} = 2.2$ mm, corresponding to the atomizer dimensions as given in sec. 3.3.1

are presented in fig. A.1, closely following the pioneering work of [143–146] and typical compilations in textbooks as [147].
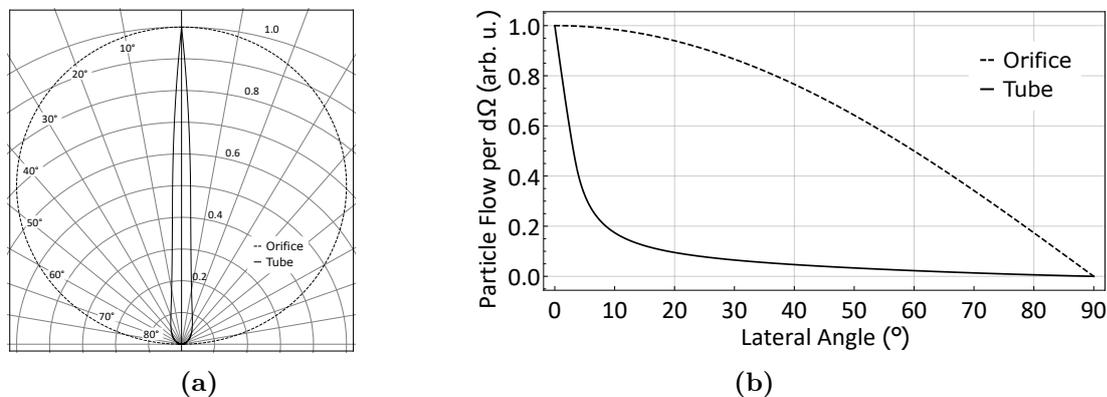
Figure A.1: Visualization of the atom beam shape (relative atom flow per solid angle element dΩ) in respect to lateral angle as predicted by models for a simple orifice [143] and a tubular channel [146] with the dimensions of the atomizer. Figure (a) follows the presentation in [146], while (b) gives the correlation in a direct way. Figures taken from [30].

The fundamental difference of both situations is evident: The tube produces a well directed, sharp atomic beam, while the emersion from an orifice exhibits a significantly wider distribution. E.g., 90 % (50 %) of the maximum intensity at forward direction is already reached at a lateral angle of just 0.6° (3.1°) for the tube, but 25.8° (60°) for the orifice. The following investigations' results will be compared to these two cases, but also stand for themselves as insight in actual operation experience.

Complementary to the work presented here, experimental information on the opening angle with direct scope to ion source applications can also be deduced from laser

spectroscopic absorption in the effusing atomic beam cone. Such investigations were carried out in preparation for simulation studies for the earliest LIST concept for comparable source geometries (length $l_{cav} = 20$ mm, inner diameter $d_{cav} = 3$ mm) and yielded a convolution of a $\approx 15\,\%$-abundant cone with $\pm 4°$ opening angle and respectively a $\approx 85\,\%$-abundant one exhibiting $\pm 20°$ [49]. In later experiments, values of $\pm 13°$ were reported from spectroscopic investigations of lateral Doppler classes in an uranium atom beam from a hot cavity [23], yet as a lower limit. Monte Carlo simulations based on the cosine-law for the angle-dependence of particle reflection on surfaces [148] yielded values of $\pm 4°$ [149]. These different results already imply that a sole description by models of emersion from a tube-like source might be insufficient.

A.1.2 Screening of the Central Axis using the PI-LIST

The PI-LIST with its lateral laser access represents a ready-to-use tool to probe the atom density in the cylindrical laser interaction volume along the central axis behind the hot cavity. In the presented case, the LIST geometry used is the one described in sec. 3.4.3, featuring a dual repeller configuration, but an overall length of only 45 mm of the quadrupole structure. The measurements were carried out on ^{165}Ho with a three-step resonant ionization laser scheme ($\lambda_1 = 405.5$ nm, $\lambda_2 = 818.8$ nm, $\lambda_3 = 837.8$ nm). The second and third step lasers were set up in standard configuration and irradiated anti-parallel to the ion beam into the source. The first step was introduced perpendicularly, and widely expanded to cover multiple times more elongation than the 30 mm diameter of the side entrance window in the vacuum vessel. This window consequentially cuts out the central part of the beam with an essentially uniform spatial power profile, as was confirmed by power measurements. By using a movable 1 mm slit diaphragm before this window, a distinct, well-defined ionization point at the intersection of all lasers (bound radially by the collinear beams' diameter and by the lateral beam's width in direction towards the extraction system) inside the quadrupole structure was selected. Through stepwise translation of the diaphragm, ionization rates were probed axially along the structure (fig. A.2).
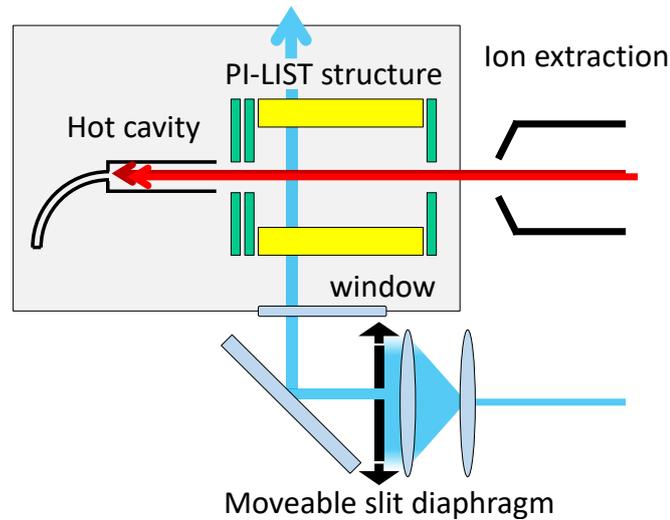
Figure A.2: Schematic overview of the measurement setup using the PI-LIST. The first step laser of a three-step ionization scheme on holmium is applied perpendicularly, while the other two are used in standard collinear geometry. By moving a slit diaphragm in the widened perpendicular beam outside the vacuum vessel, the atom density on the intersection volume of all lasers on the central axis is probed. See text for details. Figure adapted from [30].

As neither laser beam intensity nor size changes, and assuming a constant ion transport efficiency towards the extraction system independent of the point of creation, the signal rate directly represents the available atom density in the intersection region. Figure A.3 shows the evolution, recorded for $-20\,\mathrm{V}$ on the first and $20\,\mathrm{V}$ on the second repelling electrode.
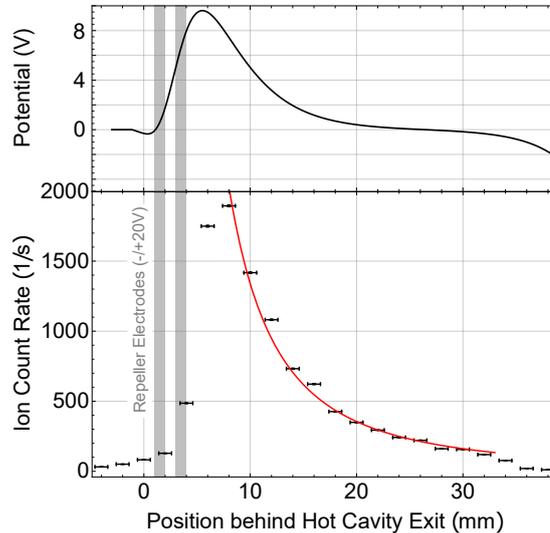
Figure A.3: Evolution of ion signal rate in a tubular volume defined by the diameter of the collinear lasers on the LIST's central axis as a function of distance from the hot cavity exit. After a steep increase behind the repelling electrode structure, up to where the top of the electric potential on the central axis (upper panel) is located. Subsequently, a reciprocally quadratic behavior is observed, fitted with a solid red line. Lower panel taken from [30].

Immediately behind the two repelling electrodes of $1\,\mathrm{mm}$ thickness each, installed with a distance of $1\,\mathrm{mm}$ between them and towards the cavity exit, a steep increase of ion signal is visible. This behavior can be understood from the electric potential along the central axis for the given repeller voltages, as shown by the upper panel of fig. A.3 (calculated using SIMION [98]). Only after a certain distance behind the repelling electrodes, created ions are able to surpass towards extraction. Behind this limit, where all ions are enabled to leave the LIST, a reciprocally quadratic decline is observed, as also expected from the geometry of an opening cone for the effusing atoms. The data was therefore fitted using the model

$$I(z) = I_0 \frac{1}{(z - z_0)^2} \tag{A.1}$$

for signal rate intensity I in relation to distance z from the atomizer exit. The offset z_0 describing the location of the cone's origin inside the atomizer is represents a characteristic property, as higher z_0 values imply a more confined effusion.

For the measurement method and data presented here, besides the mere scaling factor I_0, the effusing atom cone can thus be uniquely described by its mathematical starting point at

$$z_0 = -1 \pm 1\,\mathrm{mm}, \tag{A.2}$$

where besides the fit routine error an uncertainty of $0.5\,\mathrm{mm}$ for mechanical positioning of the repeller electrodes was taken into account.

An investigation like this has been already performed during the first operation of the $90\,\mathrm{mm}$ version of the PI-LIST described in sec. 3.4.3 and yielded at value of $z_0 =$

$-5(3)$ mm in the thesis of T. Kron [66]. It was derived by assuming the highest count rate stemming from the position directly behind the repeller electrode. This expectation corrected considering also the shape of the electric potential with its top roughly 2 mm behind this position. Thus, the value can be corrected retrospectively to

$$z_{0,\mathrm{Kron}} = -3 \pm 3\,\mathrm{mm}, \tag{A.3}$$

which is in good agreement with the result obtained in this work.

After the next section gives a discussion of additional possibilities using the PI-LIST for spatially resolved time structure investigations, emphasizing the adequacy of the method described above, this result is also compared to previous values obtained with a different method.

Spatially Resolved Time Structure Investigations

Time-resolved data which was taken with a multi-channel analyzer card (FAST ComTec Model P7882) also allows for analysis of the ion bunch structure. Because of the short laser pulse of ≈ 50 ns length, ionization of the atoms inside the LIST can be treated as simultaneous. Their temporal behavior is then determined by their point of creation, as they might be exposed to different accelerating electric fields, an travel different distances. The obtained experimental data is compared to ion trajectory simulations, on the one hand to gain additional confidence in understanding the ion guidance and extraction characteristics, or on the other hand to vice-versa verify the adequacy of the utilized simulation models. Corresponding investigations have been performed extensively in several works [77, 91, 92], using a 90 mm long "standard" LIST as described in sec. 3.4.2.
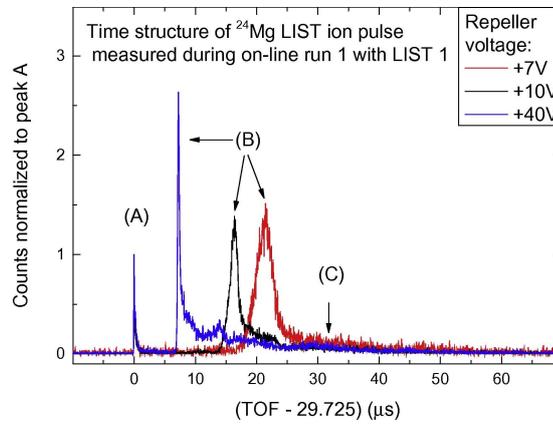
Figure A.4: Time structure of a laser ionized ion bunch from a 90 mm long LIST measured on-line at ISOLDE. The structure is well-understood as described in the text. Figure taken from [92].

The features are well-understood and depicted in fig. A.4. These are

(A) immediately accelerated ions created in the direct vicinity of the penetrating extraction field,

(B) an intense peak of ions in the volume influenced by the repeller and thus near the LIST entrance, and

(C) a broad structure of ions created in between whose time behavior is governed by the temperature-related initial ion velocity.

The spatially resolved approach using lateral laser access in the PI-LIST can ultimately verify these findings by tracking the arrival time of ions with explicitly known origin. A contour plot of the relative ion arrival rate in bins of 100 ns at the detector versus the position of origin is given in fig. A.5. It was recorded with a 45 mm long PI-LIST unit and a two stage extraction from 30 kV to 10.5 kV and subsequently to laboratory ground potential. As the overall intensity decreases rapidly with distance to the entrance as shown in fig. A.3 (where the same data is used), the individual data sets for each spatial position have been scaled to their respective maxima, to best visualize the individual temporal behavior.
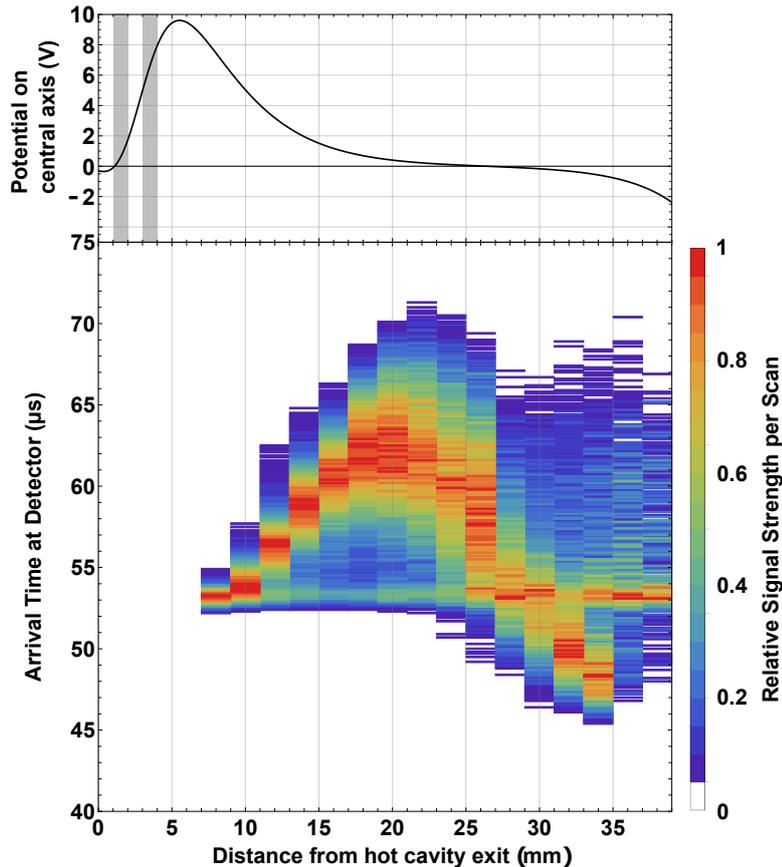
Figure A.5: Ion bunch time structure patterns in respect to their point of creation inside the 45 mm long LIST structure. The data sets for each position were scaled to their respective maxima for better visibility. The spatial scale shows the distance to the ion source exit, with the upper panel depicting the calculated electric potential on the central axis of the LIST. See text for details.

The investigation clearly confirms the previous results. The earliest arriving ions with arrival times earlier then 52 µs indeed are produced at the end of the investigated area, where the penetration of the extraction field is already apparent. The temporal middle part at 52 µs is dominated by ions created near the repeller electrodes, which also exhibit a very sharp, short bunch structure. This is due to the immediate "push-out" by the repeller potential. The more shallow this potential gets towards inside the LIST structure, the more the ion bunch arrives later and spreads in width. The Maxwell-Boltzmann distribution of the atom ensemble (which is already forward-directed due to its origin from inside the cavity) now has a more pronounced role and is not compressed by any additional acceleration. Surprisingly, there also is signal for positions at the

very end ($> 35\,\mathrm{mm}$) present at the same arrival time as ions created directly at the beginning. As the lateral laser is already located at the edge of the side window for this case (see fig. A.3), this feature is ascribed to light being scattered from this edge into the region behind the repeller electrode. Here, due to the high atom density, already weak illumination might cause ionization rates comparable to the intrinsically low rates at the end of the LIST with direct laser radiation.

To round up these investigations, an ion trajectory simulation of the geometry was carried out using SIMION 8.1 [98]. These simulation comprised atom ensembles of 60.000 particles each, created uniformly inside a cylindrical volume of $2\,\mathrm{mm}$ diameter along the LIST's central axis, representing availability for laser ionization. Different investigated parameter sets were:

a) All atoms have an initial velocity of $v = 0$.

b) All atoms have an initial longitudinal velocity corresponding to the most probable speed $\hat{v} = \sqrt{2k_BT/m}$ at the experimental temperature of $1700\,\mathrm{K}$.

c) The longitudinal velocity component is distributed corresponding to a Maxwell-Boltzmann distribution for the experimental temperature of $1700\,\mathrm{K}$.

The results are presented in fig. A.6 in direct comparison to the experimental data of fig. A.5. The simulation cases exhibiting identical starting velocities on all ions are nicely consistent with the upper boundary for atoms starting at rest (case a), and with the evolution of the most intense, main part of the structure (case b). They appear in a line-like fashion in the graph, as temporal spread is only due to slight differences in lateral starting position. The ensemble initiated with Maxwell-Boltzmann velocity distribution (case c) in contrast fully reproduces the temporally broader central structure as well as the time-focused components from the entrance and exit areas.

This result shows that the simulation model is indeed applicable to describe and predict the situation in the LIST realistically. Thus, the model can be employed as reliable starting point for studies of different geometries in development of LIST type ion sources. Vice versa, the PI-LIST was shown to be a valuable tool in evaluation of designs in the prototyping phase, e.g. to quantify confinement of the effusing atomic beam for novel, tailored atomization cavity geometries.

The results obtained from this comparison were also used to determine the absolute positioning of the lateral laser in respect to the repeller electrodes. While a relative movement of the slit diaphragm could be reproduced easily, the absolute position of the laser could not directly be monitored inside the vacuum vessel. Thus, the offset of the x-axis given in the plot was calibrated to best overlap of simulation and experimental data. The exact knowledge of the lateral laser position in respect to the hot cavity exit is especially crucial to mathematically describe the reciprocally quadratic decline in signal depicted in fig. A.3, where this calibration was also applied.

A.1.3 Investigation by Mass Separator Transmission Behavior

As described at the beginning of section A.1.2, the PI-LIST was used to describe the atom effusion from a standard hot cavity as an expanding cone with a characteristic value describing the location of its origin inside the cavity. This section will summarize the investigations initially performed by S. Richter on the time structure of RILIS source ion bunches (without any LIST unit attached) in relation to the chosen nominal transmission mass of the separator magnet [77]. Besides enabling an additional method of probing the atom vapor density in front of a standard hot cavity, it also is the basis
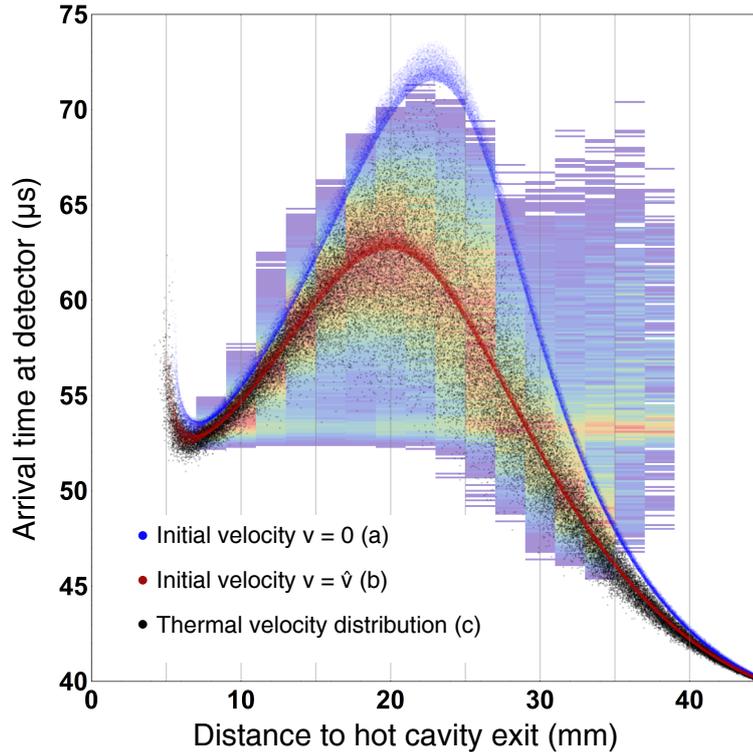
Figure A.6: Comparison of simulated and experimental ion bunch time structures with spatial ion origin resolution. The data presented in figure A.5 is superimposed by three different sets of simulated particle ensembles as described in the text. Agreement for the simulated set which exhibits thermal Maxwell-Boltzmann distributed starting velocity is evident.

for understanding and counteracting a specific form of cross-mass beam contamination, as will be discussed later. The description also closely follows, comprehensively excerpts and reproduces the figures of the correspondent section in the recent publication [30] of this thesis' author, which also is based on the work of Richter.

Information about the spatial distribution of atoms downstream of a standard RILIS configuration can be obtained by investigating the kinetic energy of ions created by the anti-collinear laser beams at a distance z outside the hot cavity in the acceleration field. A different starting potential $U(z)$ of (singly charged) ions of the same mass then translates into a different momentum

$$\frac{p}{q} = \frac{mv}{q} = \frac{m}{q}\sqrt{\frac{2qU(z)}{m}} = \sqrt{\frac{2mU(z)}{q}} \tag{A.4}$$

and therefore a transmission on different trajectories through the analyzing magnet. Particularly, ions of mass m with lower starting potential $U_{\text{start}}(z)$ compared to the source's full nominal potential U_{nom} will thus be transmitted as if they had lower apparent masses m_{app} according to

$$m_{\text{app}}(z) = \frac{U_{\text{start}}(z)}{U_{\text{nom}}}m. \tag{A.5}$$

To unambiguously distinguish these beam constituents and to quantify their significance, the bunch structure of the ion beam imprinted by the pulsed laser ionization process is

used. Figure A.7 shows an exemplary record of the time structure of resonantly ionized ^{174}Yb at the detector after the magnet, accumulated over several laser shots.
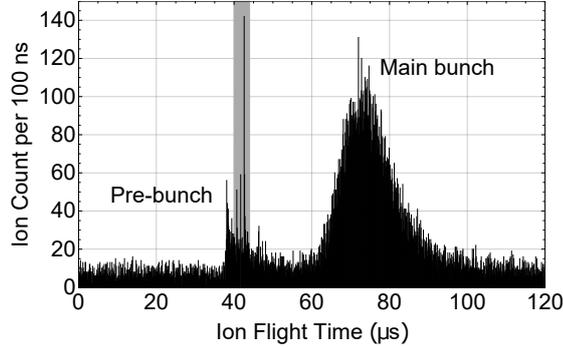
Figure A.7: Time structure of an ion bunch of laser-ionized ^{174}Yb from a standard RILIS source after transmission through the mass separator on nominal mass 174 u, acquired over several laser pulses. The interval marked in gray shows a very narrow feature within the pre-bunch of immediately extracted ions from the source: These spikes represent heavier ions which are created within the extraction field and which are transmitted on the trajectory of lower nominal mass through the magnet. Figure taken from [30].

The main features are well-understood [150] and reproduced by ion trajectory simulations [81, 151], similar to the LIST structure depicted in fig. A.4: A short, time-focused pre-bunch stemming from the exit region of the source, where the penetrating extraction field accelerates the ions immediately after creation, is followed by a broader, more intense main peak of ions (typically containing far more than 90 % of the overall yield) from inside the source which are guided by the potential gradient of the heating current along the cavity. Of special interest are additional, very narrow peaks occurring shortly after this pre-bunch.

An extensive investigation over a broader mass range in this time window was done by Richter and allows for tracking these species on the energy scale. The following description reproduces his work, using the same data [77].

For the investigation, a two-step resonance laser ionization scheme for ytterbium ($\lambda_1 = 267.3$ nm, $\lambda_2 = 736.7$ nm), exploiting an auto-ionizing state above the first ionization potential, was used in a tantalum hot cavity heated to about 1850 °C. Besides driving the resonant transitions in ytterbium, especially the UV laser is also capable of non-selectively photo-ionizing various molecules present in the hot vapor. Figure A.8 depicts the flight time versus nominal mass.

It features three main structural components: Most prominent in intensity are straight vertical lines. These are ions created by non-laser pulse related mechanisms as e.g. surface ionization inside the hot cavity with well-defined starting potential. Therefore, no energy spread and dispersion appears on the mass scale. A specific diagonal structure, marking the origins of additional vertical lines, leads from lighter to heavier masses and earlier to later arrival times. It shows ions created in the vicinity of the extraction field, but inside the ionizer on the full starting potential, which are immediately accelerated. They correspond to the pre-bunch in fig. A.7. Their trend is explained by the mass dependence of the acceleration's total duration t, derived by simple consideration from the motion equations

$$s = \frac{1}{2}at^2 \Leftrightarrow t = \sqrt{\frac{2s}{a}} \qquad \text{and} \qquad F = ma \Leftrightarrow a = \frac{F}{m} \tag{A.6}$$
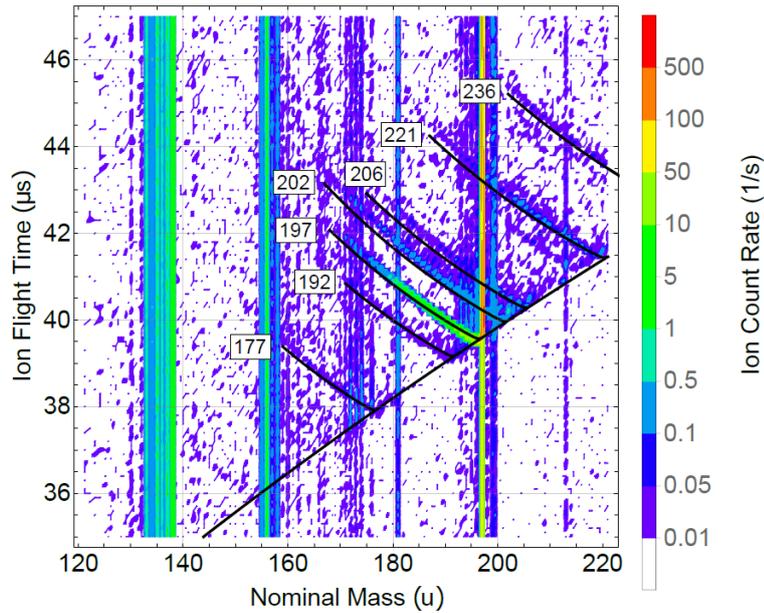
Figure A.8: Laser pulse correlated ion flight time structure in the domain between pre- and main bunch recorded over a broad mass regime. Diagonal traces towards lighter masses and later arrival times indicate ions created at respectively lower starting potentials, which are therefore transmitted on lower nominal masses. For comparison, simulation results from a complete electrostatic model of the separator are shown for selected species (solid black lines, indicated with respective mass number at upper left endings). See text for details. Figure taken from [30], originally produced by [77].

resulting in

$$t = \sqrt{\frac{2ms}{F}} \tag{A.7}$$

with the electric accelerating force $F = Uq$ (simplified to be constant) causing an acceleration a along a distance s. As after acceleration the velocity stays constant, this $\sqrt{m}$-dependence of the extraction duration appears on the detector position without alteration.

The second narrow peak mentioned above is formed by the traces starting at this structure's border and stretching towards lighter nominal masses and later arrival times. These are the particles ionized outside the cavity in the extraction gap: With increasing distance, their transmission smoothly alters as in eq. A.4 to lower momentum, associated with lower terminal velocity and thus later arrival time at the detector.

Richter generated a complete electrostatic computer model of the separator, including the two-stage extraction system as well as the beam shaping ion optics downstream. The structures mentioned above were reproduced by calculating trajectories of ions with respective mass and starting positions along the central axis, both within the ionizer cavity and inside the extraction field. These results are indicated by the solid black lines in fig. A.8. At the same time, a translation of starting energy into the position z of ion creation in the extraction field becomes possible via the calculated potential from the simulation model. For the most abundant mass m = 197, the evolution of relative ion signal intensity in relation to the distance from the hot cavity exit is depicted in fig. A.9 and can be compared to the direct screening techniques presented in sec. A.1.2.
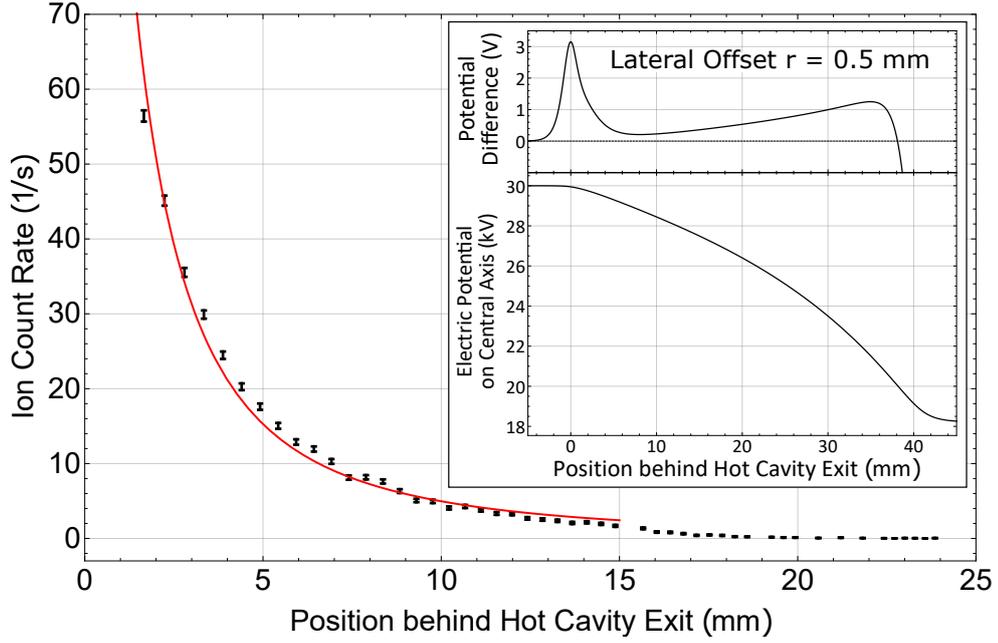
Figure A.9: Signal rate evolution of ions with mass 197, as a function of distance from the hot cavity exit, extracted from the data of fig. A.8 as calculated by [77]. The inset shows the starting potential as determined from an electrostatic model of the system, which is used for translation into spatial positions. The upper part of the inset depicts the difference of starting potential at a lateral position 0.5 mm away from the central axis, where ions will also be created by the Gaussian shaped laser beam profile. The relative change is below 10^{-4} and therefore negligible. A reciprocally quadratic function corresponding to a homogeneous cone-like effusion is used to describe the rapid decline. Figure taken from [30], originally produced by [77].

A rapid decline is clearly visible also in this case. The analogue description via the reciprocally quadratic density function with eq. A.1 yields, besides the scaling factor I_0, the characteristic parameter of

$$z_0 = -1.6 \pm 0.1 \, \text{mm} \tag{A.8}$$

for the location of the cone origin inside the atomizer cavity.

This result, obtained with a different, more indirect method is in perfect agreement to the one derived in section A.1.2. A brief compilation is given in tab. A.1. As a sharp, directed atom "beam" would correspond to a value depicting the cone's top far inside the hot cavity, these findings already suggest the contrary case, i.e. a large lateral opening angle.

A comparison to the theoretical predictions from sec. A.1.1 can be established in a semi-qualitative way. The resolution of both experimental methods is limited by the radial extent of the collinear lasers. If an effective beam diameter of 1 mm is assumed, a lateral angle of ± 5.7 (2.9, 1.4)$°$ is covered inside this cylindrical volume at a distance of 5 (10, 20) mm. To be consistent with the observed reciprocally quadratic behavior, angular effusion density should be nearly constant in this regime. Figure A.1 indeed suggests this for wide angle effusion following the cosine law. In contrast, the sharply directed beam of effusion from a tube would cause a less pronounced decline in ionization rate when covering less solid angle around the central axis, as relative angular density

Table A.1: Overview of the emerging atom cone top's distance z_0 to the hot cavity exit as derived in this and previous works. The original value given by Kron as $-5(3)$ mm [26] was corrected according to refinement of the method. All results are in good agreement and suggest a significant lateral cone opening angle, as otherwise a starting point deeper inside the cavity would be expected.

	Method	z_0 (mm)
This work	Lateral laser screening	-1(1)
Kron [66]	Lateral laser screening	-3(3)
Richter [77]	Magnet transmission behavior	-1.6(1)

already decreases significantly for these lateral angle values and less atoms would be lost. Therefore, sole description as a sharply directed atom cone seems to be insufficient, and a higher effective opening angle has to be assumed. Yet, a quantitative statement on the magnitude of this angle can not be deduced from the presented measurements on the central axis only. This subject is addressed in the following section.

A.1.4 Opening Angle Investigations by Angular Dependent Material Deposition

While the previous section summarized the work of S. Richter [77], the experiment described here extends the investigation of the effusing atom cone characteristics towards the areas lateral to the central axis. Also this section is part of the work published in [30] by this thesis' author.

An investigation of atom emergence characteristics laterally off the central axis was conducted by analyzing deposition of material stemming from the hot cavity on the surrounding structures. As one specific LIST unit has been used at Mainz University for several measurement campaigns on long-lived radioactive isotopes of numerous elements (holmium, actinium, promethium and protactinium), deposition of sample material inside this structure can be screened by spatially resolved radioactive decay detection. Therefore, the LIST unit was dismantled and parts were investigated in a simple setup: A commercial hand-held contamination monitor (Berthold LB 122) was placed behind a 3 mm wide slit diaphragm made from aluminum plates. The parts under investigation were then moved past this opening on a guiding sled. The four quadrupole rods are of highest interest, as they cover a significant area besides the central axis and were, unlike other parts, neither cleaned nor exchanged throughout the whole operation period of the unit.

A CAD cut view of the LIST setup is given in fig. A.10, together with the measurement results for simultaneous screening of all rods on α and β radiation intensity. The obtained activity is background-corrected and normalized to solid angle coverage of the investigated part as seen from a point 1.5 mm inside the cavity, derived from the investigations in section A.1.3.

It is clearly visible that deposition is uniform on the majority of the back part, while decreasing towards the hot cavity. The onset of this decrease coincides with the direct line of sight to the cavity orifice, as confirmed by inspection of the visible coloring of the metal due to heat radiation. Therefore, the hypothesis that at least a fraction of the expanding cone of atoms from the cavity exhibits a significant lateral opening angle is supported. A lower limit of roughly 45° for the overall maximum opening angle (corresponding to 22.5° lateral angle in respect to the central axis) can be deduced, while higher values are geometrically blocked by the LIST electrodes. A comparison of the
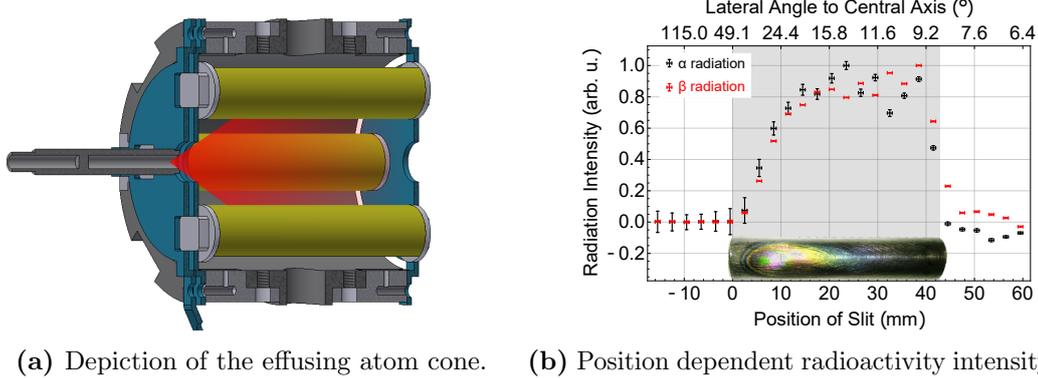
(a) Depiction of the effusing atom cone.

(b) Position dependent radioactivity intensity.

Figure A.10: (a) CAD view of the LIST with sketched emersion cone of atoms from the hot cavity, constrained by the repeller electrodes.
(b) Spatial radiation screening of the LIST's four quadrupole rods after operation for long-lived radioisotopes over several months. The data is normalized to solid angle coverage. A photograph of one rod is shown for comparison to the heat radiation induced coloring, which also indicates direct line of sight to the hot cavity. The lateral angle is calculated in respect to a point 1.5 mm inside the hot cavity, as indicated from section A.1.3. Figures taken from [30].

results from the accessible range of only roughly 9° to 20° to the theoretical predictions in sec. A.1.1 does unfortunately not allow a differentiation, as the relative intensity is predicted to be roughly constant and within the scattering range of the obtained data points for both models (see fig. A.1).

In conclusion, the findings favor the assumption of quite large opening angles, stated e.g. as $\beta = \pm20°$ in [49], even succeeding this value. The investigated standard hot cavities of 34 mm and 2.2 mm diameter do not exhibit a significantly confined effusion corresponding to a preference of atoms stemming from the back end. On the contrary, thermal effusion from the tip area of the cavity seems to be a dominating effect. This suggests that most atoms have wall contacts in this part before they leave the structure. More work is needed to resolve the discrepancies to the theoretical description, which are related to temperature gradients and depend on desorption characteristics of the source material. Consequences which are derived from these findings for the geometry of LIST-type ion sources are discussed in the subsequent section.

A.2 Implications for Laser Ion Sources

Based on the background described above, this section discusses derived geometric constraints for the construction of LIST-type ion sources, and the effects arising from the transmission of ions which are created in the extraction field of a standard RILIS source and are transmitted on lower nominal masses. Especially the latter is of importance and could favor immediate application at existent ion beam facilities employing laser ion sources.

A.2.1 Geometric Constraints for LIST-type Ion Sources

High purity LIST-type sources which comprise spatial separation of the hot atomization volume from a clean laser-atom interaction region by electrostatic repelling electrodes are employed at several ion beam facilities, as described in section 3.4.2. As already seen in the process of implementation of these devices, a minimum longitudinal spacing

between the oven exit and the active ionization volume ahead is extremely critical, as e.g. a reduction from 5 mm to 2.5 mm already caused a doubling of the achievable ion rate in respect to in-source ion guide mode. Indeed, the reciprocally quadratic behavior demands distances as small as possible as design goal for electrode layout and isolator design. At the same time, perpendicular laser irradiation for Doppler-reduced spectral resolution using an unexpanded laser beam produced by reflection within the vacuum vessel (see section 4.1) is reasonable with acceptable geometric losses in efficiency. In fact, integrating equation A.1 with the values obtained in table A.1 yields that more than 90 % of all atoms inside the ionization volume defined by the collinear lasers around the central axis are found within the first 2 cm behind the source exit.

On the other hand, the overall length of the RFQ unit shielding the extraction field is a more variable parameter and can be adapted to other concepts. Matching its length to that of the cavity e.g. is suggested for a time-of-flight based source concept producing temporally very sharp ion bunches [82, 152] and is discussed in section A.3. Special attention must also be paid to the solid angle coverage of parts in the unit, namely vicinity and diameter of the RFQ rods, on which material is deposited within line of sight to the hot cavity. This effect was identified as a possible cause for contaminations arising within the structure [92].

A.2.2   Cross Mass Contamination Suppression via Ion Beam Gating

A direct application of the effects systematically studied in section A.1.3 is found in characterization and suppression of a specific type of ion beam contamination appearing at standard RILIS laser ion sources. Species which are laser-ionized in the extraction gap (either resonantly ionized heavier isotopes of the element of interest or non-resonantly photo-ionized different species) pass the separation magnet on trajectories of lower nominal masses and appear as quasi-isobaric contaminations afterwards. Although this admixture may only contribute a small fraction of the initial beam intensity, it can be crucial if the contaminating isotopes are produced at a much higher rate, or if highest beam purity is required.

The effect is visible as a tailing of the ion signal in the mass spectrum towards lower masses. Figure A.11 depicts this behavior. It was recorded at the RISIKO mass separator for resonantly ionized holmium isotopes, with stable ^{165}Ho being the most abundant. Fortunately, the time structure of the ion bunch imprinted by the pulsed laser system also opens up a way to counteract this effect: As shown in fig. A.8 and A.7, the transmission of heavier species on lower nominal mass is limited to a very short time interval within the whole structure. Inhibiting transmission of the ion beam for this brief period therefore completely eliminates these interferences, while only slightly affecting the main constituent which appears in the later and significantly longer main peak. For this purpose, a fast high voltage pulser (CGC Instruments, AMX500-3) was connected to electrostatic deflection plates in the beam line 1 m behind the extraction system (see fig. 3.4 in section 3.3.1). A voltage of 300 V was applied for 1 µs, in synchronization and with an appropriate delay to the 10 kHz trigger signal of the laser system. This is sufficient to completely deflect the ion beam from the detector a distance of 4 m downstream for the critical time duration. The resulting mass scan clearly shows complete disappearance of the asymmetry in the tailing, and a more pronounced appearance of the ion signal of ^{163}Ho which was also present in the sample. The resulting symmetric peak shape is very similar to the one received from operation of the source without laser irradiation, where surface ionization solely takes place on the well-defined starting potential within the cavity.
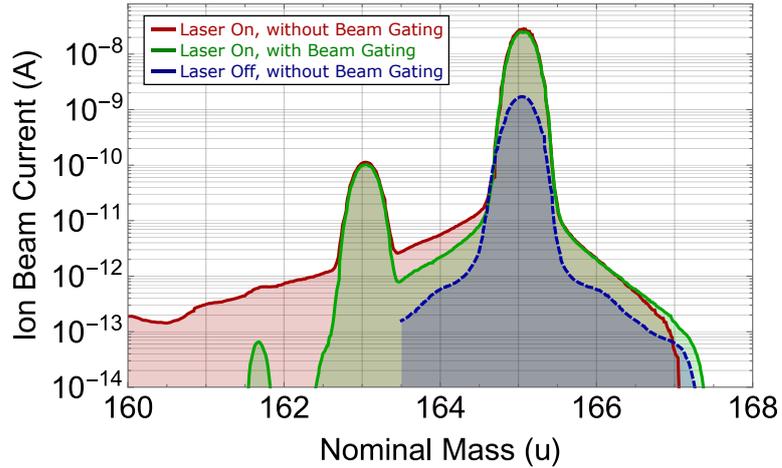
Figure A.11: Mass scans in the holmium region for different ion source and separator configurations. Ions produced in standard laser configuration exhibit an asymmetric tailing towards lower nominal masses, caused by ionization outside the hot cavity in the extraction field. This effect can completely be suppressed at cost of an only negligible reduction of transmission of the species of interest by applying laser synchronized ion beam gating. Thus, a symmetric peak shape is obtained, very similar to the one of operation in sole surface ionization mode with well-defined starting potential of the ions. Scans with and without lasers were taken on different days and do not reflect actual signal ratios. Figure taken from [30].

As the time window of deflection lies within the bunch of ions of interest, this method nevertheless inherently introduces a slight loss in the overall transmission efficiency. The actual quantity of this depends on the time behavior of the particles, i.e. mass, chosen acceleration voltage and position of the deflector in the beam line. Although the contaminating species are extracted directly, they have a lower terminal velocity then the ones from the source itself. Therefore, at some point they merge into the broad main time structure, and thus higher losses are caused when deflection is applied further downstream in the beam line.

While the gain in contamination suppression can be quantified to be at least one order of magnitude for differences of two masses or more in this mass regime, a change in shape on the base of the peak is still apparent. This broad symmetric tailing is ascribed to elastic and inelastic scattering processes in the ion beam throughout the whole separator system [153, 154]; it is unavoidable and will not be discussed here. Comparison to the peak shape of an ion beam produced by sole surface ionization confirms that it is not a laser-related effect.

At the on-line radioactive ion beam facility ISOLDE at CERN, such a fast laser pulse-synchronized beam gating system has already been installed. It can be used for blocking the ion beam in between laser-related ion bunches, which contain the majority of laser-ionized species. Thus, beam contaminations which appear in a continuous, not laser-correlated temporal behavior can be suppressed proportionally to the system's duty cycle. Also, shot-to-shot multiplexing between different experiments or for in-situ ion beam diagnosis is possible [82]. Yet, it was not applied for low mass tailing suppression, as this effect was not significant enough in previous experiments.

Nevertheless, for the ECHo project (neutrino mass determination by Electron Capture in ^{163}Ho) [7], utilizing ultra-pure implantation of ^{163}Ho into calorimeter arrays, this method is considered as further useful step to meet the design goal of reaching a relative ^{166m}Ho contamination of below 10^{-9}. A correspondent proposal and extrapolation of

the existing data by F. Schneider in [142] has thus now been verified to properly work by the experimental results obtained and presented here.

A.3   The LIST as Part of a Time-of-Flight Based Laser Ion Source Concept

Both techniques described in the previous section, i.e. the proper adaption of the LIST's length as well as the routine application of kHz repetition rate ion beam gating, can be utilized in a technical concept for improving selectivity of standard RILIS sources. This so-called Time-of-Flight Laser Ion Source (ToF-LIS) was proposed and described for the first time by V.I. Mishin [152] and comprises the exploitation of ion beam time structure in relation to the pulsed ionization laser pulse sequence. Ions are created inside the standard RILIS hot cavity simultaneously by the laser pulse, and with a rather uniform spatial distribution in the atom vapor. The electric current applied to resistively heat the cavity imposes a potential gradien alongside, and thus an accelerating electric field within. Naturally, the polarity is chosen in a way to guide the ions towards the beam line. In standard operation mode, the ions would be extracted at this point into the separator, with a bunched time structure as shown in fig. A.7, which is well understood [150]. The profile can be utilized for suppression of contaminations arising from non-laser related ionization inside the hot cavity, most commonly surface ionization: Ions from these processes exhibit no temporal relation to the laser pulses and thus appear as a continuous pedestal of the ion beam current. By deflection of the beam in the time duration when no laser related ions pass, the contaminants can be suppressed down to the ratio of deflection time versus laser pulse duty cycle. Consequently, bunches of short duration are obviously highly desirable.

The technical installation described by Mishin is depicted in fig. A.12 and features free ion trajectory evolution in a region directly adjacent to the hot cavity. Ions which are created near the rear end of the cavity have to travel a longer distance towards the exit, but also developed a higher velocity v_{out} from the electric field:

$$v_{\text{out}} = \sqrt{\frac{2s\,\Delta U}{L\,m}} \tag{A.9}$$

with the respective traveled distance s, the overall voltage drop ΔU over the cavity length L, and the ions' mass m. After a certain distance of acceleration-free evolution with constant velocity, this will cause ions from the rear end to merge with and finally overtake the ions from the front region. Actually, at the distance equal to the length over which the ions were initially created (i.e. the cavity), the ion bunch exhibits a temporal focus. High voltage extraction of the ions at this point then conserves the compressed structure during transmission through the entire beam line system and permits to apply the gating techniques.

For the simplified simulation of trajectories as shown in fig. A.12 (especially not featuring initial thermal velocity), the effect is evident: While the overall duration at the ion source exit is around 25 μs, at the point of extraction (i.e. the position of the LIST's exit electrode) compression to below 10 μs for the whole ensemble is achieved. Mishin reports measured pulse durations (half-height width) ranging from 1.17 μs for natural lithium (mass 7 u) to 5 μs for thulium (mass 169 u), following the expected $\sqrt{m}$-dependent trend [152]. With the 10 kHz repetition rate laser system used at most on-line facilities, this already implies a 20-fold improvement in sensitivity. At the same
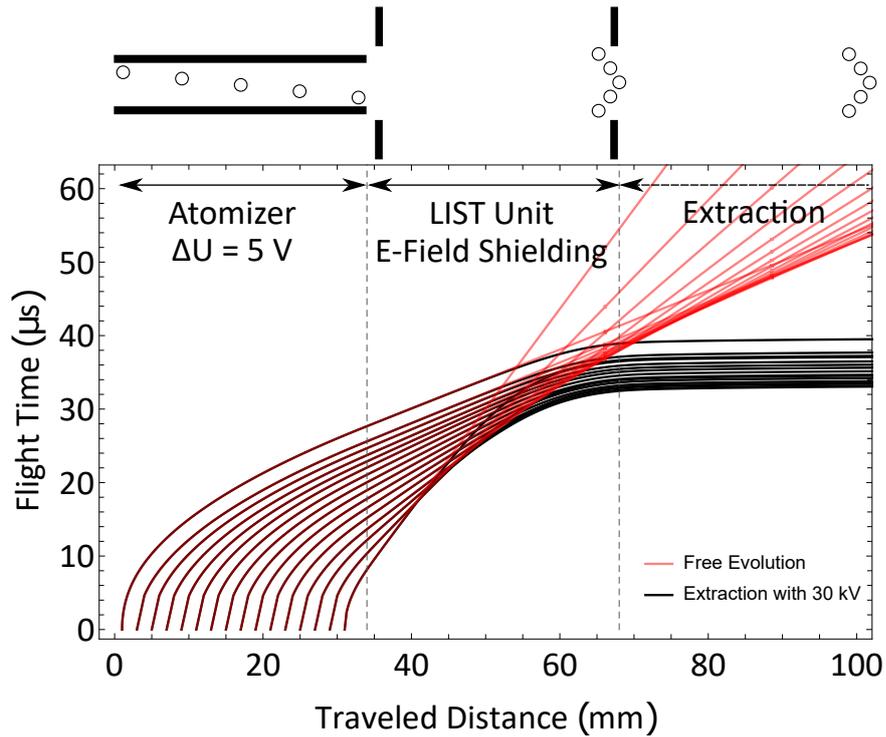
Figure A.12: Simplified simulation of ion trajectory behavior of particles with a mass of 150 u in the time-of-flight laser ion source concept. Ions are created simultaneously by a laser pulse inside the hot cavity and accelerated by the potential gradient imposed by the heating current. If a field-free region is directly adjacent to the cavity (as e.g. in the LIST), the free evolution of the trajectories results in a time focus in a distance corresponding to the length of the atomizer (red lines), where the ions can be extracted as a short bunch (black lines). The ion flight sequence is depicted in the top panel.

time, overall efficiency can almost completely be preserved by ensuring best possible transmission through the field-free region towards extraction.

The device to provide this field-free region behind the hot cavity can naturally be the LIST corpus, with an adapted overall length. Lateral confinement can then directly be provided by the quadrupole field.

A.3.1   Simulation Study of the LIST for the ToF-LIS Concept

As no experimental time could be attributed to systematic investigations on different geometries, the LIST's applicability for this technique was explored by a series of ion trajectory simulations implemented in SIMION 8.1 [98]. The presented results should thus just be seen as a starting point towards an actual experimental investigation.

Of special interest is the actual overall length of the LIST unit. Intrusion of the strong extraction field through the exit electrode orifice has a significant influence, implying differences between the geometric length of the structure and the effective field-free drift region. At the same time, the relevance of the total quantity of the atomizer potential gradient was taken into account. The implemented simulation model is shown in fig. A.13. It is similar to the one presented in fig. 4.6 in section 4.1.2 for investigations on the shape of the extraction electrode.

Initial tests were performed to investigate the difference in results obtained with a three-dimensional, cylindrical distribution of ion starting positions inside the atomizer to
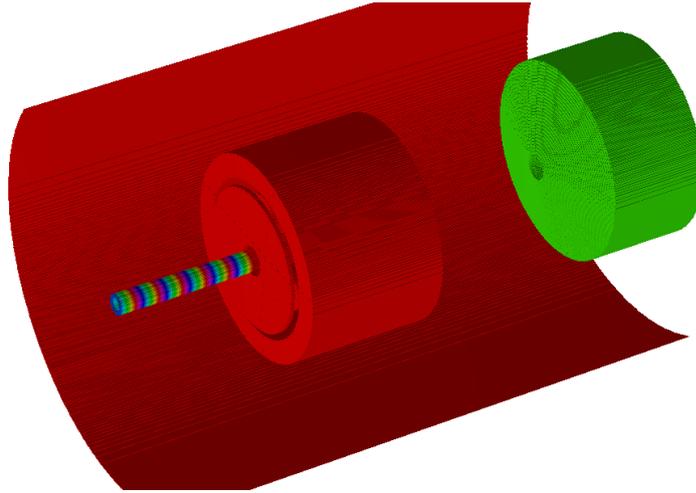
Figure A.13: Simulation geometry for investigations on the LIST's applicability for the ToF-LIS
concept, implemented in SIMION 8.1. While the LIST corpus and quadrupole are fixed on
environment potential, a linear potential gradient can be applied along the atomizer, and
the extraction electrode can be set to different negative high voltage values. The geometry,
i.e. especially the LIST's overall length, was altered in between runs.

the results obtained in a simpler approach with ions starting only along the central axis.
In the first case, also a full three-dimensional implementation of a Maxwell-Boltzmann
velocity distribution was applied (analogue to the simulations in section 4.1.2), while the
second case used the respective projection onto the longitudinal axis. These tests revealed
no apparent deviations, so that the subsequent simulations were implemented with a
linear distribution, resulting in significantly less complex and thus faster computing.

For experimental validation of the results, a comparison to the data available in [152]
was conducted. In this case, a 30 mm long graphite ionization tube with a potential
gradient of 15.3 V and an adjacent cooled copper drift tube of equal length was used.
Downstream of an exit orifice of 5 mm diameter, the ions were accelerated towards a
channel electron multiplier arranged laterally, on an attractive potential of -2700 V.
The situation was approximated in the simulation by adding a 30 mm long LIST corpus
to an ionizer of 30 mm length, depicted in fig. A.13. An extraction voltage of -2700 V
was set on the electrode 40 mm away. At this point, the resemblance to the experiment
in [152] can not be guaranteed, as no precise geometric information is available. Ion
starting parameters in the simulation were based on a uniform distribution along the
atomizer's central axis, and with a velocity distribution corresponding to 2300 K, which
fits the $\approx 2000\,°C$ quoted in the publication. There, the evolution of the FWHM $\Delta\tau$ of
the corresponding ion bunch was examined as a function of atomic mass using lithium
(6 u), sodium (23 u), potassium (39 u), thulium (169 u) and ytterbium (173 u). The
corresponding relation was evaluated to be $\Delta\tau = 0.36\sqrt{m}$. Mishin's experimental values
are shown in fig. A.14, in comparison to the ones derived from the simulations in this
work.

In the simulations, three methods of evaluating the resulting data set for a run of
ions of a specific mass have been applied, and obvious differences can be understood
from the way of evaluation. Figure A.15 exemplarily depicts the data set for potassium
(39 u), with the number of ions arriving at the end of the simulated extraction electrode
in distinct time windows of 0.05 µs width.
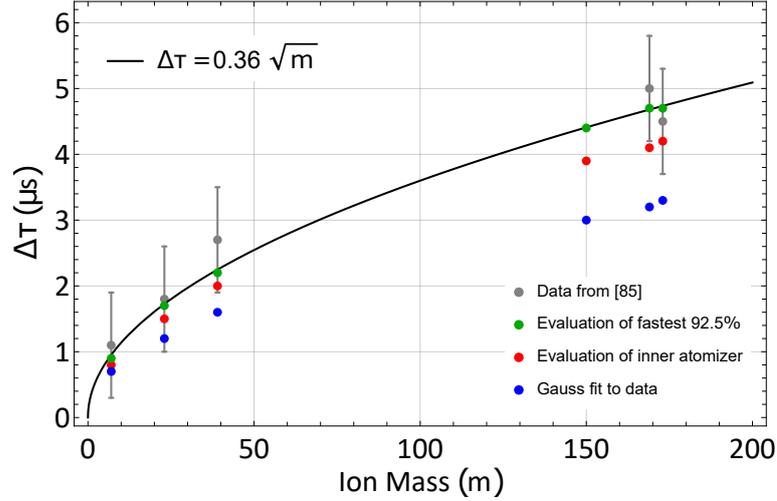
Figure A.14: Comparison of the half-width heights obtained in the experiment in [152] with different methods for evaluating the simulation data for a similar setup (see text for details). While with an adapted selection of the simulation data the experimental results can be nicely reproduced, independent models produce systematically lower values. Nevertheless, the underlying $\sqrt{m}$-trend is reproduced and qualitative predictions are feasible. Graph adapted from [152].

There is no direct analytic way of describing the distribution as a function and extracting the FWHM of the asymmetric bunch with its characteristic tailing towards longer arrival times, which is caused by ions originating from the very end of the cavity where ejecting forces are weak. Thus, three methods of automatic numerical data processing procedures have been applied to this and all other data sets:

a) A fraction of the slowest ions (i.e. latest arrival times, apparent in the right-hand side tailing) was omitted, resulting in a more symmetric bunch shape. The standard deviation σ from the remaining particle arrival times was calculated. Coarsely assuming a Gaussian profile, an FWHM value was derived as $2\sqrt{2\ln(2)}\sigma$.

b) As the slowest ions are those starting at the end of the cavity, where the superimposed voltage gradient already fades due to fringe effects, the right-most starting 10% (i.e. $3.4\,\text{mm}$ from the cavity exit) of the ions were omitted, and the remaining particles treated analogously to the method above.

c) A simple Gauss profile was fitted to the whole data set including all particles, yielding corresponding standard deviation σ and FWHM parameters.

The remaining datasets for a) and b) and the resulting parameters are also shown in fig. A.16. For case a), acceptance of the 92.5% fastest ions was chosen to best reproduce the results from [152] depicted in fig. A.14. This choice is of course artificial, but somewhat constitutes a calibration to experimental data. The two other methods, especially c), are independent from this bias and provide a stand-alone description of the obtained data. While they produce significantly and systematically briefer bunch widths compared to the experiment, all reproduce the expected $\sqrt{m}$-trend and can thus provide qualitative, inter-comparing information for upcoming actual experimental investigations. It should be noted that discrepancies to the results in [152] can, besides to the intrinsically simplifying character of the simulations, also be due to an insufficient
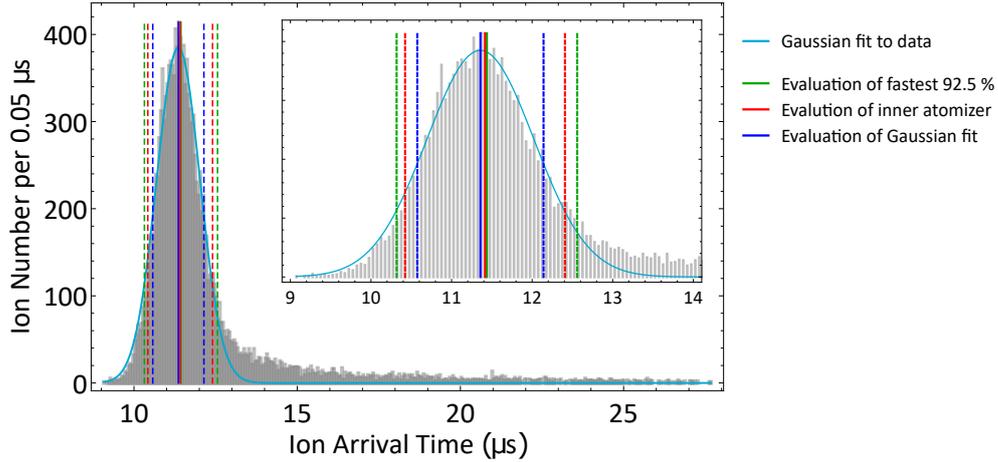
Figure A.15: Simulated arrival time distribution for ^{39}K in the setup resembling the experiment of [152]. Three different evaluation methods have been applied to extract the half-height width of the resulting bunch (see text for details). The solid lines indicate the center of the respective method, while the dashed lines margin the half-height width. While the large graphic shows the whole dataset, the inset depicts a closeup on the bunch itself.

resemblance to its experimental setup, as not all geometric information is available in the publication.
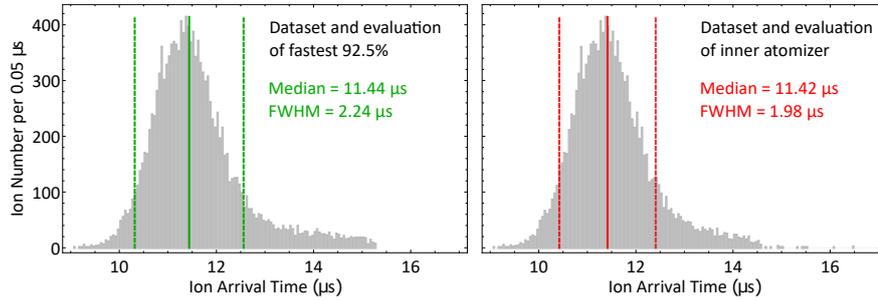
Figure A.16: Reduced datasets of the cases presented in fig. A.15. For the left-hand case, the overall slowest 7.5 % of ions have been omitted (a), while on the right-hand side the 10 % of ions closest to the atomizer exit were not included (b). The solid lines show the respective median value, the dashed lines delimit the FWHM derived from the respective standard deviation of the remaining data.

An additional number of interest is the fraction of overall ions which are actually within the FWHM region around the center, which would be a natural choice for the time window in bunch-synchronized beam gating techniques. For the results on potassium presented in fig. A.15, cases a) and b) yield 77 % and 74 %, respectively, while within the FWHM of the Gaussian profile from case c) only 66 % of all ions can be found. The discrepancy to the 76.1 % which are contained within the FWHM of an ideal Gaussian curve are naturally due to the tailing and nicely depictthe variation of the bunch profile from an ideal Gaussian function.

As especially a comparison to the bunch characteristics of a standard RILIS source without an adjacent field-free drift volume is of interest, simulation results for this case are also included. The evaluation and respective data handling has to be different here, as the time structure exhibits other features (see fig. A.7). The penetrating extraction

field into the cavity, causing the part of the ensemble which is nearest to its exit to not be transmitted on their nominal mass (see sec. A.1.2), has to be taken into account. For this reason, only the dataset omitting the 10 % of ions created nearest to the source exit (case b), cutting off 3.4 mm) has been used, and a Gauss fitting procedure (case c) was applied on this reduced data set. An exemplary figurative explanation is given in fig. A.17 for simulation of an ensemble of mass 150 u. The automatic data handling produces a sufficient approximation of the FWHM of the bunch.
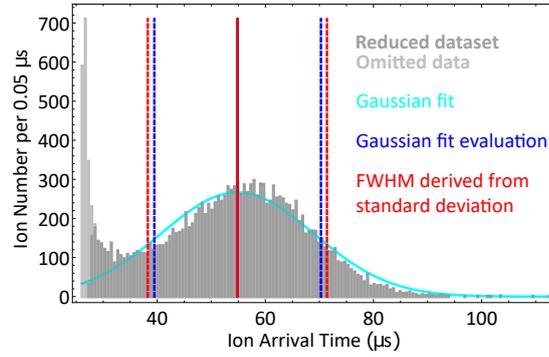
Figure A.17: Visualization of data handling for the simulation of direct extraction from the ion source, without a shielding LIST structure. The high peak at the very beginning stems from ions created at the exit of the source, where the penetrating extraction field causes transmission on lower nominal masses, thus they are omitted for evaluation. The resulting structure's width is extracted by the methods b) and c) described in the text.

With these procedures at hand, the time structure of resulting ion bunches can be described in relation to various geometric source parameters or variations ins particle characteristics, such as mass or temperature defining the underlying Maxwell-Boltzmann distribution. The complete results for all simulated data sets are shown in tables B.2 to B.4 in appendix B.1. The most interesting dependence, i.e. the bunch width against the length of field-free drift volume is depicted in fig. A.18 for different electric potential gradients along the cavity. The presented data is obtained with fixed additional parameters of particle mass 150 u, an extraction voltage of 30 kV towards an electrode 4 cm downstream of a LIST exit orifice of 7 mm diameter, and an underlying ensemble temperature of 2300 K. The temporal structure was recorded at a position directly inside the extraction electrode, after the ions have reached their terminal velocity.

The different aspects of this summarizing overview have to be discussed in detail. The three different methods of data evaluation described above have all been included, to provide a feeling of possible limitations of the outcome and reliability of the results. Very prominent is the explicit deviation of the Gauss fit method for long LIST bodies at high cavity potential gradients and thus for intrinsically more compressed bunches, towards shorter bunch widths. The discrepancy can be understood from the fact that the relative asymmetry and tailing towards later arrival times is significantly more pronounced here. Thus, a lower fraction is found within the derived FWHM width of the Gaussian function: Only 55 % compared to 78 % (method a) and 76 % (method b) at the example of the 10 V potential gradient depicted in the figure. In contrast, for a length of 34 mm, all evaluation methods yield very similar values between 70 % and 72 %. Ergo, the shorter bunch widths for long drifts distances are accompanied by lower transmission, and can be disregarded.

Essentially two main results can be derived from the simulations:
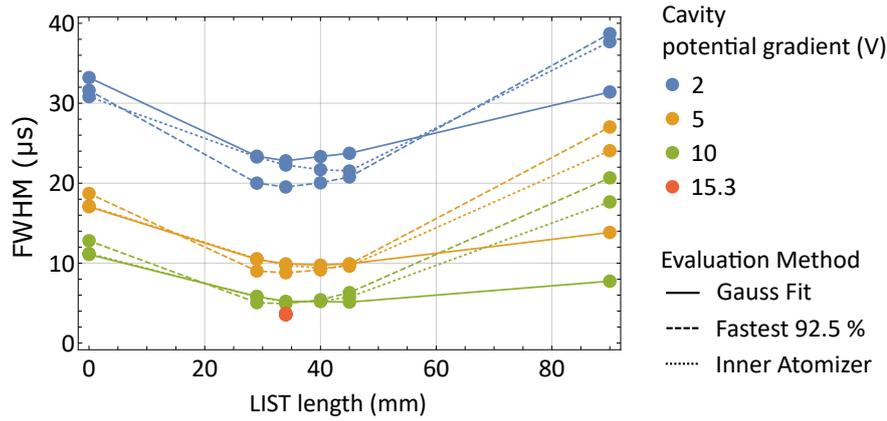
Figure A.18: Overview of selected results from the simulations on the applicability of the
LIST for a time-of-flight based laser ion source. An intermediate length in the range of the
calculated 34 mm is desired for best compressed bunches, yet the influence of the cavity
potential drop appears to be of even higher importance. See text for details.

1. The most desirable geometry for compressed ion bunches is indeed found near the
   value of the length of the ion source itself, i.e. 34 mm. Nevertheless, in that range
   margins for minor changes are still present, i.e. no deviation in bunch width can
   be extracted from the data for lengths between 29 mm and 45 mm.

2. The potential gradient along the source plays a very important role. Actually,
   going from 2 V typical for the routinely used metal tubes up to 5 V for a standard
   RILIS source already seems to have a greater effect than adding the drift distance.
   Methods for increasing the voltage gradient are discussed in sec. A.4.

Apart from this, the simulation data also allows for extraction of additional infor-
mation, particularly if the outcome is sensitive to specific parameter variations. An
illustrating example is the dependence on the temperature as characterizing parameter
for the velocity distribution, shown in fig. A.19.
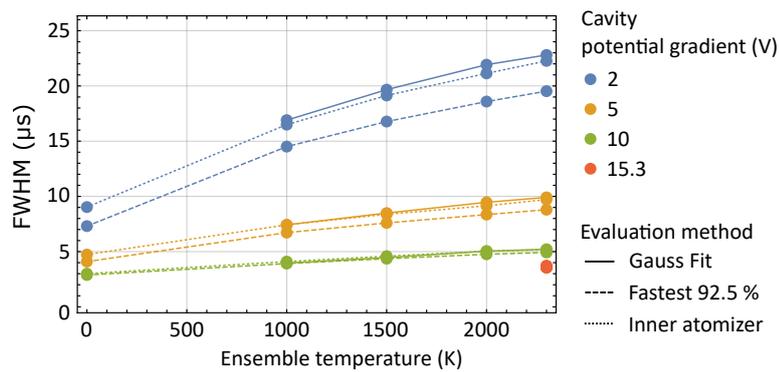
Figure A.19: Dependence of the bunch width on the temperature of the underlying Maxwell-
Boltzmann distribution as derived from the simulation results. Incorporating this parameter
is essential. For higher voltage gradients, the absolute difference is less pronounced, yet a
$\approx 25\,\%$ relative prolongation from 1000 K to 2300 K is apparent in all cases.

Here, a nominal temperature of 0 K corresponds to all particles at rest at the start
of the simulation. The result shows that incorporating the velocity distribution indeed

has a considerable influence. While for higher voltage gradients, the absolute difference is less pronounced, a $\approx 25\%$ relative prolongation from $1000\,\text{K}$ $2300\,\text{K}$ is apparent in all cases.

More information can be extracted from the comprehensive simulation investigations in tables B.2 to B.4, briefly summarized as follows:

- The voltage of the extraction electrode, always held at the same distance of $40\,\text{mm}$ from the LIST exit electrode, plays no significant role in the investigated range of $10\,\text{kV}$ - $30\,\text{kV}$.

- The diameter of the LIST's exit electrode orifice was varied for the theoretically optimum LIST length of $34\,\text{mm}$ to investigate the influence of extraction field leakage. For the tested values of $3\,\text{mm}$, $7\,\text{mm}$ and $15\,\text{mm}$, no significant influence was observed.

- With their individual terminal velocity recorded after entering the extraction electrode, the bunch structure of the ensemble can also be calculated for different positions in the downstream beam line, corresponding to longer evolution times. This is especially interesting for beam gating deflectors, which might only be installed at certain points. Also here, no differences are seen, as was expected from the involved velocity and time dimensions: At an extraction voltage of $30\,\text{kV}$, atoms of mass $150\,\text{u}$ travel with roughly $2\,\text{m/µs}$, compared to velocity differences in the order of mm/µs for potential gradients of $10\,\text{V}$.

The first two points are naturally consistent to the other results from shorter or longer LIST bodies with the same exit electrode diameter and extraction voltage as shown in fig. A.18, as both effects effectively alter the field-free drift length before the acceleration field play a role.

As stated in the introduction to these investigations, the results from these simulations can clearly only be seen as a starting point towards systematic experimental investigations.

A.4 A Microsecond-scale Heating Current Switch

As pointed out in sec. A.3, besides the introduction of a field-free drift track adjacent to the ion source, the overall electric potential gradient along the cavity might play an even more important role for creation of temporally well-defined, compressed ion bunches imprinted by the pulsed laser system, and correspondingly for beam purification by fast ion beam gating techniques. In fact, such kind of experimental investigations have already been performed e.g. at the ISOLDE off-line separator [82]. In this work, the FWHM of laser-ionized gallium ion bunches was reduced from $13\,\text{µs}$ to $3.8\,\text{µs}$ by replacing the standard tantalum capillary with a voltage drop of $2.2\,\text{V}$ by a thin-walled graphite tube ($9.3\,\text{V}$), exhibiting higher specific electric resistance because of smaller cross section area and different material properties. Thus, a given electric current demands a higher voltage. With this setup, a beam gate of $10\,\text{µs}$ width was employed in synchronization with the $10\,\text{kHz}$ repetition rate laser system and corresponding contamination suppression of a factor 10 was shown at negligible losses in laser ion current. The authors also present the vitreous ("glassy") carbon variant SIGRADUR® G with an even higher intrinsic resistivity, and show that this material could potentially be applicable as ion source cavity. Similar investigations for increasing the voltage for a given heating current are also presented for a thin-wall niobium cavity ($0.5\,\text{mm}$ wall thickness, yielding $14\,\text{µs}$ bunches) [155], or a $0.03\,\text{mm}$ thick tantalum/tungsten foil combination ($4\,\text{µs}$) [156].

In general, the voltage gradient along the cavity is strictly coupled to the heating current via the Ohm's law. The current in turn is determined by the envisaged operation temperature of the source, governed by the dissipated electric power. Decoupling these two parameters, i.e. operating temperature and potential gradient, would bring essential advantages. The influence of the potential gradient at a given operation condition could directly be measured, and the dependence on specific materials of high resistivity (which might exhibit disadvantageous behavior in terms of robustness or chemical reactiveness) would be diminished. The application of pulsed ohmic heating for this purpose has been described in [152], was followed up in [82] and is briefly recapitulated here. The concept comprises a pulse-width modulated heating scheme, in which the current is only applied in a fraction of the time. To dissipate the same effective power and thus keep the source on the same constant temperature, a significantly higher current and consequently higher voltage drop in comparison to DC operation is needed for the duration of actual heating, as no power is dissipated in the remaining time. Assuming no additional losses in the system, a duty factor D can be calculated from the fraction of the ohmic heating power $P_{\mathrm{Ohm}} = U^2/R$ with desired voltage U along a total resistance R to the demanded overall heating power P_{Heat} to maintain a desired temperature as

$$D = \frac{P_{\mathrm{Heat}}}{P_{\mathrm{Ohm}}} = \frac{P_{\mathrm{Heat}} R}{U^2}. \tag{A.10}$$

In order to keep stable operation conditions, the cycling time should be fast enough to not be followed by the more inert temperature behavior of the source. Moreover, a potential ability to synchronize these cycles to the repetition rate of the ionizing laser system is highly favorable, so that ions are always created in a phase of heating and applied accelerating voltage to be efficiently guided towards the cavity exit. Therefore, the requirements for a technical system are

- shortest possible switching times in the µs regime and

- capability of handling up to some 100 A of current.

Additionally, the power supply has to be compliant to provide both high currents and voltages at the same time and work with quickly changing load properties.

Current switches capable of these requirements are found in the product line of solid-state Insulated-Gate Bipolar Transistors (IGBT). On top, they should feature low collector-emitter saturation voltages, which define the power dissipated by the high current running through the switch itself and therefore the demanded cooling capacities. Tests were initially performed at ISOLDE with an IXYS MID145-12A3 IGBT switch[1], with both 10 kHz and 10100 Hz repetition rate and a duty cycle of 50 % [82]. Indeed, an increase in effective, time-averaged voltage and a decrease in current was observed while keeping the same temperature, yet a 3-fold higher power dissipation occurred in the whole system. These additional loss sources are to be evaluated and must be taken into account for a future, robustly working setup at an actual ion source assembly.

A.4.1   An H-bridge Model Prototype

Within the work of this thesis, a more sophisticated setup was developed. It is still in an initial prototype testing configuration to identify potential problems and perform long-term performance tests and has not been coupled to an ion source setup yet, so this section's aims to describe the status of the ongoing developments.

---

[1]Data sheet available e.g. via https://www.mouser.de/datasheet/2/205/MID145-12A3-476640.pdf

Instead of one single switch, the system was extended to an H-bridge configuration with four switches. This assembly features the possibility of not only performing on/off switching, but also current direction reversal in a fast way. The principle is shown in fig. A.20.
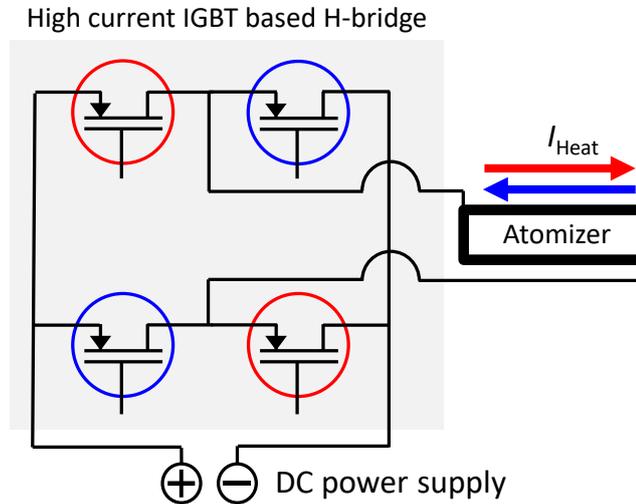
Figure A.20: Schematic overview of the H-bridge type design for fast current pulsing and direction reversal from a DC power supply, based on IGBT switches. Depending on which two color-coded switches are "open", the direction of the heating current I_{heat} and thus voltage gradient can be chosen. The system is operated by a home-built electronic control unit via TTL input.

The specific IGBT switches were chosen as IXGN200N60B3[2], featuring maximum current capacites of 300 A at optimum cooling conditions, and are designed for switching rates up to 40 kHz. The four switches are mounted onto a water-cooled copper block. Galvanically isolated, home-built active driver modules which supply voltages of 14 V within 1 µs are directly connected to their respective gate connections. These drivers are individually addressed by a control and power supply unit, which is able to toggle between opening two switches and closing the two remaining ones, or perform simultaneous on/off switching of two selected IGBTs. This can be done either directly manually on the control unit, or by means of TTL signal input from an external source (e.g. the 10 kHz laser system trigger). Thus, the two modes of operation are realized: Fast on/off switching of the whole current flow circuit for the pulse-width modulation heating technique described above, and fast heating current reversal on the load. The respective circuits were developed, designed and built by the QUANTUM working group's electronics specialist, M. Boeßenecker, and can be found in appendix B.2.

While a laser repetition rate synchronization is a medium range goal, the second operation mode of on-demand current direction reversal can be of immediate use. It allows in-situ polarity change of the voltage gradient while the ion source is heated, and only introduces minute changes to the system: The power supply has to be capable of providing the additional power dissipated in the two switches as $V_{CE} \cdot I_{Heat}$ with the the IGBT's collector-emitter saturation voltage V_{CE} (= 1.50 V for the units chosen for this prototype). For LIST-type ion sources, where laser ionization takes place outside the

---

[2]Data sheet available e.g. via https://www.mouser.de/datasheet/2/205/DS99941B(IXGN200N60B3)-1110106.pdf

hot cavity and ions created within are suppressed, the voltage gradient direction can be selected to support this effect by holding ions back in the cavity itself. Additionally, this will preserve species of interest ionized by the lasers inside the cavity, which would otherwise also be deflected by the repeller electrodes and thus be lost. If hold back in the source, they can later on re-neutralize and effuse into the LIST volume as atoms. The current reversal then provides a measure to immediately switch between this additional suppression and "conventional" guiding of ions towards extraction, in an analogue way to toggling between ion guide and LIST mode for the established LIST source (sec. 3.4.1).

The method of switching current polarity to reduce surface ion contamination and perform high resolution spectroscopy in the effusing atom cone in front of the cavity (yet without a shielding structure as the PI-LIST described in sec. 3.4.3), is used routinely in the small, low energy Mainz Atomic Beam Unit (MABU), e.g. for hyperfine structure investigations of copper [25] and technetium [24]. Up to now, a change from the standard source voltage gradient configuration for initial setup and optimization to this operation mode required time-consuming cooling, manual cable-swapping at the power supply and re-heating of the ion source, while with quasi-immediate polarity change this procedure becomes obsolete.

The capability of this system to work in the required range was shown in a pump stand on a graphite source heated to roughly $2000\,\mathrm{K}$, exhibiting a DC current of $87\,\mathrm{A}$, a voltage of $3.7\,\mathrm{V}$ along the cavity, and an overall voltage on the system of $12\,\mathrm{V}$, delivered by a Xantrex XFR 12-100 DC power supply. The polarity switching event monitored by an oscilloscope connected directly to the cavity's front and exit, is shown in fig. A.21.
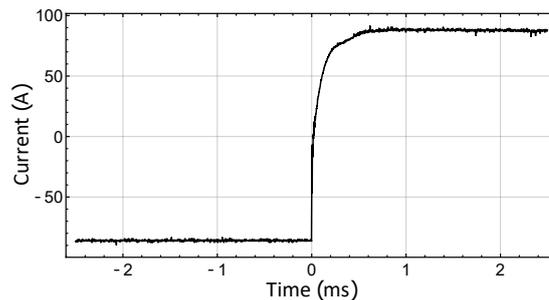
Figure A.21: Test measurement of fast high current polarity switching on a graphite hot cavity. The event was measured with an oscilloscope directly across the cavity via wires connected to its front and rear. The measured voltage of $3.7\,\mathrm{V}$ corresponds to a heating current of $87\,\mathrm{A}$. The overall switching duration of below $0.5\,\mathrm{ms}$ is well suited to not impose mechanical stress, as the inert temperature stays constant in this period.

For this test setup, the total current was limited by the maximum output voltage of $12\,\mathrm{V}$ of the power supply. Yet, it already provided realistic working conditions for graphite sources. The fast overall switching time of below $0.5\,\mathrm{ms}$ is well suited to not impose excessive mechanical stress on the construction by temperature changes, as this parameter is too inert to change within this short time regime.

More rigorous tests with more powerful supplies for higher currents and voltages, and automatic switching will be performed in the future. The scope is also to characterize the decoupling of voltage and current for given temperatures by the pulse-width modulation method, quantify losses in the system compared to DC operation, and eventually provide a ready-to-use module for easy implementation in between power supply and hot cavity at the separator front end.

Supplemental Material

B.1 Time-of-Flight Laser Ion Source Simulation Results

Table B.1: Abbreviations used in the following table compilations. See sec. A.3.1 for details especially on evaluation methods.

L	Length of LIST unit ($L = 0\,\mathrm{mm}$ means no LIST included)
ΔU	Overall potential drop across the cavity
m	Mass of simulated particles
U_{Ex}	Extraction voltage
d_{EE}	Diameter of exit electrode orifice
T	Temperature of underlying Maxwell-Boltzmann velocity distribution
$\Delta\tau$	Half-height width of ion bunch
$\%_{\Delta\tau}$	Fraction of all simulated ions within a symmetric region $\Delta\tau$ around the distribution's median value
Method A	Omitting the latest arriving $7.5\,\%$ of simulated ions
Method B	Omitting the simulated ions created within the $10\,\%$ of the cavity length nearest to its exit
Gaussian Fit	Fit of a Gaussian distribution to the whole data, or the data of method B in case of no LIST attached. In the purely academic case of $T = 0\,\mathrm{K}$, the data is not describable with a Gaussian profile, indicated by "-" in the table.

Table B.2: Compilation of simulation results for the time-of-flight based laser ion source for compressed ion bunches as described in sec. A.3.1. Bunch widths are recorded at a position directly inside the extraction electrode. For abbreviations see tab. B.1.

						Method A		Method B		Gaussian Fit	
L	ΔU	m	U_{Ex}	d_{EE}	T	$\Delta\tau$	$\%_{\Delta\tau}$	$\Delta\tau$	$\%_{\Delta\tau}$	$\Delta\tau$	$\%_{\Delta\tau}$
mm	V	u	kV	mm	K	µs	%	µs	%	µs	%
34	2	150	10	7	2300	19.83	69	21.79	73	23.19	76
34	2	150	30	7	2300	19.53	69	22.27	75	22.80	77
34	2	150	60	7	2300	19.56	69	22.64	76	22.79	76

Table B.2 – continued from previous page

						Method A		Method B		Gaussian Fit	
L	ΔU	m	U_{Ex}	d_{EE}	T	$\Delta\tau$	$\%_{\Delta\tau}$	$\Delta\tau$	$\%_{\Delta\tau}$	$\Delta\tau$	$\%_{\Delta\tau}$
mm	V	u	kV	mm	K	µs	%	µs	%	µs	%
34	5	150	10	7	2300	8.98	69	9.39	71	9.81	73
34	5	150	30	7	2300	8.80	69	9.72	73	9.91	74
34	5	150	60	7	2300	8.79	69	9.92	74	10.04	75
34	10	150	10	7	2300	5.12	70	5.12	71	5.14	71
34	10	150	30	7	2300	4.92	70	5.17	72	5.21	72
34	10	150	60	7	2300	4.89	69	5.41	73	5.33	72
45	2	150	10	7	2300	21.60	69	21.95	70	23.95	73
45	2	150	30	7	2300	20.78	69	21.52	70	23.73	75
45	2	150	60	7	2300	20.36	69	21.51	71	23.44	75
45	5	150	10	7	2300	10.69	71	10.26	69	10.17	69
45	5	150	30	7	2300	9.85	70	9.62	69	9.92	70
45	5	150	60	7	2300	9.36	69	9.42	70	9.72	71
45	10	150	10	7	2300	7.11	77	6.28	73	5.14	65
45	10	150	30	7	2300	6.31	74	5.76	71	5.12	67
45	10	150	60	7	2300	5.77	73	5.37	71	4.95	67
40	2	150	10	7	2300	20.61	69	21.64	71	23.41	75
40	2	150	30	7	2300	20.05	68	21.70	73	23.33	76
40	2	150	60	7	2300	19.64	68	21.75	73	22.91	76
40	5	150	10	7	2300	9.62	70	9.58	70	9.84	71
40	5	150	30	7	2300	9.15	69	9.39	70	9.75	72
40	5	150	60	7	2300	8.94	69	9.43	71	9.78	73
40	10	150	10	7	2300	6.02	74	5.55	71	5.09	68
40	10	150	30	7	2300	5.42	72	5.24	69	5.21	70
40	10	150	60	7	2300	5.15	70	5.12	70	5.17	71
29	2	150	10	7	2300	19.65	68	22.51	75	22.92	76
29	2	150	10	7	2300	19.50	69	22.56	76	22.94	76
29	2	150	30	7	2300	20.01	68	23.27	75	23.37	75
29	2	150	60	7	2300	20.71	68	23.60	74	24.58	76
29	5	150	10	7	2300	8.83	68	9.85	74	10.10	75
29	5	150	30	7	2300	9.01	68	10.55	77	10.46	76
29	5	150	60	7	2300	9.28	69	10.98	77	10.84	76
29	10	150	10	7	2300	4.99	69	5.40	73	5.41	73
29	10	150	30	7	2300	5.06	68	5.80	75	5.83	76
29	10	150	60	7	2300	5.16	69	6.06	77	6.09	77
34	2	150	30	15	2300	21.22	68	24.05	74	25.27	76
34	2	150	60	15	2300	22.23	67	24.68	72	27.01	77
34	5	150	30	15	2300	9.40	69	11.01	77	11.01	76
34	5	150	60	15	2300	10.28	68	11.72	74	12.26	77
34	10	150	30	15	2300	5.25	68	6.19	76	6.22	76
34	10	150	60	15	2300	5.66	68	6.67	75	6.79	77
34	2	150	30	3	2300	20.69	68	21.54	70	23.61	75
34	2	150	60	3	2300	20.43	69	21.63	71	23.56	75
34	5	150	30	3	2300	9.66	70	9.52	69	9.75	70

Table B.2 – continued from previous page

						Method A		Method B		Gaussian Fit	
L	ΔU	m	U_{Ex}	d_{EE}	T	$\Delta\tau$	$\%_{\Delta\tau}$	$\Delta\tau$	$\%_{\Delta\tau}$	$\Delta\tau$	$\%_{\Delta\tau}$
mm	V	u	kV	mm	K	μs	%	μs	%	μs	%
34	5	150	60	3	2300	9.43	69	9.47	70	9.94	72
34	10	150	30	3	2300	6.02	73	5.55	71	5.16	67
34	10	150	60	3	2300	5.66	73	5.36	71	5.09	68
34	2	50	60	7	2300	11.33	68	13.16	76	13.34	76
34	2	100	60	7	2300	16.03	68	18.59	76	18.81	76
34	2	150	60	7	2300	19.62	69	22.51	76	22.98	76
34	2	200	60	7	2300	22.75	68	26.24	75	26.53	76
34	2	250	60	7	2300	25.34	68	29.49	76	29.78	77
34	5	50	60	7	2300	5.14	69	5.85	76	5.92	76
34	5	100	60	7	2300	7.22	69	8.16	75	8.33	76
34	5	150	60	7	2300	8.87	69	10.05	75	10.15	75
34	5	200	60	7	2300	10.24	69	11.60	75	11.82	75
34	5	250	60	7	2300	11.45	68	13.05	74	13.23	75
34	10	50	60	7	2300	2.83	68	3.13	73	3.15	75
34	10	100	60	7	2300	4.01	69	4.41	73	4.42	73
34	10	150	60	7	2300	4.90	69	5.41	73	5.46	73
34	10	200	60	7	2300	5.71	69	6.28	73	6.33	73
34	10	250	60	7	2300	6.37	69	7.05	73	6.96	73
34	2	150	30	7	0	7.31	74	9.03	80	-	-
34	2	150	30	7	1000	14.50	68	16.50	74	16.90	76
34	2	150	30	7	1500	16.77	69	19.14	75	19.66	77
34	2	150	30	7	2000	18.59	69	21.14	75	21.92	77
34	2	150	60	7	0	8.39	65	10.45	85	-	-
34	2	150	60	7	1000	14.89	68	17.34	76	17.50	77
34	2	150	60	7	1500	16.83	69	19.60	76	19.58	76
34	2	150	60	7	2000	18.66	69	21.69	76	21.75	76
34	5	150	30	7	0	4.10	75	4.73	78	-	-
34	5	150	30	7	1000	6.72	68	7.43	73	7.42	73
34	5	150	30	7	1500	7.60	69	8.38	73	8.49	74
34	5	150	30	7	2000	8.35	69	9.15	73	9.46	75
34	5	150	60	7	0	4.45	71	5.45	79	-	-
34	5	150	60	7	1000	6.82	69	7.86	75	7.86	75
34	5	150	60	7	1500	7.70	68	8.82	75	8.85	75
34	5	150	60	7	2000	8.54	69	9.73	75	9.84	76
34	10	150	30	7	0	2.88	79	3.00	79	-	-
34	10	150	30	7	1000	3.92	70	4.10	72	3.96	71
34	10	150	30	7	1500	4.36	70	4.59	72	4.46	70
34	10	150	30	7	2000	4.76	70	5.03	72	5.04	72
34	10	150	60	7	0	2.90	75	3.35	79	8.48	28
34	10	150	60	7	1000	3.89	69	4.34	73	4.16	72
34	10	150	60	7	1500	4.31	69	4.78	74	4.75	74
34	10	150	60	7	2000	4.70	69	5.20	73	5.15	73
34	15.3	7	30	7	2300	0.77	66	0.80	72	0.77	66

Table B.2 – continued on next page

Table B.2 – continued from previous page

						Method A		Method B		Gaussian Fit	
L	ΔU	m	U_{Ex}	d_{EE}	T	$\Delta\tau$	$\%_{\Delta\tau}$	$\Delta\tau$	$\%_{\Delta\tau}$	$\Delta\tau$	$\%_{\Delta\tau}$
mm	V	u	kV	mm	K	µs	%	µs	%	µs	%
34	15.3	23	30	7	2300	1.42	73	1.48	73	1.42	70
34	15.3	39	30	7	2300	1.83	70	1.90	72	1.83	70
34	15.3	150	30	7	2300	3.58	70	3.71	71	3.55	69
34	15.3	169	30	7	2300	3.79	70	3.90	71	3.81	70
34	15.3	7	2.7	7	2300	0.96	77	0.87	70	0.72	65
34	15.3	23	2.7	7	2300	1.74	75	1.55	73	1.32	65
34	15.3	39	2.7	7	2300	2.28	76	2.05	71	1.74	65
34	15.3	150	2.7	7	2300	4.45	76	4.02	72	3.41	66
34	15.3	169	2.7	7	2300	4.74	76	4.25	73	3.60	66
90	2	150	30	7	2300	38.70	73	37.69	73	31.40	66
90	2	150	60	7	2300	38.19	73	36.69	72	31.01	66
90	5	150	30	7	2300	27.02	77	24.06	75	13.84	59
90	5	150	60	7	2300	25.68	77	22.98	75	13.61	59
90	10	150	30	7	2300	20.67	77	17.66	75	7.74	55
90	10	150	60	7	2300	19.78	78	16.94	75	7.58	55
0	2	150	30	7	2300	31.61	66	30.82	66	33.20	77
0	2	150	60	7	2300	31.65	65	31.32	66	34.01	77
0	5	150	30	7	2300	18.71	70	17.15	68	17.05	76
0	5	150	60	7	2300	19.01	70	17.61	68	17.59	76
0	10	150	30	7	2300	12.80	73	11.21	69	11.08	76
0	10	150	60	7	2300	13.02	72	11.64	69	11.32	76
30	15.1	7	1.15	5	2300	1.03	78	0.88	71	0.65	66
30	15.1	23	1.15	5	2300	1.87	78	1.62	74	1.19	64
30	15.1	39	1.15	5	2300	2.42	79	2.10	74	1.57	62
30	15.1	150	1.15	5	2300	4.80	78	4.14	74	3.11	64
30	15.1	169	1.15	5	2300	5.09	78	4.40	74	3.26	64
30	15.1	173	1.15	5	2300	5.13	78	4.41	74	3.30	64
30	15.1	7	2.7	5	2300	0.94	76	0.83	72	0.65	62
30	15.1	23	2.7	5	2300	1.72	77	1.51	73	1.18	65
30	15.1	39	2.7	5	2300	2.24	78	1.98	74	1.57	63
30	15.1	150	2.7	5	2300	4.41	77	3.90	73	3.02	66
30	15.1	169	2.7	5	2300	4.68	77	4.12	73	3.24	64
30	15.1	173	2.7	5	2300	4.75	77	4.21	74	3.27	64
0	2	69	30	7	2300	21.28	66	20.81	67	22.31	77
0	2	69	32	7	2300	21.39	66	21.02	66	22.58	77
0	9.3	69	30	7	2300	9.03	72	7.97	69	7.90	76
0	9.3	69	32	7	2300	9.04	72	7.97	69	7.93	76

Table B.3: Compilation of simulation results for the time-of-flight based laser ion source for compressed ion bunches as described in sec. A.3.1. Bunch widths are calculated for a position 5 m downstream the extraction electrode. For abbreviations see tab. B.1.

						Method A		Method B		Gaussian Fit	
L	ΔU	m	U_{Ex}	d_{EE}	T	$\Delta\tau$	$\%_{\Delta\tau}$	$\Delta\tau$	$\%_{\Delta\tau}$	$\Delta\tau$	$\%_{\Delta\tau}$
mm	V	u	kV	mm	K	µs	%	µs	%	µs	%
34	2	150	10	7	2300	19.83	69	21.79	73	23.19	76
34	2	150	30	7	2300	19.53	69	22.27	75	22.80	77
34	2	150	60	7	2300	19.56	69	22.64	76	22.79	76
34	5	150	10	7	2300	8.98	69	9.39	71	9.81	73
34	5	150	30	7	2300	8.80	69	9.72	73	9.91	74
34	5	150	60	7	2300	8.79	69	9.92	74	10.04	75
34	10	150	10	7	2300	5.12	70	5.12	71	5.14	71
34	10	150	30	7	2300	4.92	70	5.17	72	5.21	72
34	10	150	60	7	2300	4.89	69	5.41	73	5.33	72
45	2	150	10	7	2300	21.60	69	21.95	70	23.95	73
45	2	150	30	7	2300	20.78	69	21.52	70	23.73	75
45	2	150	60	7	2300	20.36	69	21.51	71	23.44	75
45	5	150	10	7	2300	10.69	71	10.26	69	10.17	69
45	5	150	30	7	2300	9.85	70	9.62	69	9.92	70
45	5	150	60	7	2300	9.36	69	9.42	70	9.72	71
45	10	150	10	7	2300	7.11	77	6.28	73	5.14	65
45	10	150	30	7	2300	6.31	74	5.76	71	5.12	67
45	10	150	60	7	2300	5.77	73	5.37	71	4.95	67
40	2	150	10	7	2300	20.61	69	21.64	71	23.41	75
40	2	150	30	7	2300	20.05	68	21.70	73	23.33	76
40	2	150	60	7	2300	19.64	68	21.75	73	22.91	76
40	5	150	10	7	2300	9.62	70	9.58	70	9.84	71
40	5	150	30	7	2300	9.15	69	9.39	70	9.75	72
40	5	150	60	7	2300	8.94	69	9.43	71	9.78	73
40	10	150	10	7	2300	6.02	74	5.55	71	5.09	68
40	10	150	30	7	2300	5.42	72	5.24	69	5.21	70
40	10	150	60	7	2300	5.15	70	5.12	70	5.17	71
29	2	150	10	7	2300	19.65	68	22.51	75	22.92	76
29	2	150	10	7	2300	19.50	69	22.56	76	22.94	76
29	2	150	30	7	2300	20.01	68	23.27	75	23.37	75
29	2	150	60	7	2300	20.71	68	23.60	74	24.58	76
29	5	150	10	7	2300	8.83	68	9.85	74	10.10	75
29	5	150	30	7	2300	9.01	68	10.55	77	10.46	76
29	5	150	60	7	2300	9.28	69	10.98	77	10.84	76
29	10	150	10	7	2300	4.99	69	5.40	73	5.41	73
29	10	150	30	7	2300	5.06	68	5.80	75	5.83	76
29	10	150	60	7	2300	5.16	69	6.06	77	6.09	77
34	2	150	30	15	2300	21.22	68	24.05	74	25.27	76
34	2	150	60	15	2300	22.23	67	24.68	72	27.01	77
34	5	150	30	15	2300	9.40	69	11.01	77	11.01	76
34	5	150	60	15	2300	10.28	68	11.72	74	12.26	77

Table B.3 – continued on next page

Table B.3 – continued from previous page

						Method A		Method B		Gaussian Fit	
L	ΔU	m	U_{Ex}	d_{EE}	T	$\Delta\tau$	$\%_{\Delta\tau}$	$\Delta\tau$	$\%_{\Delta\tau}$	$\Delta\tau$	$\%_{\Delta\tau}$
mm	V	u	kV	mm	K	µs	%	µs	%	µs	%
34	10	150	30	15	2300	5.25	68	6.19	76	6.22	76
34	10	150	60	15	2300	5.66	68	6.67	75	6.79	77
34	2	150	30	3	2300	20.69	68	21.54	70	23.61	75
34	2	150	60	3	2300	20.43	69	21.63	71	23.56	75
34	5	150	30	3	2300	9.66	70	9.52	69	9.75	70
34	5	150	60	3	2300	9.43	69	9.47	70	9.94	72
34	10	150	30	3	2300	6.02	73	5.55	71	5.16	67
34	10	150	60	3	2300	5.66	73	5.36	71	5.09	68
34	2	50	60	7	2300	11.33	68	13.16	76	13.34	76
34	2	100	60	7	2300	16.03	68	18.59	76	18.81	76
34	2	150	60	7	2300	19.62	69	22.51	76	22.98	76
34	2	200	60	7	2300	22.75	68	26.24	75	26.53	76
34	2	250	60	7	2300	25.34	68	29.49	76	29.78	77
34	5	50	60	7	2300	5.14	69	5.85	76	5.92	76
34	5	100	60	7	2300	7.22	69	8.16	75	8.33	76
34	5	150	60	7	2300	8.87	69	10.05	75	10.15	75
34	5	200	60	7	2300	10.24	69	11.60	75	11.82	75
34	5	250	60	7	2300	11.45	68	13.05	74	13.23	75
34	10	50	60	7	2300	2.83	68	3.13	73	3.15	75
34	10	100	60	7	2300	4.01	69	4.41	73	4.42	73
34	10	150	60	7	2300	4.90	69	5.41	73	5.46	73
34	10	200	60	7	2300	5.71	69	6.28	73	6.33	73
34	10	250	60	7	2300	6.37	69	7.05	73	6.96	73
34	2	150	30	7	0	7.31	74	9.03	80	-	-
34	2	150	30	7	1000	14.50	68	16.50	74	16.90	76
34	2	150	30	7	1500	16.77	69	19.14	75	19.66	77
34	2	150	30	7	2000	18.59	69	21.14	75	21.92	77
34	2	150	60	7	0	8.39	65	10.45	85	-	-
34	2	150	60	7	1000	14.89	68	17.34	76	17.50	77
34	2	150	60	7	1500	16.83	69	19.60	76	19.58	76
34	2	150	60	7	2000	18.66	69	21.69	76	21.75	76
34	5	150	30	7	0	4.10	75	4.73	78	-	-
34	5	150	30	7	1000	6.72	68	7.43	73	7.42	73
34	5	150	30	7	1500	7.60	69	8.38	73	8.49	74
34	5	150	30	7	2000	8.35	69	9.15	73	9.46	75
34	5	150	60	7	0	4.45	71	5.45	79	-	-
34	5	150	60	7	1000	6.82	69	7.86	75	7.86	75
34	5	150	60	7	1500	7.70	68	8.82	75	8.85	75
34	5	150	60	7	2000	8.54	69	9.73	75	9.84	76
34	10	150	30	7	0	2.88	79	3.00	79	-	-
34	10	150	30	7	1000	3.92	70	4.10	72	3.96	71
34	10	150	30	7	1500	4.36	70	4.59	72	4.46	70
34	10	150	30	7	2000	4.76	70	5.03	72	5.04	72

Table B.3 – continued from previous page

						Method A		Method B		Gaussian Fit	
L	ΔU	m	U_{Ex}	d_{EE}	T	$\Delta\tau$	$\%_{\Delta\tau}$	$\Delta\tau$	$\%_{\Delta\tau}$	$\Delta\tau$	$\%_{\Delta\tau}$
mm	V	u	kV	mm	K	µs	%	µs	%	µs	%
34	10	150	60	7	0	2.90	75	3.35	79	8.48	28
34	10	150	60	7	1000	3.89	69	4.34	73	4.16	72
34	10	150	60	7	1500	4.31	69	4.78	74	4.75	74
34	10	150	60	7	2000	4.70	69	5.20	73	5.15	73
34	15.3	7	30	7	2300	0.77	66	0.80	72	0.77	66
34	15.3	23	30	7	2300	1.42	73	1.48	73	1.42	70
34	15.3	39	30	7	2300	1.83	70	1.90	72	1.83	70
34	15.3	150	30	7	2300	3.58	70	3.71	71	3.55	69
34	15.3	169	30	7	2300	3.79	70	3.90	71	3.81	70
34	15.3	7	2.7	7	2300	0.96	77	0.87	70	0.72	65
34	15.3	23	2.7	7	2300	1.74	75	1.55	73	1.32	65
34	15.3	39	2.7	7	2300	2.28	76	2.05	71	1.74	65
34	15.3	150	2.7	7	2300	4.45	76	4.02	72	3.41	66
34	15.3	169	2.7	7	2300	4.74	76	4.25	73	3.60	66
90	2	150	30	7	2300	38.70	73	37.69	73	31.40	66
90	2	150	60	7	2300	38.19	73	36.69	72	31.01	66
90	5	150	30	7	2300	27.02	77	24.06	75	13.84	59
90	5	150	60	7	2300	25.68	77	22.98	75	13.61	59
90	10	150	30	7	2300	20.67	77	17.66	75	7.74	55
90	10	150	60	7	2300	19.78	78	16.94	75	7.58	55
0	2	150	30	7	2300	31.61	66	30.82	66	33.20	77
0	2	150	60	7	2300	31.65	65	31.32	66	34.01	77
0	5	150	30	7	2300	18.71	70	17.15	68	17.05	76
0	5	150	60	7	2300	19.01	70	17.61	68	17.59	76
0	10	150	30	7	2300	12.80	73	11.21	69	11.08	76
0	10	150	60	7	2300	13.02	72	11.64	69	11.32	76
30	15.1	7	1.15	5	2300	1.03	78	0.88	71	0.65	66
30	15.1	23	1.15	5	2300	1.87	78	1.62	74	1.19	64
30	15.1	39	1.15	5	2300	2.42	79	2.10	74	1.57	62
30	15.1	150	1.15	5	2300	4.80	78	4.14	74	3.11	64
30	15.1	169	1.15	5	2300	5.09	78	4.40	74	3.26	64
30	15.1	173	1.15	5	2300	5.13	78	4.41	74	3.30	64
30	15.1	7	2.7	5	2300	0.94	76	0.83	72	0.65	62
30	15.1	23	2.7	5	2300	1.72	77	1.51	73	1.18	65
30	15.1	39	2.7	5	2300	2.24	78	1.98	74	1.57	63
30	15.1	150	2.7	5	2300	4.41	77	3.90	73	3.02	66
30	15.1	169	2.7	5	2300	4.68	77	4.12	73	3.24	64
30	15.1	173	2.7	5	2300	4.75	77	4.21	74	3.27	64
0	2	69	30	7	2300	21.28	66	20.81	67	22.31	77
0	2	69	32	7	2300	21.39	66	21.02	66	22.58	77
0	9.3	69	30	7	2300	9.03	72	7.97	69	7.90	76
0	9.3	69	32	7	2300	9.04	72	7.97	69	7.93	76

Table B.4: Compilation of simulation results for the time-of-flight based laser ion source for compressed ion bunches as described in sec. A.3.1. Bunch widths are calculated for a position 20 m downstream the extraction electrode. For abbreviations see tab. B.1.

						Method A		Method B		Gaussian Fit	
L	ΔU	m	U_{Ex}	d_{EE}	T	$\Delta\tau$	$\%_{\Delta\tau}$	$\Delta\tau$	$\%_{\Delta\tau}$	$\Delta\tau$	$\%_{\Delta\tau}$
mm	V	u	kV	mm	K	µs	%	µs	%	µs	%
34	2	150	10	7	2300	19.83	69	21.79	73	23.19	76
34	2	150	30	7	2300	19.53	69	22.27	75	22.80	77
34	2	150	60	7	2300	19.56	69	22.64	76	22.79	76
34	5	150	10	7	2300	8.98	68	9.39	71	9.81	73
34	5	150	30	7	2300	8.80	69	9.71	73	9.91	74
34	5	150	60	7	2300	8.79	69	9.91	74	10.04	75
34	10	150	10	7	2300	5.12	70	5.11	70	5.13	71
34	10	150	30	7	2300	4.92	70	5.17	71	5.21	72
34	10	150	60	7	2300	4.89	69	5.41	73	5.33	73
45	2	150	10	7	2300	21.60	69	21.96	70	23.96	73
45	2	150	30	7	2300	20.78	69	21.52	70	23.73	75
45	2	150	60	7	2300	20.37	69	21.51	71	23.44	75
45	5	150	10	7	2300	10.70	71	10.27	69	10.17	69
45	5	150	30	7	2300	9.85	70	9.62	69	9.92	70
45	5	150	60	7	2300	9.36	69	9.42	70	9.72	71
45	10	150	10	7	2300	7.14	76	6.30	73	5.14	65
45	10	150	30	7	2300	6.31	74	5.76	71	5.12	67
45	10	150	60	7	2300	5.78	73	5.37	71	4.95	67
40	2	150	10	7	2300	20.61	69	21.64	71	23.41	75
40	2	150	30	7	2300	20.05	68	21.70	73	23.33	76
40	2	150	60	7	2300	19.64	68	21.75	73	22.91	76
40	5	150	10	7	2300	9.62	70	9.58	70	9.85	71
40	5	150	30	7	2300	9.15	69	9.39	70	9.75	72
40	5	150	60	7	2300	8.94	69	9.43	71	9.78	73
40	10	150	10	7	2300	6.03	74	5.56	71	5.09	68
40	10	150	30	7	2300	5.42	72	5.24	70	5.21	70
40	10	150	60	7	2300	5.15	71	5.12	70	5.17	71
29	2	150	10	7	2300	19.65	68	22.50	75	22.91	76
29	2	150	10	7	2300	19.50	69	22.56	76	22.94	76
29	2	150	30	7	2300	20.01	68	23.27	75	23.37	75
29	2	150	60	7	2300	20.71	68	23.60	74	24.58	76
29	5	150	10	7	2300	8.83	68	9.84	74	10.09	75
29	5	150	30	7	2300	9.01	68	10.54	77	10.46	76
29	5	150	60	7	2300	9.27	69	10.98	77	10.84	76
29	10	150	10	7	2300	4.98	69	5.37	73	5.39	73
29	10	150	30	7	2300	5.05	68	5.79	75	5.83	76
29	10	150	60	7	2300	5.15	68	6.06	77	6.09	77
34	2	150	30	15	2300	21.22	68	24.05	74	25.26	76
34	2	150	60	15	2300	22.23	67	24.68	72	27.00	77
34	5	150	30	15	2300	9.40	69	11.01	76	11.00	76
34	5	150	60	15	2300	10.28	68	11.71	74	12.25	77

Table B.4 – continued from previous page

						Method A		Method B		Gaussian Fit	
L	ΔU	m	U_{Ex}	d_{EE}	T	$\Delta\tau$	$\%_{\Delta\tau}$	$\Delta\tau$	$\%_{\Delta\tau}$	$\Delta\tau$	$\%_{\Delta\tau}$
mm	V	u	kV	mm	K	µs	%	µs	%	µs	%
34	10	150	30	15	2300	5.24	68	6.18	76	6.21	76
34	10	150	60	15	2300	5.65	67	6.66	76	6.79	77
34	2	150	30	3	2300	20.69	68	21.54	71	23.61	75
34	2	150	60	3	2300	20.43	69	21.63	71	23.56	75
34	5	150	30	3	2300	9.66	70	9.52	69	9.75	70
34	5	150	60	3	2300	9.43	70	9.47	70	9.95	72
34	10	150	30	3	2300	6.02	73	5.55	71	5.16	68
34	10	150	60	3	2300	5.66	73	5.36	70	5.09	68
34	2	50	60	7	2300	11.33	68	13.16	75	13.34	76
34	2	100	60	7	2300	16.03	69	18.59	76	18.81	76
34	2	150	60	7	2300	19.62	69	22.51	76	22.98	76
34	2	200	60	7	2300	22.75	68	26.24	75	26.53	76
34	2	250	60	7	2300	25.34	68	29.49	76	29.78	76
34	5	50	60	7	2300	5.14	70	5.85	75	5.92	76
34	5	100	60	7	2300	7.22	69	8.16	75	8.33	76
34	5	150	60	7	2300	8.87	69	10.04	75	10.15	76
34	5	200	60	7	2300	10.23	69	11.59	75	11.82	76
34	5	250	60	7	2300	11.45	68	13.05	75	13.23	75
34	10	50	60	7	2300	2.83	68	3.13	74	3.14	73
34	10	100	60	7	2300	4.01	69	4.41	74	4.41	73
34	10	150	60	7	2300	4.90	69	5.40	73	5.45	73
34	10	200	60	7	2300	5.71	69	6.28	73	6.33	73
34	10	250	60	7	2300	6.36	69	7.05	73	6.96	73
34	2	150	30	7	0	7.31	74	9.03	80	-	-
34	2	150	30	7	1000	14.50	68	16.49	74	16.90	76
34	2	150	30	7	1500	16.77	69	19.14	75	19.66	77
34	2	150	30	7	2000	18.59	69	21.14	75	21.92	77
34	2	150	60	7	0	8.39	65	10.45	85	-	-
34	2	150	60	7	1000	14.89	68	17.34	76	17.50	77
34	2	150	60	7	1500	16.82	69	19.60	76	19.58	76
34	2	150	60	7	2000	18.66	69	21.69	76	21.75	76
34	5	150	30	7	0	4.09	75	4.73	78	-	-
34	5	150	30	7	1000	6.72	68	7.42	73	7.42	73
34	5	150	30	7	1500	7.60	69	8.38	73	8.49	74
34	5	150	30	7	2000	8.35	69	9.15	73	9.46	75
34	5	150	60	7	0	4.45	70	5.45	79	-	-
34	5	150	60	7	1000	6.82	68	7.86	75	7.86	75
34	5	150	60	7	1500	7.70	68	8.82	75	8.85	75
34	5	150	60	7	2000	8.54	69	9.73	75	9.84	76
34	10	150	30	7	0	2.88	77	3.00	79	-	-
34	10	150	30	7	1000	3.91	70	4.10	72	3.96	71
34	10	150	30	7	1500	4.36	70	4.58	72	4.45	70
34	10	150	30	7	2000	4.76	70	5.03	72	5.04	73

Table B.4 – continued on next page

Table B.4 – continued from previous page

|						Method A		Method B		Gaussian Fit	
L	ΔU	m	U_{Ex}	d_{EE}	T	$\Delta\tau$	$\%_{\Delta\tau}$	$\Delta\tau$	$\%_{\Delta\tau}$	$\Delta\tau$	$\%_{\Delta\tau}$
mm	V	u	kV	mm	K	µs	%	µs	%	µs	%
34	10	150	60	7	0	2.90	76	3.34	79	-	-
34	10	150	60	7	1000	3.88	69	4.34	73	4.16	71
34	10	150	60	7	1500	4.31	69	4.77	74	4.76	74
34	10	150	60	7	2000	4.70	69	5.20	73	5.15	73
34	15.3	7	30	7	2300	0.77	66	0.80	72	0.77	66
34	15.3	23	30	7	2300	1.42	70	1.48	70	1.41	70
34	15.3	39	30	7	2300	1.83	70	1.89	72	1.83	70
34	15.3	150	30	7	2300	3.58	70	3.70	71	3.55	69
34	15.3	169	30	7	2300	3.79	69	3.90	72	3.80	70
34	15.3	7	2.7	7	2300	1.00	77	0.89	73	0.72	64
34	15.3	23	2.7	7	2300	1.82	76	1.61	72	1.32	65
34	15.3	39	2.7	7	2300	2.38	77	2.11	72	1.72	67
34	15.3	150	2.7	7	2300	4.64	77	4.14	73	3.39	66
34	15.3	169	2.7	7	2300	4.94	77	4.37	73	3.58	66
90	2	150	30	7	2300	38.70	73	37.69	73	31.40	66
90	2	150	60	7	2300	38.19	73	36.69	72	31.01	66
90	5	150	30	7	2300	27.03	77	24.06	75	13.84	59
90	5	150	60	7	2300	25.69	77	22.98	75	13.62	59
90	10	150	30	7	2300	20.68	77	17.66	75	7.75	55
90	10	150	60	7	2300	19.79	78	16.95	75	7.58	56
0	2	150	30	7	2300	31.59	66	30.82	66	33.20	77
0	2	150	60	7	2300	31.64	65	31.32	66	34.01	77
0	5	150	30	7	2300	18.68	70	17.14	68	17.05	76
0	5	150	60	7	2300	18.99	70	17.61	68	17.59	76
0	10	150	30	7	2300	12.76	73	11.20	69	11.07	76
0	10	150	60	7	2300	13.00	72	11.64	69	11.32	76
30	15.1	7	1.15	5	2300	1.29	78	1.11	74	0.77	64
30	15.1	23	1.15	5	2300	2.34	77	2.03	75	1.36	60
30	15.1	39	1.15	5	2300	3.04	78	2.65	74	1.82	62
30	15.1	150	1.15	5	2300	6.01	78	5.19	74	3.56	62
30	15.1	169	1.15	5	2300	6.38	78	5.52	74	3.71	62
30	15.1	173	1.15	5	2300	6.43	78	5.55	74	3.75	62
30	15.1	7	2.7	5	2300	1.00	78	0.87	71	0.66	61
30	15.1	23	2.7	5	2300	1.82	78	1.58	74	1.18	64
30	15.1	39	2.7	5	2300	2.37	78	2.07	74	1.58	65
30	15.1	150	2.7	5	2300	4.64	77	4.06	74	3.04	64
30	15.1	169	2.7	5	2300	4.93	78	4.30	73	3.24	64
30	15.1	173	2.7	5	2300	5.00	78	4.39	74	3.26	63
0	2	69	30	7	2300	21.27	66	20.81	67	22.30	77
0	2	69	32	7	2300	21.38	66	21.02	66	22.59	77
0	9.3	69	30	7	2300	9.01	72	7.96	69	7.89	76
0	9.3	69	32	7	2300	9.02	73	7.97	68	7.92	77

B.2 Fast High Current Switch
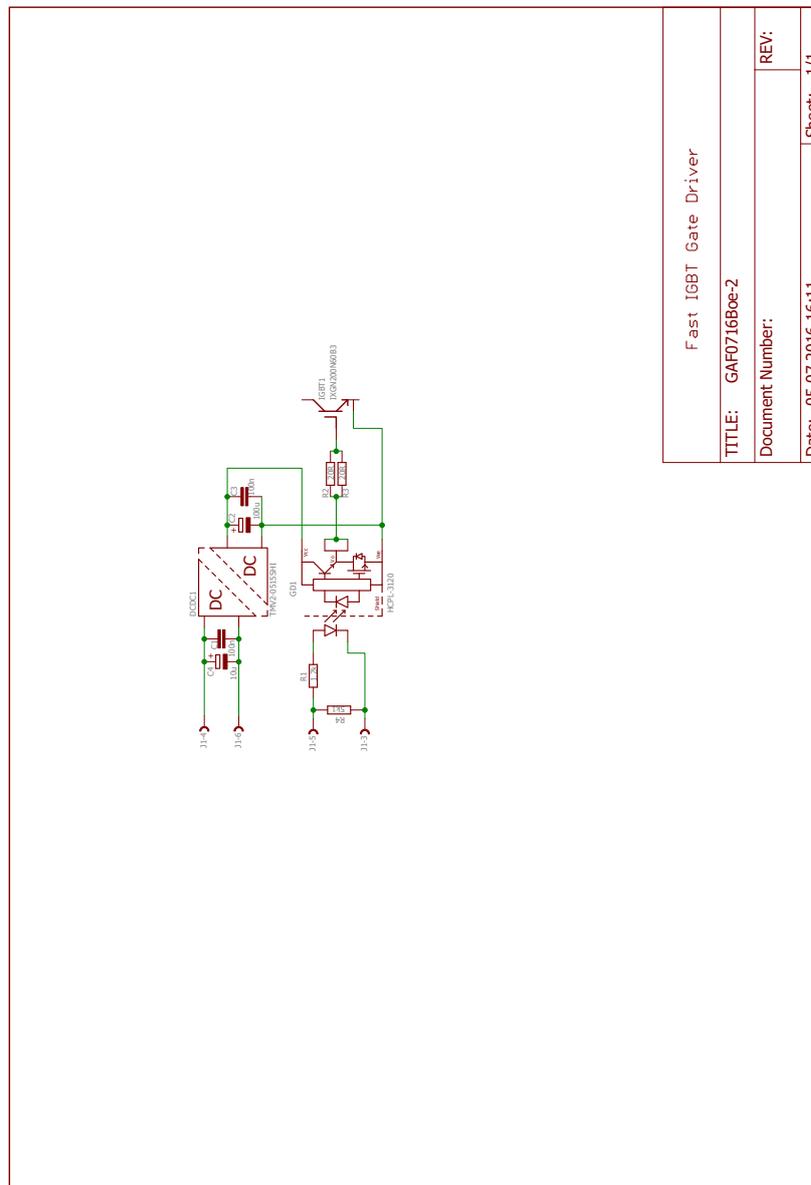
Figure B.1: Circuit diagram for the high current IGBT gate drivers. The active parts are controlled by the unit shown in fig. B.2 provide fast rise and fall times for switching. Design and manufacturing by the QUANTUM working group's electronics specialist M. Boeßenecker.
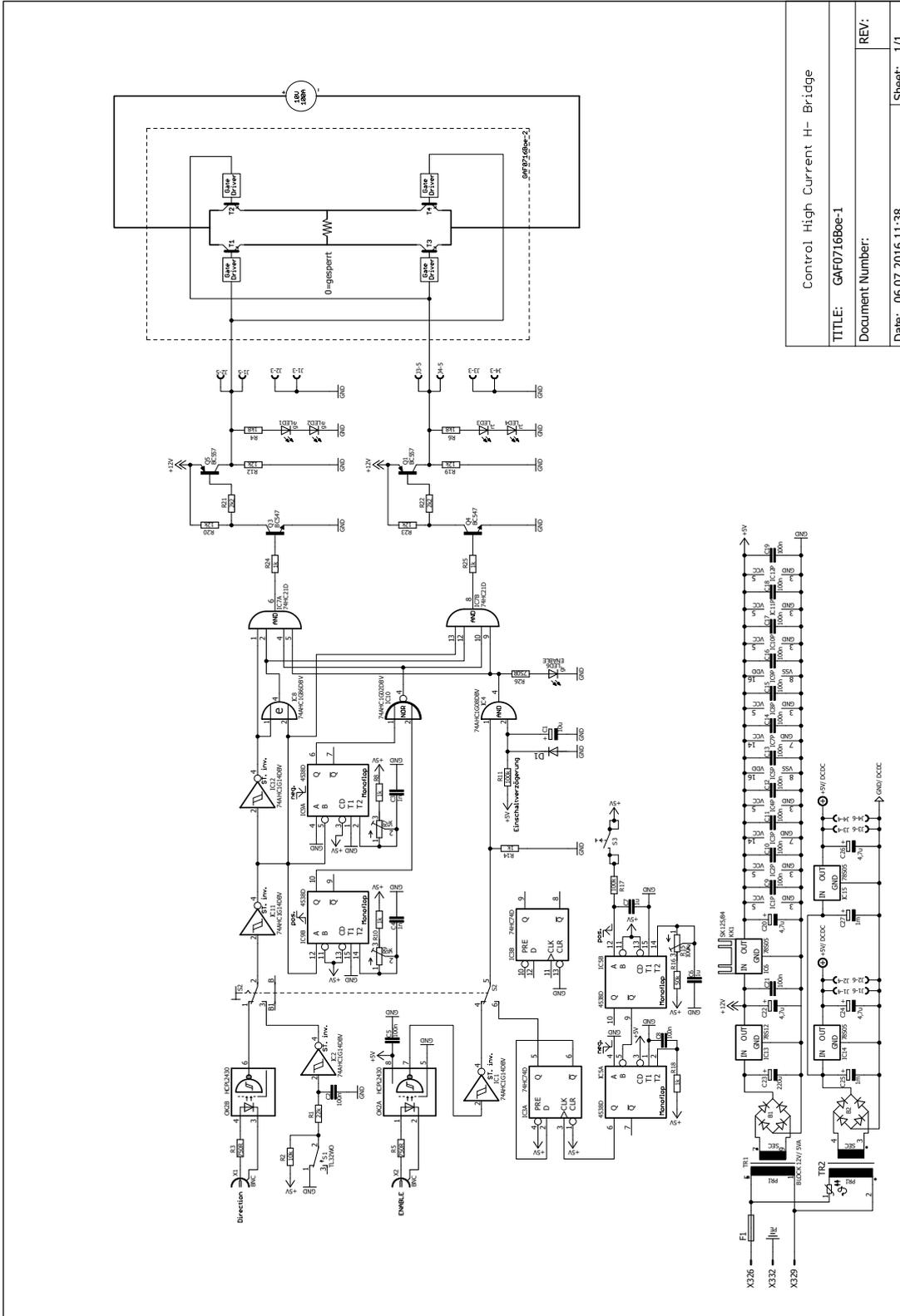
Figure B.2: Circuit diagram for the high current H-bridge. The unit controls individual driver modules (fig. B.1) either by manual or TTL input. Design and manufacturing by the QUANTUM working group's electronics specialist M. Boeßenecker.

Bibliography

[1] T. Maiman. "Stimulated optical radiation in ruby". In: *Nature* 187.4736 (1960), pp. 493–494. DOI: 10.1038/187493a0.

[2] G. D. Alkhazov et al. "Application of a high efficiency selective laser ion source at the IRIS facility". In: *Nuclear Instruments and Methods in Physics Research Section A: Accelerators, Spectrometers, Detectors and Associated Equipment* 306.1-2 (1991), pp. 400–402. DOI: 10.1016/0168-9002(91)90348-T.

[3] P. Campbell, I. D. Moore, and M. R. Pearson. "Laser spectroscopy for nuclear structure physics". In: *Progress in Particle and Nuclear Physics* 86 (2016), pp. 127–180. DOI: 10.1016/j.ppnp.2015.09.003.

[4] Klaus D. A. Wendt et al. "Laser based techniques for ultra trace isotope production, spectroscopy and detection". In: *Hyperfine Interactions* 162.1-4 (2006), pp. 147–157. DOI: 10.1007/s10751-005-9219-8.

[5] N. Trautmann, G. Passler, and K. D. A. Wendt. "Ultratrace analysis and isotope ratio measurements of long-lived radioisotopes by resonance ionization mass spectrometry (RIMS)". In: *Analytical and bioanalytical chemistry* 378.2 (2004), pp. 348–355. DOI: 10.1007/s00216-003-2183-8.

[6] N. Erdmann et al. "Resonance ionization mass spectroscopy for trace determination of plutonium in environmental samples". In: *Fresenius' Journal of Analytical Chemistry* 359.4-5 (1997), pp. 378–381. DOI: 10.1007/s002160050591.

[7] L. Gastaldo et al. "The electron capture in 163Ho experiment – ECHo". In: *The European Physical Journal Special Topics* 226.8 (2017), pp. 1623–1694. DOI: 10.1140/epjst/e2017-70071-y.

[8] P. Schumann. "Selektiver Nachweis von Uran-236 mittels hochauflösender Resonanzionisationsmassenspektrometrie". Ph.D. thesis. Johannes Gutenberg-Universität Mainz, 2005.

[9] G. Pantelić et al. "Qualitative overview of indoor radon surveys in Europe". In: *Journal of environmental radioactivity* 204 (2019), pp. 163–174. DOI: 10.1016/j.jenvrad.2019.04.010.

[10] R. dos Santos Augusto et al. "CERN-MEDICIS (Medical Isotopes Collected from ISOLDE): A new facility". In: *Applied Sciences* 4.2 (2014), pp. 265–281. DOI: 10.3390/app4020265.

[11] V. Gadelshin et al. "Laser resonance ionization spectroscopy on lutetium for the MEDICIS project". In: *Hyperfine Interactions* 238.1 (2017), p. 265. DOI: 10.1007/s10751-017-1406-x.

[12] K. Wendt et al. "Ionization potentials of the lanthanides and actinides – towards atomic spectroscopy of super-heavy elements". In: *Hyperfine Interactions* 227.1-3 (2014), pp. 55–67. DOI: 10.1007/s10751-014-1041-8.

[13] S. Rothe et al. "Measurement of the first ionization potential of astatine by laser ionization spectroscopy". In: *Nature communications* 4 (2013), p. 1835. DOI: 10.1038/ncomms2819.

[14] D. Studer et al. "Laser spectroscopy of the 1001-nm ground-state transition in dysprosium". In: *Physical Review A* 98.4 (2018). DOI: 10.1103/PhysRevA.98.042504.

[15] P. Naubereit et al. "Excited atomic energy levels in protactinium by resonance ionization spectroscopy". In: *Physical Review A* 98.2 (2018). DOI: `10.1103/PhysRevA.98.022505`.

[16] P. Naubereit et al. "Intrinsic quantum chaos and spectral fluctuations within the protactinium atom". In: *Physical Review A* 98.2 (2018). DOI: `10.1103/PhysRevA.98.022506`.

[17] R. Neugart et al. "Collinear laser spectroscopy at ISOLDE: New methods and highlights". In: *Journal of Physics G: Nuclear and Particle Physics* 44.6 (2017), p. 064002. DOI: `10.1088/1361-6471/aa6642`.

[18] R. Ferrer et al. "Towards high-resolution laser ionization spectroscopy of the heaviest elements in supersonic gas jet expansion". In: *Nature communications* 8 (2017), p. 14520. DOI: `10.1038/ncomms14520`.

[19] D. Allan Bromley, ed. *Treatise on Heavy Ion Science: Volume 8: Nuclei Far From Stability*. Boston, MA: Springer US, 1989. ISBN: 978-1-4613-0713-6. DOI: `10.1007/978-1-4613-0713-6`.

[20] B. A. Bushaw. "High-resolution laser-induced ionization spectroscopy". In: *Progress in analytical spectroscopy* 12.3 (1989), pp. 247–276.

[21] K. Wendt et al. "Ultratrace analysis of calcium with high isotopic selectivity by diodelaser resonance ionisation mass spectrometry". In: *Fresenius' Journal of Analytical Chemistry* 359.4-5 (1997), pp. 361–363. DOI: `10.1007/s002160050587`.

[22] S. Raeder. "Spurenanalyse von Aktiniden in der Umwelt mittels Resonanzionisationsmassenspektrometrie". Ph.D. thesis. Johannes Gutenberg-Universität Mainz, 2010.

[23] A. Hakimi. "Diodenlaserbasierte Resonanzionisationsmassenpektrometrie zur Spektroskopie und Ultraspurenanalyse an Uranisotopen". Ph.D. thesis. Johannes Gutenberg-Universität Mainz, 2013.

[24] Sebastian Raeder et al. "High resolution spectroscopy of the hyperfine structure splitting in 97,99Tc". In: *Hyperfine Interactions* 238.1 (2017), p. 1. DOI: `10.1007/s10751-016-1389-z`.

[25] R. P. de Groote et al. "Double-resonance-ionization mapping of the hyperfine structure of the stable Cu isotopes using pulsed narrowband Ti: Sapphire lasers". In: *Physical Review A* 92.2 (2015), p. 355. DOI: `10.1103/PhysRevA.92.022506`.

[26] T. Kron et al. "High efficiency resonance ionization of palladium with Ti: Sapphire lasers". In: *Journal of Physics B: Atomic, Molecular and Optical Physics* 49.18 (2016), p. 185003. DOI: `10.1088/0953-4075/49/18/185003`.

[27] H. Marshak. "Nuclear orientation of 166mHo in 165Ho single crystal". In: *Hyperfine Interactions* 10.1-4 (1981), pp. 1183–1188. DOI: `10.1007/BF01022073`.

[28] T. Kieck. "Source production for the neutrino mass experiment ECHo: Highly efficient ion implantation of ultrapure 163Ho". Ph.D. thesis. Johannes Gutenberg-Universität Mainz, 2019.

[29] R. Heinke et al. "High-resolution in-source laser spectroscopy in perpendicular geometry". In: *Hyperfine Interactions* 238.1 (2017), p. 127. DOI: `10.1007/s10751-016-1386-2`.

[30] R. Heinke et al. "Atom beam emersion from hot cavity laser ion sources". In: *Nuclear Instruments and Methods in Physics Research Section B: Beam Interactions with Materials and Atoms* (2019). DOI: `10.1016/j.nimb.2019.04.026`.

[31] T. Kron et al. "Hyperfine structure study of 97-99Tc in a new laser ion source for high-resolution laser spectrsocopy". In: *Preparation for publication* (2019).

[32] K. Chrysalidis et al. "First demonstration of Doppler-free 2-photon in-source laser spectroscopy at the ISOLDE-RILIS". In: *Nuclear Instruments and Methods in Physics Research Section B: Beam Interactions with Materials and Atoms* (2019). DOI: `10.1016/j.nimb.2019.04.020`.

[33] W. Demtröder. *Experimentalphysik*. 4., überarb. Aufl. Springer-Lehrbuch. Berlin: Springer, 2010. ISBN: 978-3-642-03910-2.

[34] W. Demtröder. *Laserspektroskopie: Grundlagen und Techniken*. Fünfte, erweiterte und neubearbeitete Auflage. Berlin, Heidelberg: Springer-Verlag Berlin Heidelberg, 2007. ISBN: 978-3-540-33792-8. DOI: 10.1007/978-3-540-33793-5.

[35] W. Demtröder. *Laserspektroskopie 2: Experimentelle Techniken*. 6. neu bearb. und aktualisierte Aufl. Berlin and Heidelberg: Springer, 2013. ISBN: 978-3-642-21446-2. DOI: 10.1007/978-3-642-21447-9.

[36] G. Drake, ed. *Springer Handbook of Atomic, Molecular, and Optical Physics*. New York, NY: Springer Science+Business Media Inc, 2006. ISBN: 978-0-387-20802-2. DOI: 10.1007/978-0-387-26308-3.

[37] A. Bohr. "On the quantization of angular momenta in heavy nuclei". In: *Physical Review* 81.1 (1951), pp. 134–138. DOI: 10.1103/PhysRev.81.134.

[38] J. Bieroń and P. Pyykkö. "Nuclear quadrupole moments of bismuth". In: *Physical review letters* 87.13 (2001), p. 133003. DOI: 10.1103/PhysRevLett.87.133003.

[39] J. E. Rosenthal and G. Breit. "The isotope shift in hyperfine structure". In: *Physical Review* 41.4 (1932), pp. 459–470. DOI: 10.1103/PhysRev.41.459.

[40] A. Bohr and V. F. Weisskopf. "The influence of nuclear structure on the hyperfine structure of heavy elements". In: *Physical Review* 77.1 (1950), pp. 94–98. DOI: 10.1103/PhysRev.77.94.

[41] J. R. Persson. "Table of hyperfine anomaly in atomic systems". In: *Atomic Data and Nuclear Data Tables* 99.1 (2013), pp. 62–68. DOI: 10.1016/j.adt.2012.04.002.

[42] B. Cheal, T. E. Cocolios, and S. Fritzsche. "Laser spectroscopy of radioactive isotopes: Role and limitations of accurate isotope-shift calculations". In: *Physical Review A* 86.4 (2012). DOI: 10.1103/PhysRevA.86.042501.

[43] W. H. King. *Isotope shifts in atomic spectra*. Physics of Atoms and Molecules. Boston, MA and s.l.: Springer US, 1984. ISBN: 978-1-4899-1786-7. DOI: 10.1007/978-1-4899-1786-7.

[44] M. J. Dresser. "The Saha–Langmuir equation and its application". In: *Journal of Applied Physics* 39.1 (1968), pp. 338–339. DOI: 10.1063/1.1655755.

[45] Megh Nad Saha. "Versuch einer Theorie der physikalischen Erscheinungen bei hohen Temperaturen mit Anwendungen auf die Astrophysik". In: *Z. Physik (Zeitschrift für Physik)* 6.1 (1921), pp. 40–55. DOI: 10.1007/BF01327962.

[46] I. Langmuir and K. H. Kingdon. "Thermionic Effects Caused by Vapours of Alkali Metals". In: *Proceedings of the Royal Society A: Mathematical, Physical and Engineering Sciences* 107.741 (1925), pp. 61–79. DOI: 10.1098/rspa.1925.0005.

[47] R. Kirchner. "On the thermoionization in hot cavities". In: *Nuclear Instruments and Methods in Physics Research Section A: Accelerators, Spectrometers, Detectors and Associated Equipment* 292.2 (1990), pp. 203–208. DOI: 10.1016/0168-9002(90)90377-I.

[48] F. Schwellnus et al. "The laser ion source and trap (LIST) – A highly selective ion source". In: *Nuclear Instruments and Methods in Physics Research Section B: Beam Interactions with Materials and Atoms* 266.19-20 (2008), pp. 4383–4386. DOI: 10.1016/j.nimb.2008.05.065.

[49] K. Blaum et al. "A novel scheme for a highly selective laser ion source". In: *Nuclear Instruments and Methods in Physics Research Section B: Beam Interactions with Materials and Atoms* 204 (2003), pp. 331–335. DOI: 10.1016/S0168-583X(02)01942-0.

[50] E. D. Donets. "Review of the JINR Electron Beam Ion Sources". In: *IEEE Transactions on Nuclear Science* 23.2 (1976), pp. 897–903. DOI: 10.1109/TNS.1976.4328375.

[51] R. Kirchner and E. Roeckl. "Investigation of gaseous discharge ion sources for isotope separation on-line". In: *Nuclear Instruments and Methods* 133.2 (1976), pp. 187–204. DOI: 10.1016/0029-554X(76)90607-8.

[52] V. S. Letokhov. *Laser photoionization spectroscopy*. 1st ed. Orlando, Fla.: Academic Press, 1987. ISBN: 0-12-444320-6.

[53] T. Gottwald. "Studium hochkomplexer atomarer Spektren mittels Methoden der Laser-resonanzionisation". Ph.D. thesis. Johannes Gutenberg-Universität Mainz, 2010.

[54] M. L. Citron et al. "Experimental study of power broadening in a two-level atom". In: *Physical Review A* 16.4 (1977), pp. 1507–1512. DOI: 10.1103/PhysRevA.16.1507.

[55] R. P. de Groote et al. "Efficient, high-resolution resonance laser ionization spectroscopy using weak transitions to long-lived excited states". In: *Physical Review A* 95.3 (2017), p. 1693. DOI: 10.1103/PhysRevA.95.032502.

[56] N. V. Vitanov et al. "Power broadening revisited: Theory and experiment". In: *Optics Communications* 199.1-4 (2001), pp. 117–126. DOI: 10.1016/S0030-4018(01)01495-X.

[57] N. B. Delone and Vladimir P. Krainov. "AC Stark shift of atomic energy levels". In: *Physics-Uspekhi* 42.7 (1999), pp. 669–687. DOI: 10.1070/PU1999v042n07ABEH000557.

[58] S. M. Abrarov and B. M. Quine. "Efficient algorithmic implementation of the Voigt/complex error function based on exponential series approximation". In: *Applied Mathematics and Computation* 218.5 (2011), pp. 1894–1902. DOI: 10.1016/j.amc.2011.06.072.

[59] S. M. Abrarov and B. M. Quine. *On the Fourier expansion method for highly accurate computation of the Voigt/complex error function in a rapid algorithm*.

[60] J. J. Olivero and R. L. Longbothum. "Empirical fits to the Voigt line width: A brief review". In: *Journal of Quantitative Spectroscopy and Radiative Transfer* 17.2 (1977), pp. 233–236. DOI: 10.1016/0022-4073(77)90161-3.

[61] C. Mattolat. "Spektroskopische Untersuchungen an Technetium und Silizium - Ein Festkörperlasersystem für die Resonanzionisationsspektroskopie". Ph.D. thesis. Johannes Gutenberg-Universität Mainz, 2010.

[62] V. Sonnenschein. "Laser developments and high resolution resonance ionization spectroscopy of actinide elements". Ph.D. thesis. University of Jyväskylä, 2014.

[63] P. F. Moulton. "Spectroscopic and laser characteristics of Ti:Al2O3". In: *Journal of the Optical Society of America B* 3.1 (1986), p. 125. DOI: 10.1364/JOSAB.3.000125.

[64] Bahaa E. A. Saleh and Malvin Carl Teich. *Grundlagen der Photonik*. 2., vollst. überarb. und erw. Aufl. Lehrbuch Physik. Weinheim: Wiley-VCH, 2008. ISBN: 9783527406777.

[65] P. Naubereit et al. "Resonance ionization spectroscopy of sodium Rydberg levels using difference frequency generation of high-repetition-rate pulsed Ti:sapphire lasers". In: *Physical Review A* 93.5 (2016). DOI: 10.1103/PhysRevA.93.052518.

[66] T. Kron. "Pushing the limits of resonance ionization mass spectrometry - ionization efficiency in palladium and spectral resolution in technetium". Ph.D. thesis. Johannes Gutenberg-Universität Mainz, 2016.

[67] T. Kieck et al. *Highly efficient isotope separation and ion implantation of 163Ho for the ECHo project*.

[68] U. Köster. "Resonance ionization laser ion sources". In: *Nuclear Physics A* 701.1-4 (2002), pp. 441–451. DOI: 10.1016/S0375-9474(01)01625-6.

[69] R. Horn. "Aufbau eines Systems gepulster, abstimmbarer Festkörperlaser zum Einsatz in der Resonaznionisations-Massenspektrometrie". Ph.D. thesis. Johannes Gutenberg-Universität Mainz, 2003.

[70] S. Rothe. "An all-solid state laser system for the laser ion source RILIS and in-source laser spectroscopy of astatine at ISOLDE/CERN". Ph.D. thesis. Johannes Gutenberg-Universität Mainz, 2012. DOI: 10.17181/CERN.0HNZ.7Z6X.

[71] R. E. Rossel. "Programming of the wavelength stabilization for a Titanium:sapphire laser using LabVIEW and implementation into the CERN ISOLDE RILIS measurement system". B.Sc. Thesis. Hochschule RheinMain, 2011.

[72] R. E. Rossel. "A distributed monitoring and control system for the laser ion source RILIS at CERN-ISOLDE". M.Sc. thesis. Hochschule RheinMain, 2015. DOI: 10.17181/CERN.L5N9.2GCS.

[73] V. Sonnenschein et al. "Characterization of a pulsed injection-locked Ti:sapphire laser and its application to high resolution resonance ionization spectroscopy of copper". In: *Laser Physics* 27.8 (2017), p. 085701. DOI: 10.1088/1555-6611/aa7834.

[74] T. Fischbach. "Aufbau und Charaktersisierung einer interferometrischen Frequenzstabilisierung für Diodenlaser". Diploma thesis. Johannes Gutenberg-Universität Mainz, 2012.

[75] Volker Sonnenschein et al. "A direct diode pumped continuous-wave Ti:sapphire laser as seed of a pulsed amplifier for high-resolution resonance ionization spectroscopy". In: *Nuclear Instruments and Methods in Physics Research Section B: Beam Interactions with Materials and Atoms* (2019). DOI: 10.1016/j.nimb.2019.03.017.

[76] K. Zimmer. "Konzeption, Aufbau und Test der Ionenoptik des RISIKO-Massenseparators". Diploma thesis. Johannes Gutenberg-Universität Mainz, 1990.

[77] S. Richter. "Implementierung der Laserionenquellenfalle LIST bei ISOLDE und Validierung der Spezifikationen Effizienz und Selektivität". Ph.D. thesis. Johannes Gutenberg-Universität Mainz, 2015.

[78] V. Fedosseev et al. "Ion beam production and study of radioactive isotopes with the laser ion source at ISOLDE". In: *Journal of Physics G: Nuclear and Particle Physics* 44.8 (2017), p. 084006. DOI: 10.1088/1361-6471/aa78e0.

[79] E. Bouquerel et al. "Beam purification by selective trapping in the transfer line of an ISOL target unit". In: *Nuclear Instruments and Methods in Physics Research Section B: Beam Interactions with Materials and Atoms* 266.19-20 (2008), pp. 4298–4302. DOI: 10.1016/j.nimb.2008.05.060.

[80] F. Schwellnus et al. "Study of low work function materials for hot cavity resonance ionization laser ion sources". In: *Nuclear Instruments and Methods in Physics Research Section B: Beam Interactions with Materials and Atoms* 267.10 (2009), pp. 1856–1861. DOI: 10.1016/j.nimb.2009.02.068.

[81] J. L. Henares et al. "Optimization of a hot-cavity type resonant ionization laser ion source". In: *The Review of scientific instruments* 87.2 (2016), 02B701. DOI: 10.1063/1.4931618.

[82] S. Rothe et al. "Advances in surface ion suppression from RILIS: Towards the Time-of-Flight Laser Ion Source (ToF-LIS)". In: *Nuclear Instruments and Methods in Physics Research Section B: Beam Interactions with Materials and Atoms* 376 (2016), pp. 86–90. DOI: 10.1016/j.nimb.2016.02.060.

[83] T. Kieck et al. "Optimization of a laser ion source for 163Ho isotope separation". In: *The Review of scientific instruments* 90.5 (2019), p. 053304. DOI: 10.1063/1.5081094.

[84] S. Schmidt. "Optimierung der Temperaturverteilung in der Ionenquelle des RISIKO-Massenseparators". Staatsexamensarbeit. Johannes Gutenberg-Universität Mainz, 2015.

[85] J. R. Pierce. *Theory and Design of Electron Beams*. 2nd ed. D. Van Nostrand Co., Inc., 1954.

[86] F. Schneider. "First Steps of the ECHo Experiment: Penning-Trap Mass Measurements of the 163Ho Electron Capture Process and Implantation of ultrapure Ho into Microcalorimeter Arrays". Ph.D. thesis. Johannes Gutenberg-Universität Mainz, 2016.

[87] D. A. Fink et al. "First application of the Laser Ion Source and Trap (LIST) for on-line experiments at ISOLDE". In: *Nuclear Instruments and Methods in Physics Research Section B: Beam Interactions with Materials and Atoms* 317 (2013), pp. 417–421. DOI: 10.1016/j.nimb.2013.06.039.

[88] D. A. Fink et al. "On-line implementation and first operation of the Laser Ion Source and Trap at ISOLDE/CERN". In: *Nuclear Instruments and Methods in Physics Research Section B: Beam Interactions with Materials and Atoms* 344 (2015), pp. 83–95. DOI: 10.1016/j.nimb.2014.12.007.

[89] K. Wies. "Entwicklung des Laserionenquellen- und fallenprojekts LIST für Ultraspurendetektion und Grundlagenforschung". Ph.D. thesis. Johannes Gutenberg-Universität Mainz, 2006.

[90]   F. Schwellnus. "Entwicklung von Ionenquellen zur Optimierung von Selektivität und Effizienz bei der resonanten Laserionisation". Ph.D. thesis. Johannes Gutenberg-Universität Mainz, 2010.

[91]   D. A. Fink. "Improving the selectivity of the ISOLDE resonance ionization laser ion source and in-source laser spectroscopy of polonium". Heidelberg University Library. 2014. DOI: 10.11588/heidok.00016725.

[92]   D. A. Fink et al. "In-source laser spectroscopy with the laser ion source and trap: First direct study of the ground-state properties of 217,219Po". In: *Physical Review X* 5.1 (2015). DOI: 10.1103/PhysRevX.5.011018.

[93]   S. Raeder et al. "An ion guide laser ion source for isobar-suppressed rare isotope beams". In: *The Review of scientific instruments* 85.3 (2014), p. 033309. DOI: 10.1063/1.4868496.

[94]   T. E. Cocolios et al. "High-resolution laser spectroscopy with the Collinear Resonance Ionisation Spectroscopy (CRIS) experiment at CERN-ISOLDE". In: *Nuclear Instruments and Methods in Physics Research Section B: Beam Interactions with Materials and Atoms* 376 (2016), pp. 284–287. DOI: 10.1016/j.nimb.2015.11.024.

[95]   S. Raeder et al. "Developments towards in-gas-jet laser spectroscopy studies of actinium isotopes at LISOL". In: *Nuclear Instruments and Methods in Physics Research Section B: Beam Interactions with Materials and Atoms* 376 (2016), pp. 382–387. DOI: 10.1016/j.nimb.2015.12.014.

[96]   A. Zadvornaya et al. "Characterization of supersonic gas jets for high-resolution laser ionization spectroscopy of heavy elements". In: *Physical Review X* 8.4 (2018), p. 357. DOI: 10.1103/PhysRevX.8.041008.

[97]   M. Trümper. "Weiterentwicklung der Laserionenquellenfalle LIST zur Untergrundunterdrückung bei der Resonanzionisation in kollinearer und transversaler Geometrie". B.Sc. thesis. Johannes Gutenberg-Universität Mainz, 2015.

[98]   D. Manura and D. Dahl. "Simion 8 3-D electrostatic and charged particle trajectory simulation program". In: *Idaho National Laboratory, distributed by Scientific Instrument Services Inc., Ringoes, NJ, USA* (2008).

[99]   A. Kramida and Y. Ralchenko. *NIST Atomic Spectra Database, NIST Standard Reference Database 78*. 1999. DOI: 10.18434/T4W30F.

[100] C. Weichhold. "Entwicklung, Charakterisierung und Anwendung eines Aufbaus zur dopplerfreien Laserresonanzionisationsspektroskopie in einer hochselektiven Ionenquelle". Diploma thesis. Johannes Gutenberg-Universität Mainz, 2016.

[101] Douglas B. Chrisey, ed. *Pulsed laser deposition of thin films*. New York: Wiley, 1994. ISBN: 978-0471592181.

[102] L. Winkelmann. "Charakterisierung und Optimierung des Pulslaser-Depositionsprozesses für das ECHo-Projekt". B.Sc. thesis. Johannes Gutenberg-Universität Mainz, 2017.

[103] T. Gottwald. "Messung der Emittanz der Laserionenquellenfalle LIST am RISIKO Massenseparator". Diploma thesis. Johannes Gutenberg-Universität Mainz, 2007.

[104] J. Pitters et al. "Pepperpot emittance measurements of ion beams from an electron beam ion source". In: *Nuclear Instruments and Methods in Physics Research Section A: Accelerators, Spectrometers, Detectors and Associated Equipment* 922 (2019), pp. 28–35. DOI: 10.1016/j.nima.2018.12.072.

[105] Douglas L. Martin. "Specific heat below 3 °K, melting point, and melting heat of rubidium and cesium". In: *Canadian Journal of Physics* 48.11 (1970), pp. 1327–1339. DOI: 10.1139/p70-166.

[106] T. J. Killian. "Thermionic phenomena caused by vapors of rubidium and potassium". In: *Physical Review* 27.5 (1926), pp. 578–587. DOI: 10.1103/PhysRev.27.578.

[107] R. E. Honig and D. A. Kramer. *Vapor pressure data for the solid and liquid elements.* RCA Laboratories, David Sarnoff Research Center, 1969.

[108]   S. Millman and M. Fox. "Nuclear spins and magnetic moments of 85Rb and 87Rb". In: *Physical Review* 50.3 (1936), pp. 220–225. DOI: 10.1103/PhysRev.50.220.

[109]   J. E. Simsarian et al. "Lifetime measurements of the 7p levels of atomic francium". In: *Physical Review A* 57.4 (1998), pp. 2448–2458. DOI: 10.1103/PhysRevA.57.2448.

[110]   S. Bize et al. "High-accuracy measurement of the 87Rb ground-state hyperfine splitting in an atomic fountain". In: *Europhysics Letters (EPL)* 45.5 (1999), pp. 558–564. DOI: 10.1209/epl/i1999-00203-9.

[111]   J. Ye et al. "Hyperfine structure and absolute frequency of the 87Rb 5P_3/2 state". In: *Optics Letters* 21.16 (1996), p. 1280. DOI: 10.1364/OL.21.001280.

[112]   B. A. Palmer, R. A. Keller, and R. Engleman Jr. *Atlas of uranium emission intensities in a hollow cathode discharge.* 1980.

[113]   S. Pommé et al. "Measurement of the 225Ac half-life". In: *Applied radiation and isotopes : including data, instrumentation and methods for use in agriculture, industry and medicine* 70.11 (2012), pp. 2608–2614. DOI: 10.1016/j.apradiso.2012.07.014.

[114]   G. D. Alkhazov et al. "Nuclear deformation of holmium isotopes". In: *Nuclear Physics A* 504.3 (1989), pp. 549–561. DOI: 10.1016/0375-9474(89)90557-5.

[115]   Y. Nedjadi et al. "A new measurement of the half-life of 166mHo". In: *Applied radiation and isotopes : including data, instrumentation and methods for use in agriculture, industry and medicine* 70.9 (2012), pp. 1990–1996. DOI: 10.1016/j.apradiso.2012.02.063.

[116]   N. J. Stone. "Table of nuclear magnetic dipole and electric quadrupole moments". In: *Atomic Data and Nuclear Data Tables* 90.1 (2005), pp. 75–176. DOI: 10.1016/j.adt.2005.04.001.

[117]   C. M. Baglin. "Nuclear Data Sheets for A = 166". In: *Nuclear Data Sheets* 109.5 (2008), pp. 1103–1382. DOI: 10.1016/j.nds.2008.04.001.

[118]   W. Dankwort and J. Ferch. "Reevaluation of the atomic g_J-factor and the nuclear g_I-factor of165Ho". In: *Zeitschrift fr Physik* 267.3 (1974), pp. 239–241. DOI: 10.1007/BF01669226.

[119]   P. A. Baisden et al. "Measurement of the half-life of 163Ho". In: *Physical Review C* 28.1 (1983), pp. 337–341. DOI: 10.1103/PhysRevC.28.337.

[120]   Holger Dorrer et al. "Production, isolation and characterization of radiochemically pure 163Ho samples for the ECHo-project". In: *Radiochimica Acta* 106.7 (2018), pp. 535–547. DOI: 10.1515/ract-2017-2877.

[121]   M. P. Unterweger. "Half-life measurements at the National Institute of Standards and Technology". In: *Applied Radiation and Isotopes* 56.1-2 (2002), pp. 125–130. DOI: 10.1016/S0969-8043(01)00177-4.

[122]   W. C. Martin, Romuald Zalubas, and Lucy Hagan. *Atomic energy levels - the rare-earth elements.* Gaithersburg, MD: National Bureau of Standards, 1978. DOI: 10.6028/NBS.NSRDS.60.

[123]   R. L. Kurucz and B. Bell. *Atomic Line Data: CD-ROM No. 23.* Smithsonian Astrophysical Observatory, Cambridge, Mass., 1995.

[124]   J. Hostetter et al. "Measurement of holmium Rydberg series through magneto-optical trap depletion spectroscopy". In: *Physical Review A* 91.1 (2015), p. 71. DOI: 10.1103/PhysRevA.91.012507.

[125]   E. Grushka. "Characterization of exponentially modified Gaussian peaks in chromatography". In: *Analytical chemistry* 44.11 (1972), pp. 1733–1738. DOI: 10.1021/ac60319a011.

[126]   E. A. Den Hartog, L. M. Wiese, and J. E. Lawler. "Radiative lifetimes of HoI and HoII". In: *Journal of the Optical Society of America B* 16.12 (1999), p. 2278. DOI: 10.1364/JOSAB.16.002278.

[127]   M. Verlinde et al. "On the reliability of wavelength meters for medium- to high-resolution laser spectroscopy (preliminary title)". In: *Preparation for publication* (2019).

[128] H. Postma, A. R. Miedema, and Miss M.C. Eversdijk Smulders. "Angular distribution and linear polarization of gamma rays from aligned 166mHo nuclei". In: *Physica* 25.1-6 (1959), pp. 671–687. DOI: 10.1016/S0031-8914(59)97064-8.

[129] W. Dankwort, J. Ferch, and H. Gebauer. "Hexadecapole interaction in the atomic ground state of 165Ho". In: *Zeitschrift fr Physik* 267.3 (1974), pp. 229–237. DOI: 10.1007/BF01669225.

[130] K. S. Krane and J. D. Moses. "Nuclear orientation study of 166mHo". In: *Physical Review C* 24.2 (1981), pp. 654–664. DOI: 10.1103/PhysRevC.24.654.

[131] A. L. Allsop et al. "Properties of HoVO4 below 1 K: III. a nuclear orientation study of the Van Vleck enhanced nuclear antiferromagnet holmium vanadate". In: *Proceedings of the Royal Society A: Mathematical, Physical and Engineering Sciences* 372.1748 (1980), pp. 19–31. DOI: 10.1098/rspa.1980.0100.

[132] R. J. Elliott, ed. *Magnetic properties of rare earth metals*. Boston, MA: Springer, 1972. ISBN: 978-1-4757-5691-3. DOI: 10.1007/978-1-4757-5691-3.

[133] B. Burghardt et al. "Hyperfine structure measurements in metastable states of165Ho". In: *Z Physik A (Zeitschrift für Physik A Atoms and Nuclei)* 307.3 (1982), pp. 193–200. DOI: 10.1007/BF01438640.

[134] B. Olaniyi et al. "Electric quadrupole moments and strong interaction effects in pionic atoms of 165Ho, 175Lu, 176Lu, 179Hf and 181Ta". In: *Nuclear Physics A* 403.3 (1983), pp. 572–588. DOI: 10.1016/0375-9474(83)90623-1.

[135] C. J. Batty et al. "Nuclear quadrupole deformation effects on pionic and kaonic X-rays". In: *Nuclear Physics A* 355.2 (1981), pp. 383–402. DOI: 10.1016/0375-9474(81)90534-0.

[136] P. Ebersold et al. "Monopole and quadrupole strong interaction effects in pionic atoms of 175Lu and 165Ho". In: *Nuclear Physics A* 296.3 (1978), pp. 493–518. DOI: 10.1016/0375-9474(78)90087-8.

[137] R. J. Powers et al. "Muonic X-ray study of the charge distribution of 165Ho". In: *Nuclear Physics A* 262.3 (1976), pp. 493–515. DOI: 10.1016/0375-9474(76)90511-X.

[138] P. Axel et al. "Étude de la déformation du noyau d'holmium". In: *Journal de Physique* 27.5-6 (1966), pp. 262–268. DOI: 10.1051/jphys:01966002705-6026200.

[139] G. Fricke et al. "Nuclear ground state charge radii from electromagnetic interactions". In: *Atomic Data and Nuclear Data Tables* 60.2 (1995), pp. 177–285. DOI: 10.1006/adnd.1995.1007.

[140] I. Angeli and K. P. Marinova. "Table of experimental nuclear ground state charge radii: An update". In: *Atomic Data and Nuclear Data Tables* 99.1 (2013), pp. 69–95. DOI: 10.1016/j.adt.2011.12.006.

[141] G. Fricke et al., eds. *Numerical data and functional relationships in science and technology: New series*. Berlin: Springer, 2004. ISBN: 3540428291.

[142] F. Schneider et al. "Resonance ionization of holmium for ion implantation in microcalorimeters". In: *Nuclear Instruments and Methods in Physics Research Section B: Beam Interactions with Materials and Atoms* 376 (2016), pp. 388–392. DOI: 10.1016/j.nimb.2015.12.012.

[143] M. Knudsen. "Die Molekularströmung der Gase durch Öffnungen und die Effusion". In: *Annalen der Physik* 333.5 (1909), pp. 999–1016. DOI: 10.1002/andp.19093330505.

[144] M. Knudsen. "Die Gesetze der Molekularströmung und der inneren Reibungsströmung der Gase durch Röhren". In: *Annalen der Physik* 333.1 (1909), pp. 75–130. DOI: 10.1002/andp.19093330106.

[145] H. Mayer. "Über eine experimentelle Methode zur Messung von Molekularstrahlung". In: *Z. Physik (Zeitschrift für Physik)* 52.3-4 (1929), pp. 235–248. DOI: 10.1007/BF01342399.

[146] P. Clausing. "Über die Strahlformung bei der Molekularströmung". In: *Z. Physik (Zeitschrift für Physik)* 66.7-8 (1930), pp. 471–476. DOI: 10.1007/BF01402029.

[147] N. Ramsey. *Molecular beams*. Oxford University Press, 1986. ISBN: 9780198520214. DOI: 10.1093/acprof:oso/9780198520214.001.0001.

[148] M. Knudsen. "Das Cosinusgesetz in der kinetischen Gastheorie". In: *Annalen der Physik* 353.24 (1916), pp. 1113–1121. DOI: 10.1002/andp.19163532409.

[149] V. Sonnenschein. "Untersuchung zum Abdampf- und Atomisationsverhalten verschiedener Elemente zur Steigerung der Effizienz bei HR-RIMS und LIST". Diploma thesis. Johannes Gutenberg-Universität Mainz, 2008.

[150] J. Lettry et al. "Alkali suppression within laser ion-source cavities and time structure of the laser ionized ion-bunches". In: *Nuclear Instruments and Methods in Physics Research Section B: Beam Interactions with Materials and Atoms* 204 (2003), pp. 363–367. DOI: 10.1016/S0168-583X(02)01967-5.

[151] Y. Liu et al. "Time profile of ion pulses produced in a hot-cavity laser ion source". In: *The Review of scientific instruments* 81.2 (2010), 02A505. DOI: 10.1063/1.3273071.

[152] V. I. Mishin et al. "Resonant Ionization Laser Ion Source (RILIS) with improved selectivity achieved by ion pulse compression using in-source time-of-flight technique". In: *AIP Conference Proceedings*. AIP, 2009, pp. 207–212. DOI: 10.1063/1.3115604.

[153] M. Menat. "A quantitative study of scattering phenomena in an electromagnetic separator". In: *Canadian Journal of Physics* 42.1 (1964), pp. 164–192. DOI: 10.1139/p64-013.

[154] M. Menat and G. Frieder. "Scattering phenomena in double-direction focusing electromagnetic mass separators". In: *Canadian Journal of Physics* 43.8 (1965), pp. 1525–1542. DOI: 10.1139/p65-142.

[155] Y. Jading et al. "Production of radioactive Ag ion beams with a chemically selective laser ion source". In: *Nuclear Instruments and Methods in Physics Research Section B: Beam Interactions with Materials and Atoms* 126.1-4 (1997), pp. 76–80. DOI: 10.1016/s0168-583x(96)01018-x.

[156] M. Koizumi et al. "A laser ion source with a thin ohmic-heating ionizer for the TIARA-ISOL". In: *Nuclear Instruments and Methods in Physics Research Section B: Beam Interactions with Materials and Atoms* 204 (2003), pp. 359–362. DOI: 10.1016/s0168-583x(02)01962-6.

Publikationen

R. Heinke et al., *Atom beam emersion from hot cavity laser ion sources*
Nuclear Instruments and Methods in Physics Research Section B: Beam Interactions
with Materials and Atoms (2019), doi: 10.1016/j.nimb.2019.04.026.

R. Heinke et al., *High-resolution in-source laser spectroscopy in perpendicular geometry*
Hyperfine Interactions 238.1 (2017), p. 127; doi: 10.1007/s10751-016-1386-2

T. Kron et al., *Hyperfine structure study of 97-99Tc in a new laser ion source for
high-resolution laser spectrsocopy*
Publication in preparation (2019)

Dominik Studer et al., *Atomic transitions and the first ionization potential of prome-
thium determined by laser spectroscopy*
Physical Review A 99.6 (2019), p. 807; doi: 10.1103/PhysRevA.99.062513

K. Chrysalidis et al., *First demonstration of Doppler-free 2-photon in-source laser
spectroscopy at the ISOLDE-RILIS*
Nuclear Instruments and Methods in Physics Research Section B: Beam Interactions
with Materials and Atoms (2019); doi: 10.1016/j.nimb.2019.04.020

Vadim Gadelshin et al., *Measurement of the laser resonance ionization efficiency for
lutetium*
Radiochimica Acta 107.7 (2019), pp. 653-661; doi: 10.1515/ract-2019-3118

T. Day Goodacre et al., *Radium ionization scheme development: The first observed
autoionizing states and optical pumping effects in the hot cavity environment*
Spectrochimica Acta Part B: Atomic Spectroscopy 150 (2018), pp. 99-104;
doi: 10.1016/j.sab.2018.10.002

K. M. Lynch et al., *Laser-spectroscopy studies of the nuclear structure of neutron-
rich radium*
Physical Review C 97.2 (2018); doi: 10.1103/PhysRevC.97.024309

V. Gadelshin et al., *Laser resonance ionization spectroscopy on lutetium for the MEDI-
CIS project*
Hyperfine Interactions 238.1 (2017), p. 265; doi: 10.1007/s10751-017-1406-x

C. Granados et al., *In-gas laser ionization and spectroscopy of actinium isotopes near
the N=126 closed shell*
Physical Review C 96.5 (2017); doi: 10.1103/PhysRevC.96.054331

D. Studer et al., *Resonance ionization spectroscopy in dysprosium*
Hyperfine Interactions 238.1 (2017), 02A916; doi: 10.1007/s10751-016-1384-4

S. Raeder et al., *High resolution spectroscopy of the hyperfine structure splitting in
97,99Tc*
Hyperfine Interactions 238.15 (2017); doi: 10.1007/s10751-016-1389-z

S. Rothe et al., *Laser photodetachment of radioactive 128I⁻*
Journal of Physics G: Nuclear and Particle Physics 44.10 (2017), p. 104003; doi: 10.1088/1361-6471/aa80aa

R. Ferrer et al., *Towards high-resolution laser ionization spectroscopy of the heaviest elements in supersonic gas jet expansion*
Nature communications 8 (2017), p. 14520; doi: 10.1038/ncomms14520.

S. Raeder et al., *Developments towards in-gas-jet laser spectroscopy studies of actinium isotopes at LISOL"*
Nuclear Instruments and Methods in Physics Research Section B: Beam Interactions with Materials and Atoms 376 (2016), pp. 382-387; doi: 10.1016/j.nimb.2015.12.014

Forschungsaufenthalte

10/2018	Erstmalige experimentelle Bestimmung der Elektronenaffinität des Astats mit der GANDALPH-Apparatur ISOLDE On-line Facility, CERN
02 - 06/2018	Implementation einer adaptierten LIST-Ionenquelle an ISOLDE zur Messung des Verzweigungsverhältnisses des super-erlaubten Zerfalls von Magnesium-22 ISOLDE On-line Facility, CERN
06/2017	Hochauflösende in-source Laserspektroskopie an Bismut ISOLDE On-line Facility, CERN
04 & 05/2017	Hyperfeinstrukturspektroskopie an Indium innerhalb der CRIS-Kollaboration ISOLDE On-line Facility, CERN
03/2017	Aufbau und Inbetriebnahme eines geseedeten Ring-Titan:Saphirlasers für Doppler-freie 2-Photonenspektroskopie ISOLDE On-line Facility, CERN
07/2016	Hochauflösende in-source Laserspektroskopie an Bismut ISOLDE On-line Facility, CERN
06/2016	Erstmaliges Laser-Photodetachment von radioaktiven Spezies (Iod-128 und Astat) mit der GANDALPH-Apparatur an ISOLDE ISOLDE On-line Facility, CERN
04/2016	Aufbau und Inbetriebnahme des schnellen Beam-Gating-Systems am ISOLDE Off-line Separator ISOLDE On-line Facility, CERN
11/2015	Aufbau und Inbetriebnahme eines gittergestützten Titan:Saphirlasers ISOLDE On-line Facility, CERN
06 & 07/2015	Aufbau und Inbetriebnahme der GANDALPH-Apparatur; erstmaliges Laser-Photodetachment an ISOLDE ISOLDE On-line Facility, CERN
02 & 04/2015	Photodetachment-Tests mit hochrepetierendem Lasersystem GUNILLA Laboratory, Gothenburg University
12/2014	Hochauflösende Laserspektroskopie an Actinium LISOL On-line Facility, Louvain-la-Neuve & KU Leuven

Konferenzbeiträge

09/2018	International Conference on Electromagnetic Isotope Separators and Related Topics (EMIS) Genf, Schweiz *On-line results from ISOLDE's Laser Ion Source and Trap LIST* (Vortrag)
12/2017	ISOLDE Workshop and Users Meeting CERN, Schweiz *LIST 2.0 - New features and ongoing developments for ISOLDE's Laser Ion Source and Trap LIST* (Poster)
10/2017	International Conference on Ion Sources (ICIS) Genf, Schweiz *Towards Direct High-resolution Laser Spectroscopy on Exotic Isotopes at Hot Cavity Ion Sources: Crossed Laser - Atom Beam Interaction in the Laser Ion Source and Trap LIST* (Poster) **Ausgezeichnet mit dem „Young Scientist Award"**
05/2017	Advances in Radioactive Isotope Science (ARIS) Keystone (CO), USA *Towards On-Line High Resolution In-source Laser Spectroscopy: A Perpendicular Laser - Atom Beam Upgrade for the Laser Ion Source and Trap LIST* (Poster)
03/2017	DPG Frühjahrstagung, Sektion AMOP Mainz *High-resolution In-source Laser Spectroscopy of Hyperfine Structures and Isotope Shifts on ^{163,165,166m}Ho Isotopes for the ECHo project* (Vortrag) und *Towards High-resolution In-source Laser Spectroscopy On-Line: A Perpendicular Laser - Atom Beam Upgrade for the Laser Ion Source and Trap LIST at CERN/ISOLDE* (Vortrag)
12/2016	ISOLDE Workshop and User Meeting CERN, Schweiz *Towards On-Line High Resolution In-source LAser Spectroscopy: A Perpendicular Laser - Atom Beam Upgrade for the Laser Ion Source and Trap LIST* (Poster)
05/2016	Application of Lasers and Storage Devices in Atomic and Nuclei Research Poznan, Polen *Towards Isobar-free High-Resolution In-source Spectroscopy on-line: New Features of the Laser Ion Source and Trap LIST* (Poster)
03/2016	DPG Frühjahrstagung, Sektion AMOP Hannover *Towards Electron Affinity Measurements of Radioactive Elements: Laser Photodetachment of Negative Ions at CERN/ISOLDE* (Vortrag)

05/2015	International Conference on Electromagnetic Isotope Separators and Related Topics (EMIS) Grand Rapids, USA *Application and further improvement of the Laser Ion Source and Trap (LIST) at ISOLDE/CERN* (Poster)
03/2015	DPG Frühjahrstagung, Sektion AMOP Heidelberg *Einsatz und weitere Optimierung der hochselektiven Laserionenquellen-falle LIST bei ISOLDE/CERN* (Vortrag)

Curriculum Vitae not included in electronic version of this work.